π^0 PRODUCTION WITH K^- and π^+ BEAMS AT $530\,GeV/c$

by

Armando Lanaro

Submitted in Partial Fulfillment

of the

Requirement for the Degree

DOCTOR OF PHILOSOPHY

Supervised by Professor Thomas Ferbel

Department of Physics and Astronomy

University of Rochester
Rochester, New York

1989

A Elio e Nadia

Acknowledgments

I wish to thank all the people who talked to me close enough to be heard.

Not that one is the first to see something new, but that one sees as new what is old, long familiar, seen and overlooked by everybody, is what distinguishes truly original minds. The first discoverer is ordinarily that wholly common creature, devoid of spirit and addicted to fantasy - accident.

Friedrich Nietzsche

Abstract

In this thesis we report on measurements of inclusive neutral pion production at large transverse momenta (p_T) in collision of $530\,GeV/c$ ($\sqrt{s} = 31.5\,GeV$) K^- and π^+ beams with a copper and beryllium combined target. The π^0 acceptance in center-of-mass rapidity is $|y| < 0.7$, for p_T values greater than $3.5\,GeV/c$ (negative beam) and $4.25\,GeV/c$ (positive beam). The data were taken using the large acceptance liquid argon calorimeter of the E706 spectrometer at Fermilab, and analyzed using the standard E706 reconstruction package. Ratios on π^0 yields using π^+, π^-, K^- and p are presented. The results are used to examine issues of scaling in point-like hadronic collisions at high energies and large transverse momenta.

Table of Contents

List of Tables

List of Figures

Chapter 1

THEORETICAL BACKGROUND

1.1 Introduction

The observation of particles produced at large transverse momentum (p_T) has provided considerable insight into the fundamental interactions among hadronic constituents (partons). In particular, the view that mesons produced at large p_T are generated in hard collisions between quarks and gluons that are present in the initial hadrons, has been found to be very fruitful. The outgoing quarks and gluons are assumed to distribute their momentum over a collection of hadrons that form a *jet* along the direction of any outgoing parton. In this view, the production of large p_T π^0s is due to the fragmentation of partons, and not to their direct emission in the elementary parton-parton scattering process. This fact makes it difficult, even in principle, to decouple parton scattering dynamics from fragmentation. A cleaner way of gaining information about the elementary process is, for example, to investigate the production of *direct photons* at large p_T. Direct photons, i.e., photons that do not originate from the decays of hadrons, are interesting

because they provide a means for probing large-momentum-transfer subprocesses, without requiring the unravelling of unknown fragmentation functions. Although photons couple to electric charge, while quarks and gluons interact via the color force, direct-photon production yields information which is quite similar in content, but easier to interpret, than that obtained from hadron and jet production. The production of direct photons is suppressed relative to jet production by the ratio of the electromagnetic to the strong coupling constants. Nevertheless, the yield of direct photons at large p_T, is comparable to that of single hadrons, because the latter arises through the fragmentation of a parton into the observed hadron. In addition, more diagrams contribute to the jet than to the direct-photon yield. Because jets provide a large source of π^0s, any direct-photon signal is expected to have a large background from the electromagnetic decay of such neutral mesons. In this experiment, it was essential to detect π^0s and ηs with high efficiency, since unresolved $\pi^0, \eta \rightarrow \gamma\ \gamma$ decays represent the main background to direct photons. Consequently, although π^0 production is more difficult to interpret than γ production, the signal is experimentally far cleaner than that of γs, and provides complementary information on strong interactions, as well as unique data on parton fragmentation.

To investigate the possible role of hadronic constituents in large-p_T particle production, it is important to compare reactions initiated by different incident particles, with different internal structure. We will present results on inclusive

π^0s yields for a negative beam of incident pions and kaons and for a positive beam of protons and pions. The inclusive yield is more amenable to theoretical interpretation than exclusive reactions, and reflects more clearly the dynamics of multiparticle production in hadronic interactions at high energies.

In the following, we will introduce some fundamental concepts from the current theory of strong interactions. In particular, we will describe the formalism used to investigate large-p_T inclusive reactions. Far from being exhaustive, the following is intended to provide a phenomenological introduction to the subject.

1.2 Definition of Kinematic Variables

Before going into the detail of the formalism used to describe inclusive production of particles at large transverse momentum, we will define the common variables and notation that will follow in the rest of this thesis. Unless specified to the contrary, we will restrict ourselves to definitions of variables in the center-of-mass system. Upper case letters will designate the hadrons that participate in the scattering, while lower case letters will refer to hadron constituents.

In order to discuss the kinematics of single-particle inclusive processes, we will use the standard Mandelstam variables. A general inclusive single-particle reaction can be written in the form:

$$A + B \rightarrow C + X$$

where X refers to any objects produced in association with particle C in the

scattering of particles A and B. If p_A, p_B and p_C are the respective four-momenta of the particles, then the Mandelstam variables are defined as:

$$s = (p_A + p_B)^2$$

$$t = (p_A - p_C)^2$$

$$u = (p_B - p_C)^2$$

where s is the square of the center of mass energy, and t and u are the squares of the four-momenta transfered from hadron A to C and from B to C, respectively. The same variables, but with a carrot symbols above them, will be used to refer to the same inclusive process but at the constituent level. In the case of scattering of purely massless constituents ($a + b \rightarrow c + d$), these last set of variables satisfy the energy-momentum conservation requirement:

$$\hat{s} + \hat{t} + \hat{u} = 0$$

We denote by p_T and p_L the transverse and the longitudinal component of momentum, choosing the beam axis as reference. The transverse momentum p_T is invariant under a Lorentz transformation along the line of collision between the incident particles. We define two scaled variables x_T and x_F as follows:

$$x_T = \frac{2p_T}{\sqrt{s}} \ , \ 0 < x_T < 1$$

$$x_F = \frac{2p_L}{\sqrt{s}} \ , \ -1 < x_F < 1$$

A useful variable for describing the longitudinal motion of relativistic particles of energy E is the rapidity y, defined in any frame as:

$$y = \frac{1}{2} \ln \frac{E+p_L}{E-p_L}$$

When the mass of a particle can be ignored relative to its p_T, this variable is called the pseudo-rapidity η, and takes the simple form

$$\eta = \ln \cot \frac{\theta}{2} = -\ln tan \frac{\theta}{2}$$

where θ is the center-of-mass scattering angle. At large p_T, a particle's mass can usually be neglected. For a boost along the z direction (usually chosen as the beam axis), the rapidity changes by a constant Δ, which can be defined using the velocity of the transformation (β), or the Lorentz factor (γ) as:

$$\gamma = \cosh \Delta$$

$$\beta = \tanh \Delta$$

When considering elementary subprocess, one introduces the fraction of longitudinal momenta x_a and x_b carried by the interacting partons a and b, respectively. Using these variables, we can rewrite the Mandelstam relations for massless parton in the form:

$$\hat{s} = x_a \, x_b \, s$$

$$\hat{t} = x_a \, t = -x_a \sqrt{s} p_T \, e^{-y}$$

$$\hat{u} = x_b \, u = -x_b \sqrt{s} p_T \, e^{y}$$

where p_T and y now refer to the scattered parton c.

1.3 QCD Phenomenology of High p_T Inclusive Processes

During the past ten years, great experimental effort has been devoted to verify the fundamentals of the theory that best describes the strong interactions among the hadronic constituents (quarks and gluons), namely Quantum Chromodynamics (QCD). One of the key features of the theory is the discovery of *asymptotic freedom* [1,2,3,4]. This concept is based on the weakening of the effective quark-gluon coupling at short distances or, equivalently, at large momentum transfer Q^2. If correct, then, in the large-Q^2 limit, short-range hadronic interactions can be described by means of well known perturbative techniques. If the description of large-p_T meson production in hadron-hadron collisions were consistent with QCD predictions at large Q^2, then experimental data could be used to extract unambiguous information on quantities such us the momentum distributions of constituents within hadrons (structure functions). From a theoretical point of view, a rigorous calculation of structure functions would require knowledge of hadron wave-functions in a region where Q^2 is small, and perturbation theory therefore cannot be applied. In the absence of a complete theory, in practice one obtains information on structure from experimental results by measuring structure functions at large Q^2, and evolving them via QCD to any desired Q^2 regime.

Another QCD process involving small momentum transfers is *hadronization* of outgoing quarks and gluons. This represents the major mechanism for large-p_T neutral mesons production. The so called *fragmentation functions*, describing

the materialization of quark and gluon jets into detectable particles, also cannot be calculated from first principles (that is from non-perturbative techniques). Once again, this type of information must therefore be derived from experimental data. From our discussion, we can see that production of neutral mesons involves more complicated mechanisms (fragmentation) than the production of single photons. Nevertheless, both processes present very interesting aspects of particle phenomenology, and provide useful general tests of the theory. Direct-photon physics provides the possibility for a precise extraction of quark and gluon structure functions, while production of π^0s involves a convolution of hadron structure and fragmentation of the elementary constituents.

1.3.1 Cross Section

In QCD, in order to write the expression for the invariant cross section for hadronic processes involving large-p_T particles, one has to convolute the hard-scattering two-body subprocess with the constituents structure functions, and the eventual fragmentation functions. Consider the inclusive reaction $A + B \rightarrow C + X$ (see Fig. 1.1). The probability of emitting hadron C into a four-volume element d^4p of 4-momentum space is proportional to the invariant cross section $d\sigma/d^4p_c$.

When the particle has a real mass m_c (is *on the mass shell*), namely when $m_c^2 = E_c^2 - p_c^2c^2$ is constant, $d\sigma/d^4p_c$ reduces to $2\,E_c\,d\sigma/d^3p_c$, which can be written

In fixed-target experiments, inclusive neutral meson production has been investigated using beams of different particles (p, $\pi^{\pm}$, $K^{\pm}$) incident on a variety of targets. In this section we summarize some of the results from previous experiments, and in the last chapter we will compare these results to those obtained in our analysis.

The CERN-Columbia-Oxford-Rockefeller (CCOR) Collaboration [14] published inclusive cross sections for the production of large-p_T π^0s near 90^0, for center-of-mass energies $\sqrt{s} = 30.7,\ 53.1$ and $62.4\,GeV$, for pp collisions at the CERN ISR. Detection of photons from π^0 decays was provided by a stack of Pb-glass shower counters surrounding the interaction point. Figure 1.5 shows inclusive π^0 invariant cross sections from CCOR for the above energies and, for comparison, also some earlier measurements from the CERN-Columbia-Rockefeller-Saclay (CCRS) Collaboration [15]. The π^0 p_T spectrum extends up to $14\,GeV/c$ at the highest available energy. The simultaneous fit of the cross sections at the three $\sqrt{s}$ values is also shown; this uses a universal scaling law of the form:

$$E\,\frac{d\sigma}{d^3p} = \frac{F(x_T)}{p_T^n} \tag{1.4}$$

The results (dashed lines) appear to be inconsistent with either a constant n ($n = 4$ is predicted by the parton model), or with n purely a function of x_T. Only the highest p_T data ($p_T > 7.5\,GeV/c$), at the two highest energies, were consistent with a scaling law of the type (1.4), with the exponent $n = 5.2 \pm 0.4$.

Another ISR experiment [16] had published similar results on large-p_T π^0 pro-

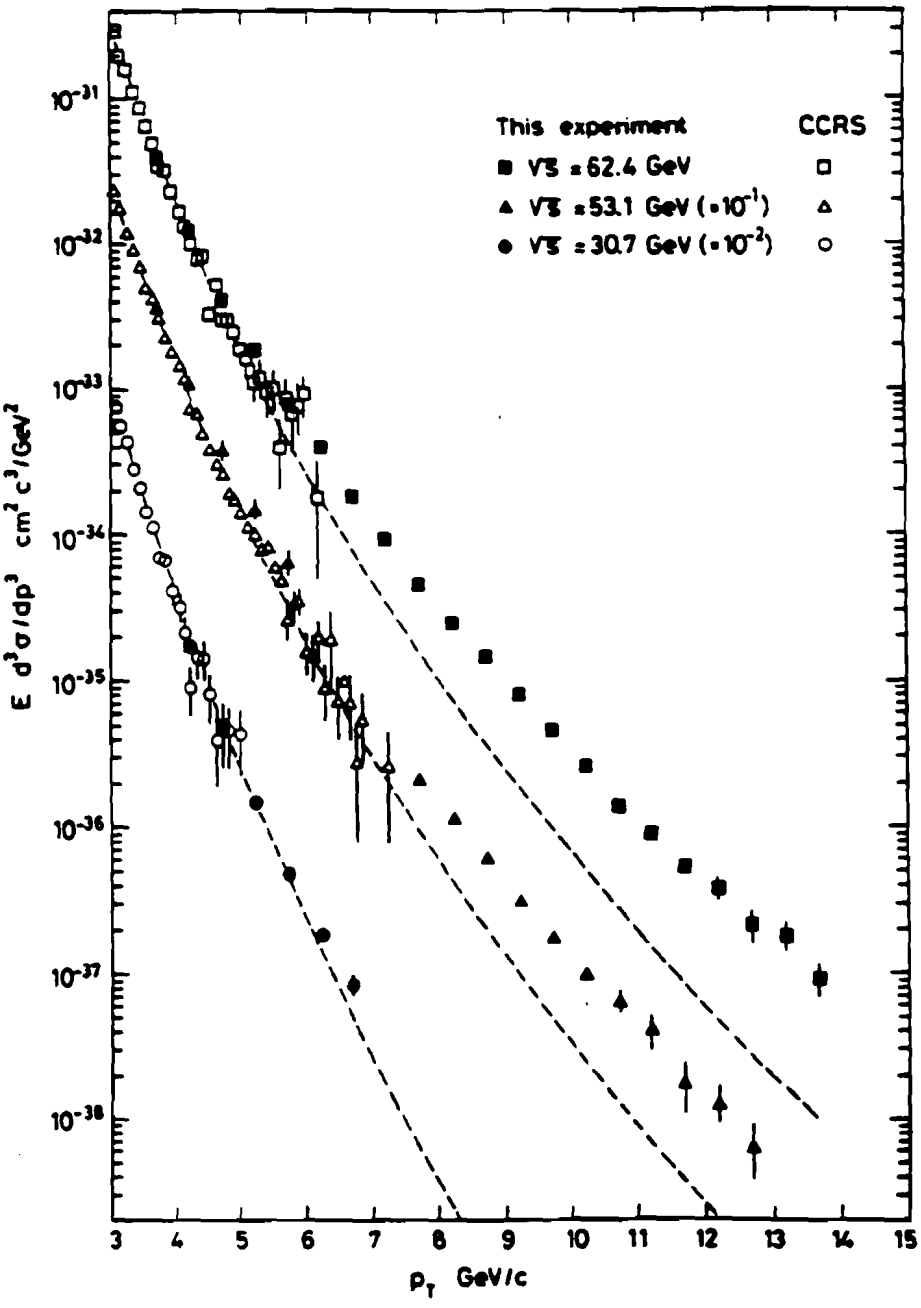

Figure 1.5: Invariant cross sections for the reaction $p + p \rightarrow \pi^0 + X$ versus p_T. Full symbols are data from the CCOR Collaboration [14]. Also shown are data from the CCRS Collaboration [15] with their best fit.

duction from pp collisions at $\sqrt{s} = 53$ and $63\,GeV$. They also used an array of Pb-glass cells to detect photons from π^0 decay. A fit to their data in the range $0.2 < x_T < 0.45$, using the parametrization function (1.4) with $F = (1 - x_T)^m$, gave for the values of the parameters: $m = 9.6 \pm 1.0$, $n = 6.6 \pm 0.8$ with $\chi^2/d.o.f. = 1$.

Donaldson and collaborators [17] had also published data from a fixed-target experiment at Fermilab, where π^0s were produced in collisions of pions and protons of 100 and $200\,GeV/c$ with protons. The experimental apparatus consisted of a set of Cherenkov counters for beam tagging and a photon detector, made of alternating layers of Pb and scintillator. π^0s were measured in the forward rapidity region for p_T up to $5\,GeV/c$. Figure 1.6, taken from an earlier publication [18], shows the invariant cross section as a function of p_T from $\pi^- p$ interactions at both energies. The invariant cross sections $E\,d\sigma/d^3p$ were fitted using a function $F(x_T, M) = (1 - x_T)^m/(p_T^2 + M^2)^n$, with $m = 7.1 \pm 0.4$, $n = 5.4 \pm 0.2$, $M^2 = 2.3 \pm 0.3\,GeV^2$ for $pp \rightarrow \pi^0 X$, and $m = 5.5 \pm 0.3$, $n = 5.0 \pm 0.1$, $M^2 = 1.8 \pm 0.2\,GeV^2$ for $\pi^{\pm} p \rightarrow \pi^0 X$. Whereas the powers of p_T are similar in both reactions, the different exponents of $(1 - x_T)$ suggest a dependence of the reaction dynamics on different internal structures of the incident particles. If, on average, the valence quarks in the meson have larger momenta than the quarks in the proton, than one would expect large-p_T π^0s would be more likely produced with pion beams than with proton beams. We will come back to this issue at the end of this thesis

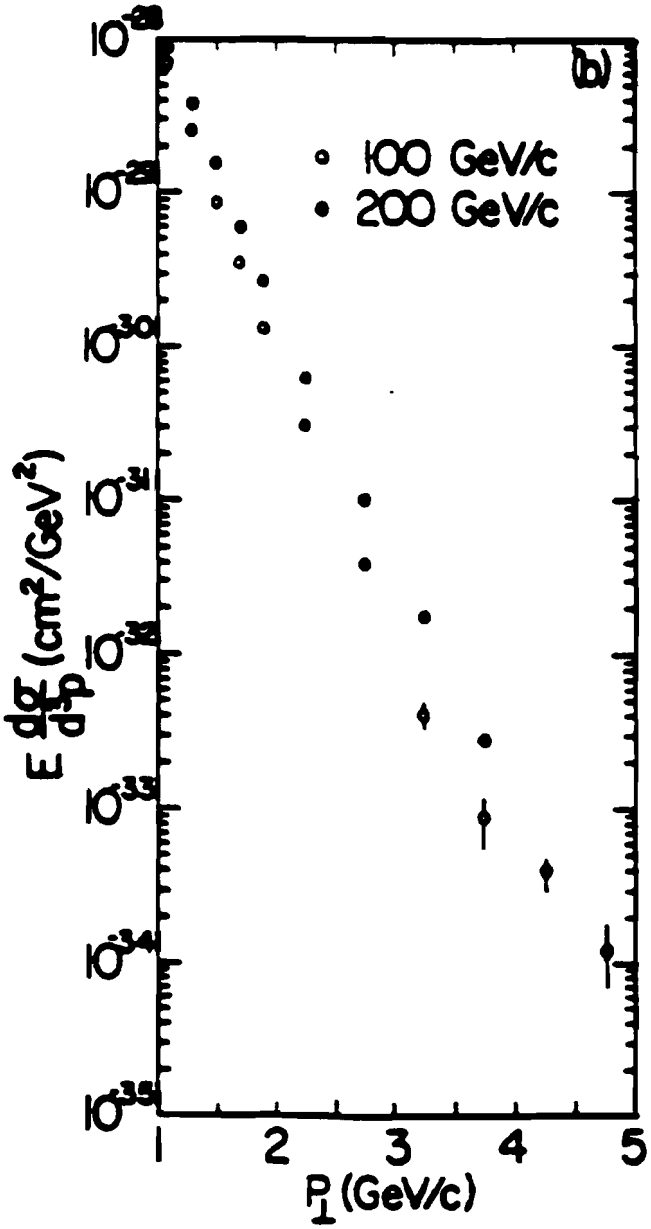

Figure 1.6: Invariant cross sections for the reaction $\pi^- + p \rightarrow \pi^0 + X$ versus p_T at 100 and 200 GeV/c and *c.m.* angles near 90^0. Data are from [17].

when discussing our own results. Figure 1.7 shows the ratio of π^0 production in p versus π^- beams as a function of p_T. The plots show that the π^0 ratio is a decreasing function of p_T for p/π^-, whereas the ratio of π^0 yields in π^+ vs π^- beams is essentially independent of p_T.

There are also available more recent data for π^0 yields with different incident particles beams. Fermilab experiment E629 [19], a predecessor of this experiment, measured large-p_T inclusive cross sections for π^0 and η production near 90^0 in the center-of-mass system, as well as the direct photon cross section, for $200\,GeV/c$ π^+ and protons incident on nuclear targets. E629 used a lead liquid argon electromagnetic calorimeter similar in design to the E706 calorimeter. The covered π^0 p_T range was $2-5\,GeV/c$. Figure 1.8 shows the published π^0 and η invariant cross sections as a function of p_T. Figure 1.9 shows the p/π^+ π^0 production ratio for different targets. The ratio seems to drop below unity at the highest p_T, although the effect is not as drammatic as in Fig. 1.7.

CERN experiment UA6 has recently measured inclusive π^0 and η cross sections at large p_T, in $p\bar{p}$ and pp collisions at $\sqrt{s} = 24.3\,GeV$ [20]. Their experimental setup involves an internal molecular-hydrogen gas-jet target in the tunnel of the CERN $p\bar{p}$ Collider. In their initial measurements, π^0s were produced in the p_T range of 2.5 to $5.1\,GeV/c$. Comparison of π^0 production in $p\bar{p}$ and in pp interactions yielded no significant differences, as shown in Fig. 1.10, where the ratio of invariant cross sections is plotted versus p_T.

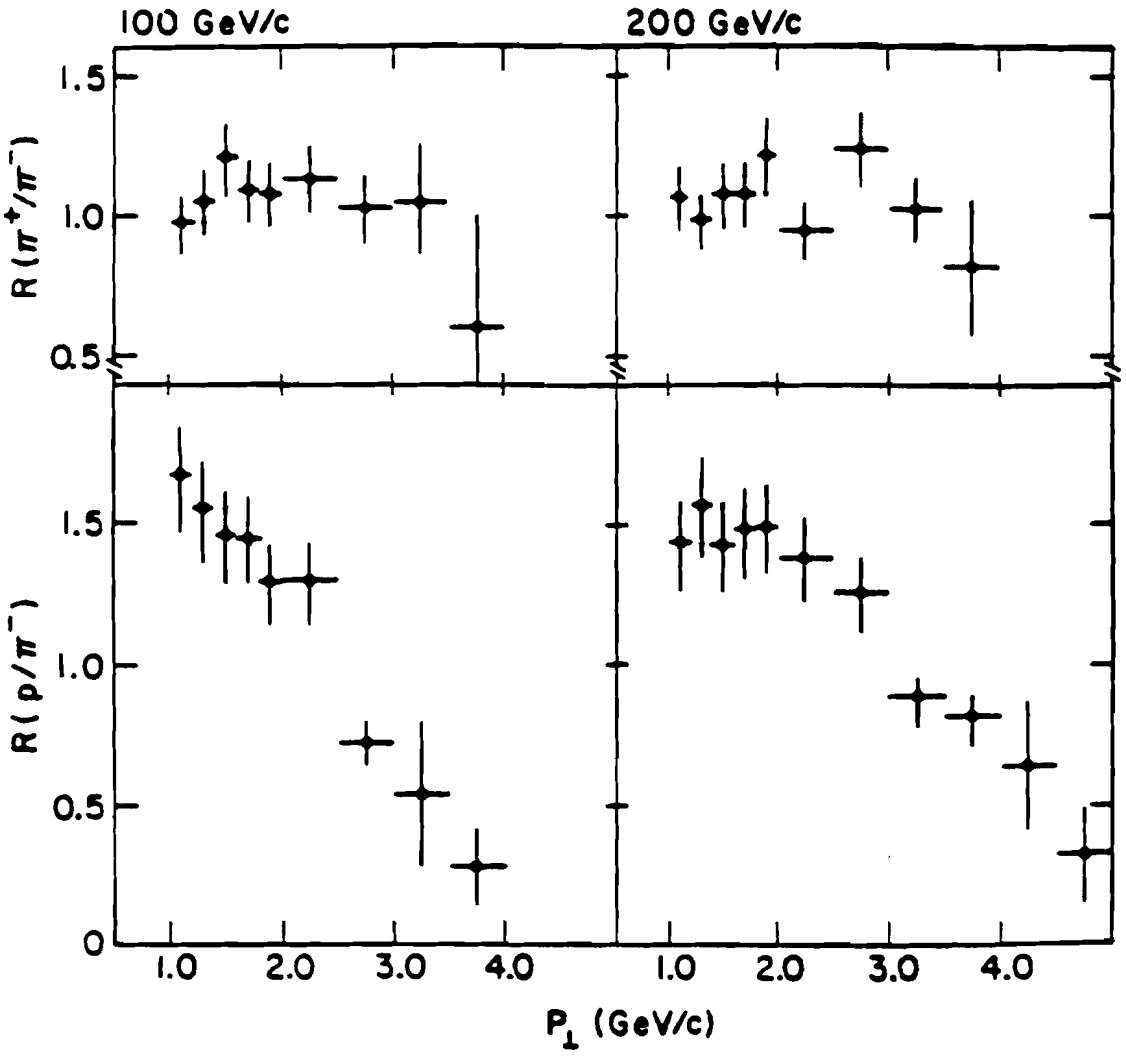

Figure 1.7: Ratios of π^0 invariant cross sections at 100 and 200 GeV/c as a function of p_T. Data are from [17].

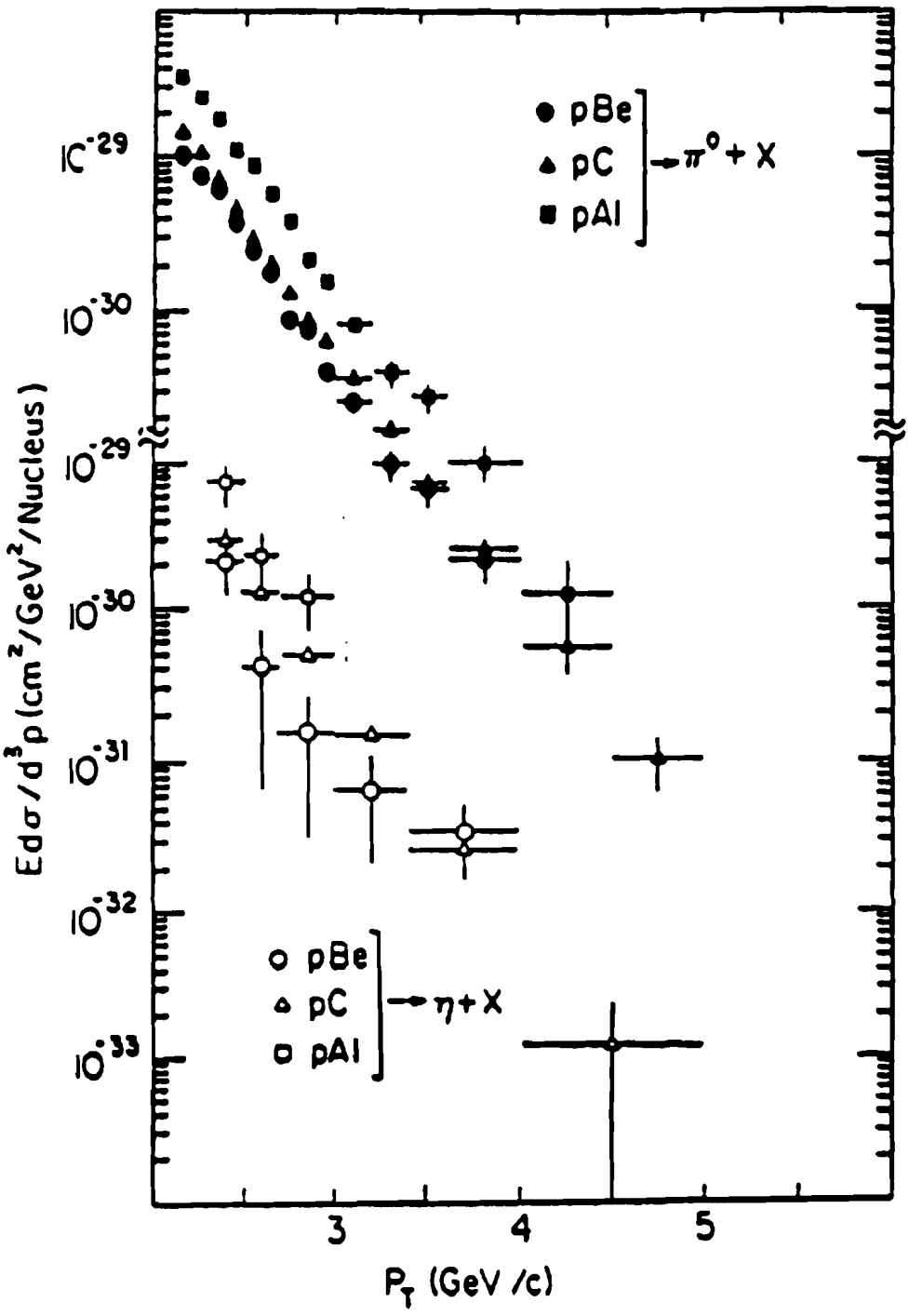

Figure 1.8: Invariant cross sections for the production of π^0 and η in proton-nucleus collisions at $200\,GeV/c$. Data are from Fermilab Experiment E629 [19].

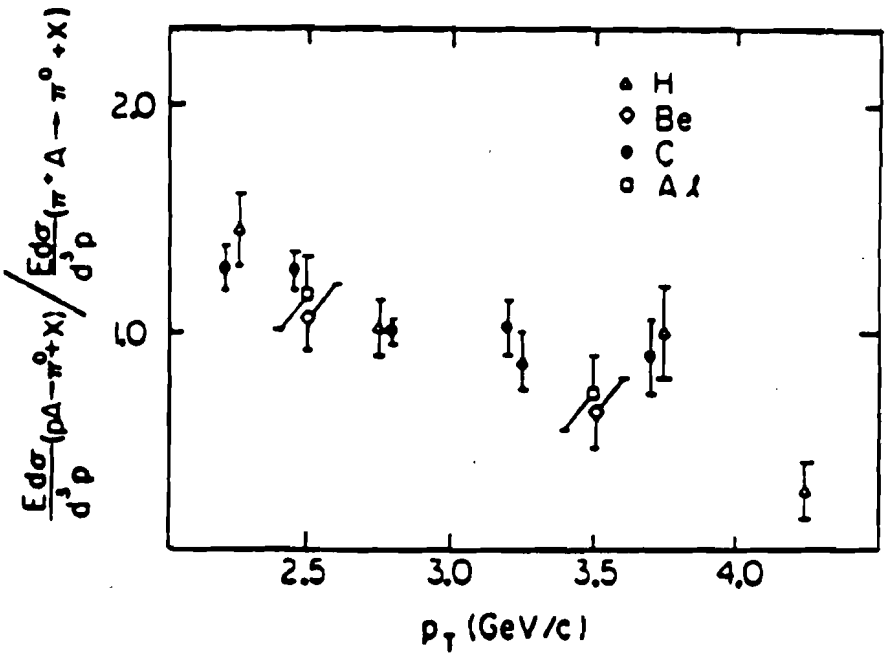

Figure 1.9: Ratio of invariant cross sections for π^0 production with p and π^+ beams at $200\,GeV/c$. *Be*, *C*, and *Al* data are from [19]; hydrogen data are from [17].

The most recent results on π^0 production at low p_T using negative pions and kaons come from the published data of the ACCMOR Collaboration [21]. Data were recorded at the CERN SPS using the WA3 large forward acceptance spectrometer. Their study concerned forward particle production in $\pi^- p$ and $K^- p$ collisions at $58\,GeV/c$. The π^0 p_T range extended up to $1.5\,GeV/c$. The good statistics at low p_T allowed them to make precise comparison with theoretical models that attribute a dependence of forward production processes on beam-particle constituents. These results provide a phenomenological understanding of the dynamics of hadron-hadron collisions in a kinematic region where perturbative QCD cannot be applied. We show in Fig. 1.11 their results for two times the ratio

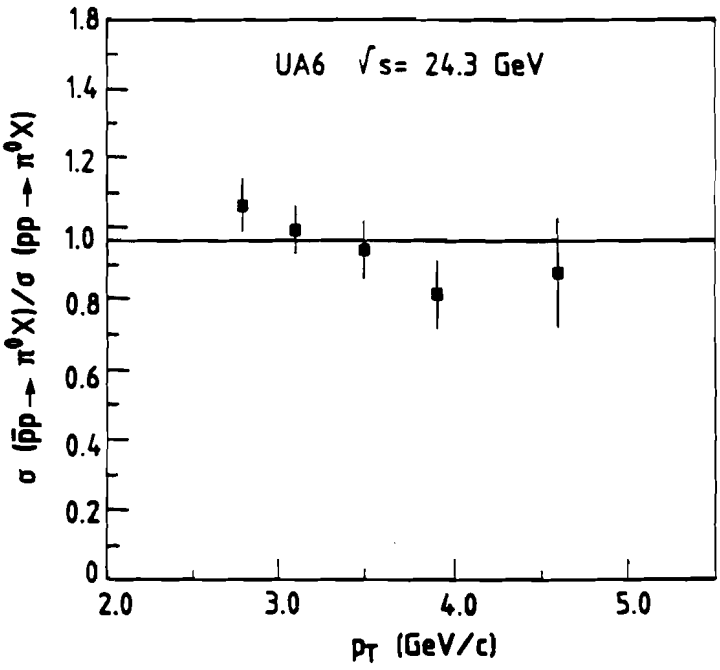

Figure 1.10: Ratio of invariant cross sections for π^0 production in $p\bar{p}$ and pp collisions as a function of p_T. Data are from CERN Experiment UA6 [20].

of π^0 cross sections using incident K^- relative to incident π^-, versus the variable x, which characterizes the fraction of the incident longitudinal momentum carried off by the π^0 ($x \simeq x_F$). The open circles are the ratios of the $\bar{u}$ quark distributions inside π^- and K^- as a function of x, as determined from lepton pair-production processes [22].

The statistical quark model of Anisovich and Shekhter [23] predicts for the ratio $2\,(K^- \to \pi^0)/(\pi^- \to \pi^0)$ a value equal to unity, as only the $\bar{u}$ quark in the K^- but both valence quarks in the π^- can recombine with a sea quark to produce a π^0. The fall-off of the ratio at large x may reflect the suppression at large x of the $\bar{u}$ quark content in the K^- relative to the π^-.

The CERN NA3 Collaboration published recently their results on inclusive

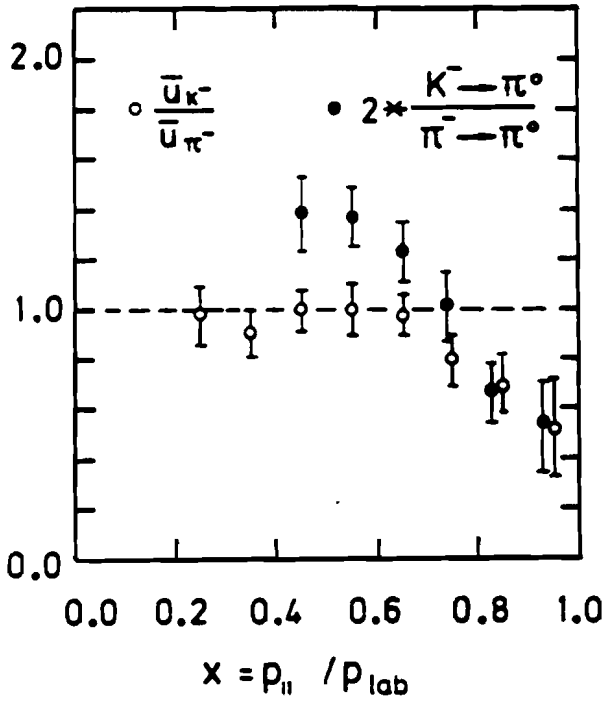

Figure 1.11: Comparison of $\bar{u}$ quark distribution inside π^- and K^- beam particles as determined from lepton pair production [22] (open dots) with π^0 distributions measured by ACCMOR Collaboration [21].

cross section for π^0 production by 200 GeV/c $\pi^\pm$ and protons on a carbon target [24]. Data were collected over a wide range of rapidity ($-0.4 < y < 1.2$) and p_T ($2.9 < p_T < 6\,GeV/c$). They used a lead-scintillator calorimeter for detection of electromagnetic energy and two different triggers: a *conversion trigger* (photons from π^0 decay converting to e^+e^- pairs in a 0.8 mm thick lead converter foil), and a *calorimeter trigger* (minimum electromagnetic energy deposition). They used two differential Cherenkov counters for tagging incoming beam particles. Figure 1.12 shows the π^0 invariant cross section in the central and forward rapidity regions for incident protons and pions. Cross sections were parametrized with a function

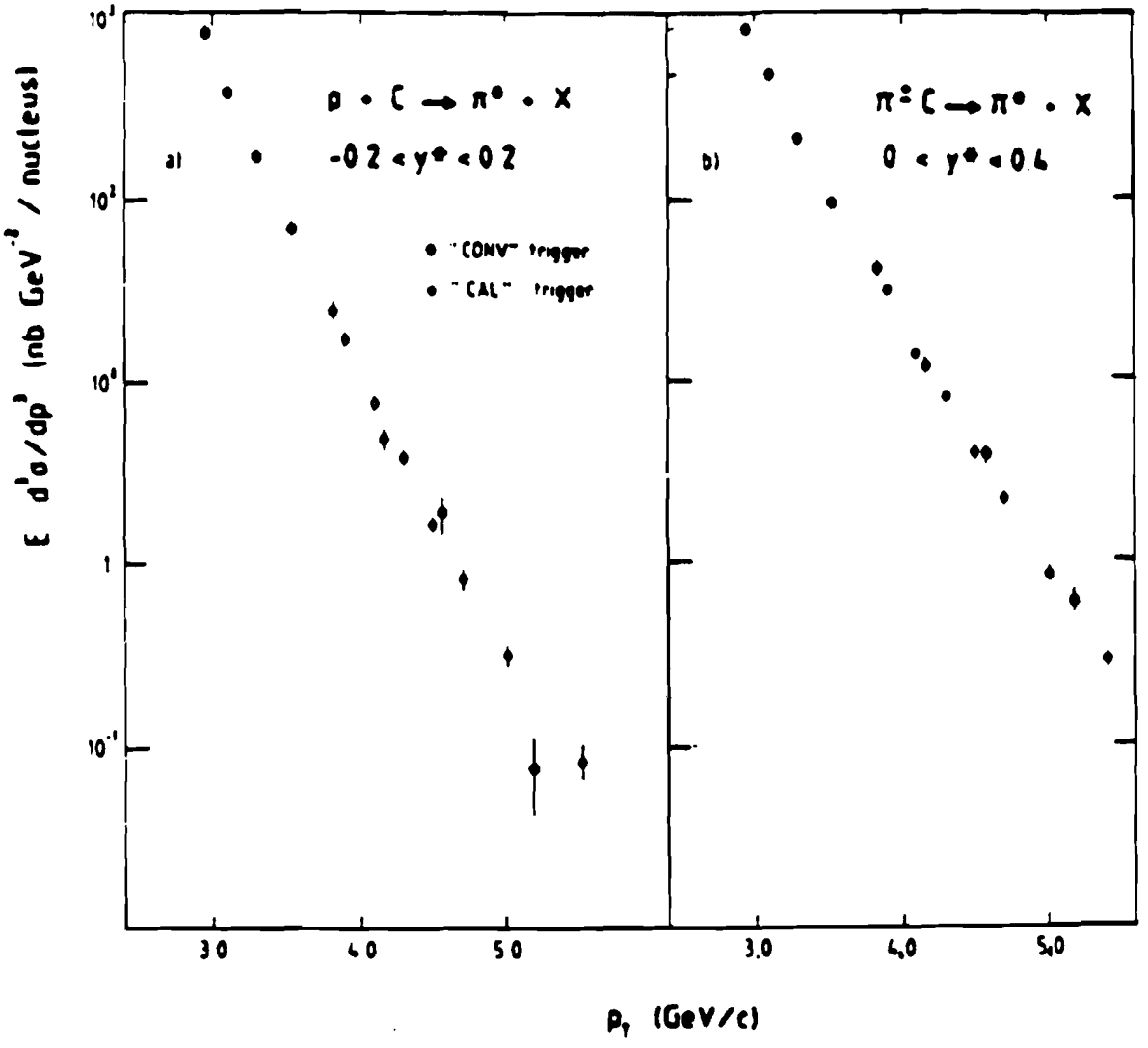

Figure 1.12: Invariant cross section for π^0 production integrated over two rapidity intervals as a function of p_T for: (a) proton interactions (b) pion interactions on carbon nuclei. Data were taken using the two trigger setups of the NA3 Collaboration [24].

of both x_F and p_T, using a form similar to Expression (1.4):

$$E\,\frac{d\sigma}{d^3p} = A\,\frac{(1-x_D)^m}{p_T^n} \tag{1.5}$$

where $x_D = (x_T^2 + (x_F - x_0)^2)^{1/2}$. Best fits were obtained using a maximum likelihood procedure which yielded the values of the parameters indicated in Table 3 of [24]. Relative π^0 production yields from incident p, $\pi^\pm$ and K^+ are shown in Fig. 1.13 as a function of p_T. The π^0 ratio for $\pi^\pm/p$ increases with p_T, and confirms the results from previous experiments.

Results on π^0 production at lower p_T were also published by CERN Experiments NA22 and NA27 using the European Hybrid Spectrometer (EHS), equipped with a Rapid Cycling Bubble Chamber (RCBC) as a target and a vertex detector [25,26]. Both experiments measured inclusive π^0 production for p_T below $1\,GeV/c$ (NA22) and below $4\,GeV/c$ (NA27), in the forward hemisphere ($x_F > 0$) in π^+p, K^+p and pp interactions at $250\,GeV/c$ (NA22), and in π^-p interactions at $360\,GeV/c$ (NA27). They used a *minimum-bias* interaction trigger, and a lead-glass calorimeter to trigger on π^0s and to detect photons from π^0 decay. In Fig. 1.14 we present NA27 published p_T^2 distribution for π^0s with $x_F > 0.01$ produced in π^-p interactions at $360\,GeV/c$. The p_T^2 spectrum was parametrized using a function of the form $d\sigma/dp_T^2 = C\,/\,(p_T^2 + \delta^2)^n$, with $\delta = 0.64 \pm 0.02\,GeV/c$ and $n = 4.03 \pm 0.07$.

Using a liquid-H_2 target, the NA24 Collaboration measured inclusive π^0 yields at large transverse momentum ($p_T < 7\,GeV/c$) using incident $\pi^\pm$ and protons at

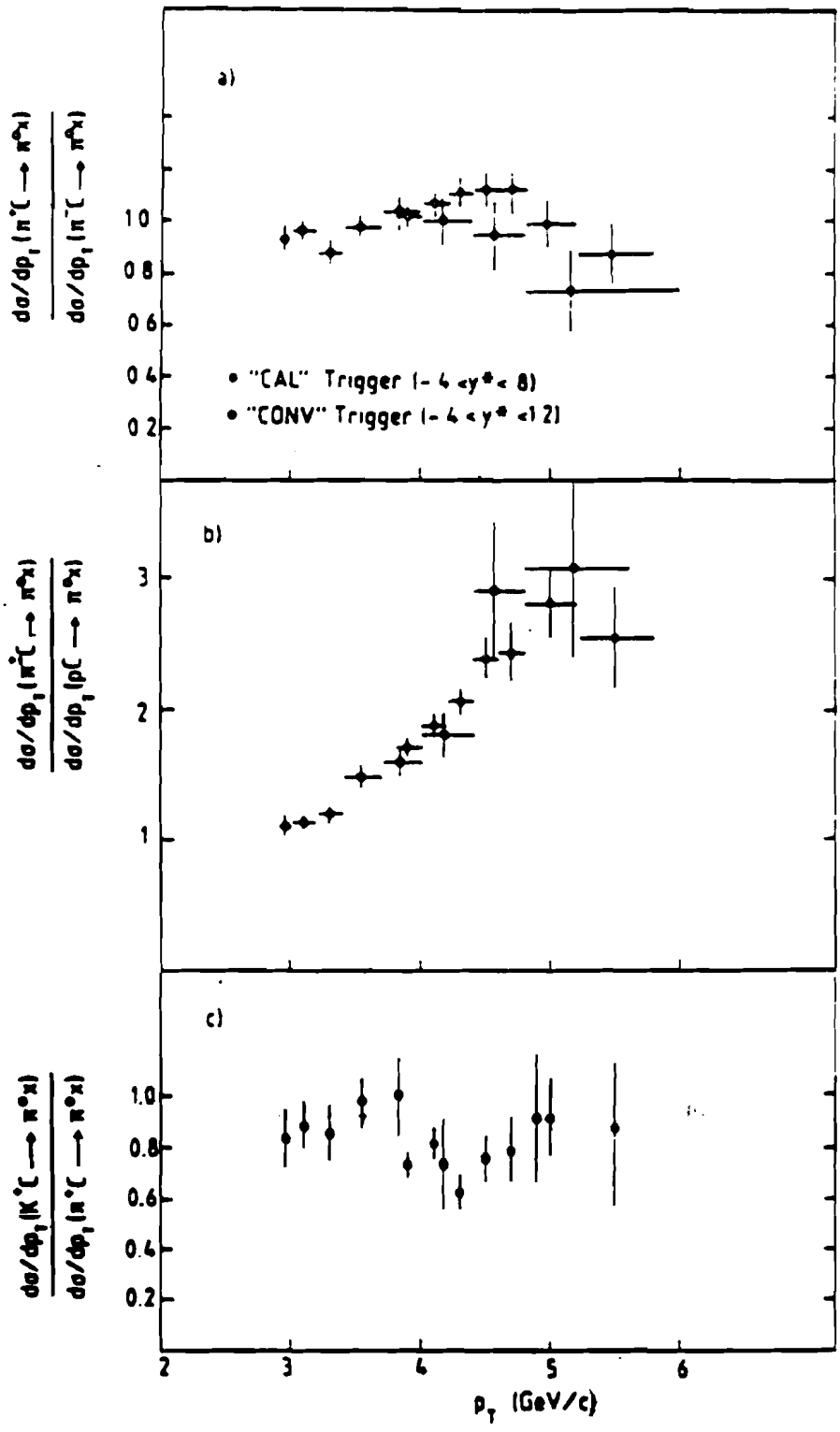

Figure 1.13: Ratios of π^0 cross sections as a function of p_T for two trigger types. Data are from [24].

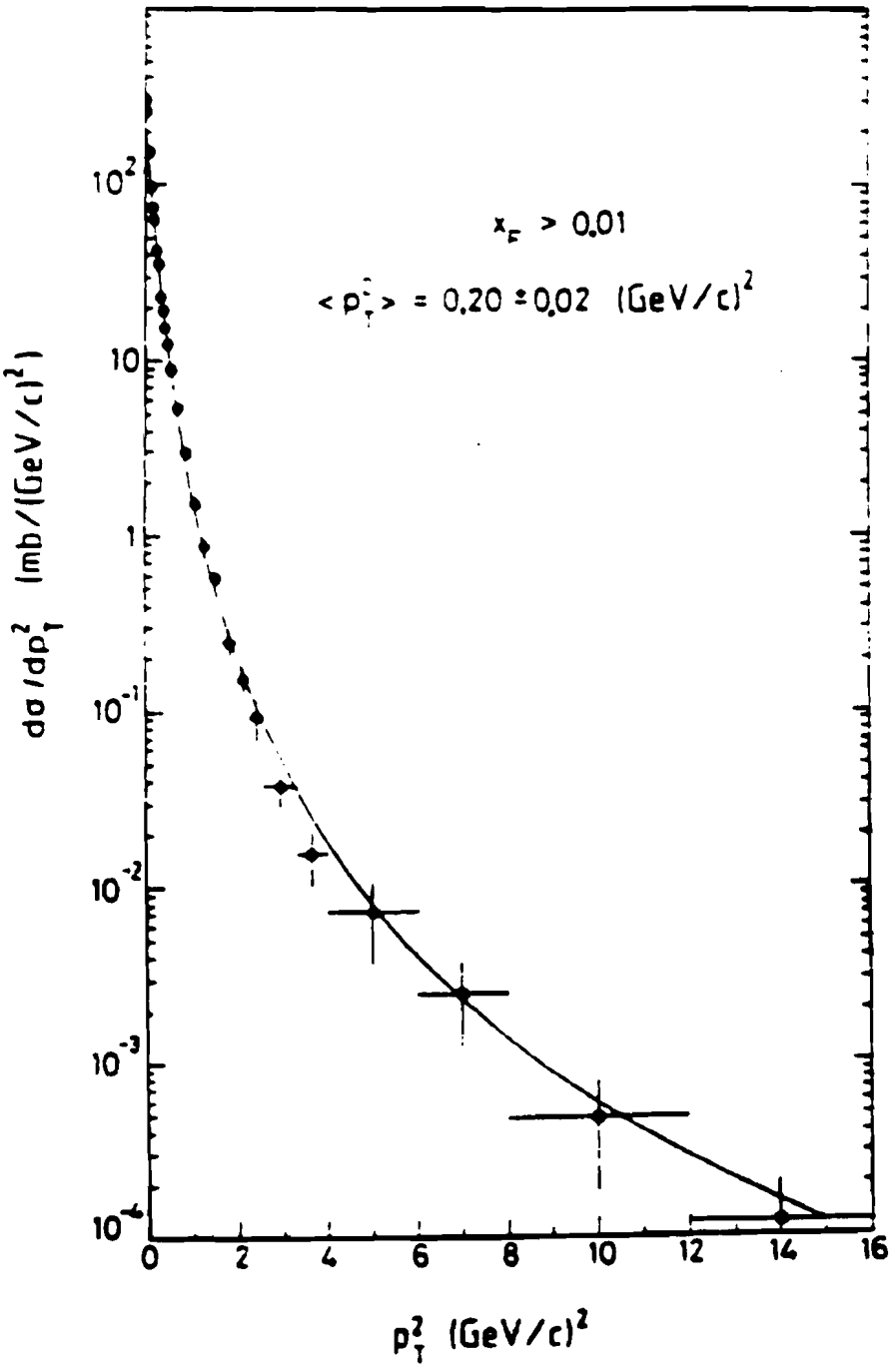

Figure 1.14: p_T^2 distribution of π^0s with $x_F > 0.01$. The solid curve is a fit to the data. Data are from CERN NA27 Collaboration [26].

$300\,GeV/c$. Photons were detected in a large acceptance lead-scintillator electromagnetic calorimeter. The π^0 p_T spectra are shown in Fig. 1.15 for different incident beams. Figure 1.16 shows the ratios of invariant cross sections versus p_T and y. Examining Fig. 1.16 one can derive conclusions similar to those derived from Fig. 1.7, namely that incident pion are more likely to produce large p_T single neutral mesons than protons. The π^0 ratio π^-/π^+ is again consistent with unity over the entire p_T range.

The latest data on π^0 inclusive production were published by the CERN WA70 Collaboration [29,31]. In [29] they presented results on π^0 production by $280\,GeV/c$ π^+ and π^- incident on a liquid hydrogen target. The kinematic region explored ($4.0 < p_T < 7.0$ and $-0.45 < x_F < 0.6$) is similar to that of E706, but at lower energy. The WA70 experimental apparatus consisted of a charged-track spectrometer (*Omega*) and a fine-grained lead liquid-scintillator electromagnetic calorimeter. Figure 1.17 shows the π^0 differential cross section as a function of p_T, for three ranges of x_F, using positive and negative pion data. Figure 1.18 shows the π^0 differential cross section in x_F, for different p_T ranges. Ratios of cross sections for different incident beam-particles are shown in Fig. 1.19 as a function of (a) p_T over the full x_F range, (b) x_F over the full p_T range.

Results in Fig. 1.17 and 1.18 were compared to leading order QCD predictions using the Lund Monte Carlo program [30], by selecting different Q^2 scales in the coupling constant α_s and in the evolution of the structure functions, and

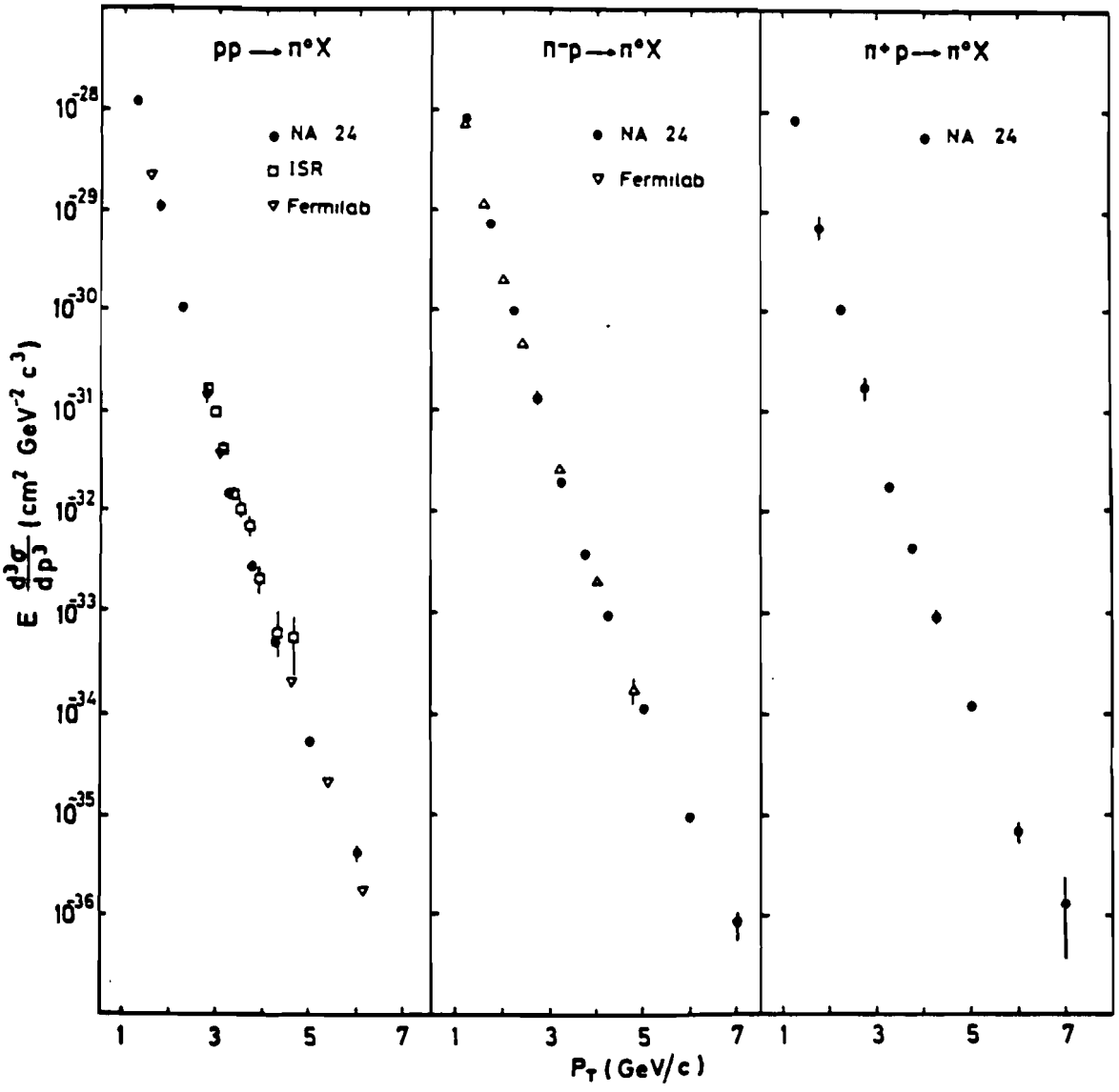

Figure 1.15: Invariant cross sections for inclusive π^0 production in pp, $\pi^- p$, and $\pi^+ p$ collisions at 300 GeV/c. Data are from NA24 Collaboration and are compared to previous results at ISR [15] and Fermilab [27].

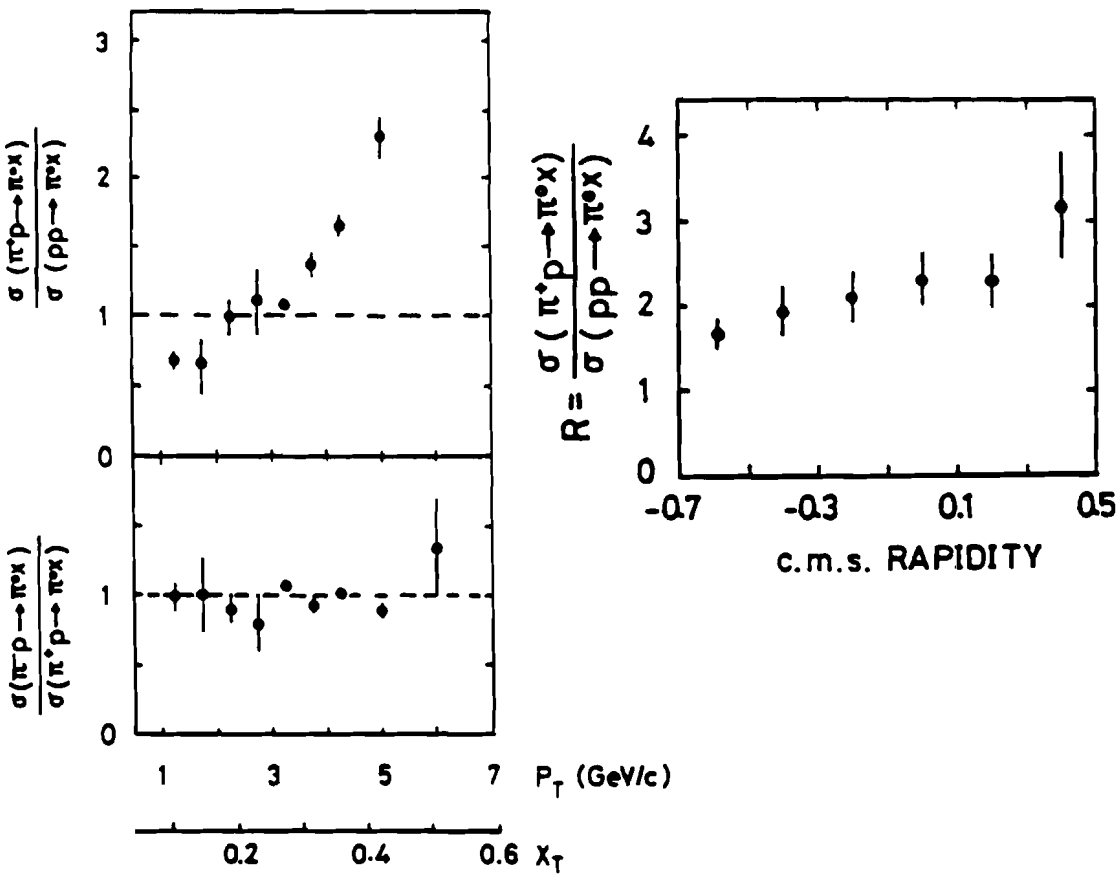

Figure 1.16: Ratios of invariant cross sections for inclusive π^0 production as a function of p_T, x_T, and *c.m.* rapidity. Data are from [28].

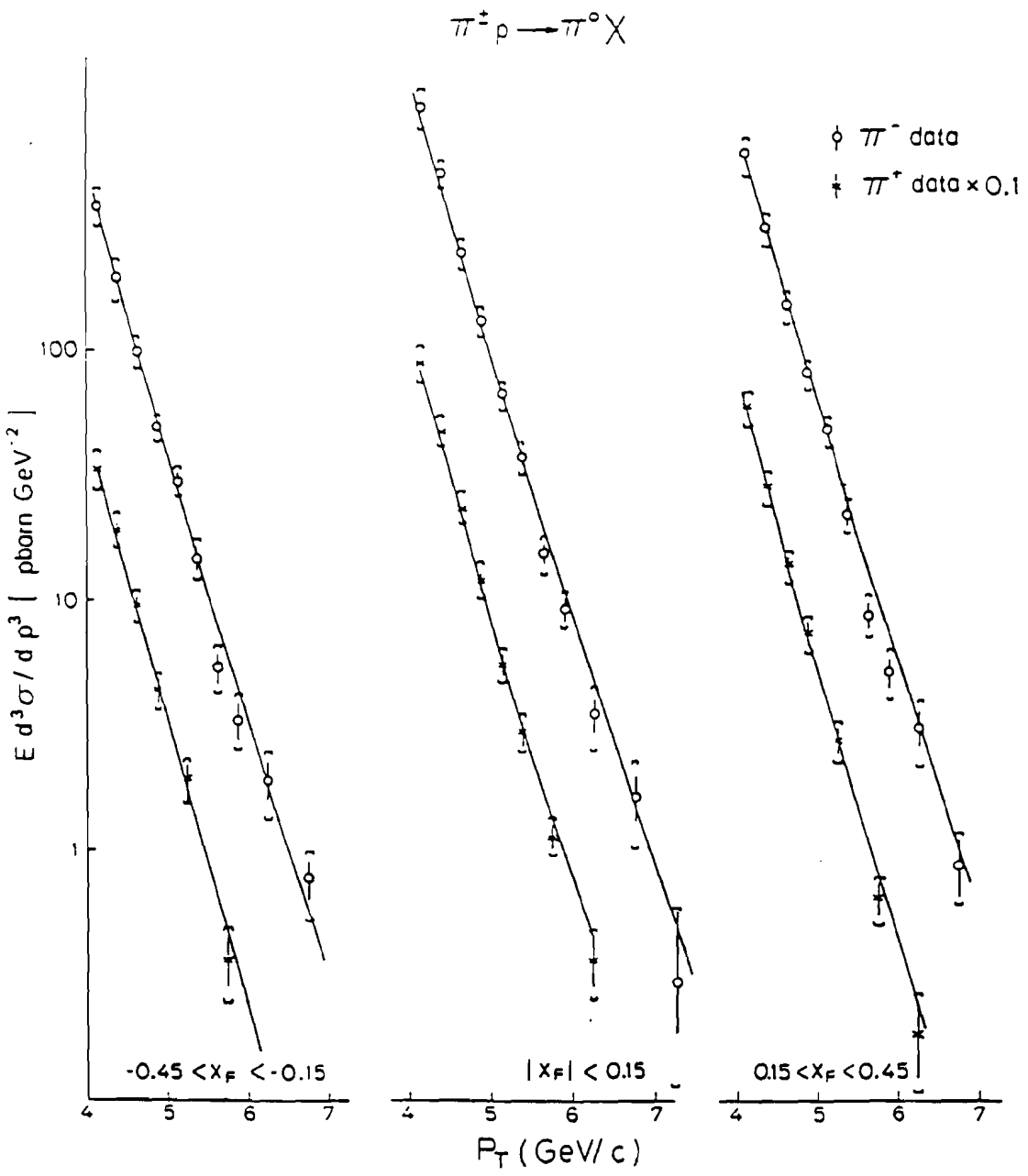

Figure 1.17: Invariant cross section for π^0 production as a function of p_T in three x_F bins. The π^+ data are scaled down by a factor ten. Data are from CERN WA70 Collaboration [29].

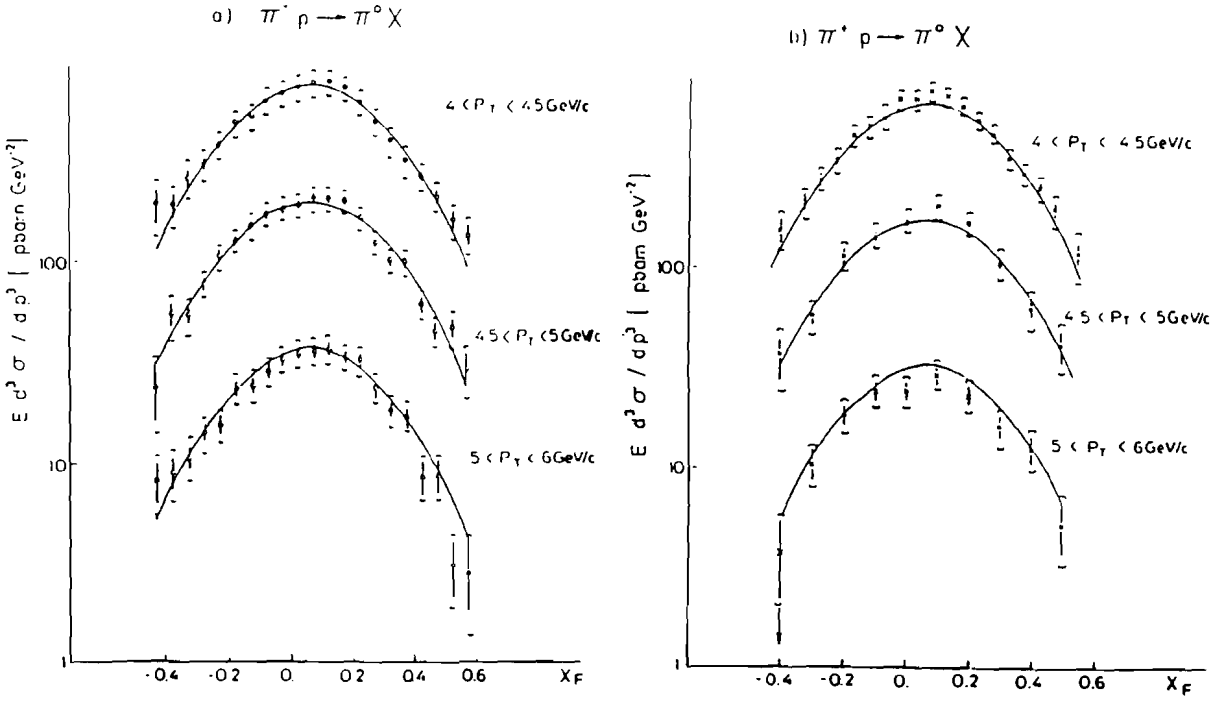

Figure 1.18: Invariant cross section for π^0 production as a function of x_F in three p_T bins. Superimposed on tha data is the result of a phenomenological fit. Data are from WA70 Collaboration [29].

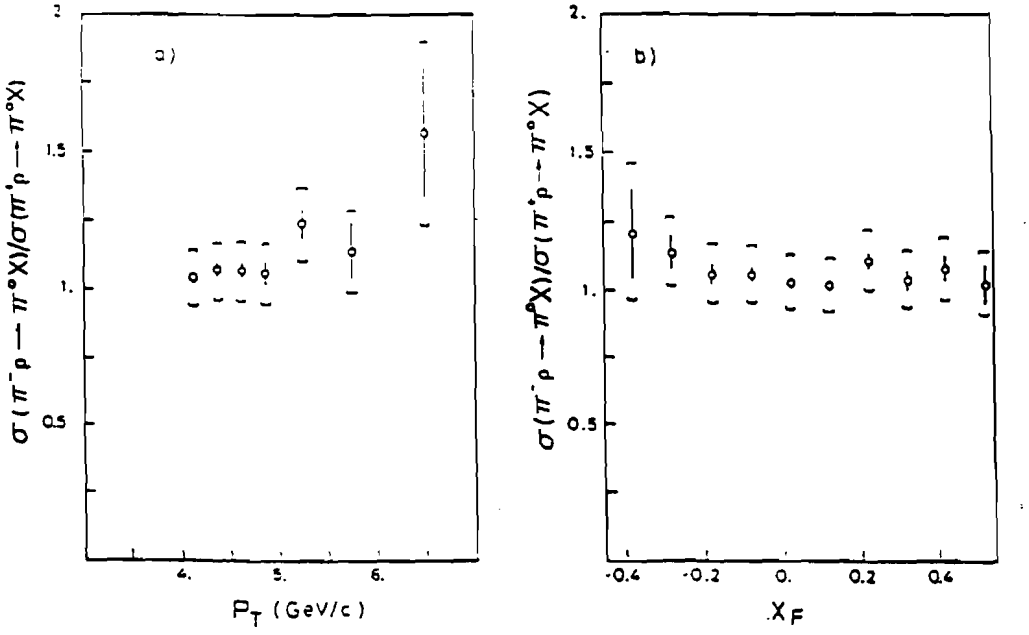

Figure 1.19: Ratios of π^0 invariant cross sections versus p_T (in the full x_F range), and x_F (in the full p_T range). Data are from WA70 Collaboration [29].

by requiring no intrinsic transverse momentum k_T. Best agreement between data and predictions was achieved by choosing for the momentum scale a kinematically dependent *optimized* Q^2 obtained from the analysis of direct-photon data. This momentum scale, given as:

$$Q^2 = 0.35\,(1 - x_T)\,p_T^2,$$

was determined using next-to-leading order QCD calculations for direct-photon processes of Aurenche et al. [10,11]. Predictions using other scales ($Q^2 = p_T^2$ or $Q^2 = 2\,\hat{s}\,\hat{t}\,\hat{u}\,/(\hat{s}^2 + \hat{t}^2 + \hat{u}^2)$ fell below the data by about a factor of three. In [31], the WA70 Collaboration presented results on the inclusive $pp \rightarrow \pi^0 X$ cross section as a function of p_T (Fig. 1.20) and x_F (Fig. 1.21), as well on the π^0 ratio in π^+/p (Fig. 1.22) in the p_T range between 4.0 and 6.5 GeV/c. Results from phenomenological fits of the Form (1.5) to the cross sections will be discussed in the last chapter of this thesis.

The above summary of the results from previous experiments on π^0 production at large p_T indicates that the conclusions that can be drawn from the experimental distributions are rather confusing and somehow contraddicting.

If the data were described by a universal form given by Eq. (1.4), then the invariant cross sections versus $x_T = 2p_T\,\sqrt{s}$ at two different values of $\sqrt{s}$ ($\sqrt{s_1}$, $\sqrt{s_2}$) would have a constant ratio equal to $(\sqrt{s_2}/\sqrt{s_1})^n$. The ISR data seem to be consistent with the scaling law described by Eq. (1.4) only at the highest energy and largest p_T of the π^0, but indicate scaling violation at lower p_T.

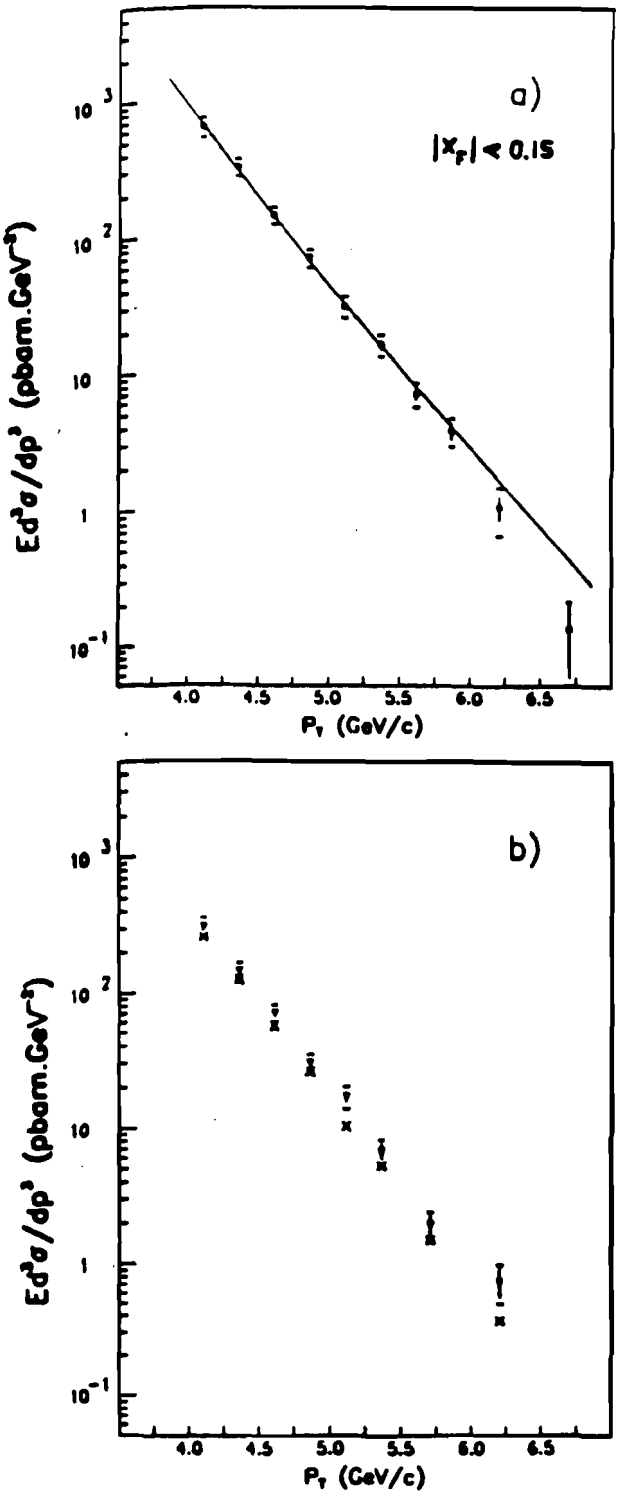

Figure 1.20: $p+p \rightarrow \pi^0 + X$ invariant cross section versus p_T. (*a*) central rapidity region, with superimposed a phenomenological fit. (*b*) forward and bakward rapidity regions. Data are from WA70 Collaboration [31].

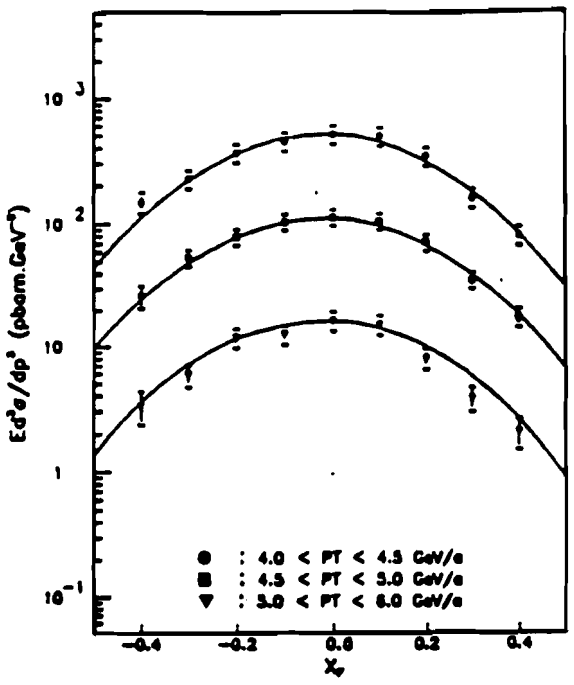

Figure 1.21: Invariant cross section for $p + p \rightarrow \pi^0 + X$ as a function of x_F in three p_T ranges. Data are from WA70 Collaboration [31].

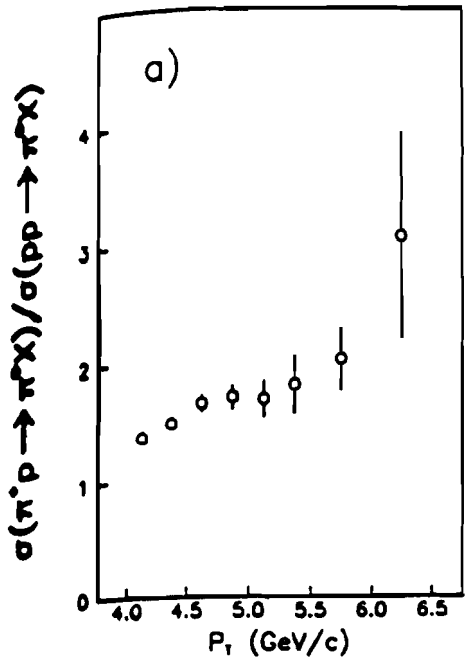

Figure 1.22: Ratio of π^0 invariant cross sections in $\pi^+ p$ and pp interactions at 280 GeV/c. Data are from WA70 Collaboration [31].

Invariant cross sections measured by fixed-target experiments show that p_T spectra of π^0s fall steeply (the power n in Eq. (1.4) varies between 9 and 10). The values obtained for the power of p_T indicate that at large p_T the hard scattering regime is reached.

Results on ratios of invariant cross sections for π^0 production with different incident beam particles ($\pi^{\pm}$, p, $K^{\pm}$) are instead consistent in all previous experiments.

In this thesis we intend to contribute to the understanding of the phenomena associated with the production of large-p_T particles in hadronic interactions.

In Chapter 2 the E706 experimental apparatus is described. Chapter 3 describes the performances of the electromagnetic calorimeter as well as the software package used for the analysis of the experimental data. Chapter 4 describes the general procedure used for the data analysis and introduces the physics subject of this thesis. Chapter 5 is dedicated to the description of the Monte Carlo simulations. Finally, in Chapter 6 the results of the analysis are presented and the conclusions are outlined.

Chapter 2

EXPERIMENTAL APPARATUS

2.1 General considerations

This chapter describes the apparatus used in the experiment, with particular emphasis on the electromagnetic calorimeter; the data acquisition procedure is also mentioned. Figure 2.1 shows the overall layout of the experiment, which was designed to cover as much of the total solid angle as possible. A right-handed coordinate system with the positive z-axis directed downstream along the beam line, the positive y-axis vertically upward and with the origin located 12 cm downstream of the midpoint of the target segments will be used in the following discussion.

2.2 Beamline

The E706 experimental hall is located at the end of the Meson West (MW) Beam Line of Fermilab. The MW beam line was designed to transport a high intensity secondary beam produced by 800 GeV/c primary protons interacting in Be, Al

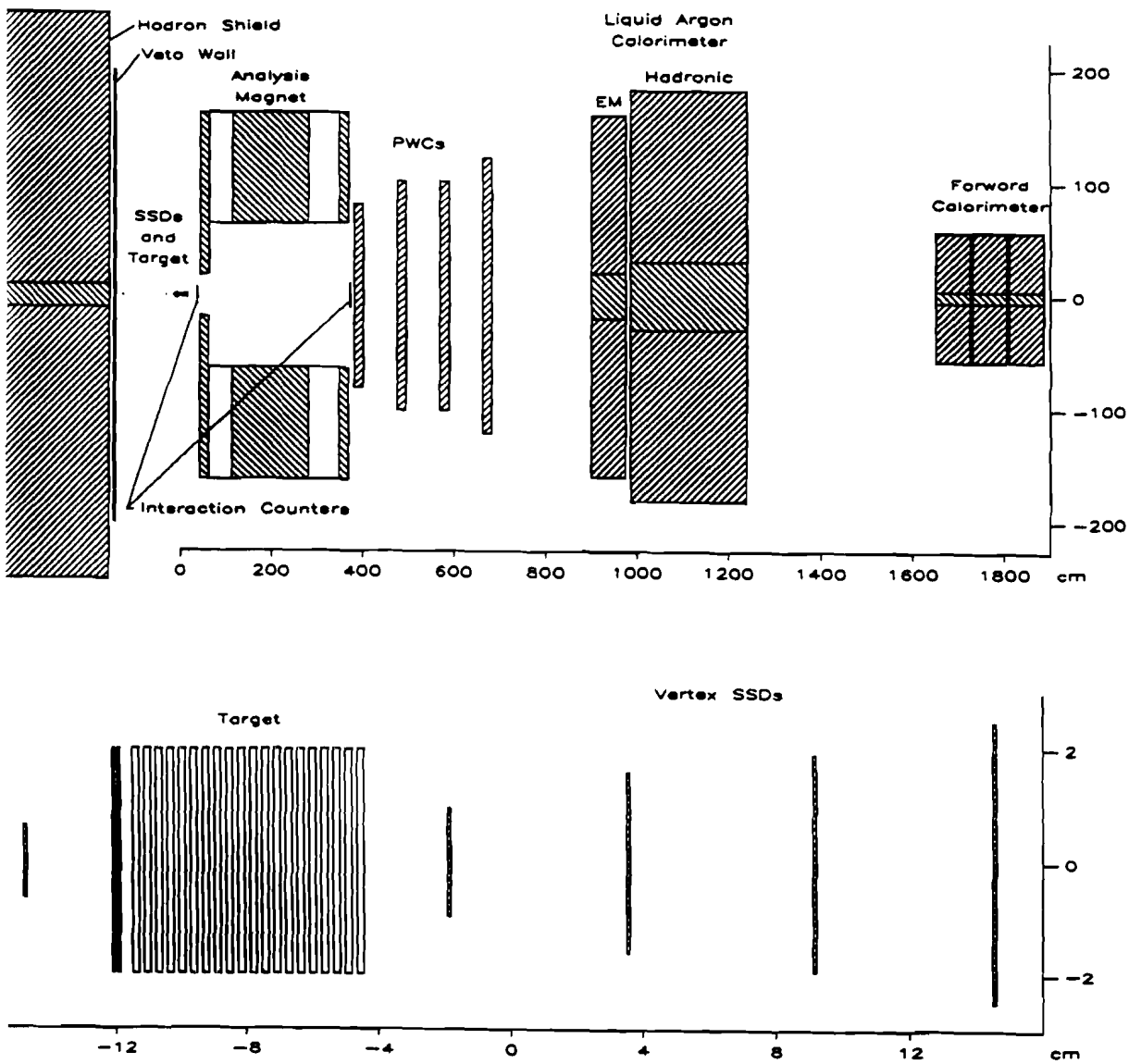

Figure 2.1: Layout of E706 experimental apparatus. The bottom figure shows an exploded view of the experimental target region.

or W production targets. The $530\,GeV/c$ secondary beam, of both positive and negative polarities, is a two-stage momentum-recombined beam, with a momentum dispersed intermediate focus. At the final focus on the experimental target, the beam was typically $1.5\,mm$ and $2\,mm$ wide in the bend plane (x) and in the vertical direction (y), respectively (half-widths at half-maxima *HWHM*). The divergence in x and y was $0.04\,mrad$ (*HWHM*), and the momentum bite was 2% and 7% for positive and negative beam, respectively (also *HWHM*). The parallel section of the beam contains a $43\,m$ long, $24.4\,cm$ radius, differential Cherenkov counter. Several small scintillation counters before and after the Cherenkov provide the beam definition. During the run the Cherenkov is filled with He radiator gas, which is kept at a variable pressure ($4-6\,psia$) for tagging different kinds of charged particles in the beam ($\pi/K/p$). The counter has one coincidence and one anticoincidence ring, each containing 6 phototubes. It was operated at a Cherenkov angle of $5\,mrad$ for the coincidence ring. The combined K^- and $\bar{p}$ component in the negative pion beam was about 3.2%. For the positive beam, the K^+ fraction was less than 2% and the π^+ was about 7.5%. These beam compositions were inferred from examining Cherenkov gas pressure excitations of the kind shown in Chapter 4, Figs. 4.1 and 4.2. During the run, the typical efficiency for tagging K^-s was $\sim 50\%$ with less than 5% contamination from π^-. For π^+s the efficiency was in the range 80-85% with $\sim 8\%$ contamination from K^+s, and negligible contamination from protons. These percentages were obtained with the

requirement of four (three) or more phototubes firing in the coincidence ring, and less than two phototubes in the anticoincidence ring for tagging minority particles in the negative (positive) beam.

The muon flux along the beam line was reduced by *spoiler* magnets made of magnetized steel and very small aperture, while the hadron halo was attenuated by an iron hadron shield placed in the experimental hall, just upstream of the interaction target. Between the iron shield and the target, two scintillation-counter veto walls were used to reduce the trigger rate from any upstream interactions and from the muon halo in the beam.

2.3 Beam and Veto Wall Counters

For defining of a beam particle, three scintillator counters are positioned just upstream of the interaction target. Two of them (BA and BB) have dimensions $2.5 \times 2.5 \times 0.15\,cm$, the third (BH), is $12.7 \times 12.7 \times 0.7\,cm$ and has a $1\,cm$ diameter hole at the center. The coincidence of BA and BB with BH in veto, defines a useful beam particle. The information from the appropriate scalers was stored during data taking on a run by run basis. To provide the trigger with information that a beam particle interacted in the experimental target, a set of four scintillator counters ($SW1$, $SW2$, $SE1$, $SE2$) were placed downstream of the SSD box, on the both faces of the analyzing magnet. The front two ($SE1$ and $SW1$) are located $\sim 35.5\,cm$ downstream of the target; the back $SE2$ and $SW2$ are located at $\sim 367.5\,cm$ from the target. They were designed to cover the full

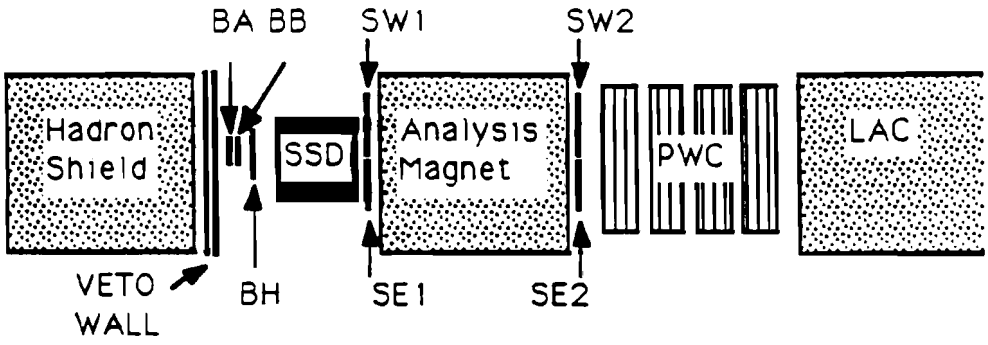

Figure 2.2: Plane View of Trigger System Counters.

vertical acceptance of the magnet, and $\pm 18\,mr$ of the horizontal acceptance. Both sets of counter are set flush against each other, but have a hole ($1.9\,cm$ diameter between $SE1$, $SW1$ and $3.8\,cm$ diameter between $SE2$, $SW2$) centered on the beam line.

In order to tag any muons entering the experimental hall outside of the beam region, we built a veto wall consisting of two overlapping planes of 32 scintillation counters each, grouped in four quadrants. Each quadrant has transverse dimensions $213 \times 160\,cm$. The two walls are slightly shifted relative to each other to minimize cracks. A hole, $10 \times 10\,cm$ dimension, was left for the beam to go through. The muon veto information was used during the off-line analysis for background-rejection purposes. Fig. 2.2 shows the location of the beam, interaction counters and veto wall.

2.4 Targets

We used C, Be, and Al nuclear targets in order to study nuclear effects in single γ, π^0 and η production. The choice of the targets was dictated by the radiation length and interaction length of the material. When one of the photons from π^0 decay converts in the target, the e^+e^- pair may be swept out by the magnet, or otherwise misidentified. To minimize conversions, calls for relatively short radiation-length targets. Also, in order to minimize secondary interactions, targets with long interaction lengths are required. Based on the scaling properties of radiation and interaction lengths as functions of atomic weight (A) and atomic number (Z), we concluded that materials with relatively low Z were the appropriate. Some of the target material specifications are shown in Table 2.1. Segmented targets were used in the experiment in order to help in localizing photon conversions and secondary interactions in the target material. For most of the data taken, the target consisted of twenty $2\,mm$-thick beryllium segments separated by $1.6\,mm$ gaps. The carbon target had the same segmentation and spatial distribution. For a portion of the run, two $0.8\,mm$-thick copper segments, separated by a $1.6\,mm$ gap, followed by a $3.2\,mm$ gap, were positioned upstream of the Be stack. A summary of the data taken with different target configurations is given in Table 2.2.

Table 2.1: Target Parameters

Parameters	*Be*	*C*	*Al*	*Si*	*Cu*
length (cm)	4	4	0.95	0.42	.16
atomic number	9.01	12.01	26.98	28.09	63.54
density (g/cm^3)	1.85	2.27	2.70	2.33	8.96
radiation length (%)	11.33	21.28	10.67	4.49	11.19
π interaction length (%)[1]	6.90	7.78	1.87	1.80	0.83
p interaction length (%)[1]	9.24	10.24	2.38	2.30	1.03
K interaction length (%)[1]	6.25	7.15	1.69	1.62	0.77

[1] **Nuclear Absorbtion lengths were computed using the absorbtion cross section measurements of [32]**

Table 2.2: Summary of Data Taking During the 1987-88 Run

Beam	Target	# Triggers	Comments
Negative	C	330 K	Shakedown Data, Nov-Dec 1987
	C	690 K	
Positive	C	160 K	Physics Data, Jan-Feb 1988
	Be	1500 K	
	$Cu + Be$	1300 K	
Negative	Be	1240 K	
	$Cu + Be$	790 K	

2.5 Silicon Strip Detectors

The region around the experimental target is surrounded by an array of Silicon Strip Detectors (SSDs). The SSD system, together with the proportional wire chamber (PWC) system, located downstream of the magnet, provided high resolution measurements of the charged particle momenta. The SSDs also serve as vertex detectors by resolving primary interactions from secondaries. There are 7 x, y modules, each consisting of two planes, with a total of 7120 active strips. All SSDs have $50\,\mu m$ pitch, and a thickness of $250 - 300\,\mu m$. The three modules upstream, and the first module immediately downstream of the target, contain $3 \times 3\,cm$ silicon wafers; the wafers in the last three modules are all $5 \times 5\,cm$ (Fig. 2.3).

A minimum-ionizing particle creates about 2×10^4 electron-hole pairs per silicon plane, and the charge is collected in about $20\,ns$; consequently, a low noise, wide-band amplifier must be used for signal processing. We used the RelLab IO-323-C charge sensitive amplifier. The Nanometric system [33] has been adapted to further amplify, discriminate and convert the analog signals to logic levels for storage as digital data. The requirements of the SSD system can be summarized as follows:

- angular resolution should be comparable with the resolution of the downstream PWC system;

- position resolution adequate for resolving track-reconstruction ambiguities

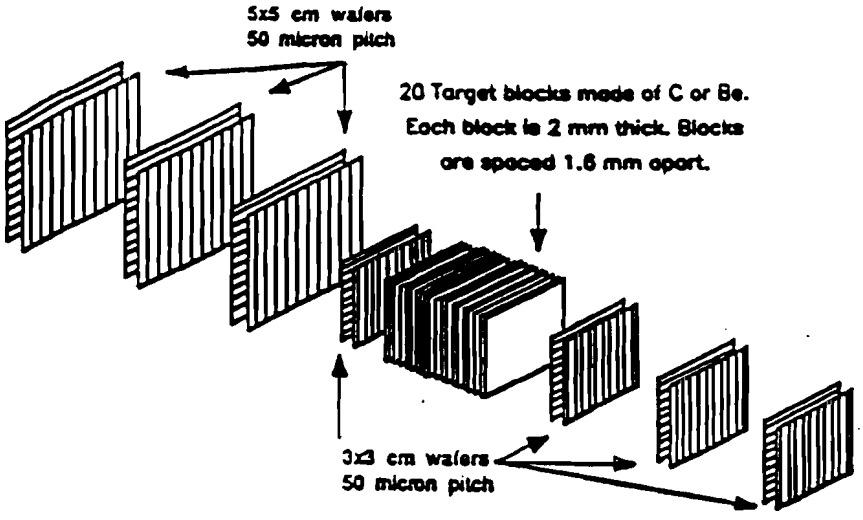

Figure 2.3: Experimental target region. The 20 target segments are inserted between the upstream three SSD stations and the downstream four SSD modules.

in the PWCs;

- good longitudinal vertex resolution for tagging secondary interactions;
- capability of withstanding high beam intensity without suffering major radiation damage.

The SSD system, designed and operated by our colleagues from the University of Pittsburgh [34], met all these criteria. It is interesting to note that the effect of radiation exposure of the detector was clearly evident after the end of the run. Prior to exposing the silicon wafers to the beam, the measured leakage current per strip varied between 2 and $3nA$. At the end of the run, the strips in the vicinity of peak beam intensity indicated increases in leakage current of up to

$14\,nA$. Nevertheless, the signal to noise was good enough so that none of the wafers had to be replaced.

2.6 Magnet and Proportional Wire Chamber (PWC) System

A large aperture analyzing magnet is centered $2\,m$ downstream of the target. The magnet was operated at a field of about $5.6\,kG$ (p_T impulse of about $450\,MeV/c$). Downstream of the magnet are four stations of PWC. Each station has four planes of sense wires with an x, y, $u(+37^0)$ and $v(-53^0)$ orientation. Figure 2.4 shows a schematic of the four PWC stations. The chambers have the capability of withstanding $\sim 1\,MHz$ of interaction rates that are needed for high p_T direct photon production, and angular segmentation of $\sim 1\,mr$ required to separate the jet-fragmentation products which accompany direct photons. The chamber sense wires are $20\,\mu m$ gold-plated tungsten, with a separation distance of $2.54\,mm$. Graphite coated mylar sheets ($25\,\mu m$ thick) are used for the cathodes of the chambers. The active areas of the modules are: one $1.22 \times 1.63\,m$, two $2.03 \times 2.03\,m$ and one $2.44 \times 2.44\,m$. The gas used to fill the chambers is an argon, isobutane, isopropyl alcohol and freon mixture. The readout is through CAMAC, and relies on the same Nanometric amplifier, discriminator and latching system used for the SSDs. Momentum resolution ($FWHM$) on charged tracks is

$$\frac{\Delta(P)}{P} = 0.001 \times P\,(GeV/c)$$

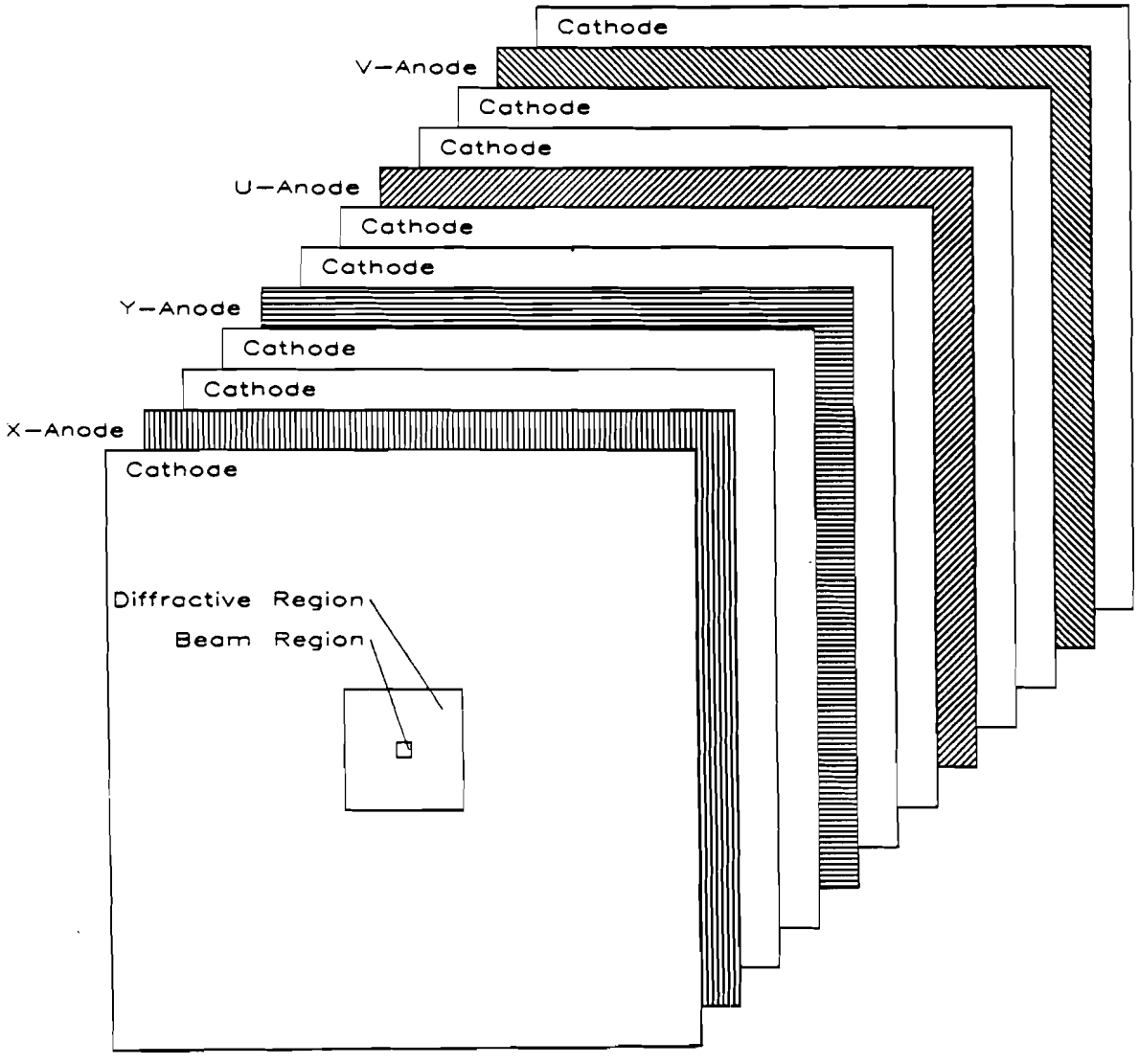

Figure 2.4: Longitudinal view of one PWC station.

2.7 Liquid Argon Calorimeter (LAC)

The E706 apparatus includes a large-acceptance liquid-argon calorimeter for measuring the energy and position of photons, electrons and hadrons. The LAC has two separate parts: an electromagnetic calorimeter (EMLAC) and a hadronic calorimeter (HALAC). Both detectors are enclosed in a cryogenic dewar, filled with liquid argon, and suspended from a common support structure (gantry), which can move transversely to the beam. In our coordinate system, the location of the front face of the EMLAC is at $z = 900\,cm$. The transverse sizes of these detectors are 3.1 and $3.7\,m$, for the EMLAC and the HALAC, respectively. Both calorimeters are of the sampling type, with a common active material (liquid argon), but different absorbers: lead for the electromagnetic, steel for the hadronic, and different sampling fractions.

The LAC has a central hole, $40\,cm$ in diameter, which houses a tapered cylindrical beam pipe that extends along z across both calorimeters. During operation, the beam pipe is filled with helium gas to reduce the amount of material in the beam region. (An evacuated beam pipe would have been more difficult to engineer, and was not thought worth the additional expense.) A thin-walled steel filler vessel is also installed inside the dewar, just in front of the EMLAC. Its volume is filled with a low density ($0.07\,g/cm^3$) foam (Rohacell). The function of the filler is to displace liquid argon, and thereby reduce the amount of passive material in front of the calorimeters.

Both the EMLAC and the HALAC use the same type of read-out electronics. The electronic crates are housed in a Faraday room surrounding the coverplate of the cryostat. In designing the present LAC, the E706 collaboration took advantage of the experience gained previously with a similar detector in experiment E629 [35]. The E706 calorimeter was designed to match the following requirements:

1. Large acceptance to (a) maximize the yield of direct photons, and (b) to provide as unbiased a sample of π^0s as possible, through the detection of photons from π^0 decays. If one of the two photons from the π^0 decay misses the detector, the other contributes to the background of the single photon signal. The electromagnetic calorimeter was designed to have an active area delimited by an inner radius of $22\,cm$ and an outer radius of $150\,cm$. At $900\,cm$ from the target this corresponds to laboratory angles θ between 24 and $165\,mrad$. At $530\,GeV/c$ incident momentum, this translates in the center of mass to an angular acceptance of about 70% of the 4π solid angle.

2. Good resolution for electromagnetic and hadronic energy to be able to reconstruct photons, electrons and hadrons down to low laboratory energies of about $5\,GeV$. This can be achieved by selecting the proper longitudinal sampling fractions for both the electromagnetic and the hadronic calorimeters.

3. Linear response of the calorimeter up to the highest energies. This is needed to obtain the correct dependence of any yield on p_T.

4. Full containment of showers (electromagnetic and hadronic) by minimizing any energy leakage out the back. This usually improves overall energy resolution.

5. Good position resolution achieved using fine lateral segmentation so as to be able to resolve two neighboring showers.

6. Ability to discriminate between photons or electrons and neutral hadrons by means of a suitable longitudinal segmentation, and a proper choice of absorber medium for the calorimeter.

7. Ability to sustain high ($> 1\,MHz$) interaction rates.

8. Ability to easily form a trigger based on the detected transverse momentum (p_T). This was achieved by choosing $r - \phi$ geometry for the read out strips of the electromagnetic calorimeter.

The assembly of all major calorimeter components took place at Fermilab, with the final work carried out in the MWest experimental hall. The debugging of the detector was completed in the spring of 1987. Four months were spent afterwards for the cooldown of the detector before data taking started. Fig. 2.5 shows a cross section through the LAC as positioned in the cryostat; positive z orientation (beam direction) is defined as pointing from right to left. Various structure elements of the LAC and of the cryostat are indicated in the figure.

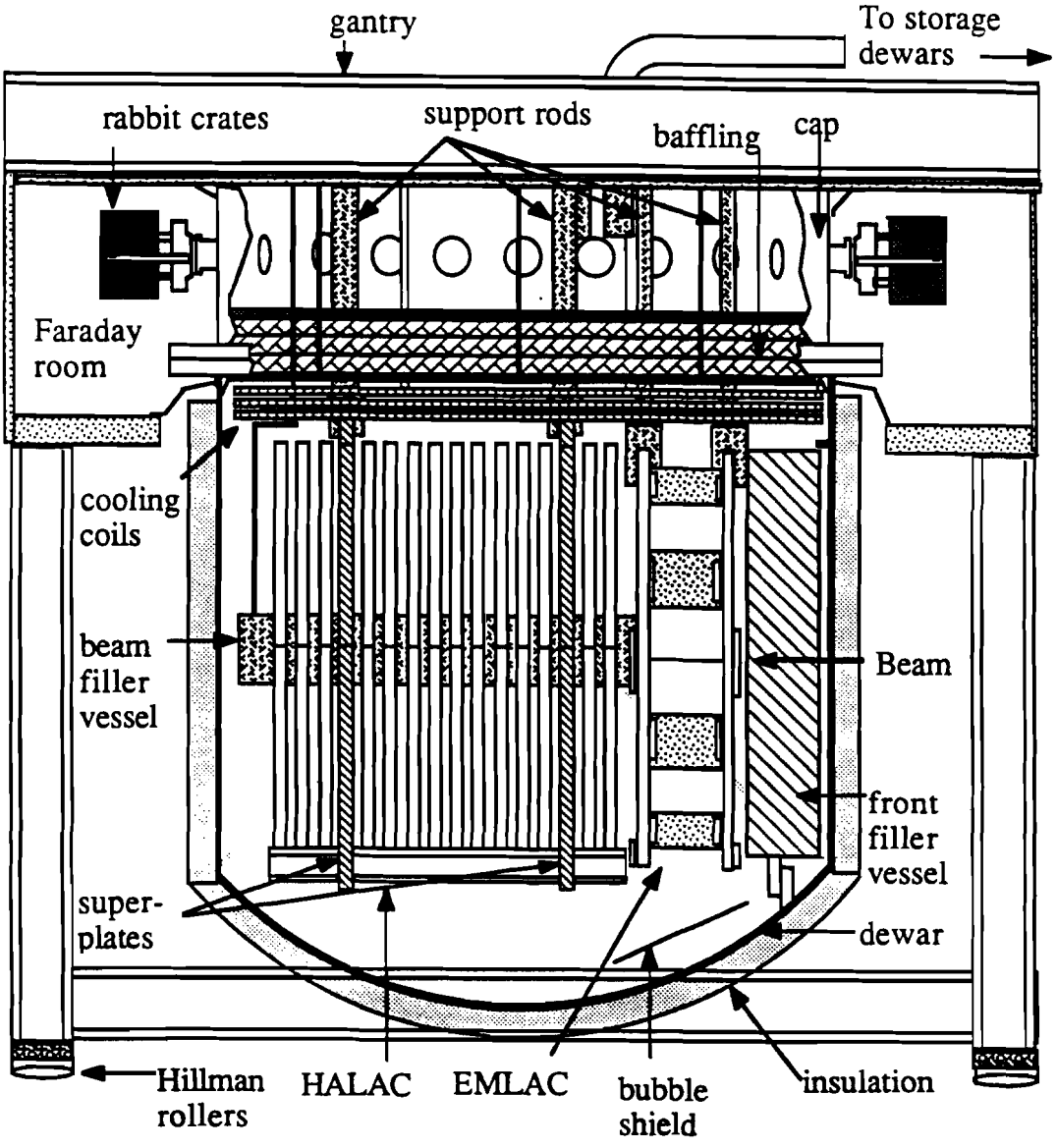

Figure 2.5: Cutaway view of LAC and Gantry.

2.7.1 Electromagnetic Calorimeter (EMLAC)

In the following we will briefly describe the design features and the geometrical characteristics of the electromagnetic calorimeter (EMLAC). We refer to W.E. DeSoi's thesis [36] for more extensive details regarding this part of the apparatus.

The EMLAC was designed to provide accurate measurements of energy of particles that interact electromagnetically within its volume. In this respect, one of the key feature of the detector was the ability to resolve photons from hadrons. This need strongly dictates the choice of absorber material, whose properties primarily determine the showering characteristics. We chose to use lead, because it has a relatively short radiation length ($\lambda_r = 0.56\,cm$), and a long interaction length ($\lambda_i = 17.1\,cm$). As is well known, these two variables characterize the spatial development of electromagnetic and hadronic showers. Geometrically, the EMLAC consists of four mechanically independent quadrants (with radii of about $1.6\,m$), held together by an overall support structure. The four quadrants have identical structure, namely a sequence of 66 lead plates (absorber medium), $2\,mm$ thick, separated by a $2.5\,mm$ liquid-argon gap (active medium) from $1.6\,mm$ copper-clad G-10 readout boards (anode), the latter being octant sized. For the readout an $r-\phi$ geometry was chosen, by alternating G-10 boards with concentric radial strips (r strips), and azimuthal strips (ϕ strips). The r strips are focused to the experimental target, $900\,cm$ upstream, and have widths of approximately $5.5\,mm$. The ϕ strips are divided into inner and outer sections. The separation between

the two ϕ regions is at a radius of $40\,cm$, corresponding to a laboratory angle relative to the experimental target of about $44.4\,mrad$. The inner and outer ϕ strips subtend an angular region of 16.4 and $8.2\,mrad$, respectively. The readout of the strips is divided in two longitudinal sections: a front and a back section. The front section has 22 calorimeter cells (the usual sequence of Pb, Ar, G-10, Ar), the back section has 44. The strips that correspond to the same $r-\phi$ tower are connected together longitudinally by custom-made connector strings. These bring the signals from the inside to the periphery of the detector, to a set of special G-10 readout boards, three for the front and three for the back section. The signal cables (about $10\,m$ long), run from the sets of special boards to the top hat of the cryostat, where they are connected through special vacuum-sealed feed-throughs to the outside electronic crates. There are a total of 6600 readout channels in the EMLAC.

The lead plates are kept at a negative high voltage (about $2.5\,kV$). Because large current drawn across the argon gap tends to drop the nominal electric field, each lead plate is connected to two $100\,nF$ ballast capacitors, whose function is to maintain a constant drift field. The total depth of the EMLAC is about $27\,\lambda_r$ of material (a formula which estimates calorimeter depth required for 95% shower containment can be found, for example, in [37]).

The 1/3, 2/3 longitudinal separation provided good capability for discriminating photons and electrons from hadrons. The longitudinal segmentation also

provided a means of determining the front and back positions of any shower, and thereby the incident direction of the particle that initiated the shower. This information was very useful in later data analysis in rejecting particles that did not originate from the experimental target.

The support structure for each quadrant, as well as additional space needed for readout connectors and G-10 spacers (to separate G-10 boards from each other and from the lead plates), produces dead areas in the detector that vary from approximately 8% of the azimuthal coverage at the inner edge to $\simeq 3\%$ along the outer edge. This loss had to be taken into account in acceptance calculations (see Chapter 5).

2.7.2 Hadron Calorimeter (HALAC)

The hadrons produced in interactions in the experimental target deposit most of their energy in the hadron calorimeter. A sizeable fraction of the hadronic shower is electromagnetic in nature, since about 1/3 of the produced pions are π^0s. The rest of the shower consists of charged hadrons (pions and protons) which interact in the absorber medium through a wide variety of physical processes. Due to the large fluctuations in the characteristics of the hadronic shower it is hard task to design hadron calorimeters with good energy resolution. Presence of neutral particles, in the form of very low energy neutrons or photons, can cause a deterioration of the resolution if such energies are not well measured.

In the following we will give only a brief description of the structure of the

E706 hadron calorimeter, for a more extensive exposition we refer to [38]. There is extensive literature on the subject of calorimetry, see for example [37,39] for a general introduction.

The HALAC is suspended from the gantry, just downstream of the electromagnetic calorimeter. It consists of 52 $\sim 3.7\,m \times 3.7\,m \times 2.5\,cm$ stainless steel (type 410) plates, interleaved with 53 readout units. The shape of the detector planes is approximately octagonal. The readout boards are subdivided into triangular pads that increase in size along the stack, with centers shifting out radially in order to maintain a focused geometry. The readout is structured by connecting a focused tower of triangular pads. The readout modules consist of complementary halves, each half being a sandwich of two $0.8\,mm$ G-10 boards separated by $3\,mm$ argon gaps. In each of the halves the spacing between the G-10 boards is maintained by $3\,mm$ thick G-10 strips. The outer G-10 boards in a module are copper-clad on both sides, with the outside copper held at ground and the inside at high voltage $(-3.0\,kV)$. The inner G-10 boards (anodes), facing the high voltage sides are also at ground. The two anode planes cover only half of the calorimeter area with charge collecting pads, leaving the space between rows of pads for the readout connections to the outer edge of the detector. To guarantee full coverage of the detector solid angle with active readout pads, the two anode boards have the rows of pads shifted vertically relative to each other by one row. Thus the two halves read out complementary areas. The anode boards are separated by $3\,mm$ vertical

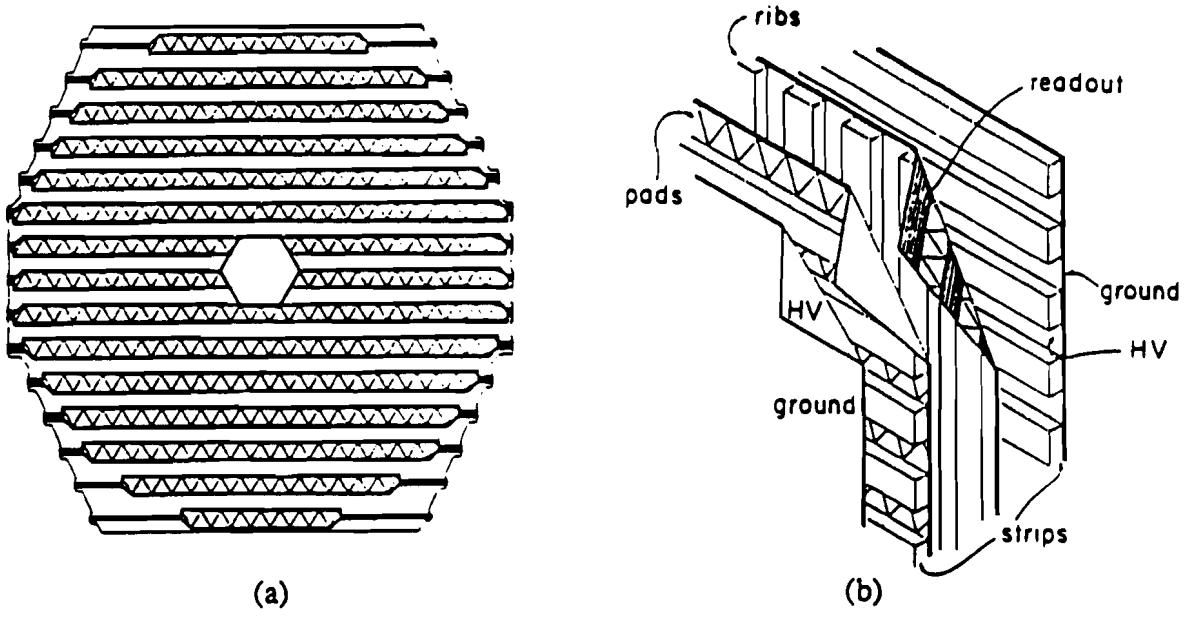

Figure 2.6: (*a*) A view of one of the HALAC readout planes showing the alternating rows of pads and readout lines. (*b*) The mechanical structure of a readout module.

G-10 ribs. Figure 2.6 shows the readout geometry of one of the anode boards, together with an exploded view of one module.

As mentioned earlier both the hadron and the electromagnetic calorimeter use the same readout electronics (see Section 2.7.3). Like the EMLAC, the hadron calorimeter read-out is divided into two longitudinal sections, with the front consisting of the first 14 units. There are a total of 2400 ganged readout-pad channels in the HALAC.

A hadron traversing the LAC samples approximately nine interaction lengths of HALAC material (about 130 cm of Fe), plus about one interaction length of

EMLAC material.

2.7.3 LAC Electronics

The readout electronics of the LAC is based upon the Fermilab-developed Redundant Analog Bus Based Information Transfer system (RABBIT) [40]. Components of the system include:

- Crate Controllers (EWE)
- Before/After Timers (BAT)
- Front End Electronic Devices (FEED).

There are 28 RABBIT crates in our system (20 to read out the EMLAC and 8 for the HALAC). The back plane of each crate has two bus lines for simultaneous access of two channels in a given crate. Each crate houses two EWE modules, one BAT and 20 FEEDs (amplifier cards).

The two EWEs, one for each bus, have a 16 bit Analog to Digital Converter (ADC) per board. They perform digitization and pedestal subtraction whenever the analog signal is above some given threshold setting, which in the following we shall refer to as zero suppression threshold.

The custom designed amplifier card (FEED or LACAMP) is a 16 channel integrating amplifier with a Time to Voltage Converter (TVC), calibrator, and fast trigger output [41].

Prior to digitization through the EWE, the signal from each amplifier is delayed by $800\,ns$ to allow enough time for the trigger decision to form. The delay output is connected to two sampling circuits (Sample and Hold). When the trigger is satisfied, two timing signals (Before and After) are generated by the BAT, causing the Sample and Hold section of the LACAMP to open a switch for each signal, and to hold the output level on a $1\,nF$ capacitor. The EWE then digitizes the difference between the two output levels. The Before signal arrives just before the amplifier signal, while the After samples the peak of the pulse. The typical Before-After time difference is of the order of $500\,ns$, its setting is progammable via an 8 bit DAC on the BAT. Another output signal (Fast Out) is derived from the amplifier output and used for trigger purposes; this is a differentiated signal obtained by subtracting the output from a delayed ($180\,ns$) copy of itself. The Fast Out signal has a $180\,ns$ risetime and a $500\,ns$ width (FWHM), and is roughly proportional to the energy deposited in the electromagnetic shower; the Fast Out is used to generate an overall calorimeter trigger. Finally, the sum of the outputs of four adjacent amplifiers is differentiated, amplified and fed into one TVC. Above a settable threshold level, the TVC produces a voltage proportional to the time between the crossing of a signal above a threshold setting and the timing of the Before pulse (trigger). If a second event occurs during the ramping time of the TVC ($1.5\,\mu sec$), a second TVC records the timing information. Typical TVC resolution was of the order of $12\,nsec$ ($HWHM$), to be compared to the RF bucket

structure of the accelerator ($19\,ns$). For calibration purposes, each LACAMP board is provided with a calibrator circuit which is able to inject a known amount of charge into any of the 16 amplifier channels. Also, each amplifier has a DC offset (pedestal) to ensure a positive output signal, even if no energy is deposited in that channel. The pedestal value was read out automatically at the beginning of each run.

The large capacitance (typically $20\,nF$ per channel) and the broad-band of energies expected to be deposited in the LAC, have driven the design characteristics of the LACAMP; the requirements were:

- a low input impedance
- high gain
- low noise
- stability.

A significant contribution to the individual channel capacitance came from the capacitance of the low impedance ($7 - 12\,\Omega$ at $89\,^0K$) cable, manufactured by the W.L. Gore Co. The detector capacitance varies between 1 and $5\,nF$ per channel (EMLAC), 3 and $15\,nF$ (HALAC). The capacitance of the $10\,m$ signal cable is about $10\,nF$ for the EMLAC, and about $5\,nF$ for the HALAC. The LACAMP was designed assuming $12\,\Omega$ impedance and $20\,pF$ feedback capacitance per amplifier. These specifications force the need for high gain. If we consider, for example, that

for each event the collected charge is shared between the detector capacitance (cable included) and the effective capacitance of the amplifier (gain times feedback capacitance), in order to collect 90% of the charge on the feedback capacitor, a value for the gain of the order of several thousands is required. The gain stability of the amplifiers was monitored periodically between runs using a pulser to inject a signal of known charge into the amplifier before reading it out.

The interface between the EWEs and the Data Aquisition System (Unibus, PDP11, VAX) is provided through a processor called MX [42]. Each MX is capable of addressing 8 EWEs, thus providing a link to four RABBIT crates. There are 9 MXs, 8 to address the RABBIT crates (3 crates for each MX), and one connected to the trigger logic system.

2.7.4 Principles of Operating a LAC

Atoms ionized in the development of an electromagnetic shower in the LAC produce electron-ion pairs which are then collected on their respective electrodes (in an electric field E), and provide the detected electric signal. The generated amount of charge and the collection time are quantities that depend on the properties of the *active* medium. We chose liquid argon because it has a low electron affinity and a high electron mobility. Many electronegative impurities are *frozen* out in liquid argon. It is dense ($\sim 1.4\, g/cm^3$) and relatively inexpensive. It is easy to purify, and is inert (i.e. non-flammable). The major disadvantage is that the containment vessel must be maintained at liquid argon temperature ($89\, K^0$).

Consequently, the structural components of the LAC must be carefully considered, and a detailed study of the cryogenic properties of different construction materials must be undertaken to minimize impurities that could cause a deterioration of the signal to noise.

To understand the physical processes which take place during the development of an electromagnetic shower in the LAC, consider the case in which there is no electron-ion recombination during the charge collection time, nor any electron absorbtion. The energy lost per cm of argon gap for minimum-ionizing particles is approximately $dE/dx = 2.1\,MeV/cm$. The measured ionization potential in liquid argon is $23.6 \pm 0.3\,eV$, slightly smaller than the value of $26.4\,eV$ for gaseous argon. Given a density of liquid argon of $1.39\,g/cm^3$, we conclude that a minimum ionizing particle (such as a muon) will produce about $10^5\ e-ion$ pairs per cm. After the pair is created, electron and ion start migrating towards their respective electrodes. The drift velocity (v) of the electrons in the gap can be written as

$$v(cm/sec) = 2.1\ \times\ 10^4\,[E\,(V/cm)]^{1/3} \tag{2.1}$$

If the argon gap has an electric field of $10\,kV/cm$ (a typical value for E706), then v, for electrons, is of the order of $4.5\ \times\ 10^5\,cm/sec$, and the drift time, through a $2.5\,mm$ argon gap, is approximately $t_{drift} = 550\,nsec$. The electron and ion drift velocities differ by a factor of about 1000 [43], therefore, for the times under consideration in E706 (0.4 - $1.5\,\mu sec$), the ions can be regarded as essentially at rest. The electron charge will drift toward the G-10 readout plane, producing a

current flow as a function of time:

$$i(t) = \frac{Ne}{t_{drift}} [1 - \frac{t}{t_{drift}}] \tag{2.2}$$

where N is the number of electrons produced in the argon gap, e is the electron charge, and t_{drift} is the drift time across the gap. The total collected charge in a time t is then:

$$Q(t) = \frac{Net}{t_{drift}} [1 - \frac{t}{2t_{drift}}] \tag{2.3}$$

This is assuming that the argon is pure. If there are electronegative impurities in the liquid argon, they can form negative ions through electron capture. The captured electrons will thereby have their mobility changed to the negligible ion mobility, and the charge collection will be affected. This loss can be characterized by adding a damping term in the Expression (2.2) for the current, which will now take the form:

$$i(t) = \frac{Ne}{t_{drift}} [1 - \frac{t}{t_{drift}}] e^{(\frac{-t}{\tau})} \tag{2.4}$$

where τ is the mean time for electron capture. The most dangerous contaminant for LAC is oxygen, because it has a large electron affinity, dissolves well in liquid argon, and is likely to be present whenever there is insufficient evacuation of the containment vessel, leaks or outgassing from the walls of the cryostat. Defining the electron mean free path $s = v\tau$, experimentally one finds:

$$s = \alpha \frac{E}{p} \tag{2.5}$$

where E is the applied electric field (kV/cm), p is the oxygen impurity content in atomic parts per million, and α is a constant which has the value

$$\alpha = 0.12 - 0.15\,cm\,\frac{(ppm\ oxygen)}{(kV/cm)} \tag{2.6}$$

Folding these quantities into Expression (2.4) for the current, and performing the time integration to get the charge, one finds:

$$Q = N\,e\,\frac{s}{d}\,[1 - \frac{s}{d}\,(1 - e^{(\frac{-d}{s})})] \tag{2.7}$$

where d is the gap width. Two limiting cases are:

1. $s << d$, then $Q = N\,e\,\frac{s}{d} \rightarrow 0$, and only the charge produced within a distance s of the electrode is collected;

2. $s >> d$, then $Q = \frac{Ne}{2}$ is the charge collected for this case of negligible amounts of impurities.

The fraction of generated charge that is collected in the LAC during normal operation can be obtained as follows. If the particle hitting the LAC deposits all its energy in the argon gap, then the number of produced electrons is the energy of the incident particle divided by the ionization potential of liquid argon. Since the E706 calorimeter is a *sampling* calorimeter, only the fraction of energy deposited in the liquid argon contributes to the observed signal. For a typical cell of the E706 LAC (two 2.5 mm argon gaps, one 2 mm lead plate, one 1.6 mm G-10 board), this fraction can be written in the form:

$$F = \frac{dE(argon)}{dE(argon) + dE(G-10) + dE(absorber)} \tag{2.8}$$

where $dE(absorber)$ is the energy lost in the absorber (lead for the electromagnetic calorimeter, and steel for the hadron calorimeter). The percentage F amounts to 25.7% and 2.9% for the electromagnetic and hadronic part of the LAC, respectively. Using Expression (2.7) in the approximation of negligible oxygen contamination, folding in the fractional factor of Expression (2.8), and assuming no further reduction in the amount of collected charge (from other impurities or electron argon-ion recombination), the detected signal per GeV is:

$$Q = e \frac{1\,GeV}{2 \times 24eV} F \tag{2.9}$$

namely $3.2 \times 10^6\, electrons/GeV$ $(500\, fC/GeV)$ for the electromagnetic calorimeter, $4.4 \times 10^5\, electrons/GeV$ $(70\, fC/GeV)$ for the hadron calorimeter.

Expression (2.9) can only be correct for incident muons (minimum ionizing), but gives a theoretical value approximately 30% too high for incident electrons. This problem created numerous controversia in the past few years. This 30% decrease in electron signal relative to muons is mainly due to undetected photons and electrons that are absorbed in the high Z (Pb) material of the calorimeter. For low Z medium (Fe), the e/μ ratio is in fact close to one [44].

2.8 Forward Calorimeter (FCAL)

The E706 forward calorimeter was designed to measure the energy of particles in the forward region not covered by the liquid argon calorimeter because of presence of the beam hole. The FCAL detector is located $15\,m$ downstream of the

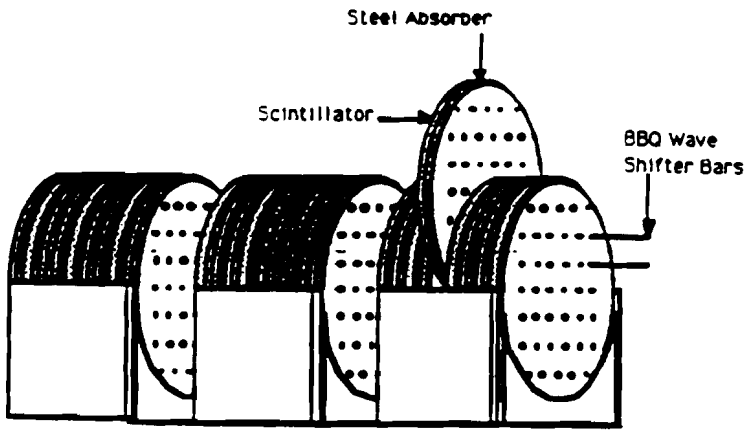

Figure 2.7: Schematic of the Forward Calorimeter.

interaction target; it is divided into three identical modules. Each module is of the sampling type and consists of 29 layers of $4.6\,mm$ thick acrylic scintillator (*Plexipop*), alternating with 28 $1.9\,cm$ thick steel plates. A central hole of $3.2\,cm$ diameter was left for allowing the non-interacting beam to go through. Each scintillator sheet has a series of 76 holes through which $1\,cm$ diameter by $86\,cm$ long wavelength-shifter rods are inserted. Figure 2.7 shows a sketch of the detector.

Light produced in the scintillator and collected on the rods, is shifted from the blue of the scintillator's emission band to the green of the rod's transmission band by an organic dye (BBQ) doped into the rods. Each wave shifter rod has a phototube attached to the downstream end. The signal from each photomultiplier is amplified (by a factor of 20), and sent over coaxial cables to Fast Analog to Digital Converters (FADC), which are configured in a non-linear mode to increase the dynamic range from 6 to 8 bits. The FADC's sampling rate was $90\,MHz$. The total number of readout channels is 228.

2.9 Trigger

This section outlines the general features of the trigger system implemented during the 1987-1988 run. For a more detailed description see [45].

As already mentioned, the goal of this experiment was to measure the production of high p_T neutral particles (direct γ, π^0, η, etc.) in fixed-target hadronic interactions. The interaction rate in hadronic collisions ($\sim MHz$) is in general much higher than the event rate stored for analysis ($10 - 20\,Hz$). The trigger system provides the necessary rate reduction by limiting the data acquisition only to events of interest. Particles are not produced very often at large p_T in hadronic interactions. In this experiment, to discriminate against low p_T events which constitued the bulk of data, a trigger system was implemented to select events on the basis of transverse momentum. The estimate of a particle's transverse momentum was obtained by weighting the energy deposited in the EMLAC according to the position of the particle in the detector. This had to be done immediately after the interaction time in order to determine whether to accept or reject the event. The next section will illustrate this point more extensively.

In the following we will describe the sequence of trigger decisions, and the trigger types. At the end of Chapter 5, we will present some results characterizing the trigger performance. Figure 2.8 shows a simplified layout of the overall trigger logic. The decision for triggering on a particular event contained three main steps: beam and interaction definition, preselection of the interaction, and final selection

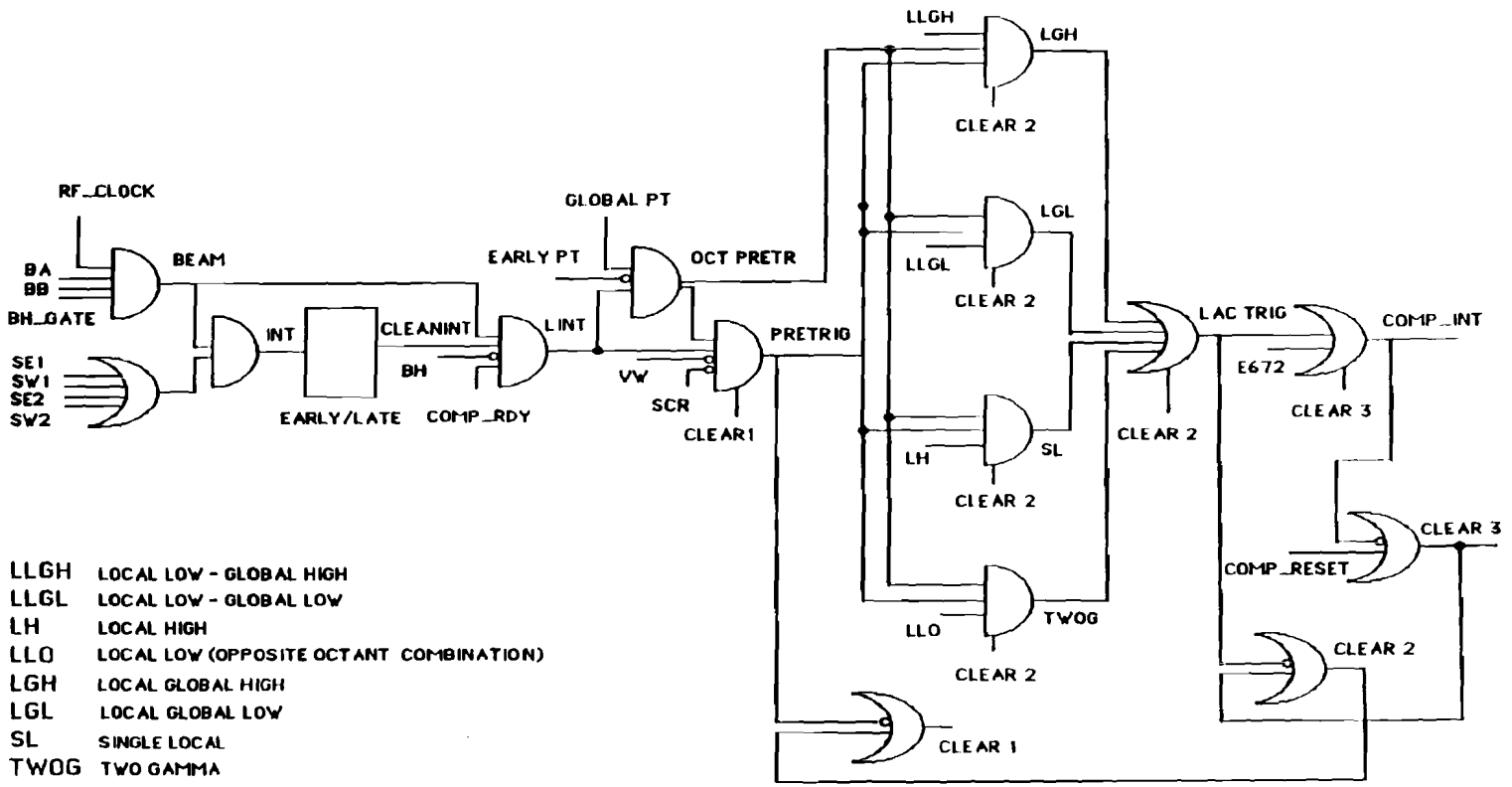

Figure 2.8: Layout of the LAC Trigger Logic.

of the event.

The accelerator beam spill lasted about 23 *sec*, and the spill cycles were ~ 60 *sec*. As described in Section 2.3, a beam particle was defined when a coincidence occurred between the two beam-defining scintillation counters BA and BB. To define an interaction, the beam signal had to be in coincidence with the logical OR of the discriminated signals from the four interaction counters $SW1$, $SW2$, $SE1$, $SE2$, located downstream of the target. (The logical OR of the four interaction counters was replaced later in the run with the requirement that at least two interaction counters fire). The interaction signal (INT) was defined as:

$$INT = BA * BB * (SW1 + SW2 + SE1 + SE2) * BM\_GATE \qquad (2.10)$$

The beam gate (BM_GATE) was a reference pulse from the main ring used to set the time interval during which the trigger was enabled; it remained open throughout the length of the beam spill. If the above definition was satisfied, the interaction signal was sent through a pile-up filter to check that no additional interaction had occurred within three RF beam buckets (lasting 19 *nsec* each) before or after the bucket containing the useful interaction signal. Two signals, CL_EARLY and CL_LATE, were generated reflecting the satisfaction of this requirement. The interaction signal, defined in Expression (2.10), was further required to be in coincidence with a computer ready signal ($COMP\_RDY$), and in anticoincidence with the beam-halo counter BH (clean interaction). If all the

above conditions were met, a triggerable interaction, *LINT*, was defined as:

$$LINT = INT * \overline{BH} * COMP\_RDY * (CL\_EARLY + CL\_LATE) \qquad (2.11)$$

From *LINT*, an interaction strobe signal was generated to be used in the definition of a pretrigger.

The pretrigger preselected high p_T events by requiring a minimum global transverse momentum deposition of $\sim 1.7\,GeV/c$ in one of the EMLAC octants. The global p_T signal (*GLOBAL_PT*) was put in coincidence with the interaction strobe signal (*LINT*) defined above, and in anticoincidence with an early interaction signal (*EARLY_PT*), to form an octant pretrigger signal (*OCTPRT*).

$$OCTPRT = LINT * GLOBAL\_PT * \overline{EARLY\_PT} \qquad (2.12)$$

The *EARLY_PT* interaction veto protected against situations in which an apparent high p_T event was in reality a superposition of two successive lower p_T interactions. This vetoing signal eliminated events in which an interaction occurred up to $300\,nsec$ earlier than the one associated with the pretrigger.

The logical OR of all octant pretriggers (*LACTIM*), in coincidence with the interaction strobe *LINT*, and in anticoincidence with two vetoing signals, VW, and SCR, formed a global pretrigger signal (*LACPRT*), to be used in the definition of the final LAC triggers.

$$LACPRT = LINT * LACTIM * \overline{VW} * \overline{SCR} \qquad (2.13)$$

The veto wall signal VW, was defined to be the logical AND of the ORs of the

counters in geometrically corresponding veto wall quadrants (see Section 2.3 for details on the veto wall structure).

A signal for vetoing Silicon-Controlled-Rectifier (SCR) spikes was generated when such noise, occurring at a few kHz rate, was produced by the 400 Hz power supplies inside the Faraday room.

Each pretrigger generated its own reset pulse, which was delayed by 500 $nsec$ to allow sufficient time for the EMLAC to collect charge and to form fast output signals (see next section) used by the p_T trigger logic.

Finally, a LAC trigger was defined by the coincidence of a pretrigger signal with the signals from the EMLAC p_T trigger logic. The latter corresponded to a local and a global p_T requirement in each octant (see next section). Each of the two p_T signals (local and global) were compared to two preset p_T thresholds (2.7 and 3.5 GeV/c). The combinations of the two p_T signals and the two thresholds defined four LAC trigger types: $LOCAL * GLOBALHIGH$, $LOCAL * GLOBALLOW$, *SINGLE LOCAL* and *TWO GAMMA*. (The p_T thresholds were reset to different values during the run). Three additional trigger types, independent on any LAC p_T requirement, were also implemented; one of these was specific to the physics goals of Experiment 672[2]. For a more detailed description of the features of the different LAC triggers the reader is referred to [45].

For reasons that will be explained in Chapter 5, in this thesis we analyzed

[2]E672 spectrometer is located downstream of the FCAL. The E706 trigger and data acquisition were in a sharing mode with E672.

only those events that satisfied the *SINGLE LOCAL* trigger requirement (a single event could satisfy multiple trigger requirements). The *SINGLE LOCAL* trigger required that one or more octants had a local p_T signal above the nominal value of the higher local p_T threshold (which was varied between 3.0 and 4.2 GeV/c during the run).

If no trigger signal was generated after a pretrigger had fired, a reset signal (*CLEAR*) was sent to clear the pretrigger logic units. After a reset time of 5 μsec, the trigger system was re-enabled for the next event. When a trigger was generated, a signal was sent to the computer to proceed with the data acquisition for the event. After data acquisition, the computer system generated a reset signal to clear the trigger memory.

2.9.1 Trigger Electronics

Two special units were designed for the trigger electronics: a p_T *module* and a *discriminator module*. The p_T module consists of a two-channel adder stage followed by an attenuation stage. It is provided with 32 high-impedance inputs for the Fast Output signals from the LACAMPs. The first stage allows the summing of two neighboring inputs, thus providing 16 inputs to the second stage which is an attenuator. In it, each of the 16 input signals receives an attenuation whose magnitude is directly proportional to the sine of the angle (θ) between the r-strip corresponding to a specific LAC channel and the beam axis. It basically provides the p_T observed at any location in the detector. An amplification stage

in the p_T module is used to maintain an overall gain close to unity. The input to each amplifier in the p_T module has four sums of eight attenuator outputs. The output of the amplifier stage consists of the four sums of eight, and a sum of all 32 channels. The latter, after further summing, provides octant and quadrant *global* p_T triggers; the sums of eight are used for forming the *local* p_T trigger. The four sums of eight outputs from the p_T modules are fed into discriminator units. Each of these has 64 inputs channels, half from the front part and half from the corresponding back part of the LAC. The first stage of the discriminator module sums the appropriate front and back signals. The second stage forms overlapping sums of 16 adjacent signals, which are then discriminated. The discriminated signals are used to generate the local p_T trigger.

As already mentioned in the previous section, the reason for the local p_T trigger is to be able to discriminate between a single high-p_T and several low-p_T electromagnetic showers. Another reason for implementing a local energy requirement is the fact that the octant global trigger, containing many channels, is sensitive to environmental coherent noise. Some sources of noise, for example the SCR spikes, are particularly troublesome and must be vetoed separately so as not to swamp the trigger.

2.10 Data Acquisition System

A MicroVax 2000 computer was used as the central event processor for the E706 on-line data acquisition system. A Fermilab supported data acquisition program

(VAXONLINE) was run on the MicroVax. The program provided the user with the software interface between the master computer and four peripheral subsystems. Each subsystem consisted of one PDP-11, which collected the event fragments from a specific part of the experimental apparatus. The four PDPs controlled the performances of the tracking (SSDs and PWCs) and of the trigger systems, of the LAC, of the forward calorimeter, of the E672 spectrometer. The event informations from each part of the apparatus was sent via the four PDPs to the MicroVax to be concatenated and form a global event. The global events were then logged to magnetic tape. For the monitoring and debugging of the different detectors we used a software package (CONSUMER) supported by the Fermilab Computing Department and run on a VAX-11/780 computer. The PDP that collected the LAC events periodically recorded values for the pedestals and gains of the LAC amplifiers. The link with the LAC RABBIT electronics system was provided by the set of nine MXs (see Section 3.6.2). The scheme used for the LAC data acquisition system is shown in Fig. 2.9.

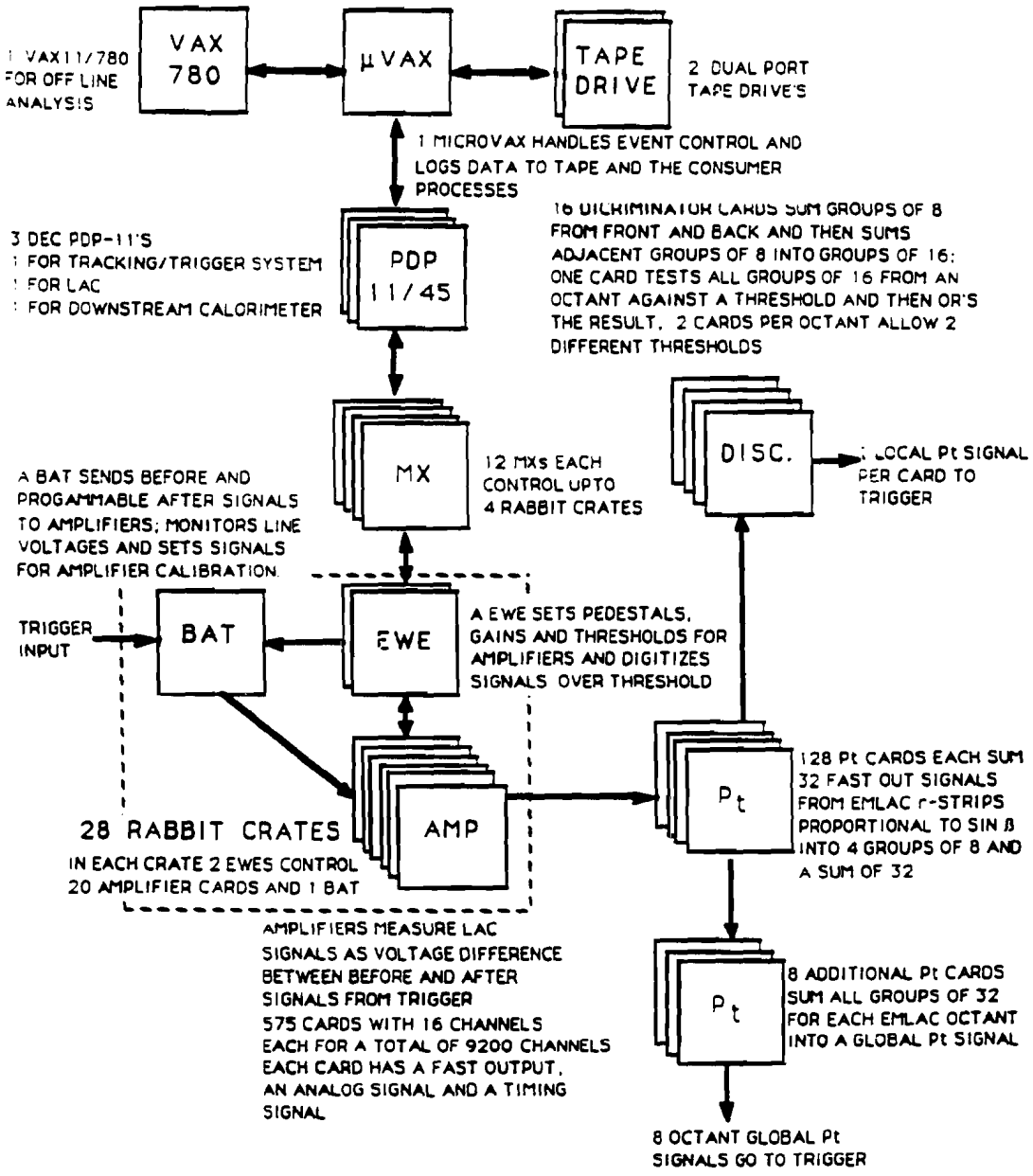

Figure 2.9: Flowchart of LAC Data Acquisition System.

Chapter 3

PHOTON AND π^0 RECONSTRUCTION

3.1 EMLAC Calibration

In order to determine an overall normalization factor which establishes the absolute energy scale, we calibrated the LAC using electron beams of known energy. This was done during a special period of the experimental run, the results of which will be discussed in the next sections.

Before event reconstruction, the ADC counts for any detected pulse height have to be converted to units of energy. The relation is:

$$E_i = A_i G_i (N_i - N_{0i}) \tag{3.1}$$

where: E_i is the energy in i-th strip, A_i is an overall normalization factor, G_i are the relative gain for channel i, N_i is the ADC count for channel i, and N_{0i} is the pedestal for channel i. The gains G_i are related both to the electronic properties of the amplifiers and to the characteristics of the charge collection mode. Average pedestal levels were recorded every few runs and stored in a specific data base. This was done by reading out the calorimeter when no energy was

present in the LAC. The pedestal subtractions were performed during off-line event reconstruction. Another approach used to estimate the pedestal level consisted of injecting charge directly at the input of the amplifier, by means of an on-board calibrator. The two independent techniques showed typical pedestal fluctuations of up to 20 ADC counts for any single LAC channel, and some correlation between the size of the fluctuation and the position of the corresponding readout strip. A contribution to this fluctuation comes from the DC offsets of the difference amplifiers in different amplifier cards. Another source of fluctuation comes from induced positive DC signals generated by the slow drifting ions. In the inner regions of the detector, where the event multiplicity is higher, larger pedestal fluctuations were noticed. A satisfactory parametrization of pedestal behavior has yet to be completed. This means that the present data still have small systematic uncertainties that should eventually be reduced.

The average gain for each amplifier was also measured between data runs. Gain variations with time were estimated to be less than or of the order of 1.5%. Although gains were designed to be the same for all amplifier channels, corrections based on observed drifts were implemented at the unpacking stage of the reconstruction program on a card-by-card basis. An incident calibration beam of 25, 50 and 100 GeV/c electrons was used to determine the overall conversion factors (A_i) from ADC counts to units of energy. By moving the gantry along x in steps of a few cm, and vertically, along y, by using a dipole pitching magnet

located $70\,m$ upstream of the target, the beam was swept horizontally across the front face of the LAC. Data were recorded with the beam hitting the LAC in many different locations. The analysis of the calibration events provided a significant improvement in the understanding of the performance both of the LAC and of part of the tracking system (PWC). The advantage of calibrating the LAC using particles of known energy and precise location in the calorimeter is that it enabled us to investigate issues such as:

- energy resolution for electromagnetic showers,
- linearity of the energy response,
- strip capacitance effects,
- charge collection efficiency,
- image charge effects,
- gains and pedestals fluctuations,
- effects due to structural variations in the detector (Pb plate-thickness variation),
- purity of the liquid argon.

An average value of $A_i = 3.1\,MeV/count$ was obtained from the electron data and, subsequently, confirmed from the analysis of the two-photon decays of π^0s in normal data.

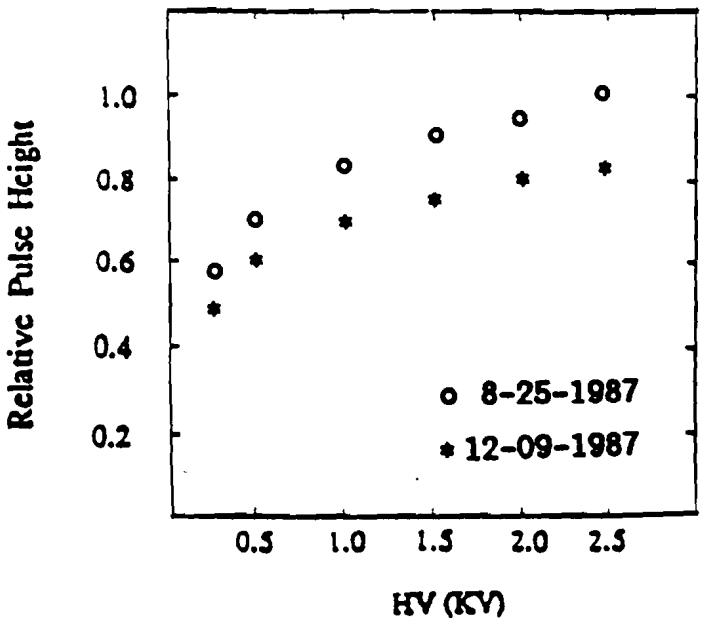

Figure 3.1: Two HV excitation curves taken using 50 GeV electrons in the electromagnetic calorimeter. The vertical scale is normalized arbitrarily to the highest data point.

The purity of the argon in the cryostat was monitored during the entire run. At the beginning, soon after the argon filling, a HV excitation curve was taken using 50 GeV/c incident electrons. Four months later a similar HV curve was taken. A drop of the pulse height of about 20% at the operating field ($10\,kV/cm$) was detected from the second measurement. The two sets of data are shown in Fig. 3.1. It should be noted that the shape of the excitation function is essentially the same for both studies. We are still investigating the nature of the contaminant that caused this drop in pulse height with time. Monitoring argon purity by sampling argon gas from the top of the cryostat, and flowing it through an oxygen analyzer, revealed that, seven months after the initial filling, an oxygen contamination of

less than $1\,ppm$ was measured. Thus we believe that O_2 is not the cause of the observed drop in pulse height.

3.2 EMLAC Resolution and Linearity

Position and energy resolution in a LAC is often limited by statistical fluctuations in the development of the shower. Pair production and photon Bremsstrahlung, which are the dominating mechanisms in electromagnetic shower multiplication, characterize the longitudinal shower profile. Multiple Coulomb scattering of electrons affects the lateral spread. The intrinsic energy resolution is therefore sensitive to these processes, while the overall energy resolution of the calorimeter is dependent also on other effects, such as mechanical non-uniformities, pedestal and gain fluctuations, amplifier noise and ADC threshold-setting variations. In this section we will attempt to describe the procedures we used to determine the properties of the EMLAC, namely its position and energy resolution. For this purpose, we performed an independent analysis of two sets of data: the beam-calibration data and a subsample of events selected from the regular data runs. For the latter, a detailed description of the results of the analysis can be found in [46]. The results of the analysis concerning the response of the HALAC to hadron-beam calibration can be found in [47]. As far as the analysis of the beam-calibration data is concerned, the response of the EMLAC was investigated both as a function of the beam energy (25, 50, $100\,GeV$) and position of the beam on the face of the EMLAC.

3.2.1 Energy Resolution

The r and ϕ views of the EMLAC can provide independent measurements of photon (or electron) energy. Because of this feature of the detector, the measured energy difference between the two interleaved r and ϕ views provides a good estimate of the energy resolution of the calorimeter. The dispersion in the energy difference $\sigma(E_r - E_\phi)$ has contributions from two sources: statistical fluctuations in the shower sampling and fluctuations due to incoherent type of noise; coherent energy fluctuations tend, in fact, to cancel out in the difference $E_r - E_\phi$. Formally, one can express this σ in the form:

$$\sigma(E_r - E_\phi) = \sqrt{\sigma^2_{intrinsic} + \sigma^2_{incoherent}} \tag{3.2}$$

The incoherent noise, which contributes to the measured energy resolution, has origin in such effects as the uncorrelated fluctuations of the pedestal levels and any possible digitization threshold variations of the ADCs. The magnitude of these effects was estimated from the analysis of the pedestal distribution for single-channel ADC values, and from runs for which the zero suppression window was not activated. In particular, we measured the width of the pedestal distribution and the relative shift between the pedestal mean value and the nominal value of the zero suppression threshold. Typical measured values were about 60 and $45\,MeV/channel$ for the width of the pedestal distribution and for the incoherent shift of the pedestal mean value, here named σ_1 and σ_2, respectively. An independent measurement, using a pulse generator to input signals at each am-

plifier, confirmed these previous values. An estimate of $\sigma_{incoherent}$, which appears in Expression (3.2), can be obtained by adding in quadrature σ_1 and σ_2, and multiplying the result by the square root of the total number of readout channels for a typical shower. Assuming that a $50\,GeV$ shower spreads laterally over an area corresponding to about 10 strips, considering the two views (r and ϕ) and two sections (front and back), then, for $N = 40$ channels, we can estimate:

$$\sigma_{incoherent} = \sqrt{N}\sqrt{\sigma_1^2 + \sigma_2^2} \simeq 475\,MeV \tag{3.3}$$

The above assumes that contributions from gain variations can be ignored. In fact, since the calibration beam was localized to a small region of the detector then any gain variation should not affect the estimate of the resolution. For normal data, electromagnetic showers are detected throughout the entire detector, and consequently another term of the type $g_i E$ could enter into $\sigma_{incoherent}$, where g_i would reflect sources such as gain variations that can contribute to deterioration in the resolution. Consequently, for calibration data, the contribution to the $\sigma_{incoherent}$ should be well described by the energy-independent form (3.3).

The term $\sigma_{intrinsic}$, being due purely to sampling fluctuations, is proportional to the square root of the incident energy, and can be written in the form:

$$\sigma_{intrinsic} = A_1\sqrt{E} \tag{3.4}$$

After removing ambiguous events that had electron showers accompanied by nearby Bremsstrahlung photons, the sample of electron data from calibration

runs was used to obtain the *rms* widths of E_r - E_ϕ distributions for single-shower energy depositions. The results for three beam energies are shown in Fig. 3.2, which shows a plot of $\sigma^2(E_r - E_\phi)$ versus E ($E = E_r + E_\phi$). We fit the three data points using a linear dependence of the form:

$$\sigma^2(E_r - E_\phi) = (A_1 \sqrt{E})^2 + A_3^2. \tag{3.5}$$

A_1 reflects the sampling, term causing the resolution to scale as the square root of E, A_3 is the incoherent noise term. In the σ^2-E plane, A_1 and A_3 correspond to the slope and the y intercept of the straight line, respectively. The values obtained for the parameters are $A_1 = 0.144 \pm 0.04$ and $A_3 = 0.36 \pm 0.3$. The value of A_3 is reasonably consistent with the expected $A_3 \simeq 475\, MeV$ (from Expression (3.3)). From earlier studies using the EGS (Electron-Gamma-Shower) Monte Carlo program [48] we predicted a value for the intrinsic energy resolution of the EMLAC stack as $A_1 = 0.11 \pm 0.01$ for electrons of energy between $10\, GeV$ and $100\, GeV$. We believe that our present experimental value for the error due to sampling fluctuations will improve once the incoherent noise contributions become better understood. More sophisticated corrections for reconstruction inefficiencies (e.g., splitting of showers that merge in one or both views, and algorithms for handling tails of showers) are also expected to decrease the above value of A_1 somewhat.

We mentioned the fact that a distribution that samples the difference between the energy deposited in the two views, r and ϕ, is likely to be insensitive to sources

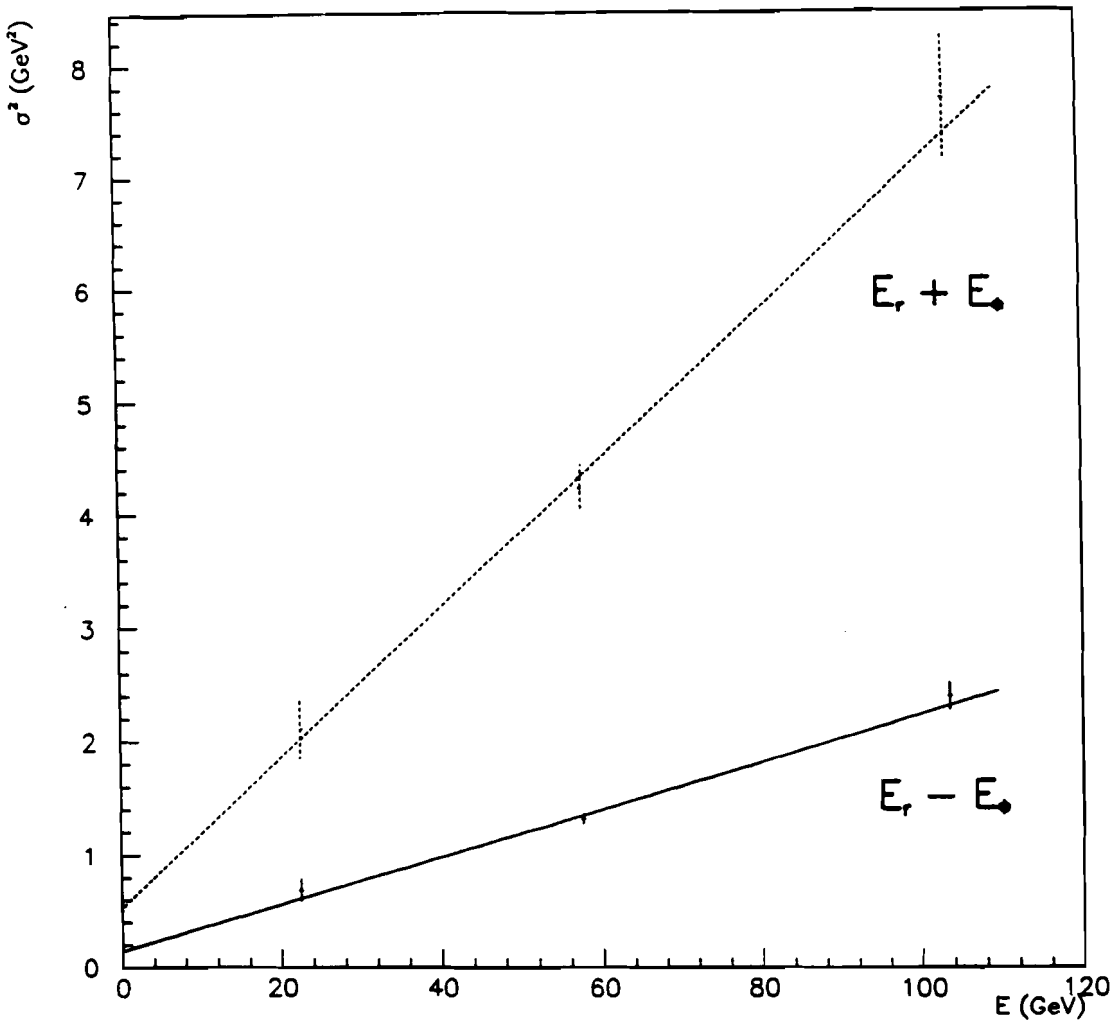

Figure 3.2: Calibration Beam data. The square of the *rms* of the distributions of the sum and the difference of the measured energies in the r and ϕ detector views is plotted versus the incident beam energies.

of coherent noise. This is not the case for distributions that measure the sum $E_\tau + E_\phi$. The width of such distributions become sensitive to contributions from coherent noise, momentum spread in the beam and residual effects such as non-uniformities in the detector. The effect of coherent noise is to change the absolute value of the energy-independent term A_3 of Expression (3.5). The momentum spread of the beam and the non-uniformity in the detector will introduce a new term linear in the total energy. Therefore Expression (3.5) will become:

$$\sigma^2(E_\tau + E_\phi) = (A_1\sqrt{E})^2 + (A_2\,E)^2 + A_3^2 \qquad (3.6)$$

Effects of detector non-uniformity are not directly measurable. The momentum bite of the calibration beam was about 2%. In Fig. 3.2 $\sigma^2(E_\tau + E_\phi)$ is plotted versus $E_\tau + E_\phi$, for three calibration beam energies. For lack of sufficient data, we used a simpler fit of the type in Expression (3.5). The slope and the y intercept of the straight line are $(0.257 \pm 0.08)^2$ and $(0.69 \pm 0.5)^2$, respectively. As expected, the constant term A_3 is larger for $\sigma(E_\tau + E_\phi)$ than it was for $\sigma(E_\tau - E_\phi)$. Since for $E_\tau + E_\phi$ distributions the parameter A_3 is the sum in quadrature of $\sigma_{incoherent}$ and $\sigma_{coherent}$, then, from its value and from the value (3.3), we can deduce a coherent noise contribution to the resolution of the order of $590\,MeV$. As far as the determination of A_2 is concerned, we can estimate its magnitude by assuming that the slope parameter 0.257 has in it the contribution from the sampling term of Expression (3.5), proportional to $A_1 = 0.144$, and from the term in Expression (3.6), which scales with the energy like $A_2 E$. For $E = 50\,GeV$, we can estimate A_2

to be about 3%. A_2 is, in fact, the sum in quadrature of a term which represents the beam momentum spread (2%), and a second term which accounts for the detector non-uniformity. (We assume here that showers induced by the calibration beam are only sensitive to longitudinal type of non-uniformity in the sampling, as they are localized to a small region of the detector). From previous discussion it follows that detector non-uniformities affect the resolution at the 2% level.

As can be gathered, our analysis of the relative error contributions to the EMLAC energy resolution is somewhat arbitrary because the number of unknown parameters is larger than the number of available measured quantities. It is, of course, even more difficult to determine separate contributions to the resolution using events with a more complex structure, with shower origins not localized in one spot, in an environment with substantial backgrounds from hadrons, and for both electron and photon showers. The normal data, as opposed to calibration data, provide just such events. The energy resolution is expected to worsen due to additional fluctuations such as those due to gain variations of the channel amplifiers, which did not contribute above, and due to non-uniformity of the detector across transverse dimensions of the shower (e.g., from thickness variations of argon gaps and lead plates). The gain variations, proportional to E, have been measured as less than or of the order of 1.5% [49], the transverse non-uniformity of the detector is presently unknown. To address these additional issues, and to confirm some of the results obtained from the analysis of calibration data, we

selected a sample of normal events, but with structure that resembled the simple calibration events in terms of presence of single isolated electromagnetic showers. Because these clean events were collected during the experimental run, and contained showers of different energy, they were particularly valuable for monitoring the performance of the detector. In the following we will briefly describe the nature of the chosen events, and will present results obtained from their analysis.

Among the events that have electron candidates, of particular interest are those in which an electron-positron pair originates from photon conversion (usually from π^0 decay) in the target. For these events, a single upstream track matches at the magnet to two downstream tracks, which then travel, with opposite curvatures, to the LAC. The downstream opening angle between the tracks, is inversely proportional to the energy of the converting photon (at least in the case of symmetric conversion), and proportional to the momentum impulse of the analyzing magnet. The event signature is characterized by two tracks with the same slope in the y-plane, and a location of their intercept in the xz-plane near the magnet center ($z = 200\,cm$). The invariant mass of the final system (electron-positron pair) is very close to zero (typically $5 - 10\,MeV/c^2$). Very little hadron background survives this kind of event selection requirement. In the following we will name events so selected as *Zero Mass Pair* (ZMP) candidates. For these events, information from the charged-particle tracking system is needed to point at an electron in the LAC. The electromagnetic shower is required to have a detected charged track as-

sociated with it, whose projection on the front face of the LAC falls within a small region (typically a circle of 0.5 cm radius) around the location of the origin of the EMLAC shower. Also, the total momentum (P) of the track has to be comparable to the total energy (E) deposited in the EMLAC ($E/P = 1$). This rejects events in which a charged hadron track accidentally overlaps an EMLAC shower. In Fig. 3.3(a) we display for the ZMP events the distribution in the ratio E/P. The histogram shows that most of the events populate a region where E/P is close to unity, indicating a clean electron signal, and proof that the ZMP selection criteria based only on information from the charged-tracking system (slope and intercept) already eliminate most of the hadron background. For comparison, the histogram of Fig. 3.3(b) shows the E/P distribution for events in which we required only one track-shower match at the EMLAC within a 0.5 cm circular region of the origin . In this case, a large hadron signal below $E/P = 0.5$ is apparent.

A further reduction of background from hadrons can be obtained by setting a limit on the ratio between the total shower energy deposited in the EMLAC and that deposited in the front section. A typical electromagnetic shower, in fact, tends to deposit most of its energy in the first few radiation lengths (more than 70% of the energy in 10 λ_r) of the detector. In Fig. 3.4(a) we show the E_{front}/E_{tot} distribution for ZMP candidates. Although most events have large values of the front/total ratio, events with E_{front}/E_{tot} of < 0.4 were rejected in the analysis because of hadronic contamination. (For comparison Fig. 3.4(b) shows

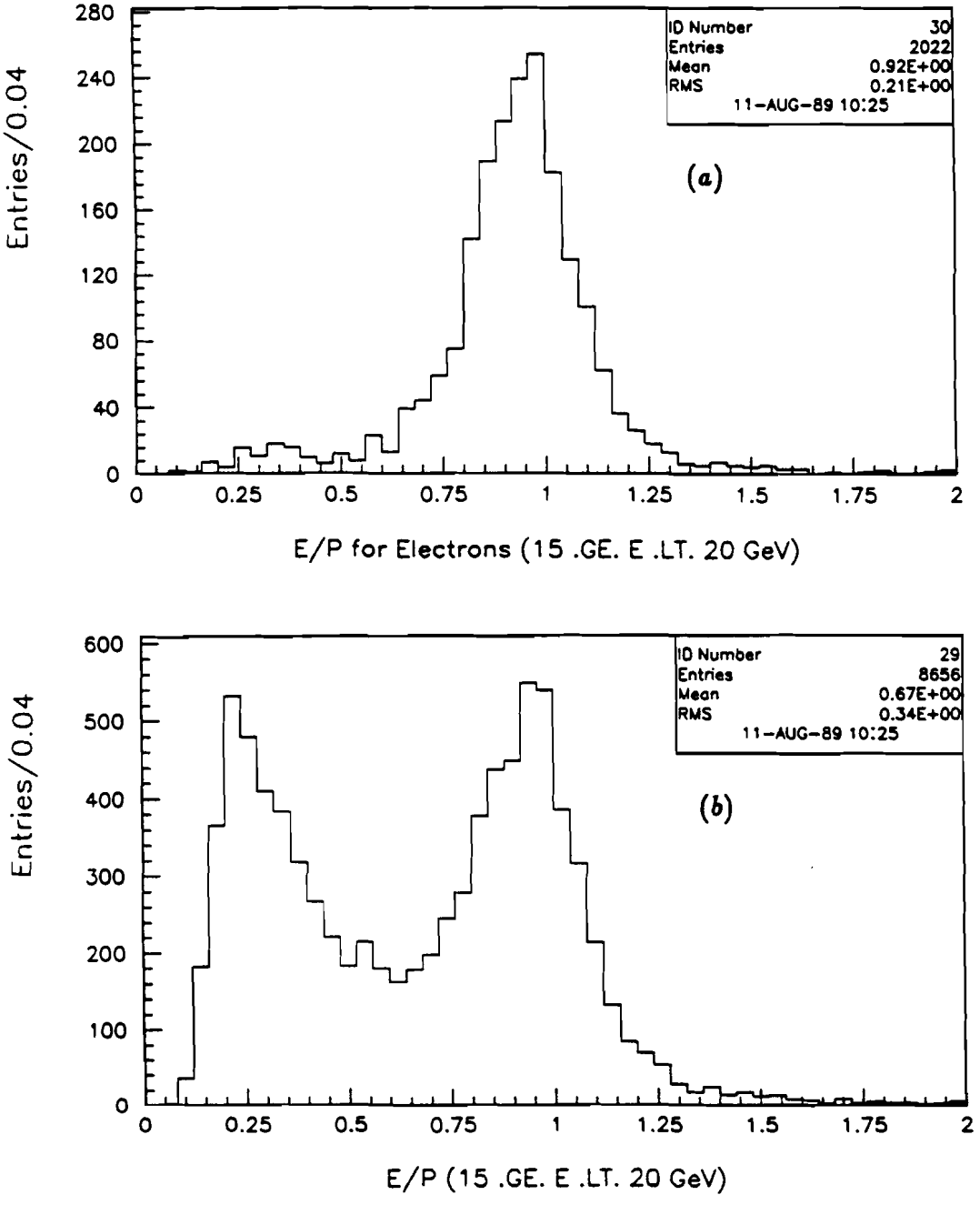

Figure 3.3: Ratio of electromagnetic energy to charged-track momentum (E/P) for (a) Zero Mass Pair events, (b) all charged-track shower matches.

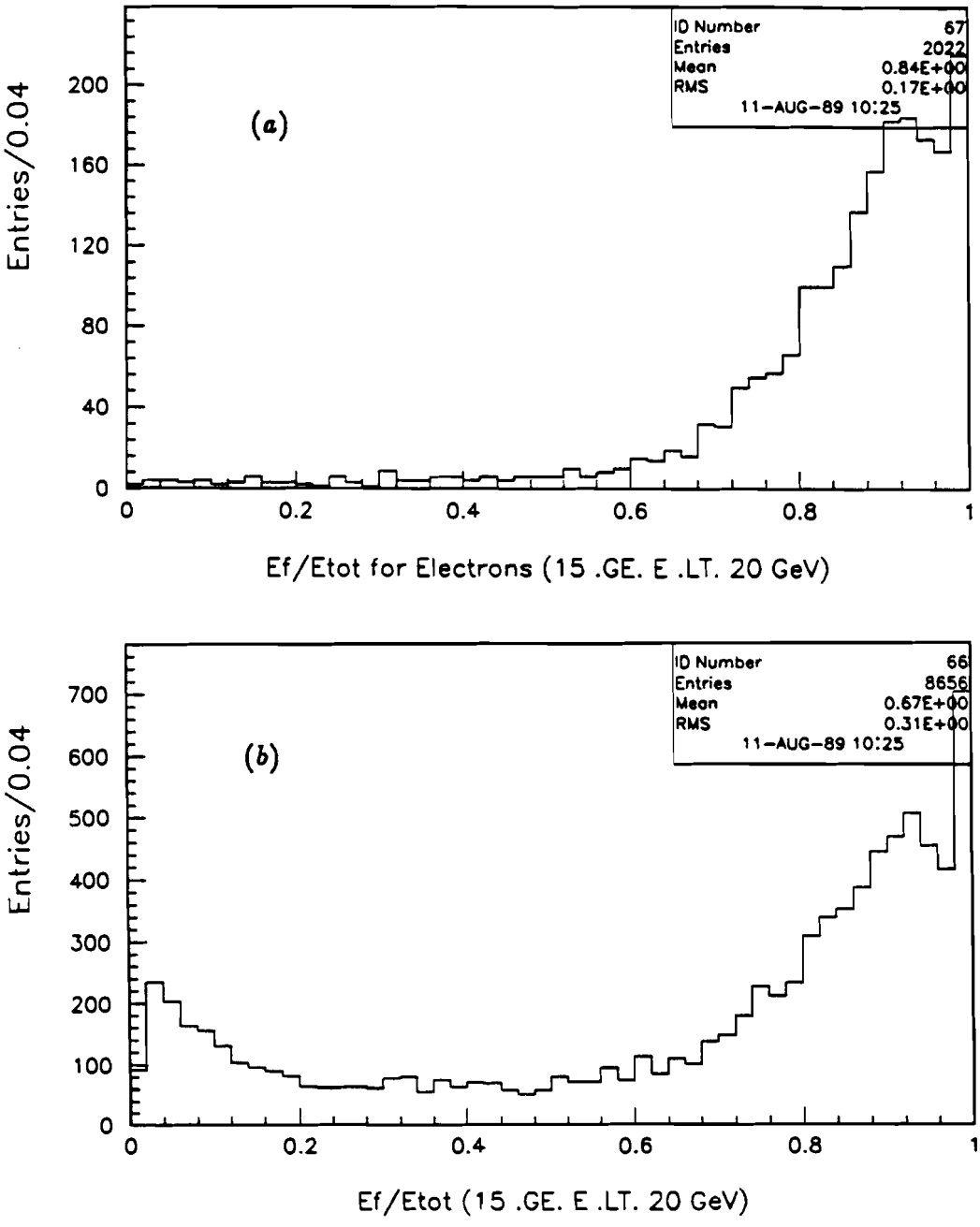

Figure 3.4: Ratio E_{front}/E_{tot} for (a) Zero Mass Pair events, (b) all charged-track shower matches.

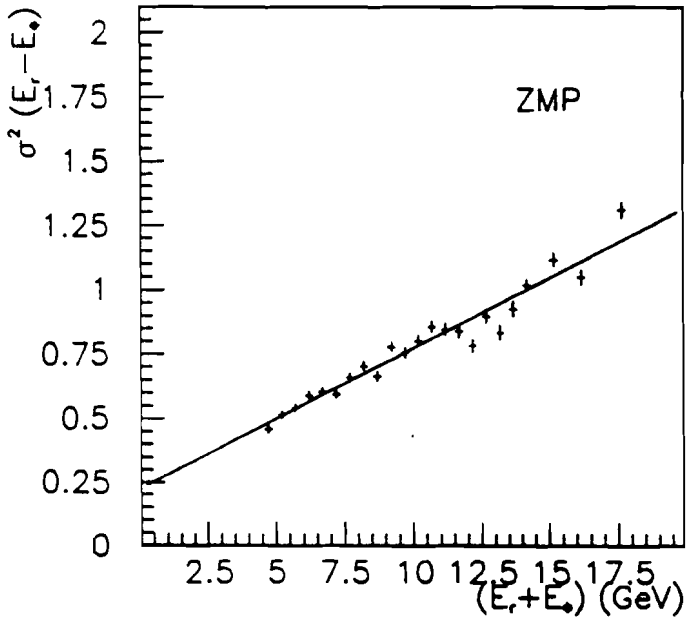

Figure 3.5: Analysis of EMLAC energy resolution using Zero Mass Pair events.The square of the *rms* of the distributions of the difference of the measured energies in the r and ϕ detector views is plotted versus the total energy.

the E_{front}/E_{tot} distribution for all track-shower matches.

In Fig. 3.5 we present plots of $\sigma^2(E_r - E_\phi)$ versus $(E_r + E_\phi)$ obtained from the study of ZMP events. Because of low statistics at higher energies, we limited the total energy E to the range $4 - 20\,GeV$. A fit of the form in Expression (3.5) was performed to the experimental points. We obtained the following values for the slope and the intercept parameters: $A_1 = 0.23 \pm 0.03$, $A_3 = 0.47 \pm 0.09$. The value of the constant term, which represents the incoherent noise contribution, is larger than the value measured with calibration data ($A_3 = 360\,MeV$), but is in agreement with our predictions from Expression (3.3). The comparison between the calibration slope parameters $A_1 = 0.144$ and the ZMP parameter $A_1 = 0.23$

suggests that the latter value has contributions from incoherent gain fluctuations ($\simeq 1.5\%$), which are linear in the energy, and from additional incoherent sources ($\simeq 2\%$) that are not understood as yet. It should be stressed that the fit to ZMP events is primarily sensitive to low energy data, a region where the reconstruction algorithm manifests substantial inefficiencies. More statistics, at higher energies, are needed to understand the general trend. At this point, with only a partial amount of data analyzed, we believe that a reasonable estimate of the intrinsic energy resolution of the EMLAC due primarily to sampling fluctuations is consistent with:

$$\frac{\sigma_E}{E} = \frac{0.15}{\sqrt{E}} \tag{3.7}$$

3.2.2 Detector Linearity

Another important aspect of the detector is the linearity of its energy response. Assuming the same produced p_T for a π^0 and a single direct photon, the energy of the direct photon is higher than the energy of either photon from the π^0 decay. A non-linear energy response would lead to a systematic shift in the p_T scale for single photons relative to π^0s. Even a small shift in p_T can cause large uncertainty in the absolute normalization of the cross sections because of the steep fall off in the p_T spectrum. As a consequence, any non-linearity would affect the p_T dependence of the γ or π^0 yield. A plot of the reconstructed energy versus the electron calibration beam energy, is shown in Fig. 3.6. Between 25 and $100\,GeV$, the dependence appears linear to within 1%. The horizontal errors in the figure

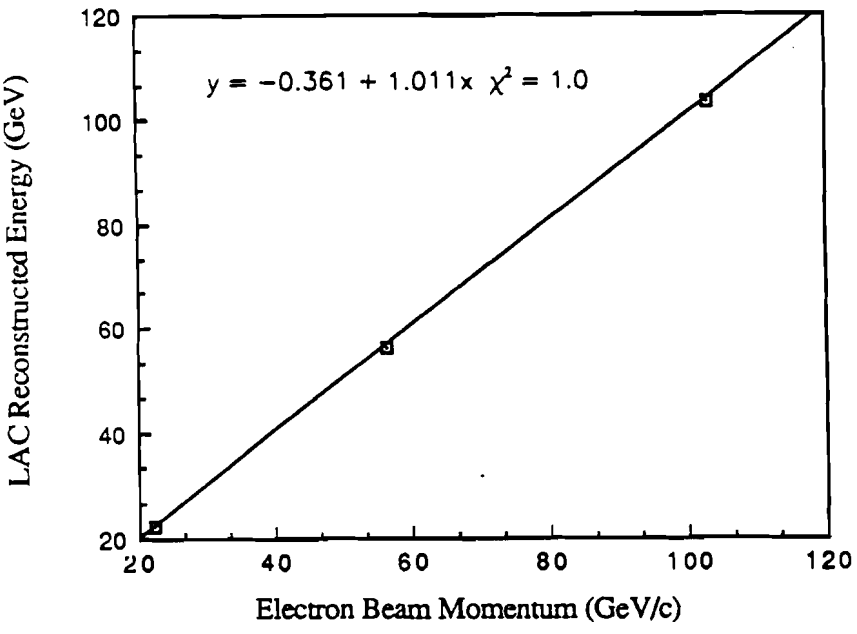

Figure 3.6: Linearity of the EMLAC energy response. The reconstructed energy is plotted as a function of the incident calibration-beam energies.

reflect the uncertainty in the determination of the beam momentum due to the nominal spread in the beam energy. In a Monte Carlo study performed during the design stage of E706, we addressed the issue of linearity of the electromagnetic calorimeter. This was done by calculating the amount of collected energy expected for energetic electron showers, generated using the EGS Monte Carlo program [48]. The detector energy response was found to be linear up to 150 GeV of incident energy. We later verified the expected linearity by processing GEANT-generated [50] π^0s through the standard E706 reconstruction package.

3.2.3 Position Resolution

So far we have implicitly assumed that the EMLAC has good position resolution. Good position resolution provides the ability to resolve neighboring showers, such as two photon showers from the decay of energetic π^0s, or any Bremmstrahlung photon accompanying an energetic electron. The fine segmentation of the readout boards, and the shower reconstruction algorithm provide possibility for resolving two neighboring showers that are within $\sim 1\,cm$ of each other.

In π^0 decay, the separation between the two photons is given by:

$$\Delta r = \Theta\, d = \frac{2m_{\pi^0}}{E_{\pi^0}} \frac{900\,(cm)}{\sqrt{1-A^2}} \tag{3.8}$$

where Θ is the opening angle between the two photons, A is their energy asymmetry [$A = \mid E1 - E2 \mid /(E1 + E2)$; for $E = 250\,GeV$ and $A = 0$, $\Delta r = 1\,cm$)], and d is the distance from the target to the LAC.

To estimate the EMLAC position resolution, we show in Fig. 3.7 a histogram of the difference between the x (y) projections of all tracks onto the front face of the LAC ($z = 900\,cm$) using PWC measurements, and the x (y) positions of the shower origins as detected using calorimeter measurements. The result is from the analysis of a partial sample of available data. The peak consists of matched track-showers, that are primarily electrons. The standard deviation of the distribution is $1.75 \pm 0.07\,mm$. The contribution of the tracking system to this dispersion has been evaluated using Monte Carlo studies [36], and found to be $1.5 \pm 0.3\,mm$. This leaves $0.9 \pm 0.3\,mm$ for the contribution due to the EMLAC

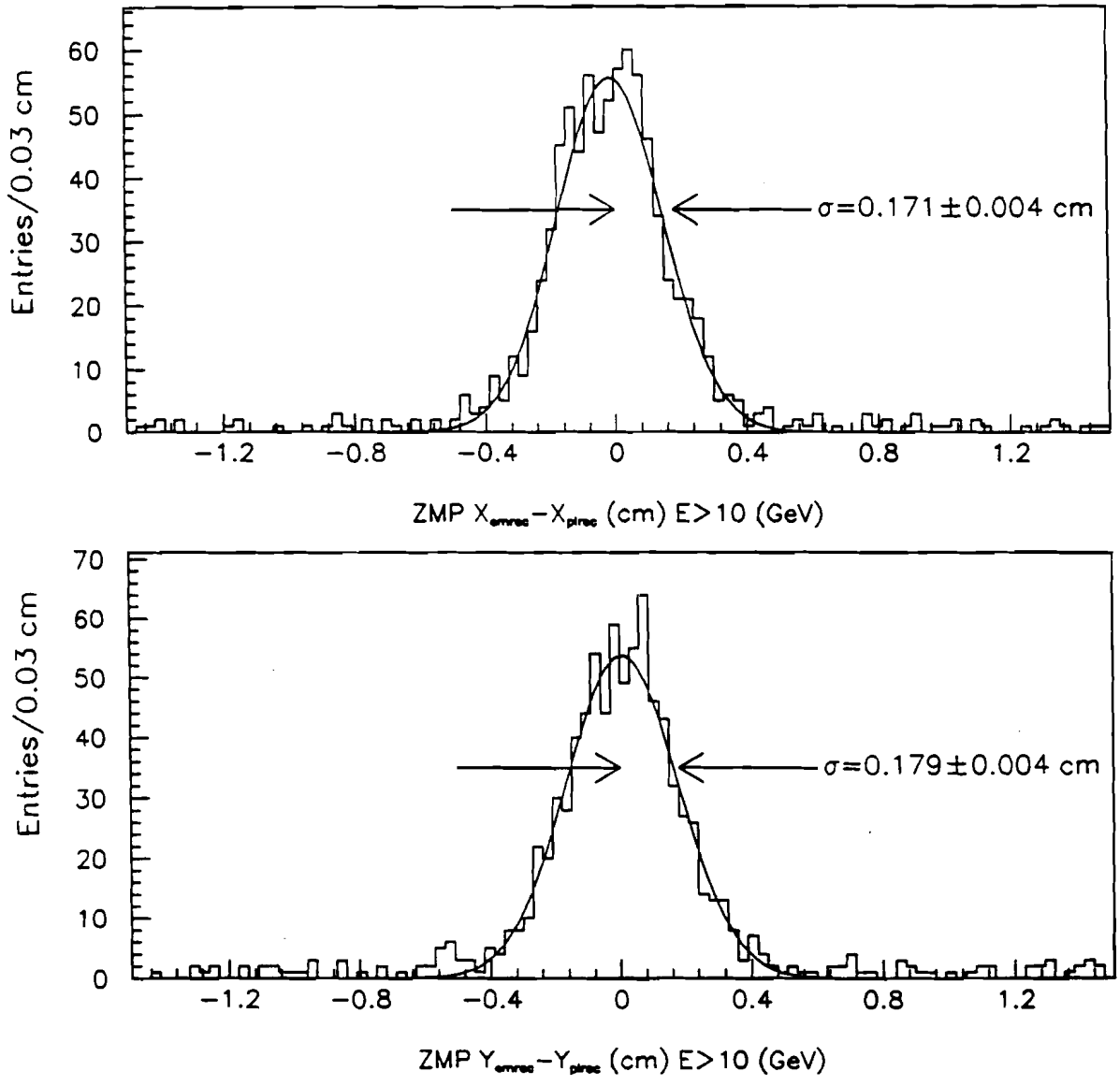

Figure 3.7: Difference between the x and y projections of the ZMP charged-tracks at the EMLAC and the x and y shower positions.

position resolution. From an analysis of a sample of completely reconstructed GEANT-generated single showers we obtained the results shown in Fig. 3.8. The difference between generated and reconstructed values of the shower origin x and y projections are plotted. The dispersion of the data is consistent with a rms of $0.7\,mm$ in each view. Both energy and position resolutions determine the accuracy of the π^0 mass measurement. The mass of the π^0 can be written as:

$$m^2 = 2E_1E_2(1 - cos\Theta) \tag{3.9}$$

where m is the π^0 invariant mass, E_1 and E_2 are the energies of the decaying photons, Θ is their opening angle. The error on the value of the mass is given by:

$$\frac{\Delta m}{m} = \frac{1}{2}[(\frac{\Delta E_1}{E_1})^2 + (\frac{\Delta E_2}{E_2})^2 + (\frac{1+\cos\Theta}{1-\cos\Theta}\Delta\Theta^2]^{\frac{1}{2}}. \tag{3.10}$$

3.3 Reconstruction Package

The E706 off-line reconstruction package is organized in an overall structure called MAGIC [51]. MAGIC (we used version 3.32 for the analysis of the data presented in this thesis) is written in FORTRAN-77 and maintained using the PATCHY file management system [52]. MAGIC provides a general framework for linking information from various reconstruction subprograms which address specific components of the experimental apparatus. It also handles many bookkeeping and organizational jobs, such as controlling the number of events to process, reading/writing data to/from disk or tape, etc. All the memory management routines are written according to the ZEBRA specifications [53], a CERN developed pack-

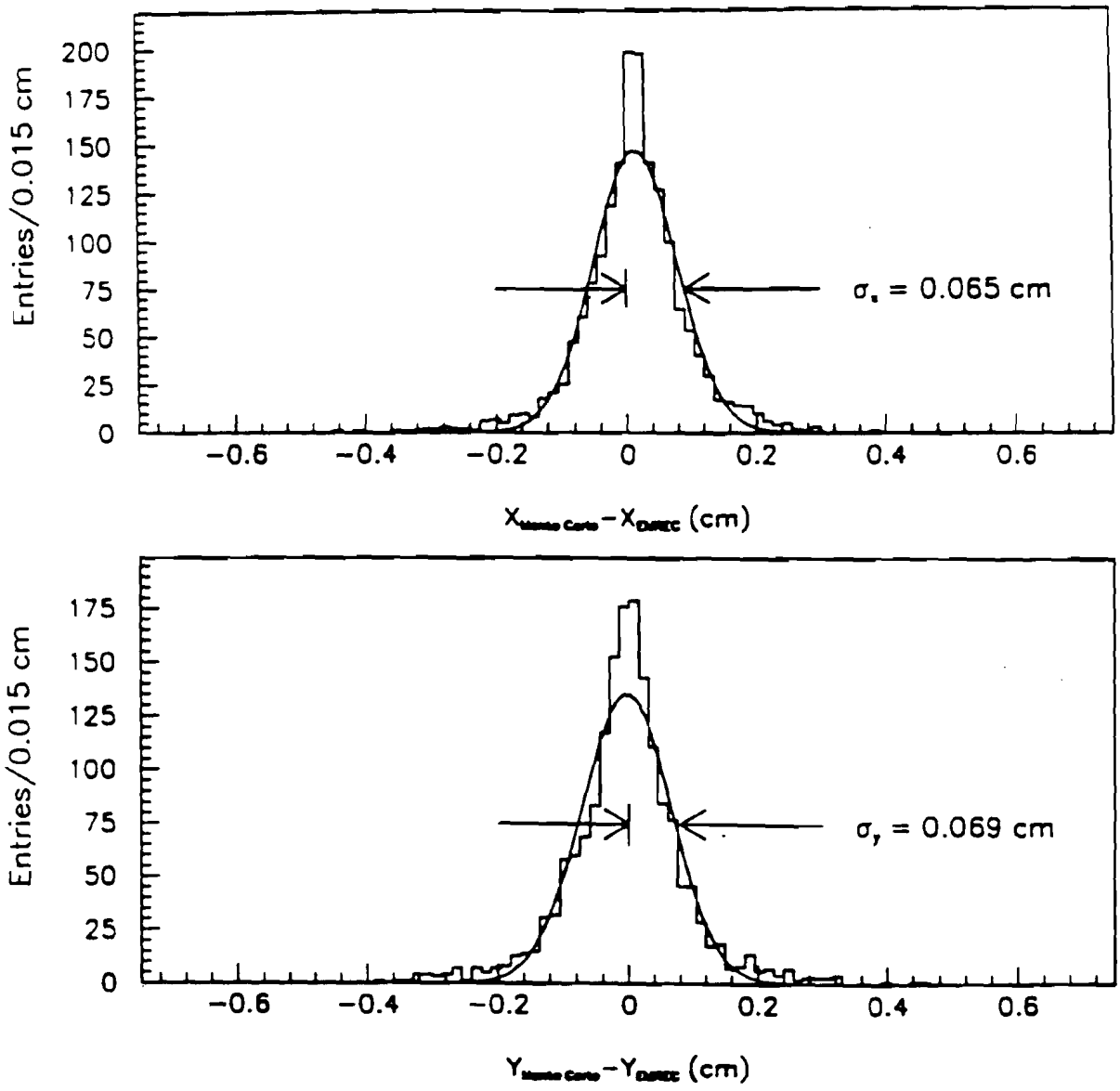

Figure 3.8: Monte Carlo result. Difference between the Monte Carlo generated shower position and the reconstructed position at the EMLAC.

age, which allows, among other features, the creation of dynamic data structures (banks and divisions) at execution-time, and the manipulation of such structures. MAGIC structures input data from the different PDPs in ZEBRA banks, one for each PDP. The packed data are fetched from the banks, passed to routines to be unpacked, and then returned to appropriate ZEBRA banks. The reconstruction subprograms receive these unpacked data organized in ZEBRA banks. MAGIC also includes a graphic routine for display of reconstructed events. The graphic routine is interfaced using the DI3000 graphic package [54], supported at Fermilab.

In the following we shall describe briefly three reconstruction routines: the reconstruction program for EMLAC events (EMREC), the one for the tracking system (PLREC), and the vertex reconstruction program.

3.3.1 Electromagnetic Reconstruction Program (EMREC)

In the following we will summarize the main features of the reconstruction program for the electromagnetic calorimeter. A more detailed description can be found in [55]. To clarify the specific software terminology, we will enclose in square parentheses the physics content of the quantity we are dealing with.

As mentioned in Section 2.7, the readout of the EMLAC is done independently for the front and the back section. During reconstruction, the energies of corresponding strips in the two longitudinal sections are added together to form summed software signals. The reason for this is to minimize the dependence of the shower shape on the point of origin of the shower. Four detector views are

defined for reconstruction purposes: two r views (left and right), corresponding to the quadrant octants, and the inner-ϕ and outer-ϕ views. The reconstruction of electromagnetic showers developing in the EMLAC is done independently in each quadrant and in each view.

The algorithm first determines whether the deposition of energy in any of the detector channels can be associated with an electromagnetic shower or just noise. For this purpose, the average energy in the strips which have been readout is compared with a software threshold set at $150\,MeV$. Contiguous strips with energy above threshold can form a *group* if at least one strip in the group has energy greater than $300\,MeV$, and if the sum of the strip energies (total group energy) is greater than $750\,MeV$. *Peaks* of energy [maximum of a shower's lateral energy deposition] are searched for in each group. To reject peaks caused by energy fluctuations, the width of the energy peak is compared to the expected detector resolution for single isolated showers (see Section 3.2)

$$\sigma_E = \sqrt{(0.14)^2 \times E + (0.1)^2} \tag{3.11}$$

where E is the maximum strip energy . The structure of groups and peaks can be very complicated. Groups can be formed from multiple peaks, e.g., two photons from π^0 decay, or Bremsstrahlung photons from electrons; peaks can be very asymmetric in shape because they can result from the overlap of two distinct peaks, e.g., coalesced and very asymmetric π^0 decay. Below, we will first assume that showers in any view arise from groups with single isolated peaks [i.e, isolated

photons or electrons].

When the reconstruction algorithm establishes that a peak is found in one of the views (shower candidate), the next step is to make an accurate determination of the energy and positon of the shower in all the views. For this purpose, the parametrization of the shower shape is used to fit the summed (front + back) energy distribution.

The fit to the shower shape was determined by simulating electromagnetic showers using the E706 GEANT Monte Carlo program. Shower shapes in the front and back sections of the detector were parametrized differently, because the lateral spread of the shower is wider in the back than it is in the front. The parametrization is done as a function of the radial distance from the center of the shower. The formulas and the parameters of the fit can be found in [55].

To determine the r and ϕ coordinates of the origin of the shower within the peak strip, a weighting algorithm is applied, based on values of the pulse heights on either side of the maximum. Once the shower position has been determined in both views, the program makes a first estimate of the shower energy in the summed r view by using the Monte Carlo fit to the front and back shower shapes. The first estimate is done by using the radial position for the shower origin, and a fixed number of strips for the transverse distance from the shower origin. The final determination of the energy in the r view is done by minimizing a χ^2 of the fit of the shower shape to the actual pulse distribution as a function of the energy.

Energy in the tails of the shower is usually poorly determined because the signals in the corresponding strips are usually below the hardware readout threshold. An energy correction is therefore applied before minimizing the χ^2.

For groups containing multiple peaks, some of which overlap, the situation is somewhat more complicated. The reconstruction algorithm first splits the group into different showers, then the energies and positions of the split peaks are calculated using the corrected pulse distributions. The splitting procedure represents perhaps the most delicate step of the reconstruction sequence. The majority of the reconstruction failures are due to inefficiencies of the splitting algorithm.

Once all the showers are reconstructed in both r and ϕ views, they are correlated to form final photons or electrons. The basic idea is to correlate a shower in one view to a shower in the other view that has approximately the same total energy, and the same ratio (E_{front}/E_{tot}) of the energy deposited in the front section to the total. The efficiency of the correlation depends however on the efficiency of the splitting algorithm. In fact, if two showers overlap in one view (r), but are well separated in the other (ϕ), then the splitting algorithm can be less effective in one view (r) than in the other (ϕ), and this may cause ambiguities in the correlation among showers. Correlation inefficiencies may also arise when a shower falls near an octant boundary, or across the inner/outer ϕ separation. These types of reconstruction inefficiencies are easy to spot because of their clear impact on experimental distributions. In order to determine the size of such effects, it is nec-

essary to process Monte Carlo generated events through the reconstructor. This way, the sources of reconstruction failures can be investigated, and the appropriate corrections determined by reproducing the experimental effects. Chapter 5 is dedicated to Monte Carlo simulations.

3.3.2 Charged Particle Reconstruction Program

The reconstruction program for finding trajectories of charged particles in the spectrometer, uses as input the particle hits in the SSD planes of the beam chambers, the SSDs downstream of the target, and the PWCs. (The beam chambers have three x and three y SSD planes upstream of the interaction target.) Hits are defined as the coordinates of a channel that displays a signal when a charged particle deposits ionization near to it. The algorithm to reconstruct charged tracks is conceptually similar in both kinds of charged particle detectors. In the following we will describe the essential ideas of the reconstruction process.

The first step involves the reconstruction of charged tracks in each of the four views. There are four PWC views per module (x, y, u, v) in each of the four downstream tracking stations, and two orthogonal views (x and y) in both sets of SSD tracking systems. In each view, the algorithm searches for three and four-hit tracks in the four similar PWC (and similar non-beam SSD) planes, by extrapolating two-hit tracks reconstructed in only two planes. This is done twice, each time selecting a different combination of planes (1^{st} and 4^{th}, 2^{nd} and 3^{rd}). Least square fits through all possible combinations of hits are then performed.

Three-hit tracks are stored only as second-best choices. All reconstructed four-hit tracks that share three or more hits among themselves are labeled as global clusters. Global clusters are analyzed using a special procedure [56] . Only three and two-hit view tracks are searched for in the SSD beam chambers.

Once all single-view tracks are reconstructed, the algorithm matches them to form space tracks. The following procedure is applied to the PWC system only. As in the procedure for finding view tracks, two passes are made. In the first pass, matches among view tracks are sought in the x and y views, and the candidate space tracks are projected onto the u and v views. In the second pass, the roles are reversed. If the matched tracks satisfy certain selection criteria, then space tracks are defined.

In the final step, the reconstruction algorithm links the downstream PWC space tracks to the upstream SSD view tracks. The linking is done by projecting all PWC tracks to the center of the analyzing magnet (which bends tracks in the xz plane). For each downstream track, all SSD tracks are also projected to the center of the magnet. The tracks slopes and intercepts are then compared among themselves in the bending plane. Best links are sought in the x and y views. Linked tracks are used to determine the location of the primary vertex of the interaction.

3.3.3 Vertex Reconstruction Program

The vertex reconstruction program uses the reconstructed charged tracks in the SSD to define the primary vertex of the interaction. Only those SSD tracks which linked at the magnet to a PWC track are considered. First, a vertex is sought in the x and y views of the SSD charged-track system. At least 4-hit tracks are required in each view to define a vertex in that view. For accepting these tracks, an impact parameter (minimum distance to the vertex) of less than $50\,\mu m$ is required. If a vertex is reconstructed in each view, the program searches for the final matched vertex, by requiring that the difference in the z position of the two vertices in each view be less than $3\,mm$. If the above is satisfied, the z-coordinate of the vertex of the interaction is finally computed by performing a weighted average between the two z-coordinates of the view vertices.

Figure 3.9 displays the z-coordinate distribution for the difference between the x and y view vertices. The half width at half height (HFHM) of the distribution (essentially, the resolution of the z-coordinate) is less than 700 μm. The vertex resolution along the direction transverse to the beam is $\sim 25\ \mu m$.

The efficiency for finding a primary vertex in the event is $\sim 90\%$. About 5% of events have a vertex reconstructed in only one view, or have unmatched vertices ($\Delta z > 3\,mm$) between the two views.

The z distribution for the reconstructed vertices in the $Cu + Be$ target data is displayed in Fig. 3.10. The target segmentation is well reproduced. The two

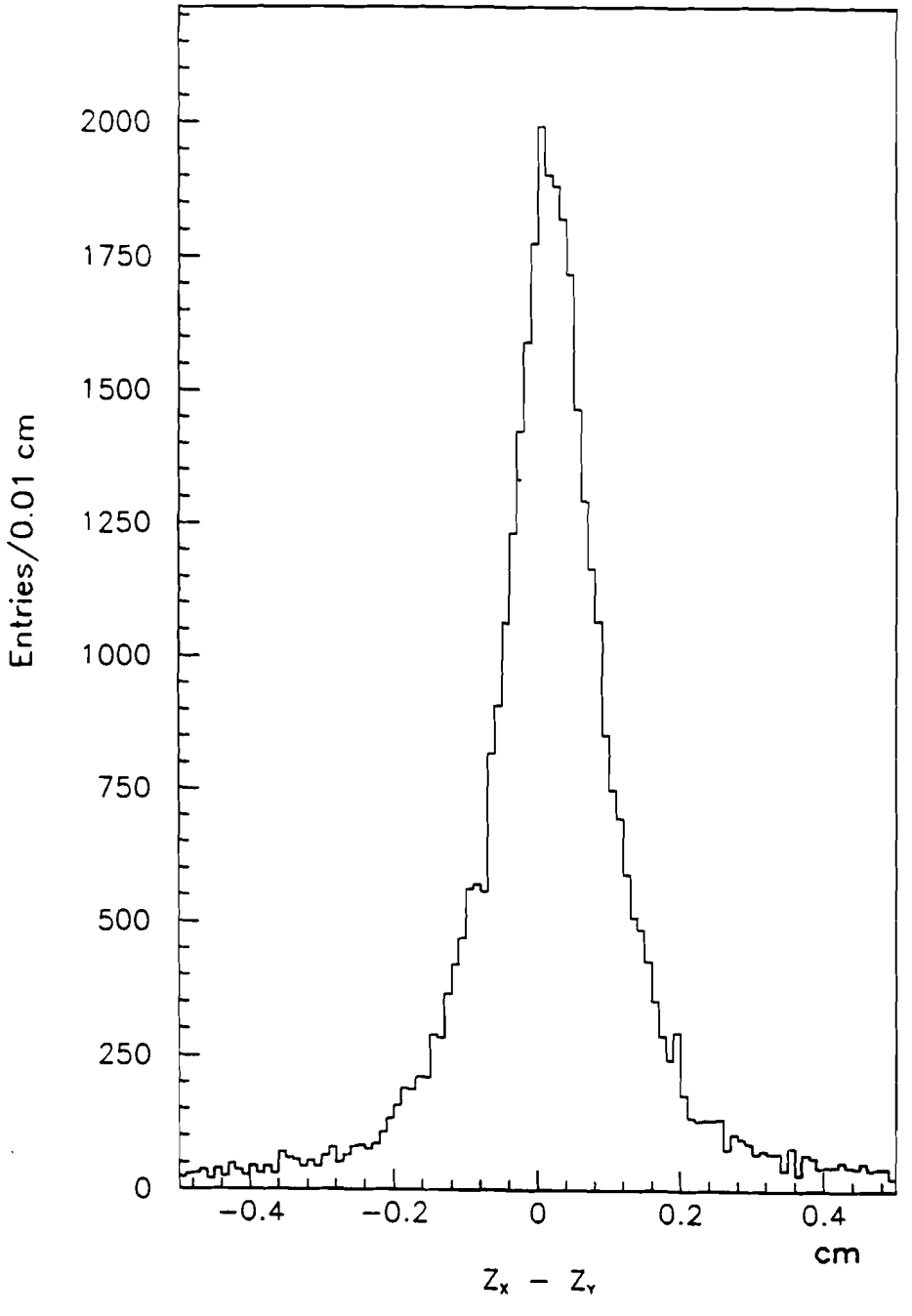

Figure 3.9: z-coordinate distribution for the difference between the x and y view vertices in the target.

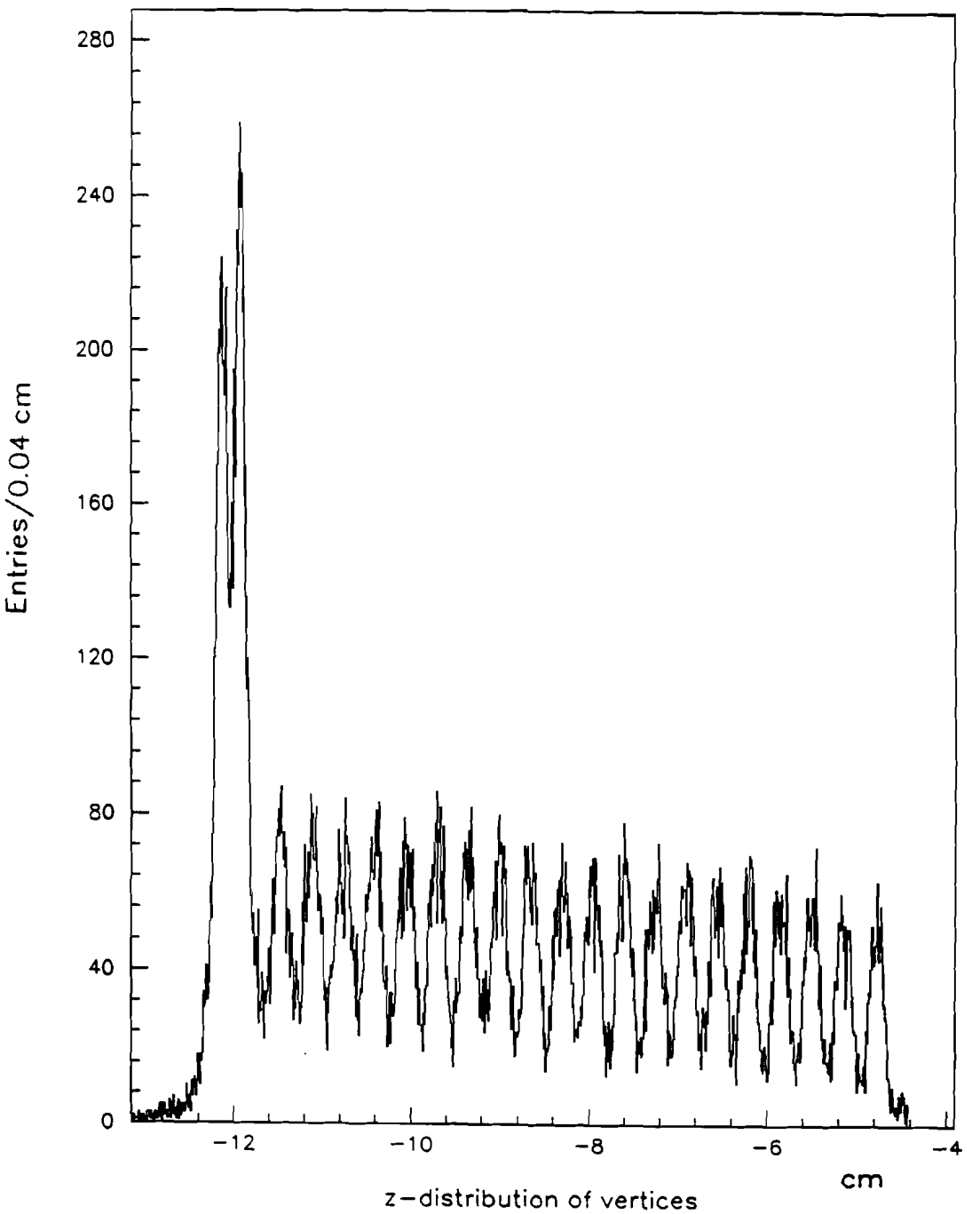

Figure 3.10: z distribution of the reconstructed vertices in the $Cu + Be$ target.

upstream Cu target segments, characterized by a large number of detected vertices, are clearly resolved, as are the 20 Be segments. (The positive z axis (beam direction) is oriented from left to right, as shown in Fig. 3.10, and the origin is $12\,cm$ downstream of the first Cu segment.)

Chapter 4

DATA ANALYSIS

4.1 General Procedure

In this chapter we describe the general procedure used for analyzing data in this thesis. In Section 4.2, the technique for determining the fraction of minority particles in both negative and positive beam will be outlined. In Section 4.3 we will discuss the event selection criteria . Finally, in Section 4.4, we shall describe the procedure for defining the π^0 signal. Some comparisons with Monte Carlo simulations will also be presented.

The primary data were processed through the E706 off-line reconstruction program using the Fermilab ACP (Advanced Computing Project) parallel processor computer system. The reconstructed events were written onto data summary tapes (DSTs), and catalogued according to specific physics goals. Each data stream contained relevant informations regarding the event structure, such as: position and energy of all reconstructed showers in the LAC, momentum and direction of the charged-tracks in the tracking system (PWC and SSD), the primary

vertex information obtained from the SSD system, information regarding the tagging of the beam particles, the trigger and the veto wall status, and clusters of energy observed in the forward calorimeter. A series of cuts was applied to the events on the DSTs, mostly to suppress backgrounds and to improve the quality of the accepted data.

For the analysis of the data presented in this thesis we used reconstructed data selected from the ACP-processed output tapes which were stored in binary files. The binary files included all events with at least one shower in the EMLAC (thereby firing one of the LAC triggers), for reconstructed transverse momenta above 3 and $4\,GeV/c$, for negative and positive beam data, respectively. For events satisfying the above requirements, data was transfered to binary files. The following was some of the information available:

- LAC trigger type (see Section 2.9),
- energy and position of each shower in the LAC,
- time of event recorded by the TVCs,
- momenta and track parameters of all tracks in the PWC,
- vertex coordinates and beam parameters in the SSD,
- beam hodoscope and Cherenkov response,
- veto wall response,

- a set of quality words (shower χ^2, charged-track hit multiplicity, etc.).

The binary files were run through an analysis program from which all the results presented in this thesis were extracted.

4.2 Tagging of Minority Particles

In order to measure the yield of π^0s with incident K^- and π^+ it is essential to determine accurately the beam composition and to tag the fraction of minority particles with good efficiency. To perform such a measurement we used the differential Cherenkov counter, already described in Section 2.2, for tagging particles in the beam. A Monte Carlo simulation of the Cherenkov response to the incident particles was performed in order to establish the exact beam composition and to infer the relative contamination levels. Two experimental Cherenkov gas pressure excitations are shown in Fig. 4.1 and 4.2, for negative and positive beam, respectively, together with the Monte Carlo expectations. The abscissa indicates the helium gas pressure in *psia*, and the vertical axis indicates the number of coincidences in the Cherenkov, normalized to total beam. The data were determined by varying the *He* pressure in the Cherenkov and by recording the number of counts from a scaler unit which had input from six possible Cherenkov coincidence logic combinations, and the beam counts from two scintillation counters upstream and downstream of the Cherenkov detector. The Cherenkov logic was driven by a series of 4508 LeCroy programmable logic units. The distributions shown in the figures correspond to the coincidence requirement of four or more phototubes fir-

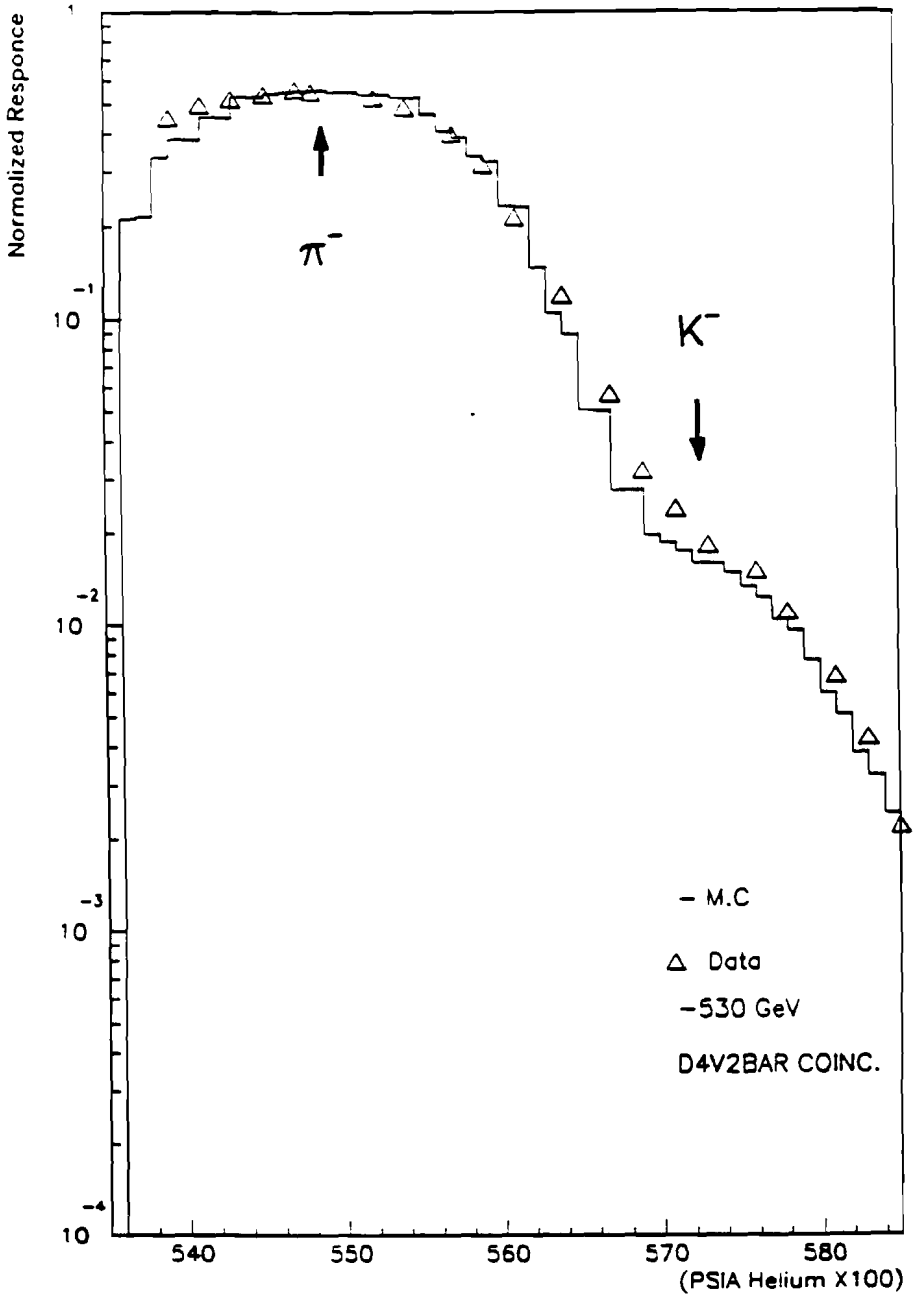

Figure 4.1: Experimental Cherenkov gas pressure excitations for negative beam. Indicated by the arrows are the particle types whose light is focused on the Cherenkov coincidence ring for specific values of the helium gas pressure. The solid line is a Monte Carlo fit.

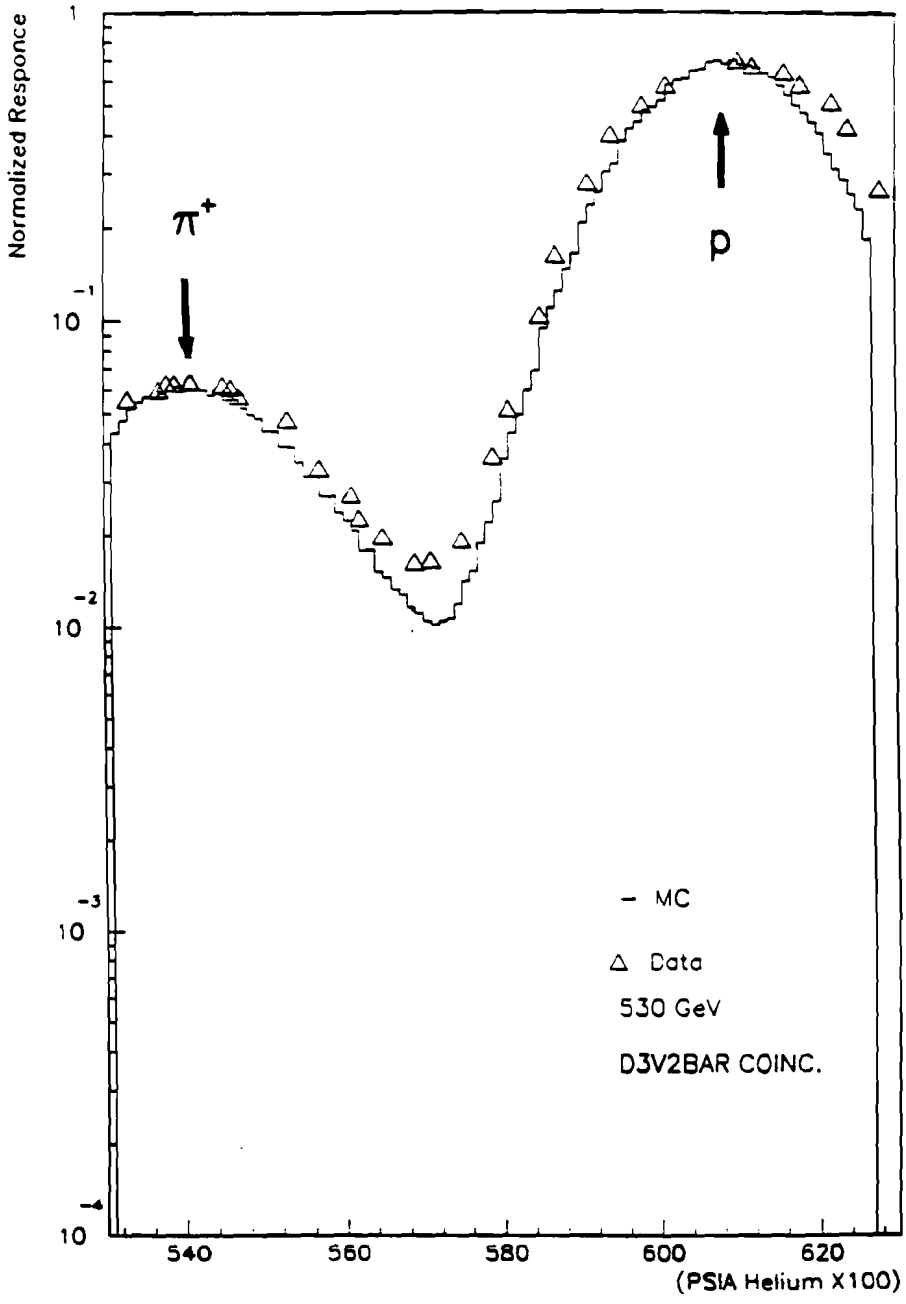

Figure 4.2: Experimental Cherenkov gas pressure excitations for positive beam. Indicated by the arrows are the particle types whose light is focused on the Cherenkov coincidence ring for specific values of the helium gas pressure. The solid line is a Monte Carlo fit.

in the coincidence ring for Fig. 4.1 (three in Fig. 4.2), and less than two in the anticoincidence ring. This particular requirement for tagging the minority charged particles in the beam is the one used in the following of this analysis. (In our notation we will indicate with $D4\overline{V2}$ and $D3\overline{V2}$ as the coincidence requirements used for the negative and positive beam, respectively).

The Monte Carlo simulation reproduces fairly well the experimental pressure curves. In Fig. 4.1 the broad peak at the lower gas pressure corresponds to the π^- signal, while the shoulder starting at $\sim 5.68\,psia$ indicates the K^- signal. The negligible $\bar{p}$ signal would show up at larger values of the Cherenkov gas pressure, outside the range of the horizontal scale of the histogram. In Fig. 4.2 the signal that peaks at $\sim 5.4\,psia$ is due to π^+s. Under the same curve there is an unresolved K^+ signal which peaks at around $5.6\,psia$. Well separated is the proton signal which peaks at a gas pressure of $\sim 6.1\,psia$ for maximum tagging efficiency. From an analysis of the gas-pressure curves, it appears that some disagreement between experimental data and Monte Carlo predictions is evident in the pressure ranges corresponding to the transition between the tagging of two different types of particles. In these regions, the data lie above the Monte Carlo points, probably reflecting noise contributions to the real signals, that were not properly modeled, and have greatest effect on the tails of distributions.

For details on the Monte Carlo analysis see [57]. From a fit of the Monte Carlo to Cherenkov pressure curves obtained using a different coincidence requirement

Table 4.1: Beam Compositions

	π^- (%)	K^- (%)	$\bar{p}$ (%)
negative beam	96.9 ± 0.2	2.9 ± 0.2	0.2 ± 0.01
	p (%)	π^+ (%)	K^+ (%)
positive beam	91.2 ± 0.1	7.2 ± 0.1	1.7 ± 0.1

from the one used here, we obtained the negative and positive beam compositions reported in Table 4.1. The compositions relevant to our analysis are discussed below.

In order to determine the exact percentages of minority particles in the beam, and to monitor this with time, it is essential to scan the Cherenkov gas pressure to check the Cherenkov performance at frequent intervals, and to record the gas pressure settings for each individual run. The latter was done by recording the pressure on summary run sheets and automatically, by mean of a pressure transducer, in the electronic data base. Since the automatic and the manual recordings were sometime in disagreement with each other, we developed an alternative method for determining the fraction of minority particles, independent of the pressure recordings. We used two different procedures, the first one of which was only applied to negative-beam runs, while the second was applied to all runs (of both beam polarities). In this section we shall describe both analysis procedures, in the next we shall present the results of the analysis.

For negative runs, we calculated the ratio between the number of $D4\overline{V2}$

Cherenkov coincidences and the total number of Cherenkov signals using the prescaled beam trigger data.

A prescaled beam trigger occurred under any of the following circumstances. A beam particle signal was defined when a coincidence occurred between the beam counters BA and BB (for their definition see Section 2.9). This beam signal was sent through an early-late filter which provided rejection against interactions occurring within 3 buckets before or after the bucket containing the useful beam particle (pile-up rejection). This defined a *clean* beam particle. If the above requirements were satisfied, the beam signal was put in anticoincidence with the beam halo counter BH, and in coincidence with the computer ready signal, to form a prescaled beam trigger. The prescaling factor was 1.5×10^6 at the beginning of the run, for typical beam intensities of the order of $0.8\,MHz$ for negative beam, and $2.3\,MHz$ for positive beam. Later in the run, when the beam intensity was increased to $1\,MHz$ (negative beam), and $2.8\,MHz$ (positive beam), the prescaling factor was changed to 2.25×10^6. The prescaled beam trigger provided a sample of unbiased interactions, because the events were completely independent of the characteristics of any final-state trigger requirement.

One limiting feature of this type of analysis is the small statistics involved ($\sim$ 10 beam particles per spill). In fact, the ratio of tagged K^- to total beam was calculated on a run by run basis, and often averaged over several runs to improve statistics and to determine unique values for the percentage of minority particles

and track their time dependence.

To improve statistics and reduce the errors on the fraction of minority particles, we had to increase the sample of events used in the analysis. The second approach used to determine the fraction of minority particles consisted in measuring the particle content of beam buckets before and after the bucket carrying a triggering beam particle.

The information from a total of 15 beam buckets, lasting 19 $nsec$ each, was recorded sequentially in latching units; the seventh bucket was the one containing the triggering interaction. The beam particles in the neighboring buckets (each bucket had about 5% probability to be occupied) have characteristics similar to the prescaled non-interacting particles, with the advantage of providing better statistics per single event. We summed the total occupation number and the number of tagged minority particles (K^- for negative runs, π^+ for positive runs) in all 14 buckets for each event. The ratio between the number of tagged minority particles and the total number of tagged particles was then calculated for each run. We averaged this over sets of runs that had consistent percentages of minority particles to extract global values.

The calculated percentages do not represent the true fractions of minority particles in the beam. One still has to apply corrections for contaminant particles that fall into the accepted signal. We estimated the contributions from contamination by using the Monte Carlo fits shown in Figs. 4.3 and 4.4(a) and (b). In Fig. 4.3

we extrapolated the π^- signal (continuous line) under the K^- peak (dashed line). In Fig. 4.4(a) we did the same for the K^+ contamination (dashed line) under the π^+ peak (continuous line), and in Fig. 4.4(b) for the proton contribution (dashed line) to the π^+ peak. Using this procedure, the contributions of other particles mistagged as minority particles could be measured at any value of gas pressure.

From the two analysis procedures just outlined above, we determined the operating point on the pressure curve, and found that the level of π^- contamination to the K^- signal was quite small ($< 5\%$), and that there was $\sim 8\%$ contamination to the π^+ signal due to K^+s, with a negligible contamination from protons.

4.2.1 Tagging of Negative Beam

The coincidence requirement chosen for tagging minority particles in the negative beam was $D4\overline{V2}$. With this requirement, we achieved the best compromise between resolution and tagging efficiency. With other coincidence requirements, such as for example $D3\overline{V2}$, it is possible to increase the efficiency for tagging K^-s, although usually this increases background contributions. During the run, we maximized the efficiency for tagging the minority particles (K^-), by setting the Cherenkov gas pressure at 5.7 *psia* (Fig.4.1). At this pressure value, using $D4\overline{V2}$ for the tagging requirement, the Cherenkov counter performed at an efficiency of $\sim 42\%$ for collecting the kaon light on the coincidence rings. The gas pressure setting was adjusted a few times during the data taking to balance temperature variations, which tended to affect the Cherenkov efficiency by introducing measur-

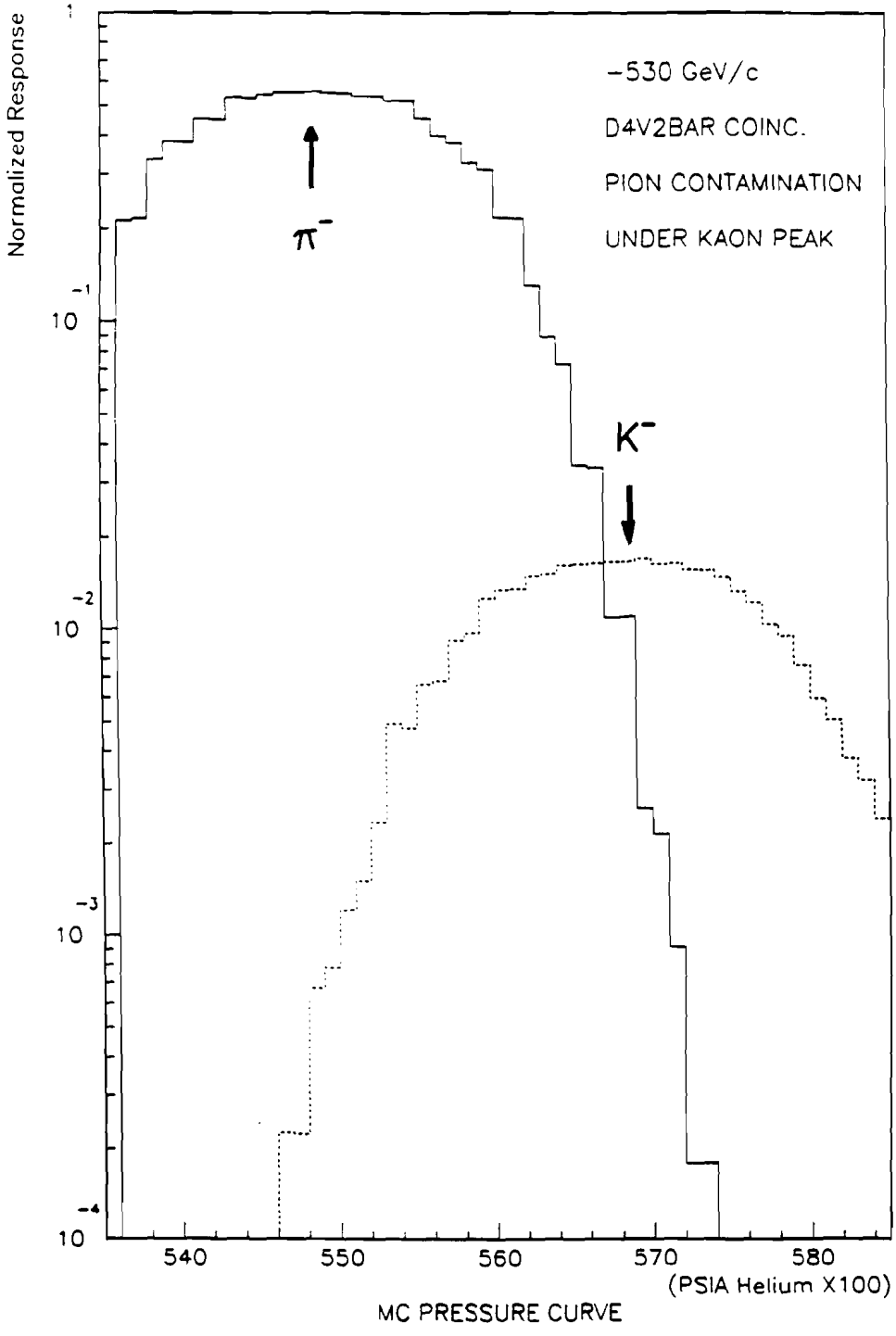

Figure 4.3: Monte Carlo simulation of the Cherenkov gas pressure curve for negative beam. The contamination levels under the π^- and K^- peaks are shown.

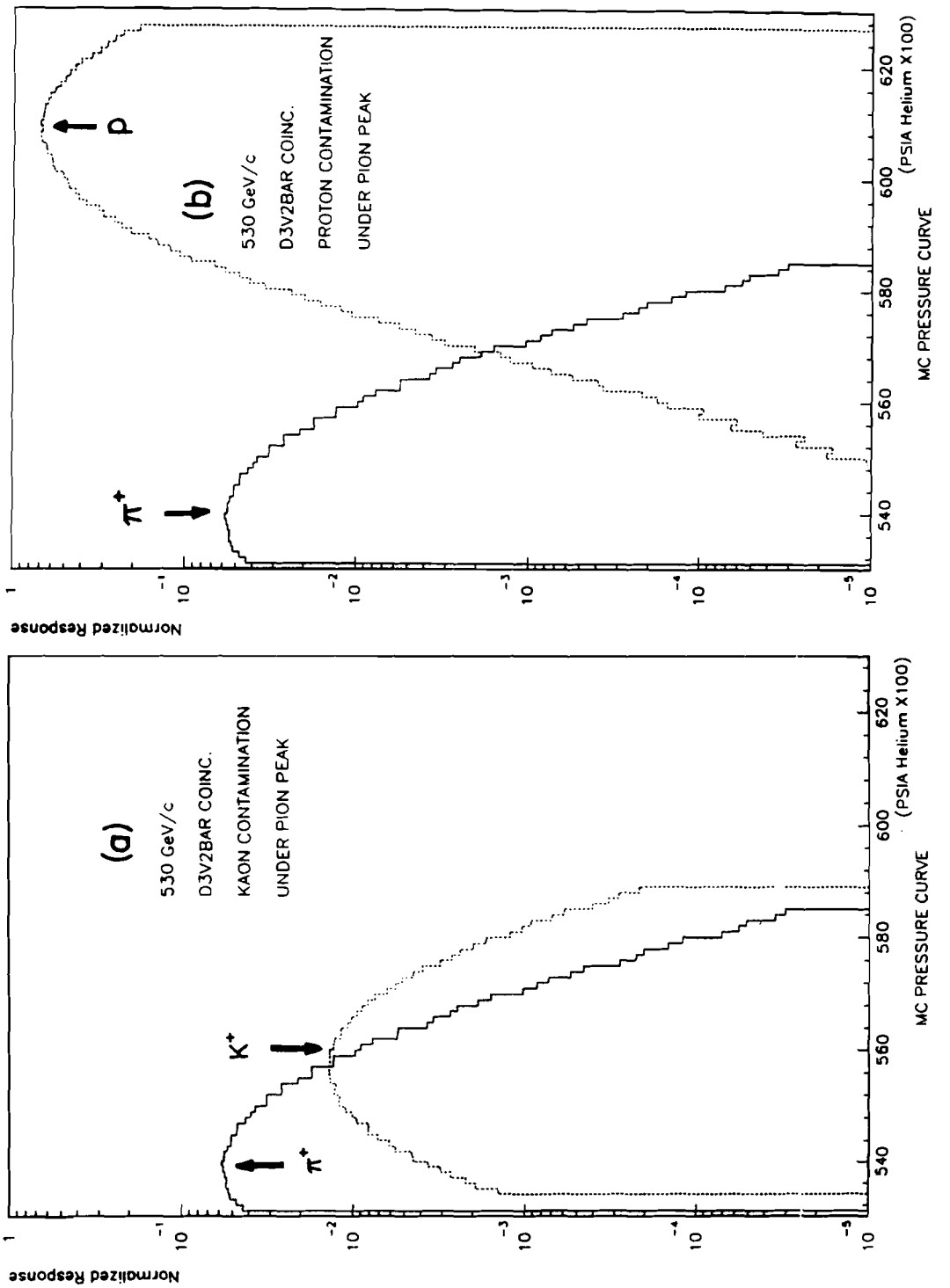

Figure 4.4: Monte Carlo simulation of the Cherenkov gas pressure curve for positive beam. The contamination levels (*a*) under the π^+ and K^+ peaks and (*b*) under the p and K^+ peaks are shown.

able horizontal shifts of the overall pressure curve (from a Monte Carlo estimate, 1^0 change in temperature shifted the pressure curve by $\sim 0.002\,psia$). Even small drifts of the pressure curve could produce variations of the order of 20% in the fraction of tagged K^-, and in the π^- contamination level. Adjusting the pressure settings to control the Cherenkov response was not always successful. However, using the analysis outlined in the previous section, we could at least track the time dependence of the fraction of tagged minority particles.

In Table 4.2 we present the results of our analysis concerning the negative-beam data. Four different sets of runs provided four different values of the percentage of K^- in the beam. Also reported are upper limits on the measured π^- contamination level in the K^- signal. The uncertainty in the percentage of π^- mistagged as K^- was as large as 50% for sets $D1$ and $A1$. For all the runs, the Cherenkov efficiency for tagging negative beam particles was $58 \pm 3\%$. Everything not tagged as K^- was considered to be π^-. The π^- identification probability was estimated by using the relations:

$$P_{\pi^-} = \frac{B_{\pi^-}}{(1 - P_{K^-})} \tag{4.1}$$

$$P_{K^-} = E\, B_{K^-} \tag{4.2}$$

where E is the Cherenkov efficiency, B_{π^-} and B_{K^-} are π^- and K^- percentages in the beam, respectively, given in Table 4.1. These identification probabilities take into account K^- mistagging and the $\sim$ 1% beam contamination due to muons from the beam halo. In fact, the denominator of Expression (4.1) can be written

Table 4.2: Relative Negative-Beam Percentages.

	Tagged K^- (%)	K^- Contamination π^- (%)	$\bar{p}$ (%)	π^- Probability (%)	Comments
set D1	$0.89 \pm .07$	2	< 0.01	97.8	Jan 18-21 1988
set D2	$1.42 \pm .06$	4	< 0.01	98.3	Jan 22-25 1988
set A1	$1.01 \pm .12$	2	< 0.01	97.9	Feb 9-10 1988
set A2	$1.46 \pm .07$	4	< 0.01	98.3	Feb 10-13 1988

as:

$$1 - P_{K^-} = B_{\pi^-} + B_{\mu^-} + (1 - E)\, B_{K^-} \tag{4.3}$$

in which the last term represent the probability of K^- mistagging.

4.2.2 Tagging of Positive Beam

The positive beam was composed mostly of protons ($> 90\%$), some π^+ ($\sim 7\%$) and a few K^+ ($\sim 1.5\%$). We set the Cherenkov gas pressure at the π^+ peak ($5.4\, psia$), and we selected $D3\overline{V2}$ to be the coincidence requirement for tagging π^+s. Examining Fig. 4.2, it can be seen that since the π^+ peak is rather wide, and well separated from the proton peak, small variations of the gas pressure setting would not affect significantly the ratio of π^+ to total beam. The Monte Carlo fits to the gas pressure curves (Fig. 4.4(a) and (b)) show that the contamination of the π^+s due to protons is negligible at the running pressure. It is more difficult to determine the contamination of π^+s caused by mistagged K^+s. In fact, the K^+ signal is completely unresolved relative to the π^+ signal. We measured a contamination of $8 \pm 3\%$ K^+ at the gas pressure at which the Cherenkov counter

Table 4.3: Relative Positve-Beam Percentages.

	Tagged π^+ (%)	π^+ Contamination K^+ (%)	p (%)	μ^+ (%)	p Identification (%)	Comments
set C	$6.23 \pm .08$	8 ± 3	< 0.1	0.3	97	Jan 27-Feb 8 1988

was operated. The muon contribution to the π^+ contamination was estimated from beam-halo muons to be about 0.3%. The combined efficiency for tagging π^+s and K^+s was $87 \pm 3\%$. In Table 4.3 we report the measured fraction of π^+ in the beam as obtained from the analysis of the early/late beam buckets. Also indicated are the different contributions to the contamination. All the particles not tagged as π^+ were considered to be protons with identification probability:

$$P_p = \frac{B_p}{(1 - P_{\pi^+})} \tag{4.4}$$

$$P_{\pi^+} = E\, B_{\pi^+} + C_{K^+}\, B_{K^+} \tag{4.5}$$

where now C_{K^+} is the contamination of the π^+ signal from K^+s (we neglected the μ^+ contamination). The proton identification probability is also given in Table 4.3. The overall Cherenkov efficiency for tagging positive-beam particles was $78 \pm 3\%$

4.3 Event Selection

The data sample used in this analysis includes all negative beam data on Be and $Cu + Be$ targets. The number of triggers (see Table 4.4) in this sample is $\sim 2,030,000$. We also analyzed a partial sample of Be and $Cu + Be$ triggers

from the total positive data of $\sim 2,800,000$ triggers. We processed all events selected for the binary data files through our analysis program. A series of cuts were subsequently applied to the data, mostly to suppress background. These requirements are discussed below.

- The first requirement was to have an interaction confined within the experimental target volume. This was done by checking the z location of the reconstructed primary vertex. The algorithm for finding the primary vertex of the event is part of the general reconstruction program, which was run on the original data tapes. A description of the algorithm was given in the previous chapter. Only events that had a primary vertex were written onto binary data files. Events with a vertex reconstructed in only one view, or with unmatched vertices reconstructed in both views, were rejected.

- Events which satisfied the above requirement were catalogued according to the nature of the beam particle which triggered the interaction. This was done by checking the Cherenkov response against the specific coincidence requirement for tagging.

- At the beginning of this chapter, we mentioned that one of the potential sources of background to the direct photon signal came from muons produced far upstream of the experimental target that appeared in the beam halo. Most of these particles, produced at low p_T, had trajectories roughly parallel to the beam axis, but distributed over a large transverse area. When such

muons, at times offset by 1-2 meters from the beam axis, radiated photons in the LAC, the apparent deposited p_T was large (small energy, but at large r). In order to eliminate events of this type, the veto wall counters were recorded and, in the off-line analysis, we rejected all events which had signals in the veto wall.

- Because of choices of software cuts used in the off-line reconstruction of the events in the EMLAC, different events had different amounts of remaining uncorrelated energy. The reconstructed uncorrelated energy spectrum peaked at $1-2\,GeV$ for most of the events, with a long tail extending up to large values of uncorrelated energy. This energy excess could be attributed primarily to noise in the detector or to reconstruction inefficiencies, caused by shower miscorrelations between the r and ϕ detector views. Also, part of the contribution was due to deposition of small amounts of hadronic energy. In the present analysis, we set an upper limit of $10\,GeV$ of allowed uncorrelated energy per quadrant, and we rejected all the events in which the uncorrelated energy in the quadrant where the π^0 was detected was above $10\,GeV$.

- In the next chapter, in a section describing the Monte Carlo analysis of the trigger response, we will present results concerning simulations of the *SINGLE LOCAL* trigger. For this type of trigger we produced trigger weighting factors to apply to the data. At present, a systematic simulation of other

Table 4.4: Data Reduction.

Beam Polarity	*negative*	*positive*
Number of Triggers	2,030,000	1,225,000
Events with $p_T > 3 - 4\,GeV/c$	458,630	192,725
Vertex in the Target	152,995	53,796
Veto Wall Requirement	120,458	31,199
Uncorrelated Energy Cut	114,302	29,943
SINGLE LOCAL Trigger Type	82,007	22,966

types of triggers is not available. Consequently, in this thesis we only use events that satisfied the *SINGLE LOCAL* trigger requirement.

For the data samples of both beam polarities analyzed in this thesis, Table 4.4 summarizes the effect of applying the above event selection criteria. Each row indicates the effect of any criterion applied in conjunction with the previous ones. The cuts in Table 4.4 are displayed in the sequence they were applied to the data.

4.4 π^0 Definition

With the procedure outlined in the previous sections, we isolated a sample of events with the following characteristics:

- for negative beam, there is at least one electromagnetic shower with a p_T value above a minimum p_T (the p_T cut was set at 3 and $4\,GeV/c$ depending on the data set used);
- the event has a reconstructed vertex located within the target volume;
- the trigger is not in coincidence with a veto wall signal;

- the uncorrelated energy is less than $10\,GeV$ in the EMLAC quadrant where the π^0 was reconstructed;

- the *SINGLE LOCAL* trigger is satisfied.

We will now describe the procedure used for defining the π^0 signal. For this purpose, all showers in the selected events were required to be within the EMLAC active volume. The latter was defined by the geometrical boundaries of the detector, with the exception of the radial region corresponding to the innermost and outermost edges, and the areas corresponding to the quadrant and octant boundaries. A detailed description of the EMLAC fiducial region will be presented in the next chapter. A search for π^0s was carried out in the $\gamma\gamma$ decay mode (the branching ratio for this mode is $98.85 \pm 0.05\%$). Using the measured energies and positions of both decay photons, π^0 signals were extracted by calculating the invariant mass of all $\gamma\gamma$ pairs detected within any single quadrant of the EMLAC. The opening angle between the photons was calculated by using the measured separation between the two showers and the distance from the target to the EMLAC. Because of the short π^0 lifetime ($10^{-16}\,sec$), the decay into two photons occurs within the target. The histogram in Fig. 4.5 shows all $\gamma\gamma$ mass combinations within each quadrant in the mass range from 0 to $1\,GeV$. The data are for incident π^- on $Cu + Be$ target, and only those $\gamma\gamma$ mass combinations are plotted that have a total p_T greater than $3\,GeV/c$. Clean π^0 and η signals are visible at the nominal mass values of $135\,MeV$ and $548\,MeV$.

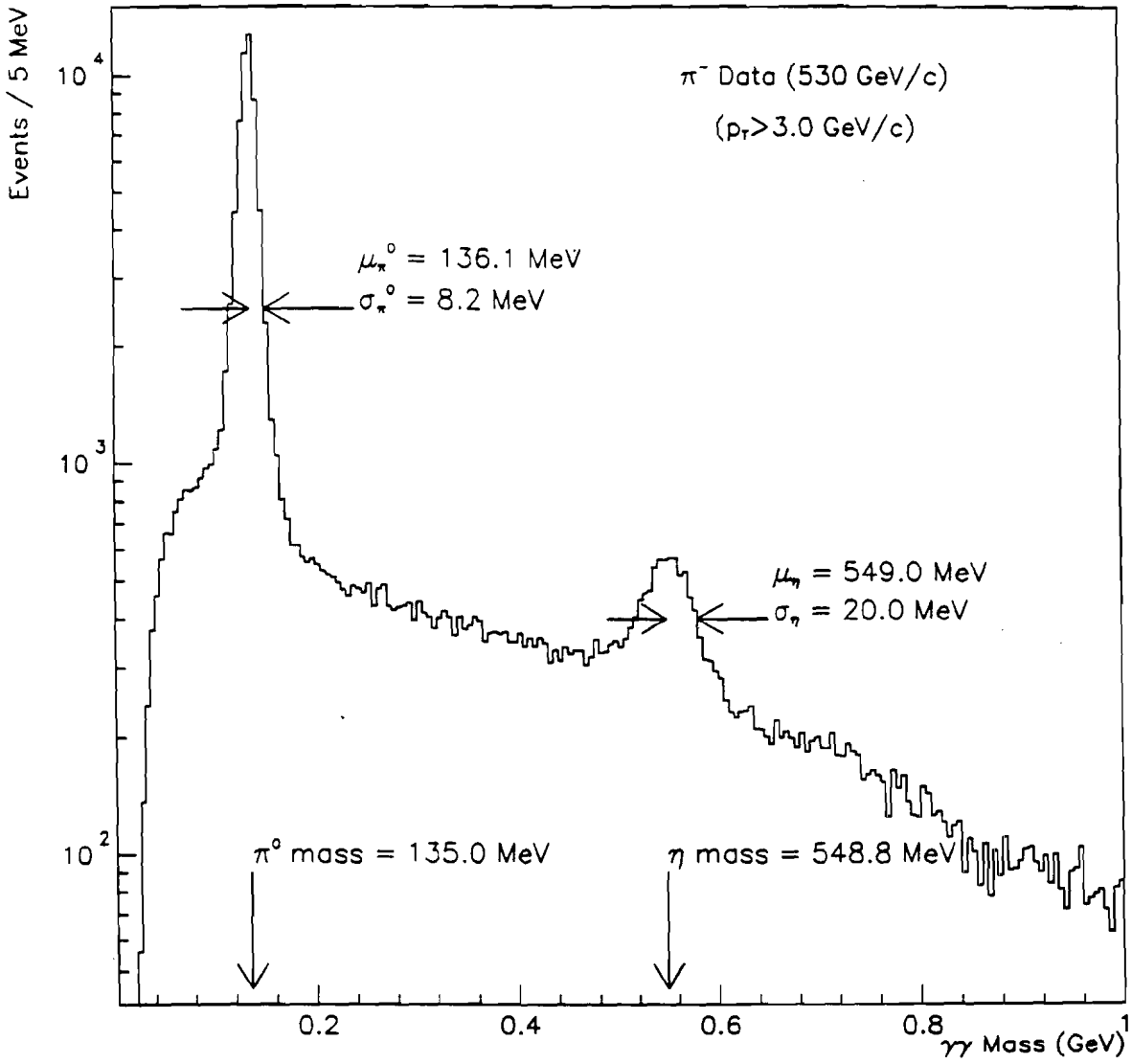

Figure 4.5: $\gamma\gamma$ mass combinations with $p_T > 3.0\,GeV/c$ from π^- interactions at $530\,GeV/c$. Experimental mean values and standard deviations for π^0 and η masses are shown together with the nominal mass values.

For further analysis, a π^0 was defined as a $\gamma\gamma$ pair with a reconstructed invariant mass within the range $135 \pm 25\,MeV$ (the mass resolution is $\sim 8.0\,MeV$). In order to subtract the background caused by two photon mass combinations falling accidentally within the selected π^0 mass limits, we defined two symmetric sidebands. The mass range covered by the sidebands was between $75 - 100\,MeV$ and $170 - 195\,MeV$. The total width of the π^0 sidebands was equal to the width of the selected π^0 mass region. The procedure we used to subtract the background to the π^0 signal was as follows.

Events in the selected π^0 mass interval, and in the π^0 sidebands, were weighted using the Monte Carlo corrections for geometric acceptance, reconstruction and trigger efficiencies, to be described in the next chapter. The event distributions in the variable of interest were evaluated separately for the peak and the sidebands regions. The combined sideband distributions were then subtracted from the distribution of events in the π^0 peak.

The above procedure assumed that events in the π^0 sidebands resembled closely the structure of the background events in the narrow π^0 mass region. A typical background π^0 in the EMLAC is characterized by the wrong combination of a high energy photon (from π^0 decay) with a background photon (from noise or other π^0s) in the event, with the $\gamma\gamma$ invariant mass falling accidentally within the π^0 mass interval. In the laboratory frame, such an event would tend to have one low energy γ, and very asymmetric $\gamma\gamma$ decay features. In Chapter 3 we introduced a

variable which characterizes the degree of symmetry of the π^0 decay. We defined the π^0 energy asymmetry to be:

$$A = \frac{|E_1 - E_2|}{E_1 + E_2} \simeq |cos\Theta^*| \tag{4.6}$$

where E_1 and E_2 are the energies of the two photons in the laboratory frame. In the π^0 rest frame, A is essentially the cosine of the angle Θ^* a photon makes with respect to the π^0 direction. The isotropic decay of the spinless π^0 causes the A distribution to be constant between 0 and 1. In practice, for large values of energy asymmetry, one reaches the experimental limits of γ energy detection. Soft photons can escape detection either because they may miss the active region of the detector or because their energy is too low to be reconstructed. Thus, experimentally, the energy asymmetry distribution for true π^0s will tend to be depleted at large asymmetry, and typical background events will tend to be more asymmetric in decay than π^0s. Figure 4.6(a) displays the A distribution for π^0 candidates with $p_T > 3.5\,GeV/c$. Figure 4.6(b) shows the energy asymmetry distribution for two photon events in the π^0 sidebands. As expected, the background distribution peaks sharply at large asymmetry. Finally, Fig. 4.6(c) displays the π^0 energy asymmetry distribution after sideband subtraction. The smooth curve superimposed to the subtracted distribution is a Monte Carlo prediction. The agreement is seen to be quite good.

We applied an energy asymmetry cut of 0.75 to the data in order to improve the signal to background ratio. Because the energy asymmetry distribution is

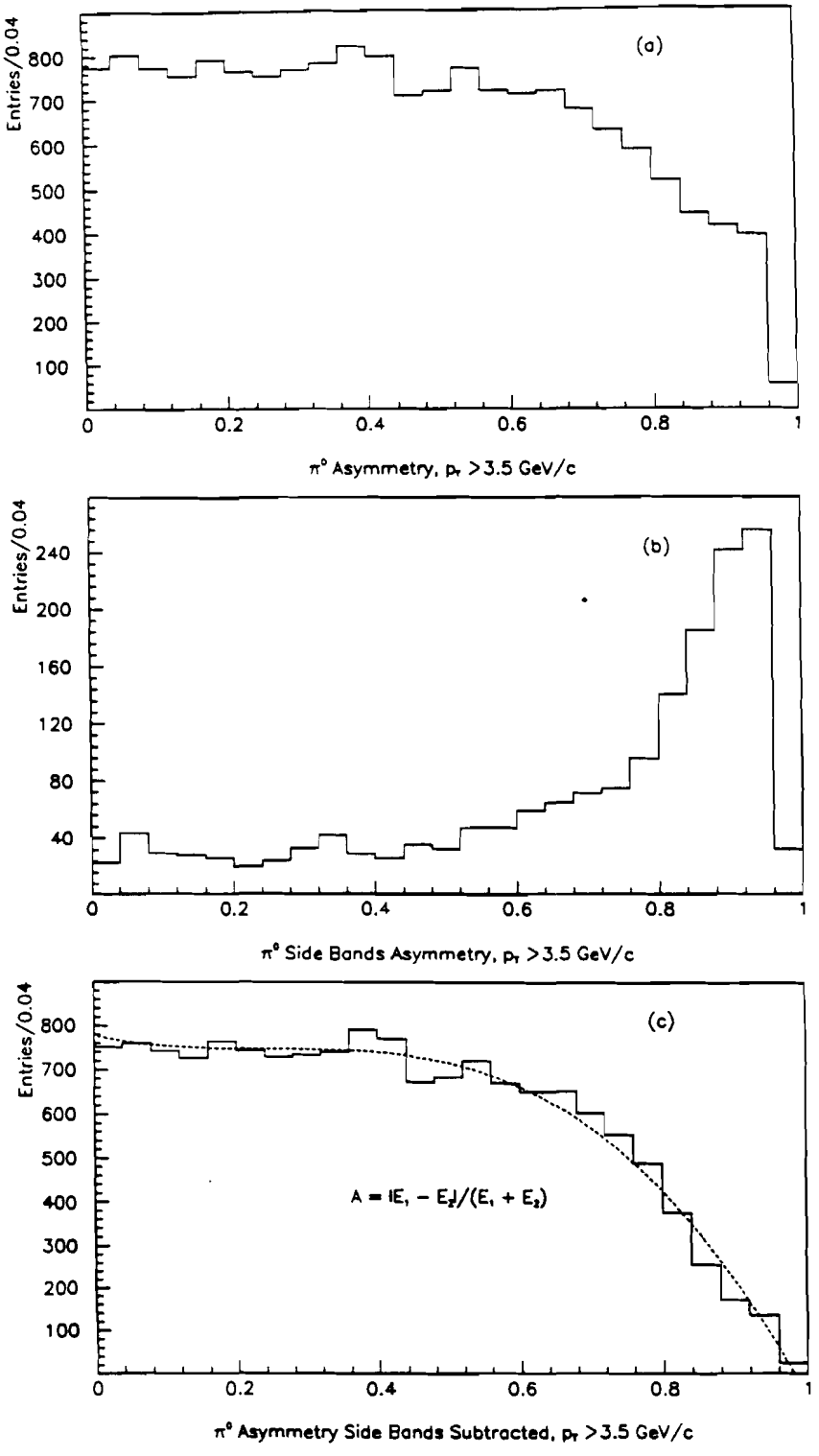

Figure 4.6: Energy asymmetry distributions for $\gamma\gamma$ mass combinations with $p_T > 3.5\,GeV/c$ from π^- interactions at $530\,GeV/c$ (*a*) under the π^0 peak, (*b*) in the π^0 sidebands, and (*c*) under the π^0 peak after sidebands subtraction. The Monte Carlo result (dotted line) is superimposed to the subtracted distribution (*c*).

Table 4.5: Experimental and Monte Carlo π^0 mass parameters.

	$mean(MeV)$	$\sigma(MeV)$
Experimental	136.13 ± 0.06	8.05 ± 0.05
Monte Carlo	136.49 ± 0.09	7.01 ± 0.08

isotropic, such a cut does not introduce any bias into the π^0 sample.

In Fig. 4.7 we show all $\gamma\gamma$ mass combinations with a $p_T > 3.5\,GeV/c$, for masses in the π^0 region, for events where the incident beam particle is a π^- (a), or a tagged K^- (b). Both distributions have the additional restriction that the energy asymmetry be ≤ 0.75. The p_T and asymmetry requirements clearly eliminate most of the background.

For comparison to Fig. 4.7, we display in Fig. 4.8 the $\gamma\gamma$ mass distribution in the π^0 mass region from the GEANT Monte Carlo simulation. The effective energy resolution of the electromagnetic calorimeter (i.e., including the noise term) used in the Monte Carlo was equal to $0.25 \times \sqrt{E}$. The Monte Carlo events had the same cuts applied as the real data, namely the π^0 $p_T > 3.5 GeV/c$, and the π^0 energy asymmetry ≤ 0.75. Both experimental and Monte Carlo mass distributions were fitted using a Gaussian term for the π^0 peak and a constant term for the background. In Table 4.5 we list the results of the fits, specifically the mean and the standard deviation of the Gaussians.

In order to investigate non-uniformities in the detector, we compared the values of the π^0 mass in different detector octants. We corrected the photon energies

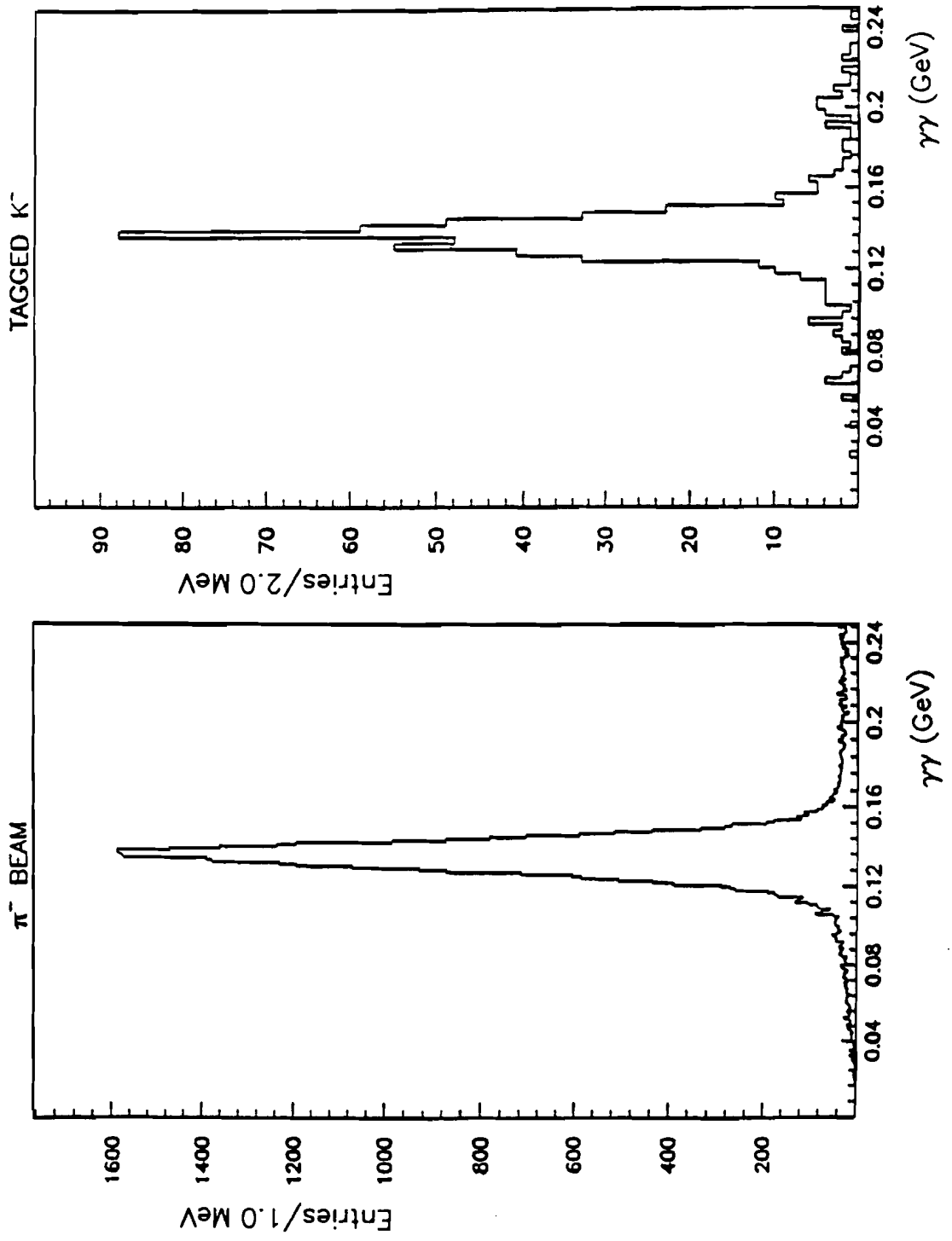

Figure 4.7: $\gamma\gamma$ mass combinations with $p_T > 3.5\,GeV/c$ and energy asymmetry ≤ 0.75 for masses in the π^0 region. Data are from (a) π^- and (b) K^- interactions at $530\,GeV/c$.

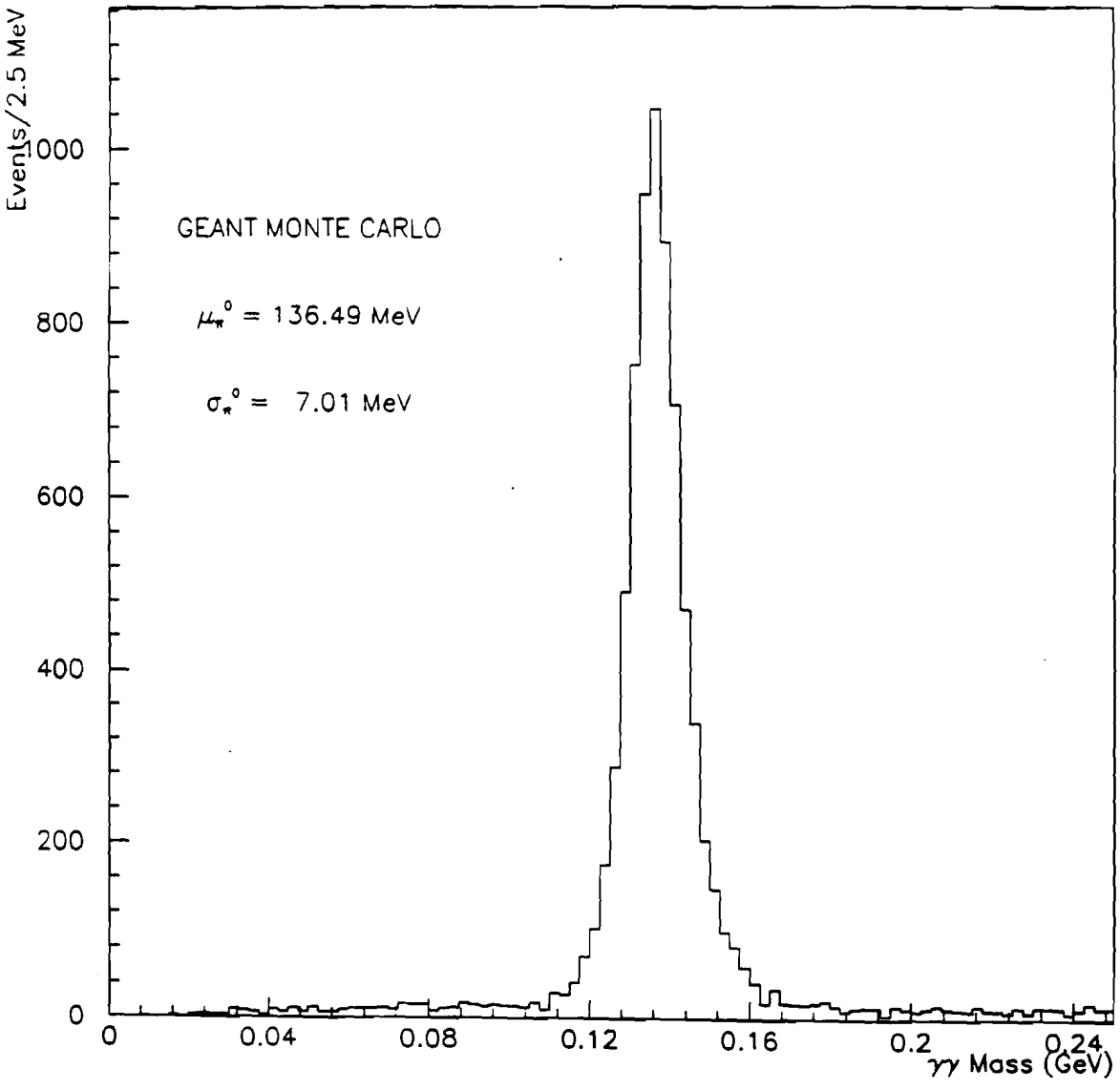

Figure 4.8: GEANT Monte Carlo prediction for $\gamma\gamma$ mass combination in the π^0 region. All mass combinations have $p_T > 3.5\,GeV/c$ and energy asymmetry ≤ 0.75.

based on the amount of rescaling needed in order to adjust the π^0 mass to the accepted value of $0.135\,GeV$. The magnitude of these corrections to the photon energies were on average of the order of 3%, with a maximum of 6% in only two octants.

The dependence of the reconstructed π^0 mass on the radial distance from the center of the detector was also investigated. The r dependence turned out to be more pronounced for low p_T π^0s ($p_T < 4.5\,GeV/c$) than for larger values of p_T. Figure 4.9 displays the reconstructed π^0 mass as a function of the radial coordinate, for π^0s with p_T between 3.5 and $4.25\,GeV/c$ (after applying the energy rescaling for the octant dependence). In the inner region of the detector, the reconstructed masses are higher than the nominal π^0 mass value by as much as 2.5%. In the outer detector region, the reconstructed masses tend to be systematically below the nominal value, but the effect is in general smaller ($< 2\%$). Furthermore, the distribution of the experimental points has a dip at a distance of $40\,cm$ from the center of the detector. This dip occurs at a radius corresponding to the boundary between the inner and the outer regions of the ϕ readout. We believe the effect is due to misreconstruction of photon showers which spread across the boundary, and to miscorrelations of the two photon showers from π^0 decay. This effect would tend to produce lower π^0 masses. A Monte Carlo simulation, using single photons generated for several energy values, partially reproduces the effect noticed in the experimental distribution in the region of the detector near the inner-outer radial

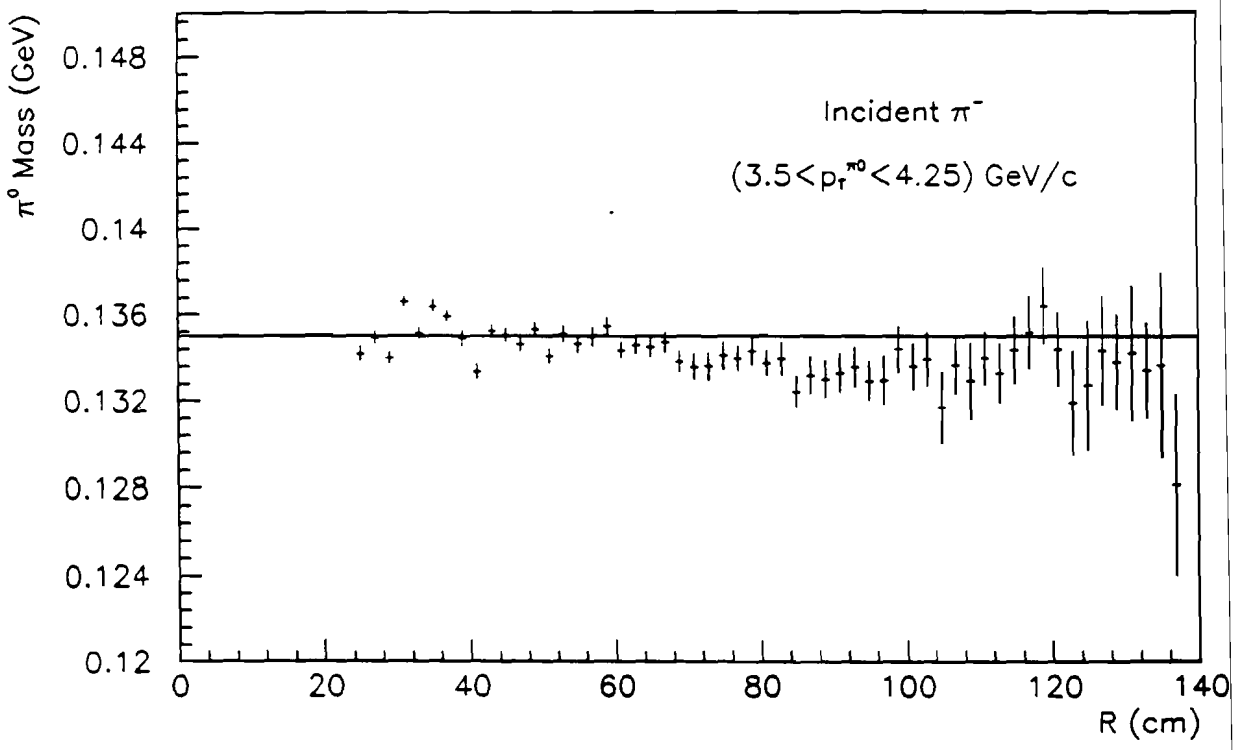

Figure 4.9: Reconstructed π^0 mass as a function of the radial coordinate in the EMLAC. π^0s were required to have a p_T between 3.5 and 4.25 GeV/c. The dip at the radius of 40 cm is due to miscorrelations of showers at the inner-outer ϕ detector boundary.

boundary. Using the reconstructed energies of the Monte Carlo generated showers, we obtained a table of correction factors to be applied to energies of photons at a radial distance between 32 and 48 cm from the center of the detector. Since this Monte Carlo correction only partially accounted for the energy loss, an additional rescaling of the π^0 energy was required; this was based on the parametrization of the residual dip in the π^0 mass distribution at $r = 40\,cm$.

Chapter 5

MONTE CARLO SIMULATION

5.1 Monte Carlo Analysis

In order to extract inclusive cross sections from differential particle distributions it is necessary to understand certain features of the experimental apparatus, namely: the geometrical acceptance, the reconstruction efficiency and the trigger response to the events of interest. Two Monte Carlo programs were written to resolve these issues: one for calculating the geometrical acceptance and reconstruction efficiency, the other for modeling the experimental trigger. The results of the calculations were used to correct the experimental distributions. In both programs, events were generated using the E706 GEANT Monte Carlo package [50], and reconstructed using the same standard programs as were used for reconstructing real data. (For details on the software cuts applied to experimental distributions refer to Chapter 4.) In this chapter we will describe the structure of the Monte Carlo programs and present some of the obtained results.

5.2 Geometric Acceptance and Reconstruction Efficiency

As implied previously, the simulation of the detector acceptance and the efficiency were carried out within one Monte Carlo program. The geometrical acceptance for π^0s was calculated as a function of p_T and rapidity. Events were generated in a two-dimensional grid in p_T and y, with p_T in the range from $3\,GeV/c$ to $10\,GeV/c$, in bins of $0.5\,GeV/c$, and center of mass rapidity in the range $-1.0 < y < 0.8$, in 0.2 bins. At each (p_T, y) point, 1,000 single π^0s were generated at the middle of a $4\,cm$ long Be target, and allowed to decay isotropically into two photons, with a random choice of decay angle. (The isotropic decay of a π^0 in its own rest frame is equivalent at high energies to an isotropic distribution in photon asymmetry.) Dalitz decays of the π^0s ($\pi^0 \rightarrow e^+e^-\gamma$) accounted for about 1% of the generated events.

The EMLAC detector's fiducial region was defined in the $x - y$ plane by the R variable as $24 < R < 138\,cm$, were R is the distance along the radial detector dimension. In terms of the center of mass rapidity, this corresponds to $-0.95 < y < 0.80$. (In the following we will assume y to be the center of mass rapidity. The transformation to the laboratory system consists of adding a constant $\Delta = 3.52$ to y).

To avoid uninstrumented areas corresponding to the steel support structures of the EMLAC quadrants, the azimuthal angle ϕ was restricted to four angular regions: $2.82^0 < \phi < 87.2^0$, $92.82^0 < \phi < 177.2^0$, $182.82^0 < \phi < 267.2^0$, $272.82^0 <$

$\phi < 357.2^0$. The above definitions of our fiducial volume required the centroid of all reconstructed showers to be at least $2\,cm$ away from the azimuthal edges of the calorimeter.

For each π^0 decaying in the target, the position of the two photons was projected to the front face of the LAC ($z = 900\,cm$). Geometric losses were then evaluated by observing how often either (or both) photons missed the detector. For consistency with cuts applied to real data, we only accepted generated π^0 energy asymmetry values of less than 0.75. At each (p_T, y) point we calculated the ratios:

$$\frac{N'_{\pi^0}(p_T, y)}{N_{\pi^0}(p_T, y)} \tag{5.1}$$

Here N'_{π^0} is the number of π^0s generated for which both photons from the decay passed criteria for inclusion in the fiducial volume, and N_{π^0} is the total number of π^0s generated. From the analysis of the results, the geometrical acceptance was found to be a rather weak function of the p_T and rapidity of the π^0. Only for very forward π^0s, corresponding to large positive values of y, do the geometric losses increase rapidly. The reason is that at small detector radius the uninstrumented region, corresponding to the detector frame and connectors, becomes a sizeable fraction of the total detector area. Since we require both photons from the π^0 to be within the fiducial region, at $y = 0.8$, the probability of loosing one of the two photons (and consequently the π^0) becomes very large. To avoid implementing sophisticated weighting schemes to account for the geometrical losses in the large

$|y|$ regions, we instead restricted our data analysis to the range $-0.7 < y < 0.7$.

After the fraction of accepted events was determined purely from geometry, the photons from the N'_{π^0} π^0s were transported to the front face of the electromagnetic calorimeter. Subsequently, the electromagnetic showers were generated using parametrizations obtained from the analysis of a sample of Monte Carlo events that were run through the full GEANT package, and from the shower shapes obtained from the analysis of shower profiles from calibration events and normal data (see Chapter 3.3). Because of the large number of Monte Carlo events required, we chose to use our parametrizations for the photon showers rather than full shower-development simulations. In addition, to improve the modeling of the data, we incorporated in our Monte Carlo several features of the detector response. A noise term was included to account for the incoherent energy fluctuations of the amplifier channels ($75\,MeV/channel$), we introduced an energy threshold to simulate the hardware zero suppression threshold ($140\,MeV/channel$), and we smeared the total shower energy according to the effective detector energy resolution of $0.25\sqrt{E}$. The latter value was obtained independently from an analysis of the calibration data and of the zero mass pair events (see Chapter 3 for details).

Accepted π^0 events were reconstructed using the standard reconstruction program, and a reconstruction efficiency was defined by the ratio:

$$\frac{N''_{\pi^0}(p_T, y)}{N'_{\pi^0}(p_T, y)} \tag{5.2}$$

where N''_{π^0} is now the number of π^0s reconstructed correctly. Once again, N'_{π^0} is

the number of events in which the two photons from π^0 decay were both within the EMLAC geometric fiducial volume, and had energies larger than $3\,GeV$. Dalitz decays and π^0 events with other complications, such as conversions of one or both photons into electron-positron pairs, were excluded from this calculation, but were corrected for at a later stage.

The analysis of a sample of Monte Carlo events revealed that reconstruction losses were mainly due to very asymmetric π^0 decays, in which one photon had very low energy, and this can occurr at all p_T. At large p_T and large π^0 energies, losses can also be caused by coalescence of the two photons in one or both views, with the consequent failure of the reconstruction algorithm to split overlapping showers. Also, many low-p_T π^0s tend to generate a soft photon whose energy is too low to cause enough channels to appear above threshold. When the energies are barely above threshold, these soft photons produce small signals of magnitude comparable to the noise level of the detector. Such events can, because of fluctuations, cause photon energy miscorrelation between the r and ϕ view, and a loss of π^0s. In fact, when the central energy for a group in one view passes the software requirement, but the energy in the tails of the shower is below threshold, the reconstruction algorithm in fitting the shower shape is often inefficient, even though an estimate of the energy in the tails is included in the process. One of the results is that the reconstructor tends to underestimate the photon energy, and systematically reconstructs a lower π^0 mass, which falls outside the selected

di-photon mass range. Reconstructed Monte Carlo π^0 masses falling outside the allowed mass range account for about 1% of the total π^0 losses. As in the analysis of the real data, we remove events with a π^0 energy asymmetry larger than 0.75 before evaluating N''_{π^0}.

The reconstruction efficiency for two isolated photons with a mass in the π^0 region ($0.11 < m_{\pi^0} < 0.16\,GeV/c^2$) was estimated to be about 98% over most of the p_T and rapidity range, with additional $\sim$ 8% losses at low p_T (between $3\,GeV/c$ and $3.5\,GeV/c$), in the backward rapidity region (loss of soft photons), and at very large p_T ($> 7.5\,GeV/c$) for large positive values of the rapidity (due to coalescence). We defined two continuos functions $GA(p_T, y)$ and $RE(p_T, y)$ for the ratios (5.1) and (5.2) for interpolating between the different locations in the $p_T - y$ grid.

In the subsequent data analysis, we corrected the observed π^0 distributions on an event by event basis, for each reconstructed value of p_T and y, by multiplying the experimental distributions by:

$$TE(p_T, y) = GA(p_T, y) \times RE(p_T, y) \tag{5.3}$$

which represents the total efficiency for observed π^0 events. Figures 5.1 shows the total efficiency distribution for π^0s as a function of p_T and rapidity.

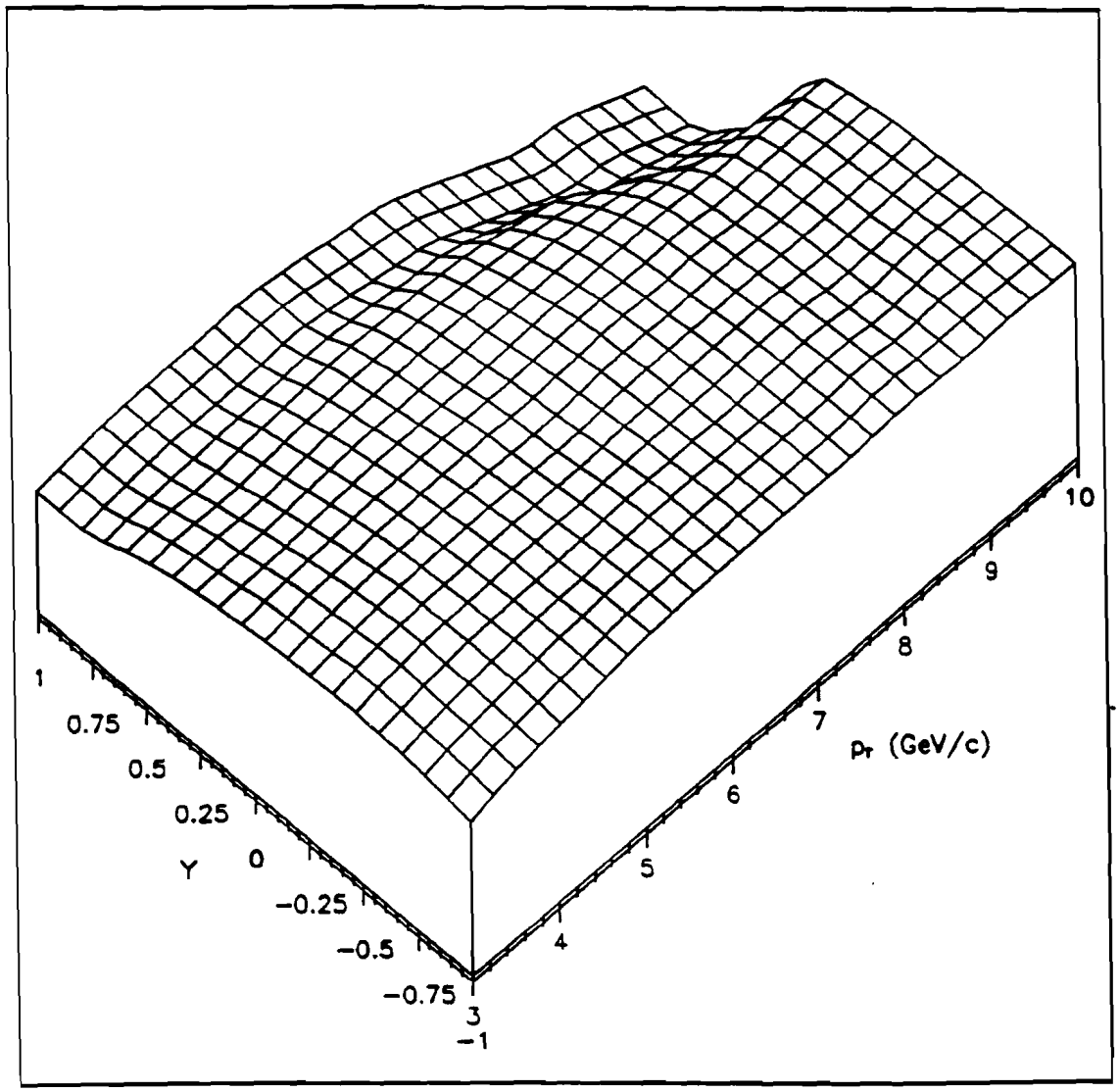

Figure 5.1: Total efficiency for π^0s as a function of p_T and rapidity.

5.3 Conversion and Bremsstrahlung

We mentioned in the previous section that photons originated from the π^0 decay can experience interactions in the target material, or later in the materials along their flight path. The main energy loss mechanism for photon energies above a few GeV, is conversion to electron positron pairs. The produced electrons (positrons) can emit Bremsstrahlung radiation both in material and in a magnetic field. Under the influence of the magnetic field, the electron-positron pair opens up at the center of the analyzing magnet as the two particles receive an equal and opposite (in direction) momentum kick of about $450\,MeV/c$ in the xz plane. Electrons (positrons) with momenta above $1.5\,GeV/c$ usually remain within the fiducial acceptance of the electromagnetic calorimeter. We are already familiar with the topology of these events, which we earlier (see Section 3.2) referred to as Zero Mass Pairs (ZMPs), and used to study detector performance. Compared to the events where only two photon showers propagate in the calorimeter, ZMP events are characterized by additional showers in the EMLAC; the ZMP event topology is therefore more complicated, and, as a consequence, when the algorithm makes all two photon mass combinations it will tend not to reconstruct the proper value of π^0 mass. These events contribute to the two γ background under the π^0 mass peak.

In the Monte Carlo used for calculating total efficiency, we did not simulate the full transport of particles through the components of the apparatus downstream

of the target. This artificially reduced the interaction probability for all particles produced within the target, and had to be corrected later in the analysis.

Photons travelling through matter will each have a probability of converting into an electron-positron pair of

$$1 - e^{-t\frac{\rho}{\lambda}}$$

were t is the distance travelled in cm, ρ is the density of the material in g/cm^3, and λ is the photon mass attenuation length in g/cm^2. For photon energies larger than $1\,GeV$, the total pair production cross section is essentially independent of energy, and scales with the mass number A as follows:

$$e^{\frac{7}{9}\frac{A}{N\lambda_r}}.$$

Here λ_r is the radiation length of the medium, N is the Avogadro number. In $2\,cm$ Be, the estimated photon conversion probability is $\simeq$ 5.5%, while in the $900\,cm$ air it is $\simeq$ 2.9%; the total conversion probability is then $\simeq$ 8.4%. This means that the probability that either of the two photons from a π^0 converts is $\simeq$ 16.8%, while the probability that both photons convert is only $\simeq$ 0.7%. The created electron-positron pairs can then undergo Bremsstrahlung.

We checked our assumptions against our Monte Carlo by generated π^0s with p_T of $5\,GeV/c$. The results indicated that 10.2% of the generated π^0s had one of the two photons converting and no Bremsstrahlung; 0.4% had both photons converting and no Bremsstrahlung; 5.5% had photon conversion followed by Bremsstrahlung. Hence, a total of about 16% (not including the Dalitz decays), 85% of which would

fall in the geometrical fiducial volume of the EMLAC, had single and double photon conversions.

As already mentioned, π^0s that have conversions tend to be lost in the analysis if one only searches for π^0s through their two γ decay mode. When evaluating π^0 cross sections, one has to account for those losses by including the appropriate correction factor in the overall normalization. The evaluation of the correction factor will be described in a following chapter.

The normal data provided a sample of π^0 events characterized by more than two electromagnetic showers. An analysis is now in progress aimed to fully reconstruct such events. Searching for π^0s in events with a single photon conversion (one ZMP), requires the combination of the four momenta of the e^+e^- pair with the four momenta of any photons in the event, so as to form $e^+e^-\gamma$ invariant mass combinations. One such histogram is shown in Fig. 5.2. A clear signal shows a peak at the π^0 and even at the η mass. Searching for π^0s in events with double photon conversion (two ZMPs), is a harder task, as it requires four tracks, with specific features, to be unambiguosly reconstructed. A plot of $e^+e^-e^+e^-$ invariant mass is shown in Fig 5.3. The π^0 signal is still evident even though the statistics are poor. In Fig 5.2, it is interesting that a small signal appears at low values of the $e^+e^-\gamma$ mass; this may be direct evidence of photon Bremsstrahlung associated with e^+e^- pairs. The peak is likely due to events in which one of the ZMP particles radiates a Bremsstrahlung photon upstream of the magnet, and the other

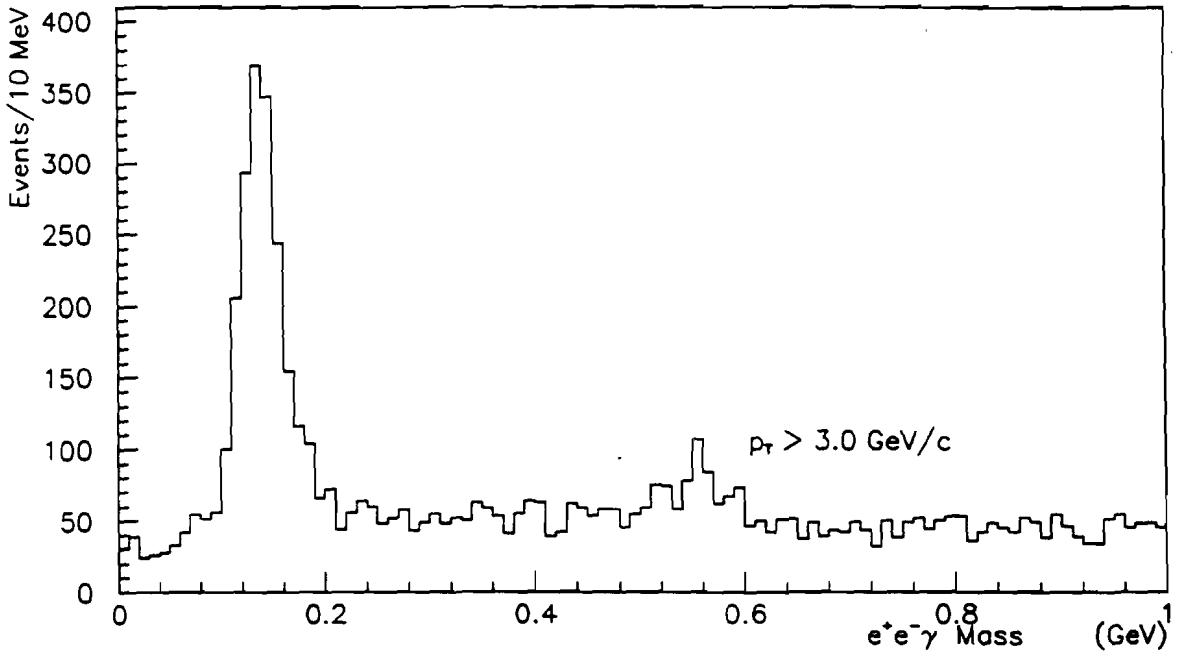

Figure 5.2: Distribution of all $e^+e^-\gamma$ mass combinations with $p_T > 3\,GeV/c$. Peaks at the π^0 and η mass are clearly visible.

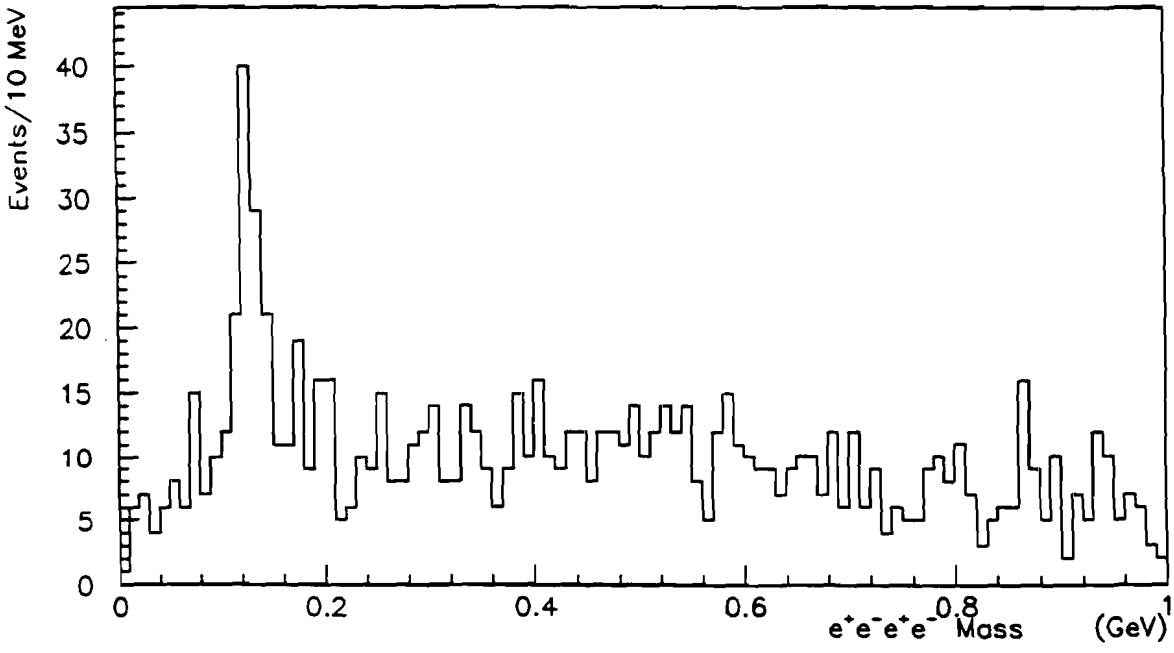

Figure 5.3: Distribution of all $e^+e^-e^+e^-$ mass combinations with $p_T > 3\,GeV/c$. A peak at the π^0 mass is clearly visible, while only an enhancement shows at the η mass.

photon from the π^0 falls outside the detector acceptance and is lost. The e^+e^- pair, which splits at the magnet, and the radiated photon, will make an entry in the histogram which will occur at a mass value very close to that of the invariant mass of the e^+e^- system (the radiated photon takes, on average, a small fraction of the momentum of the emitting particle).

5.4 Trigger Efficiency

In Section 2.9 we mentioned that for analysis we accepted only those events that satisfied the *SINGLE LOCAL* trigger requirement, namely events with a deposition of energy in an octant region above the local p_T treshold. The reason for this is that only the *SINGLE LOCAL* p_T trigger was properly modeled through Monte Carlo simulation. The global p_T trigger is currently under investigation.

In order to measure the efficiency of the *SINGLE LOCAL* trigger we analyzed a sample of events satysfying the *TWO GAMMA* trigger requirememt (see Section 2.9). This trigger was satysfyed when two *SINGLE LOCAL* low p_T ($> 1.7\,GeV/c$) triggers fired simultaneously in geometrically opposite octants. The efficiency of the *TWO GAMMA* trigger was measured to be 100%, in the p_T range in which the high p_T threshold had turned on (above 50% efficiency). Using this data sample, we measured the probability for the *SINGLE LOCAL* high p_T ($> 3.0\,GeV/c$) trigger to be satisfied by calculating in different geometrical regions of each octant the trigger efficiency, defined as the ratio $TG * SL/TG$, where $TG * SL$ is the number of times both the *TWO GAMMA* and the *SINGLE LOCAL* triggers are

satisfied, and TG is the number of times the *TWO GAMMA* trigger is satisfied. A distribution of this probability versus p_T yielded the *SINGLE LOCAL* trigger efficiency in the specific region of that particular octant. Each octant was divided into three regions, consisting of: the first 32 inner radial strips (readout by one p_T module), the following 64 r strips (readout by two p_T modules), and the last 128 radial strips (readout by four p_T modules).

The trigger efficiency is parametrized using a probability function, obtained by integrating a step function that represent the trigger discriminator threshold; this is folded with a Gaussian smearing term. The expression for the function is:

$$P(p_T, r, \phi) = \frac{1}{\sqrt{2\,\pi}\,b} \int_{-\infty}^{+\infty} dp_{T'}\ \Theta(p_T + p_{T'} - a)\ e^{\frac{-p_{T'}^2}{2\,b^2}} \qquad (5.4)$$

Here a is the position-dependent trigger threshold, and b is the standard deviation of the p_T resolution. The smearing was caused by coherent noise in the detector, pedestal and gain variations for individual strips, and variation of the hardware zero-suppression threshold with position. Figure 5.4 is a plot of the *SINGLE LOCAL* trigger efficiency for π^0 events.

Fits to the data in each of the 24 regions determined a set of values for a and b. The standard deviations for the turnons were typically of the order of $200 - 250\,MeV/c$. The threshold values varied by several hundred MeV/c from one detector region to another. The p_T threshold at the point where the trigger was 50% efficient varied going from the outer to the inner regions of the detector by as much as 20%, altough no systematic trend was discernible.

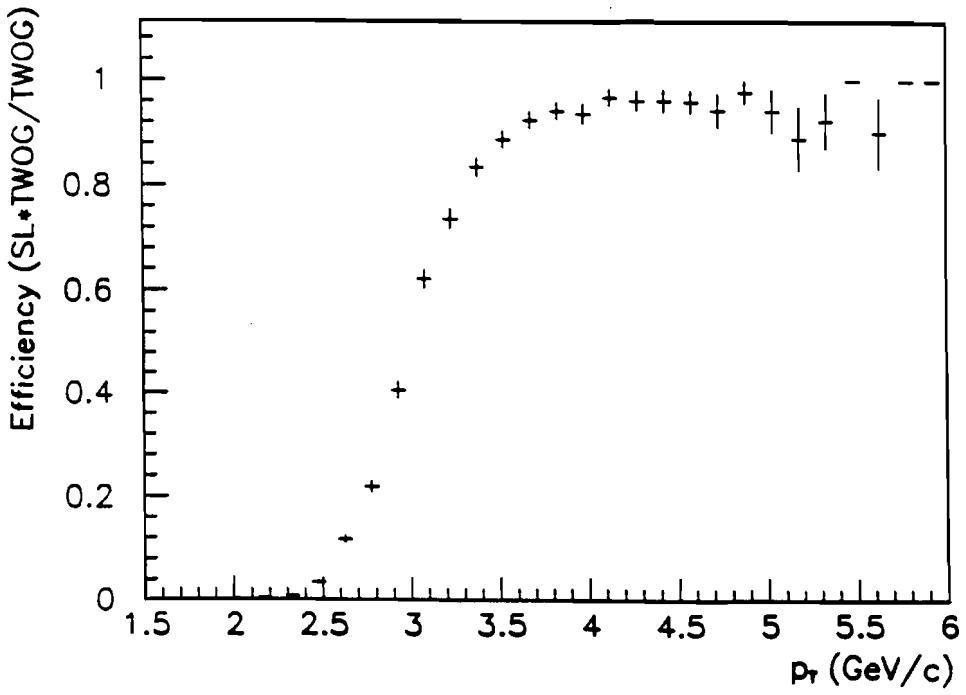

Figure 5.4: *SINGLE LOCAL* trigger efficiency for π^0 events as a function of p_T.

The values determined with Parametrization (5.4) for the *SINGLE LOCAL* trigger efficiency, were used as input to the Monte Carlo. The same π^0 events generated for the acceptance calculations (see Section 5.2) were used for trigger simulation. For each of the generated photon showers from π^0 decay that fell within the fiducial volume of the LAC, the probability of firing the *SINGLE LOCAL* trigger was calculated using Expression (5.4). If the p_T in the detector exceeded the *SINGLE LOCAL* trigger threshold for that region, the event was accepted. The number of accepted events divided by the number of generated events determined a trigger acceptance for π^0s generated in the active area of the EMLAC. Figure 5.5 shows the *SINGLE LOCAL* trigger efficiency for π^0 events as determined by the Monte Carlo simulation.

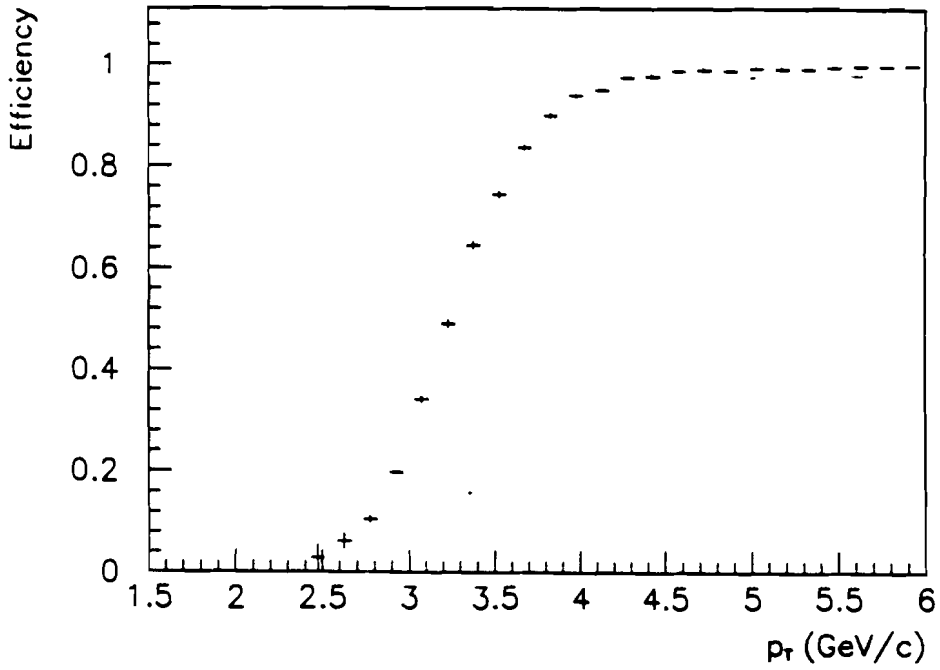

Figure 5.5: *SINGLE LOCAL* trigger efficiency for π^0 events as a function of p_T as determined by the Monte Carlo simulation.

A check on the consistency of the Monte Carlo results was made using real events selected from data files (see Section 4.1). As will be described in the next chapter, these files contained only selected informations on the events. In particular,the information on the energy deposited in each strip was no longer available on this stage. By using reconstructed values of the energy (p_T) and of the position of showers as input to the Monte Carlo parametrization of the shower shape, the shower energy per channel was regenerated. The probability of the event to satisfy the *SINGLE LOCAL* trigger was then evaluated using Expression (5.4). The two sets of trigger-weigthing corrections were found to be consistent with each other at the 1% level.

Chapter 6

RESULTS AND CONCLUSIONS

6.1 Introduction

In this chapter the results of the analysis are presented. The procedure for normalizing cross sections is outlined in Section 6.2. Section 6.3 describes the sources and magnitudes of systematic errors. In Section 6.4 the invariant cross sections for π^0 production, using different incident beam particles, are presented as a function of p_T and x_F. The absolute normalization for the π^- and p data are from a preliminary analysis, the final results of which will be presented in the thesis of J.P. Mansour [55]. It should be recognized that the measurament of the ratio of yields, to be discussed in Section 6.5, are not sensitive to uncertainties in absolute normalization. Phenomenological fits to the experimental distributions and comparisons with other experiments are also shown. Section 6.5 compares π^0 production yields using different beam particles. In the last section the results of the analysis are discussed and the conclusions summarized.

6.2 Absolute Normalization of Yields

The invariant cross section per nucleon can be written in the form:

$$E\frac{d^3\sigma}{d^3p} = \frac{1}{\rho\, l\, N_0\, B}\,\frac{N(p_T)}{\Delta y\,\Delta\phi\, p_T\,\Delta p_T} \tag{6.1}$$

where ρ and l are the density and the length of the target, respectively; N_0 is Avogadro's number; $N(p_T)$ is the corrected yield of events; B is the corrected incident beam flux; $\Delta y \Delta\phi p_T \Delta p_T$ is a volume element in phase space.

The normalization factor B which appears in the expression for the invariant cross section (6.1) represents the fraction of the total incident beam flux recorded by the beam scalers during the intervals the experiment took data. We referred to B previously as the live triggerable beam. To define B, the following conditions had to be fulfilled: (a) the incident beam signal was present (indicated with $BA * BB$ in Section 2.9); (b) this signal was in coincidence with the computer ready signal ($COMP\_RDY$), and in anticoincidence with the signal from the beam halo counter ($\overline{BH}$); (c) there was no beam-target interaction in a time window lasting $\pm 60\, nsec$. Using the terminology of Section 2.9, the live triggerable beam satisfing the above conditions can be expressed in the form:

$$B = (LIVE\_BM * \overline{BH}) \times C_1 \times C_2 \times C_3 \tag{6.2}$$

where

$$C_1 = \frac{INT * COMP\_RDY * (CL\_EARLY * CL\_LATE)}{INT * COMP\_RDY}$$

$$C_2 = \frac{PRETRIGGER\_OR + NO\_PRETRIGGER}{LINT}$$

$$C_3 = 1 - \frac{(LINT * CLEAR) * (\overline{SCR} + \overline{VW} + \overline{EARLY\_PT})}{LINT * CLEAR}$$

are correction factors. (The variables in the above expressions have already been defined in Section 2.9.) The logic signal *PRETRIGGER_OR* refers to the logical OR of all four types of pretriggers, not just to the LAC pretrigger. In practice, our definition of B yields the total number of beam particles incident during the time the computer was enabled to take data ($LIVE\_BM * \overline{BH}$), corrected for interactions too close in time to the one that triggered the event (C_1), corrected for the trigger dead time (C_2), and for the dead time introduced by different veto signals (C_3).

Let us examine the effect of these corrections. The magnitude and time stability of the correction factors can be observed in Fig. 6.1, in which C_1, C_2, and C_3 are plotted as a function of the run number. The full range of the horizontal scale is equivalent to a data-taking period of one month. The correction factor C_1 is of the order of $6 \pm 4\%$; C_2 is a rather small correction of the order of $2 \pm 1\%$, with the exception of few runs. The dead time that C_3 introduced varied between 25% and 40%, and was the source of the largest correction. Changes in the magnitude of the above corrections to the total incident beam produced live time variations from 30% to 70% in different data runs, the live time being defined by:

$$LIVE\_TIME = \frac{B}{BA * BB * \overline{BH}} \tag{6.3}$$

The live triggerable beam was corrected for the measured contamination due to the fraction of minority charged particles tagged by the Cherenkov counter. Variations with time of the relative contaminations measured with the procedure

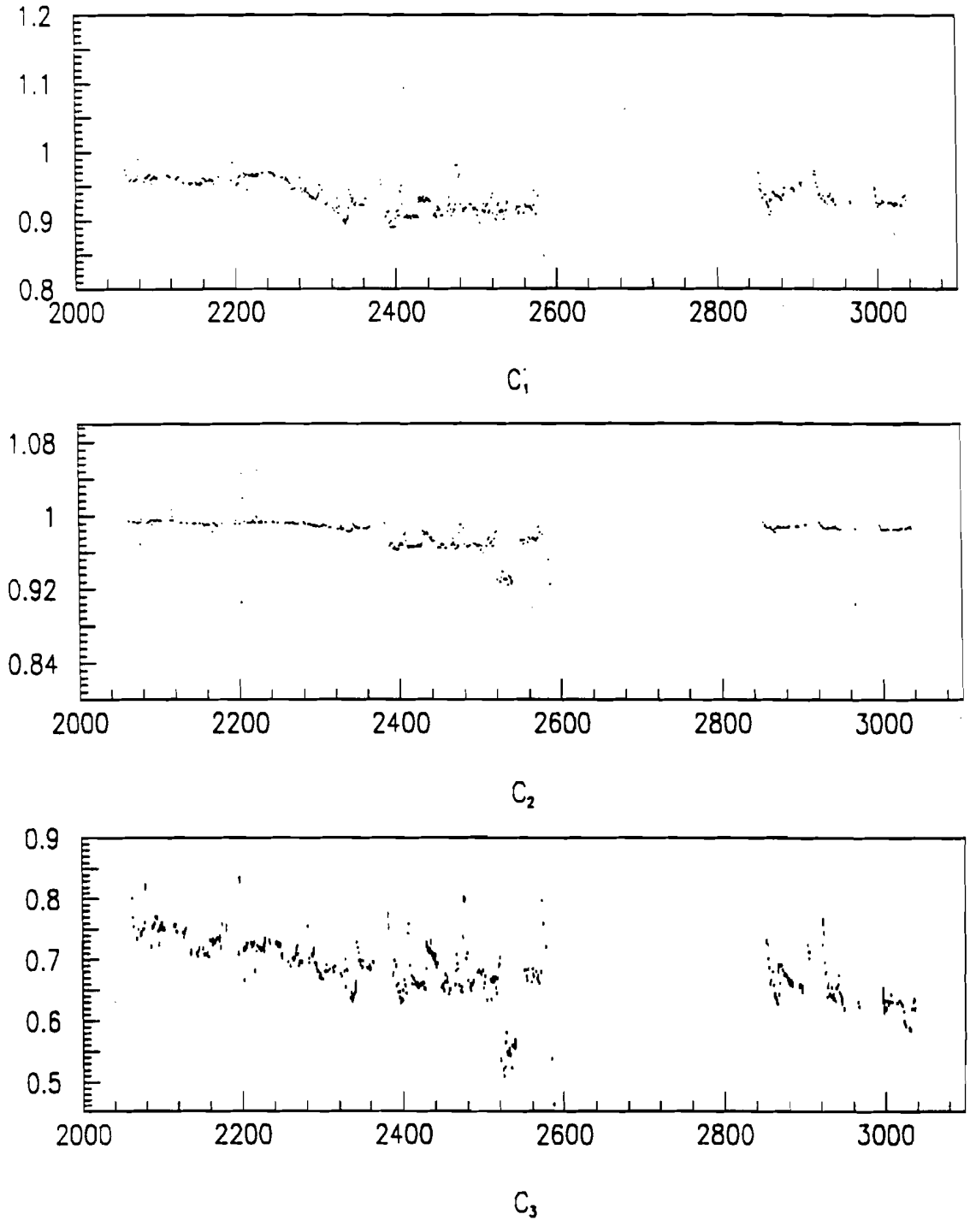

Figure 6.1: Variations of the correction factors used for the calculation of the live triggerable beam as a function of run number.

outlined in Chapter 4, were also accounted for. Furthermore, since the fraction of minority particles was determined by counting tagged particles in the non-interacting beam buckets, and not by using the Cherenkov gas pressure excitation curves, no additional correction was introduced to account for the Cherenkov efficiency.

A small correction was applied to the live beam for the probability of two or more beam particles to occur in one RF bucket (there was no pulse height information from the beam hodoscope). This correction increased the live beam by 2%.

Another correction to B was applied for the probability of particle interactions upstream of the experimental target. Beam absorption in the 6 upstream silicon planes, veto counters, and $220\,cm$ of air was corrected for.

We also evaluated the beam absorption in the target. Correction factors were independently calculated for each beam particle type. For the cross section on Cu and Be targets separately, individual correction coefficients were calculated using the beam absorption lengths as a function of target position (obtained from the reconstructed vertex). For the combined $Cu + Be$ target, the beam absorption coefficient A_i for target i was weighted according to a factor proportional to the length of the corresponding target, using the following formula:

$$A_{Cu+Be} = \frac{(\rho\, l)_{Cu}\; A_{Cu} \;+\; (\rho\, l)_{Be}\; A_{Be}}{(\rho\, l)_{Cu} \;+\; (\rho\, l)_{Be}} \tag{6.4}$$

with

$$A_{Cu} = (1 + \frac{l/2}{\lambda})_{Cu}$$

$$A_{Be} = (1 + \frac{l/2}{\lambda})_{Be}$$

Here ρ and l are the density and the length of each target, respectively; λ is the absorption length for the material, calculated using the π and proton absorption cross section measurements of [32]. The above relations assume that interactions occur on average in the middle of the target.

To obtain the correct yield of π^0 events $N(p_T)$, we corrected the p_T spectrum of events in the π^0 mass interval ($0.11 < m_{\gamma\gamma} < 0.16\,GeV$) and in the π^0 sidebands ($0.075 < m_{\gamma\gamma} < 0.11\,GeV$ and $0.16 < m_{\gamma\gamma} < 0.195\,GeV$) for the combined geometrical acceptance and reconstruction efficiency (using the interpolation function $TE(p_T, y)$ defined in Section 5.2), and for the efficiency of the *SINGLE LOCAL HIGH* p_T trigger (Section 5.4). For this analysis, all trigger weights larger than 3 (primarily in the low p_T turn-on region) were set to 3.

Furthermore, individual events were corrected for the efficiency of the vertex finding algorithm. This efficiency was parametrized with a linear function of the z-coordinate of the reconstructed vertex of the event. The correction function was of the form $F(z) = 1.0019 + 0.0079\ z$.

Another correction applied to the yield of events accounted for the probability of photon conversion in the target. The photon conversion probabilities were estimated for each target segment, and events were corrected based on the positions of the reconstructed vertices.

Throughout the run the apparatus experienced some hardware failures. Most of the breakdowns were promptly detected and fixed, thanks to the use of several routines monitoring the on-line performances of the different components of the apparatus. In particular, some of the octant p_T trigger modules experienced an uncomfortably large failure rate. When such circumstances occurred during data taking, the entire octant was temporarily disconnected from the trigger system, and the investigation of the causes of the failure postponed to the accelerator's scheduled downtimes. At the end of run, all the changes to the trigger system were recorded in a separate data base. The reduction in the number of active octants had obvious implications on the trigger rate and on the yield of π^0s. In this analysis, individual runs were checked against the information available in the trigger data base, and each event was applied a weight equal to the ratio between the number of EMLAC octants and the number of trigger-enabled octants.

To account for background under the π^0 mass peak, we subtracted the corrected π^0 sidebands distribution from the corrected p_T distribution in the π^0 mass interval.

We now describe another sequence of correction factors that was also applied to the distribution of π^0 events primarily for selection criteria used in the analysis. Each correction multiplies the original distribution of π^0 events to yield the corrected value of $N(p_T)$ of Expression (6.1) for the relevant rapidity and Δp_T interval, centered at p_T.

The corrections to the yield of events include the following.

1. A correction for the cut at 0.75 to the π^0 energy decay asymmetry.

2. A factor correcting for the π^0s rejected because of the presence of a veto wall signal in the event. This can be caused by back scattering from the target.

3. A correction was applied for those events with an excess of uncorrelated energy ($> 10\,GeV$ in the quadrant of the EMLAC where the π^0 was reconstructed), that had been rejected (see Section 4.3).

4. A correction for the probability that photons from π^0 decay could convert into electron-positron pairs downstream of the interaction target, and be lost as π^0s. (Photon conversion in the target was discussed earlier.)

5. Finally, the yield of π^0 events was corrected for the mass cut used to define a π^0 signal. As already mentioned, only π^0s with a reconstructed mass between 0.11 and $0.16\,GeV$ were accepted. Misreconstruction can shift π^0s outside of this range. The effect of the restriction was investigated by analyzing a subset of $\gamma\gamma$ events with $p_T > 4\,GeV/c$ and $A < 0.75$. This corresponds to an essentially pure π^0 sample. Assuming that misreconstructed π^0s primarily have a mass lower than the nominal value (see Section 4.4), we calculated the ratio between all $\gamma\gamma$ combinations with masses below $0.11\,GeV$ and those with masses in the π^0 mass range of 0.11 to $0.16\,GeV$. Using this procedure the yield of π^0 lost because of the mass cut was determined to be of $4.0 \pm 2\%$.

A similar study was performed using a sample of Monte Carlo events. π^0s were generated in the target, tracked through the experimental apparatus using the full GEANT simulation to determine the shower energy deposition in the EMLAC, and then reconstructed. Of all reconstructed π^0s, 10 had a mass outside the selected π^0 mass range. This determined a correction of $4.5 \pm 1.5\%$, consistent with the 4% measured value , which was used in Expression (6.1).

Table 6.1 summarizes the above correction factors. Reported are the total live triggerable beam and the relevant corrections used for cross section normalization. Also reported is the number of target nucleons per atomic weight ($1/(\rho\ l\ N_0)$ of Expression (6.1)), evaluated for the combined $Cu + Be$ target (as if it was a complex nucleus).

6.3 Systematic Errors

The results presented in the next sections have only statistical errors quoted. In this section we will investigate the major sources of systematic error affecting our measurements.

The principal source of systematic error is the uncertainty on the p_T scale. A small error on the p_T measurement implies large uncertainties in the overall normalization of the π^0 inclusive cross section because of the steepness of the π^0 p_T spectrum.

In Chapter 1 we presented phenomenological parametrizations of π^0 inclusive cross sections obtained from previous experiments. Similarly, we can fit our π^0

		Negative		Positive	
$\frac{1}{\rho l N_0}\left(\frac{mol\,cm^2}{g}\right)$		0.188×10^{-24}		0.188×10^{-24}	
B	Live Triggerable beam	10.2×10^{10}		6.4×10^{10}	
$N(p_T)^{\ddagger}$	Double Beam Occupancy	0.98		0.98	
	Tagged Incident Minority Particles	K^- fraction†	1.010 1.015 1.014 1.009	π^+ fraction	1.062
	Absorption Upstream of Target	(incident π^-)	1.010	(incident p)	1.014
		(incident K^-)	1.008	(incident π^+)	1.010
	Energy Asymmetry < 0.75		1.333		1.333
	Veto Wall and Uncorrelated Energy		1.176		1.176
	Photon Conversion Downstream of the Target		1.069		1.069
	π^0 Mass Cut ($0.11 < m_{\gamma\gamma} < 0.16\,GeV$)		1.040		1.040
	Acceptance and Efficiency	*function of position and p_T*			
	Target Absorption	*function of reconstructed vertex position*			
	Vertex Efficiency	*function of reconstructed vertex position*			

Table 6.1: Cross Section Normalization Factors.

† The different fractions correspond to different series of data runs, as described in Section 4.2.

‡ In this Table $N(p_T)$ is the uncorrected π^0 p_T distribution.

invariant cross section with a function of the form:

$$E\,\frac{d\sigma}{d^3p} = A\,\frac{(1-x_T)^m}{p_T^n} \tag{6.5}$$

(see Section 1.5). Using Function (6.5) we can estimate the error on the cross section caused by an uncertainty Δp_T on the measurement of p_T. We can rewrite the left hand side of Expression (6.5) as $d\sigma/(\pi dy dp_T^2)$, and calculate the relative error in the cross section:

$$\frac{\Delta(\frac{d\sigma}{dp_T^2})}{\frac{d\sigma}{dp_T^2}} = -\frac{2}{\sqrt{s}}\,[\frac{n}{x_T} + \frac{m}{(1-x_T)}]\,\Delta p_T \tag{6.6}$$

If we use the values of the parameters of the fit to WA70's π^0 inclusive data [29] ($\pi^- p \rightarrow \pi^0 X$), namely: $m = 3.82$, $n = 9.68$, then for π^0's p_T of $4.5\,GeV/c$, equivalent to $x_T = 0.29$ at our center-of-mass energy ($\sqrt{s} = 31.5\,GeV$), the relative error on the cross section (6.6) is roughly ten times the relative error on the p_T scale.

The error on the measurement of the photon transverse momentum is determined by the errors on the energy E and the angle θ between the direction of the photon and the beam axis. In fact, since $p_T = E\,sin\theta$, we have:

$$\frac{\Delta(p_T^2)}{p_T^2} = \frac{\Delta(E^2)}{E^2} + \frac{\Delta(sin\theta^2)}{sin\theta^2} \simeq \frac{\Delta(E^2)}{E^2} + \frac{\Delta(\theta^2)}{\theta^2} \tag{6.7}$$

In Section 3.2.3 the position resolution in the EMLAC was determined to be better than $1.0\,mm$. This implies that the inaccuracy on the value of p_T of the photon is mostly determined by the error on the shower energy.

An approximate estimate of the error on the π^0 energy scale can be derived from Expression (3.10) for the relative error on the π^0 mass. By using the approximation $(\frac{1+\cos\Theta}{1-\cos\Theta})\Delta\Theta^2 \simeq 4(\frac{\Delta\Theta}{\Theta})^2$, then, assuming $E_1 = E_2 = E$, Equation (3.10) becomes:

$$\frac{\Delta E}{E} = \sqrt{2}((\frac{\Delta m}{m})^2 + (\frac{\Delta\Theta}{\Theta})^2)^{1/2} \tag{6.8}$$

Therefore, if the percentage errors on the mass and opening angle Θ are comparable, for example 5%, then the percentage error on the energy is 10%.

We investigated energy-scale related effects using GEANT Monte Carlo events. From a sample of 400 reconstructed π^0s, generated at fixed values of p_T: 3.0, 5.0, and 7.0 GeV/c, with a rapidity distribution similar to the one obtained from data, we obtained the following results:

- The average value of the reconstructed π^0 mass was shifted by $-(5.5 \pm 0.4\%)$ relative to its nominal value.

- The average reconstructed p_T of the π^0 was shifted by $-(5.9 \pm 0.2\%)$ relative to the generated value.

- The reconstructed average opening angle between the photons from π^0 decay was shifted by only $(0.1 \pm 0.2\%)$ relative to the generated value.

In other words, the shift of the value of the reconstructed p_T is closely correlated with the shift of the mass. Rescaling of the photon energies to obtain correct π^0 mass, effectively reduces the uncertainty on the p_T scale and, consequently, the systematic error on the cross section.

Energy rescaling was done independently in each octant of the EMLAC by adjusting the π^0 mass to its nominal value using data from a selected subset of best quality runs. Furthermore, the remaining radial dependence of the π^0 mass (see Fig. 4.9) was parametrized using a p_T dependent linear function of the r-coordinate in the EMLAC. Residual variations in the observed η/π^0 mass were found to be of the order of 0.5% of the accepted value (4.066).

Residual effects after energy rescaling were investigated and the following percentage errors were included in the systematic uncertainties:

- The average π^0 mass fluctuated by a remaining 0.4% around the nominal value. Figure 6.2 shows the average values of the π^0 mass determined in each of the EMLAC octants. (At low p_T, the systematic uncertainty on the value of the mass was less than 0.3%.)

- Residual variations of the average π^0 mass with the radial distance in the detector were measured to be of the order of 0.5% at low p_T. For p_T above $4.5\,GeV/c$ the residual mass fluctuations were of the order of 0.6%. Figure 6.3 is a plot of the average π^0 mass as a function of the radius, in the

p_T range from $3.5\,GeV/c$ to $4.25\,GeV/c$, where larger mass fluctuations were previously observed.

- After energy rescaling, variations of the average π^0 mass with p_T were less than 0.1%. Figure 6.4 shows the average π^0 mass as a function of p_T of the π^0.

Some of the above variables are strongly correlated, therefore the systematic uncertainties on their values cannot simply be added in quadrature. From such considerations, we estimated a systematic error on the π^0 cross section from uncertainties on the energy scale to be $\sim 9.3\%$ for $p_T < 4.0\,GeV/c$, and $\sim 10\%$ for $p_T > 4.5\,GeV/c$. Other effects were also considered in the estimate of the overall systematic errors, these are discussed below.

The number of π^0 events versus octant improved after energy rescaling. Variations in the yield of π^0 events were on average $\sim 22\%$ before energy rescaling and decreased to $\sim 8\%$ after π^0 mass rescaling (see Fig. 6.5. Octant 5 and 8 experienced some hardware failures which were corrected for in this analysis).

Any misalignment of the LAC with respect to the chosen coordinate system has direct impact on the correct calculation of the produced p_T value of any shower. Best alignment minimizes the error on p_T. This is demonstrated in Fig. 6.6, where the p_T distributions of reconstructed π^0s, obtained from GEANT-generated π^0s with a fixed p_T $(4.5\,GeV/c)$, were artificially offset by $0.5\,cm$ in y at the position

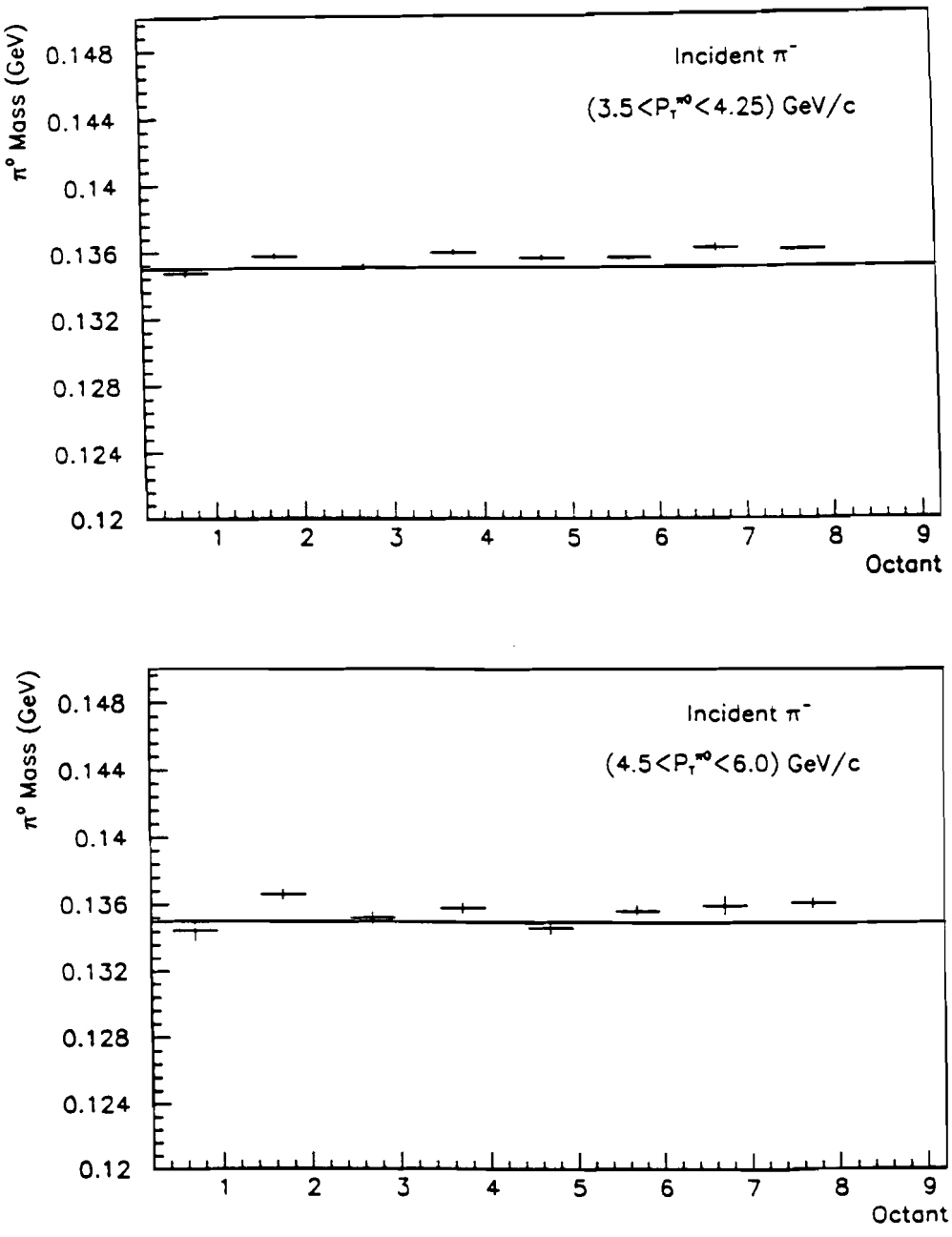

Figure 6.2: Average π^0 mass in each octant calculated after energy rescaling as a function of the EMLAC octants, both at low and high p_T.

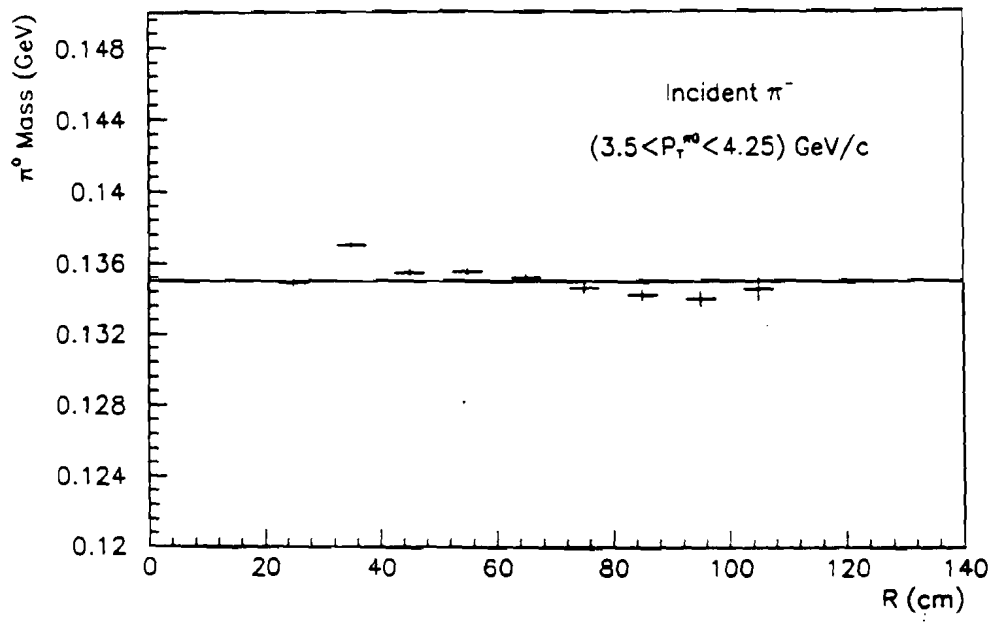

Figure 6.3: Average π^0 mass as a function of the EMLAC radial coordinate in the p_T range from 3.5 GeV/c to 4.25 GeV/c, calculated after energy rescaling.

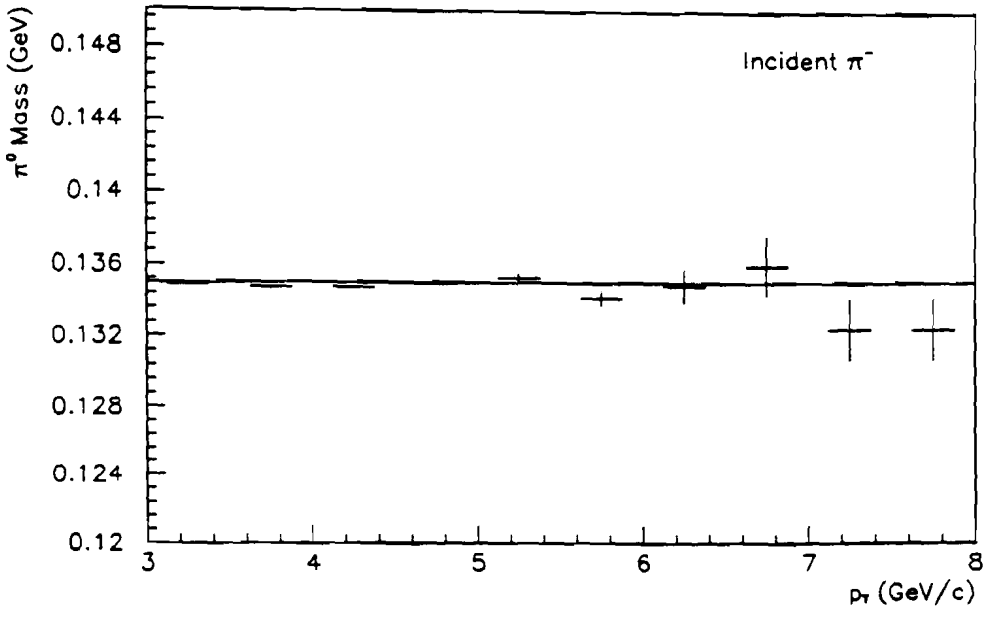

Figure 6.4: Average π^0 mass as a function of p_T of the π^0, calculated after energy rescaling.

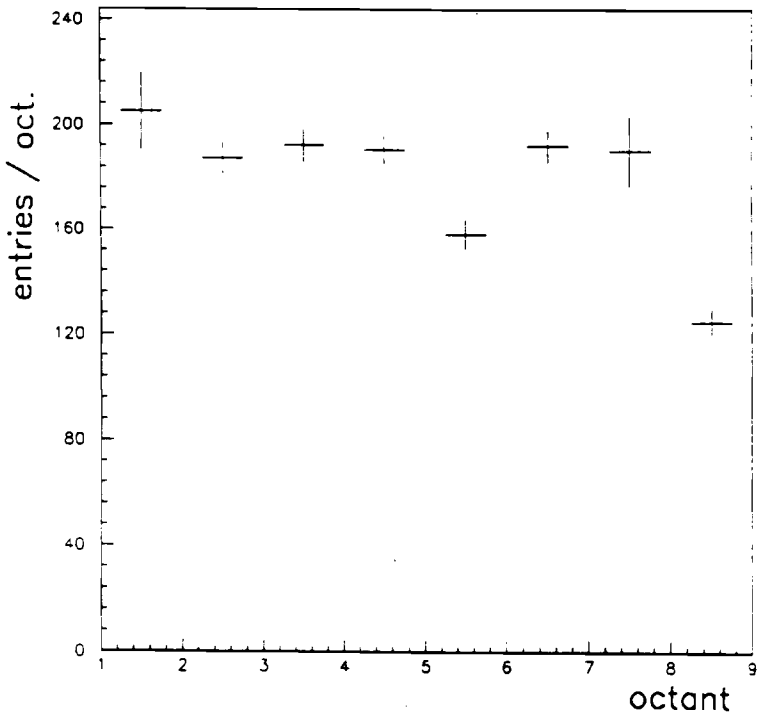

Figure 6.5: Number of π^0 events per octant.

of the LAC. Standard alignments were used to generate Fig. 6.6(a). The clear broadening of the distribution in Fig. 6.6(b) is due to misalignment. In fact, the relative error on p_T caused by an offset Δy due to misalignment is proportional to $y\,\Delta y/r^2$, where r is the radial position of the particle at the EMLAC. For example, if the position of the particle at the EMLAC is along the vertical y plane (i.e., p_T is mostly p_y), and r is small (say $25\,cm$), then $\Delta y = 0.5\,cm$ contributes as much as 2% to $\Delta p_T/p_T$. As already mentioned, the offset Δy causes a broadening of the p_T distribution rather than a shift of the mean.

To estimate the impact of any misalignment on the calculated p_T of the particle, we generated 50,000 π^0s with a p_T spectrum reproducing the p_T distribution of the data. An artificial $\Delta y = 0.5\,cm$ offset was added to the y position of the

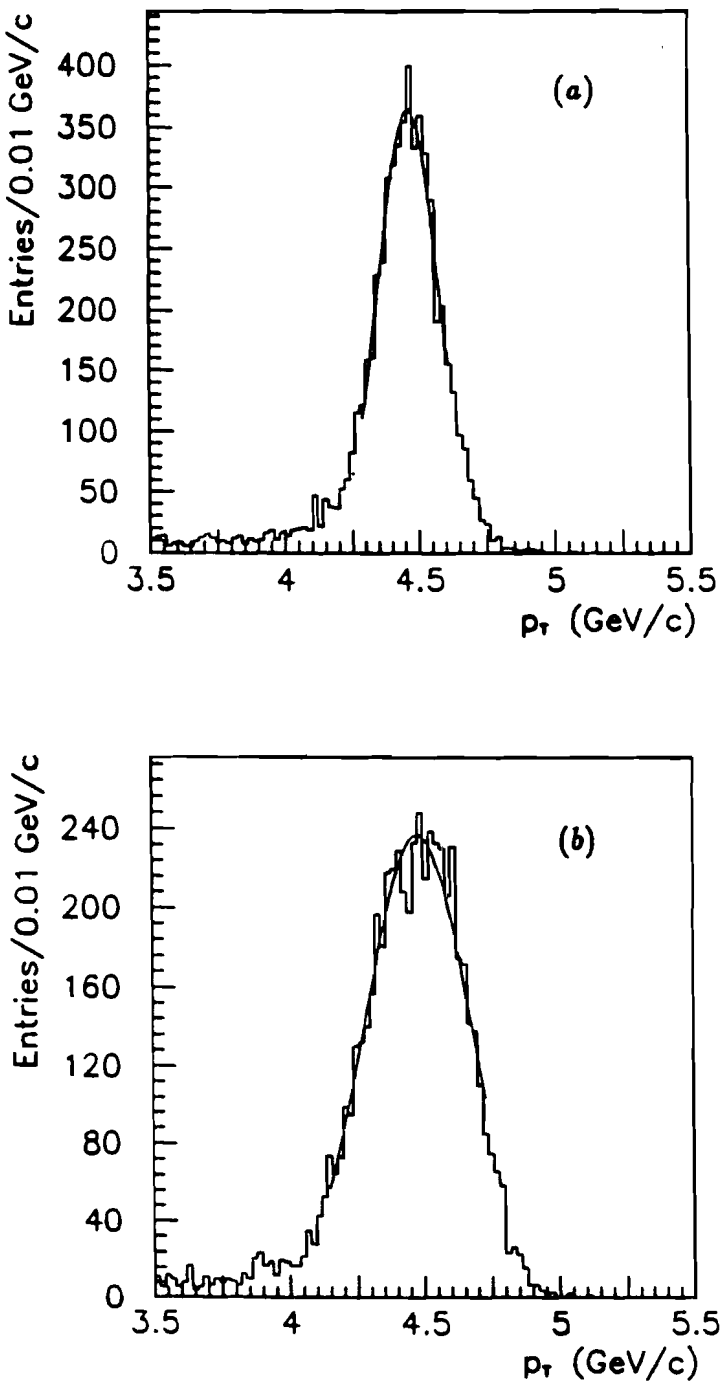

Figure 6.6: Reconstructed π^0 p_T distributions for Monte Carlo generated π^0s with $p_T = 4.5\,GeV/c$; (a) using the standard set of alignement constants, (b) adding an artificial offset of $0.5\,cm$ to the y coordinates of the shower positions at the LAC.

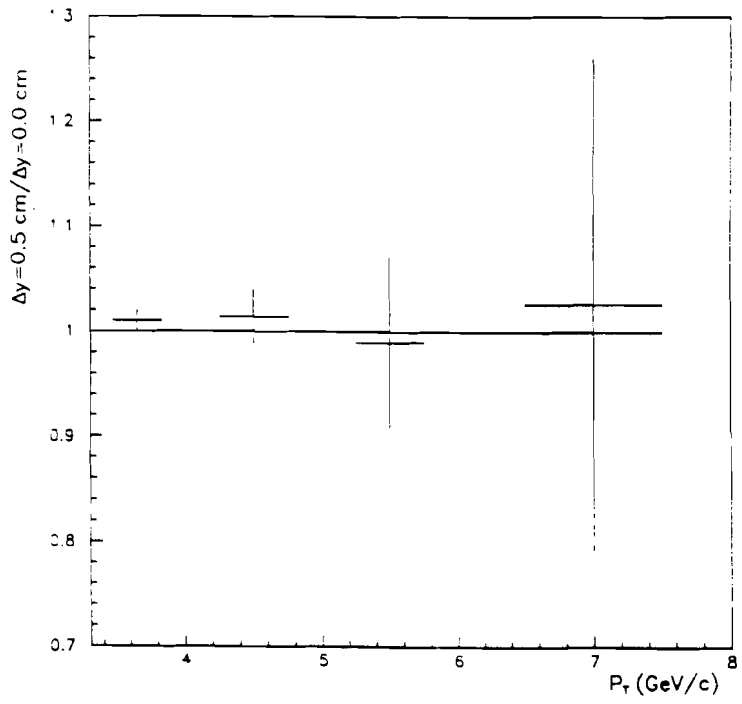

Figure 6.7: Ratio of Monte Carlo generated π^0 p_T distributions as a function of p_T without and with a $\Delta y = 0.5\,cm$ offset added to the y coordinate of the reconstructed π^0 position.

π^0s, and the new p_T distribution recalculated. The ratio between the two p_T distributions as a function of p_T is shown in Fig. 6.7. The systematic error was calculated to be $\sim 0.26\%$. Misalignment of the EMLAC quadrants were corrected during event reconstruction and the residual offsets were estimated to be negligible. We conclude that systematic effects associated with detector misalignment are negligible.

The live triggerable beam used in the cross section normalization is affected by a systematic error reflecting the uncertainty in the measurement of the beam flux. The error on the beam count is due to the inefficiency of the beam-defining hodoscope, and to any problems with beam-scaler units. The efficiency of the

beam counters was estimated to be $\sim$ 99%. The beam counts were recorded independently on two scalers, which agreed to within 0.006%.

The major source of uncertainty on the beam normalization was caused by underestimation of total beam count due to the fact that the last part of the beam spill, at the end of each data run was not recorded. A correction of the order of 2% was applied to the total beam to account for this error caused by the data acquisition system. The remnant systematic error due to this effect was less than 0.2%.

The determination of the beam composition is affected by systematic error due to variations in the characteristics of the beam tune (position of the collimators, momentum bite). These variations affect the correct determination of the relative beam-particle percentages. From Monte Carlo studies [57], we determined that variations of the positive beam momentum bite ($1.8\% < \frac{\Delta p}{p} < 2.5\%$) produce a systematic uncertainty on the fraction of π^+s of the order of 6%, whereas for protons the systematic uncertainty is $\sim$ 0.5%. For negative beam, the variations of the momentum bite were not important because all collimators were wide open. Therefore, systematic uncertainties for negative-beam particles percentages due to the above effects were judged to be less than 1%. Also, beam contamination caused by untagged minority beam-particles introduce systematic uncertainties in the calculated percentages of different particles in the beam. Based on the results presented in Chapter 4, after correcting for known contamination levels, we quote

a residual systematic error on K^- flux due to π^- mistagged as $K^- \leq 1.0\%$, a systematic uncertainty on the π^- identification probability due to untagged K^- of the order of $\pm 1.0\%$, a systematic error on π^+ flux due to K^+ mistagged as π^+ equal to $8 \pm 3\%$ (K^+ were not separated from π^+s), and on protons due to untagged π^+ of about 3%.

The efficiency of the *SINGLE LOCAL HIGH* p_T trigger was modeled on the assumption that the *LAC PRETRIGGER* was 100% efficient (the *PRETRIGGER* decision was based on a global p_T deposition in an octant). If this is not, in fact, the case, our measured cross sections would be underestimated. Estimates of the *PRETRIGGER* efficiency are currently under study.

The reconstruction efficiency was calculated with Monte Carlo generated single π^0s. The data have photon multiplicities higher than just the two photons from the decay of the detected π^0. In such environments the chances of misreconstructing the π^0 become larger. From Monte Carlo studies we estimated a 2% systematic error on the cross section due to the systematic uncertainties on the π^0 reconstruction efficiency.

Different sets of data, recorded at different times, with slightly different experimental setups, may cause variations of cross sections beyond statistical uncertainties. We studied the distributions in the deviation of cross section for individual runs from the mean cross section (the difference divided by the mean). One such distribution is shown in Fig. 6.8. The standard deviation of the distribution is

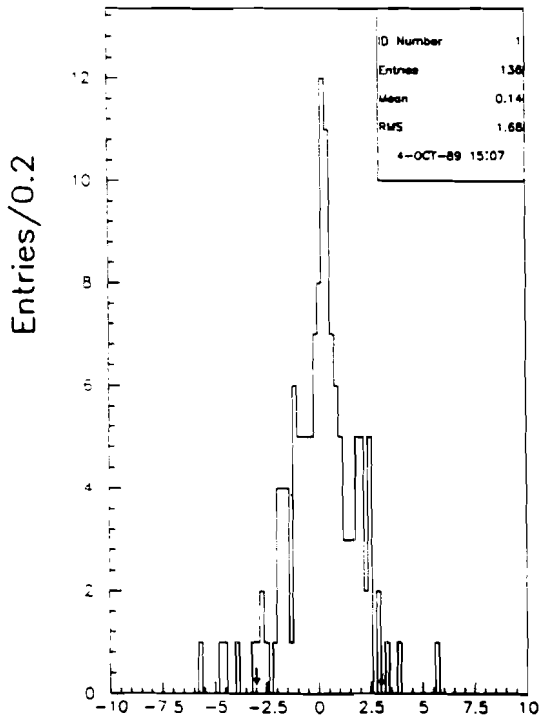

Figure 6.8: Systematic deviation of the π^0 cross section from the mean calculated for a subset of data-runs.

$\sim$ 1.7. If only statistical fluctuations were affecting our measurement, then the standard deviation of the distribution would have been equal to unity. Assuming the distributions to be gaussian, and given a statistical uncertainty (σ_{stat}) varying from 12.5 to 14.2%, then our estimate of the systematic error (σ_{sys}) on the cross section due to run-to-run variations is:

$$\sigma_{sys} = \sqrt{(1.7\,\sigma_{stat})^2 - (\sigma_{stat})^2} \simeq (17.2 - 19.5)\% \qquad (6.9)$$

We consider this range of values to be conservative upper limits. If gaussian statistics can indeed be applied, then we should divide the above limits by the square root of the number of runs included in the distribution of the type shown in Fig. 6.8. Table 6.2 is a summary of all the known systematic errors affecting

KNOWN SOURCES OF SYSTEMATICS	SYSTEMATIC UNCERTAINTY ON $E\frac{d^3\sigma}{d^3p}$			
	$p_T < 4.0$		$p_T > 4.5$	
• ENERGY SCALE				
π^0 mass *octant dependence*	±3.0%		±5.6%	
radial dependence	−7.0%		−8.5%	
p_T *dependence*	±1.4%		±1.4%	
η/π^0 mass	−(5.4 ± 0.2)%		+(0.60 ± 0.03)%	
• ABSOLUTE NORMALIZATION				
Particle Identification	±1.0%(π^-)	±1.0%(K^-)	±0.5%	±6.0%
Missing Beam Spill	±0.2%			
π^0 Event Count	±8.0%			
• SOFTWARE EFFICIENCIES				
π^0 Reconstruction Efficiency	±2.0%			
• RUN-TO-RUN VARIATIONS	±(17.2 − 19.5)%			
• BACKGROUND				
Beam Contamination	±1.0% (π^-)	±1.0% (K^-)	3.0% (p)	8.0% (π^+)
	$\pi^- \rightarrow \pi^0$	$K^- \rightarrow \pi^0$	$p \rightarrow \pi^0$	$\pi^+ \rightarrow \pi^0$
SUM IN QUADRATURE	(21.5 − 23.4)%	(21.5 − 23.4)%	(21.7 − 23.5)%	(23.5 − 25.5)%

Table 6.2: Estimates of systematic errors affecting π^0 cross sections.

our measurement of the π^0 cross section.

6.4 Inclusive Cross Section

The expression for the double differential cross section per nucleon as a function of the transverse momentum p_T and center-of-mass rapidity y, was given in Section 6.1. Using Expression (6.1) we calculated the invariant cross section for inclusive π^0 production as a function of p_T, averaged over different center-of-mass rapidity ranges, for both negative and positive beam data and both majority and minority beam-particles incident on a combined $Cu + Be$ target.

Data recorded with different p_T trigger thresholds were combined by normalizing each individual p_T distribution to the appropriate live triggerable beam count. In particular, for the data analyzed in this thesis, the negative-beam data included runs with three different p_T trigger thresholds: 3.0, 4.25, and 4.5 GeV/c, while for the positive-beam data all runs were recorded with a p_T trigger threshold set at 4.25 GeV/c.

Since one of the goals of this thesis is to compare π^0 production yields with different beam-particles (π, K, p), we decided to measure cross sections on a combined nuclear target (Cu and Be), so as to obtain a larger data sample. (Data on Cu target represent $\sim$ 19% for positive beam (set C) and $\sim$ 17% for negative beam (set A only) of the entire $Cu + Be$ target data sample.) If pion production at large p_T is charge independent, then the average of π^+ and π^- yields at large transverse momenta in proton [12] and negative pion [13] collisions should provide

the nuclear dependence of π^0 production. Using available data for $p_T > 3.5\,GeV/c$, the expected power α of the A dependence (A^α) is ~ 1.13 for incident protons, and ~ 1.1 for incident π^-. The ratio of the π^0 yields expected for Be target to $(Cu + Be)$ combined target data is ~ 1.19 for $\alpha = 1$; and it is ~ 1.16 for $\alpha = 1.1$ (incident π^-), and ~ 1.15 for $\alpha = 1.13$ (incident p). Therefore, we conclude that, for the configuration of our target, the nuclear A dependence of the ratio of π^0 invariant cross sections is rather weak, and therefore the use of all data on the combined target is reasonable.

In Tables 6.3, 6.4, and 6.5 we report the invariant cross sections for π^0 production for $530\,GeV/c$ ($\sqrt{s} = 31.5$) π^-, p and π^+ incident on $Cu + Be$, averaged over the indicated p_T bins and center-of-mass rapidity intervals. Figures 6.9, 6.10 and 6.11 show the π^0 cross section versus p_T in the indicated rapidity ranges for π^- beam data. Because of trigger inefficiencies at low p_T in the outer regions of the detector, we imposed a cutoff at $p_T = 4\,GeV/c$ to cross sections in the backward rapidity regions (Figs. 6.9, 6.10). In the forward rapidity region (Fig. 6.11) the cutoff is lowered to $p_T = 3.5\,GeV/c$.

Figures 6.12 through 6.17 show the π^0 cross section versus p_T, in the indicated rapidity ranges, for $530\,GeV/c$ incident protons and π^+. For completeness, Figs. 6.18 and 6.19 show the ratio between π^0 invariant cross sections on Be and $Cu+Be$ as a function of p_T for incident π^- and protons, averaged over the rapidity range $-0.7 < y < 0.7$. The results of these figures confirm the weak A dependence

Table 6.3: $\pi^- \; Cu/Be \; \rightarrow \pi^0 X$ invariant cross section at $\sqrt{s} = 31.5\,GeV$, as a function of p_T.

p_T (GeV/c) min	p_T (GeV/c) max	$< p_T >$ (GeV/c)	$-0.7 < y < 0.2$ $(pb\,GeV^{-2}/Nucleon)$	$< p_T >$ (GeV/c)	$0.2 < y < 0.7$ $(pb\,GeV^{-2}/Nucleon)$
3.15	3.25	–	–	3.20	72891.6 ± 2240.8
3.25	3.35	–	–	3.30	50792.1 ± 1690.2
3.35	3.45	–	–	3.40	40704.0 ± 1450.1
3.45	3.55	–	–	3.50	29609.6 ± 1166.4
3.55	3.65	–	–	3.60	23417.3 ± 969.9
3.65	3.75	–	–	3.70	16458.8 ± 796.7
3.75	3.85	–	–	3.80	11736.1 ± 644.2
3.85	3.95	–	–	3.90	9520.0 ± 586.1
3.95	4.05	–	–	4.00	7307.2 ± 498.5
4.05	4.25	4.14	4130.6 ± 182.2	4.15	4782.9 ± 276.1
4.25	4.50	4.36	2249.3 ± 76.9	4.36	2819.9 ± 117.1
4.50	4.75	4.61	1094.2 ± 44.3	4.61	1342.4 ± 66.1
4.75	5.00	4.86	594.7 ± 29.2	4.86	790.7 ± 47.3
5.00	5.50	5.19	294.4 ± 13.6	5.20	321.5 ± 19.8
5.50	6.00	5.72	80.2 ± 6.7	5.71	109.5 ± 10.7
6.00	7.00	6.34	13.9 ± 1.8	6.31	11.5 ± 2.5
7.00	8.00	7.32	2.3 ± 0.7	7.37	2.5 ± 1.0
8.00	10.00	8.46	0.23 ± 0.15	8.49	0.18 ± 0.18

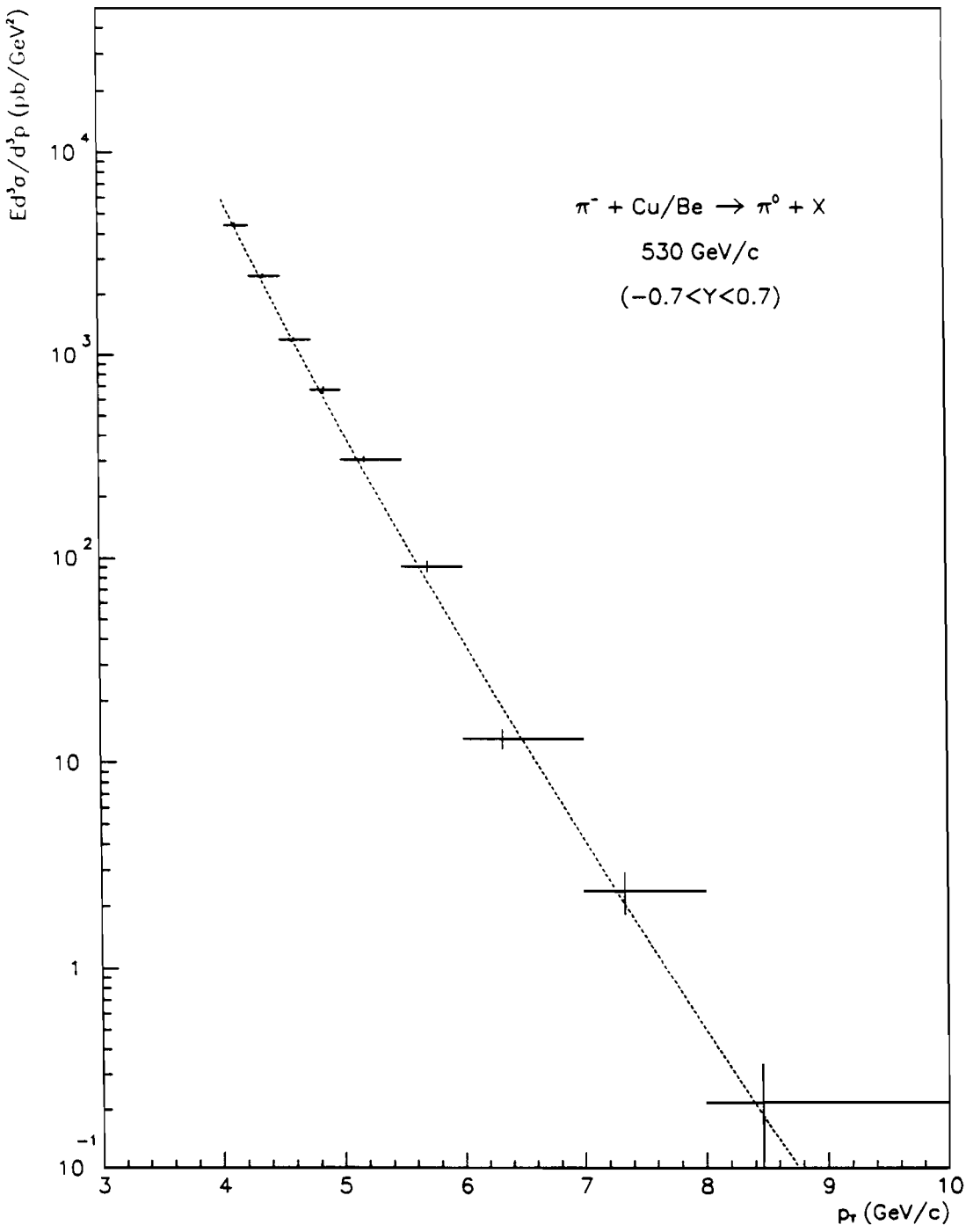

Figure 6.9: π^0 invariant cross section for 530 GeV/c incident π^- as a function of p_T in the rapidity range $-0.7 < y < 0.7$.

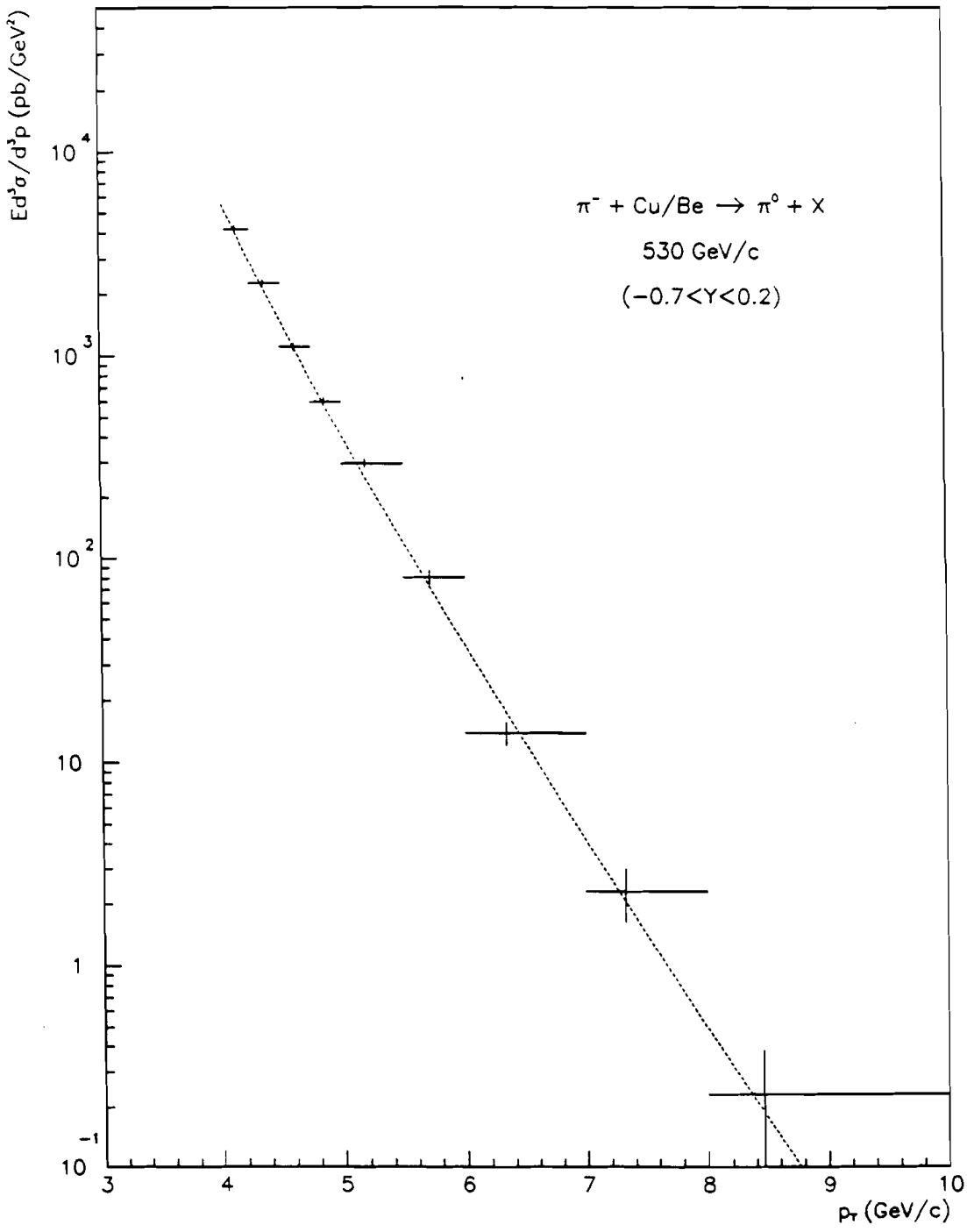

Figure 6.10: π^0 invariant cross section for 530 GeV/c incident π^- as a function of p_T in the rapidity range $-0.7 < y < 0.2$.

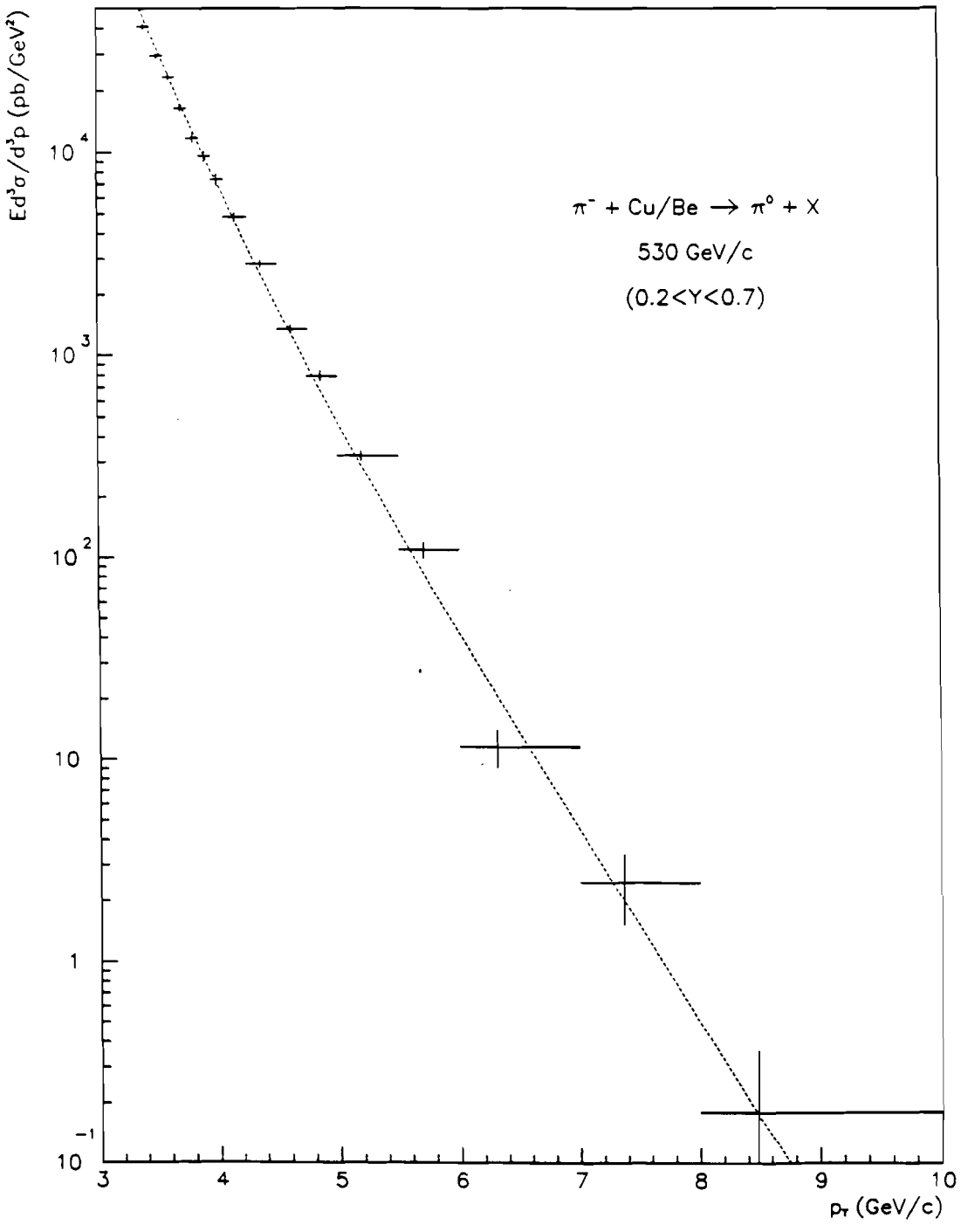

Figure 6.11: π^0 invariant cross section for 530 GeV/c incident π^- as a function of p_T in the rapidity range $0.2 < y < 0.7$.

Table 6.4: $p\ Cu/Be \rightarrow \pi^0 X$ invariant cross section at $\sqrt{s} = 31.5\,GeV$, as a function of p_T.

p_T (GeV/c) min	max	$< p_T >$ (GeV/c)	$-0.7 < y < -0.2$ $(pb\,GeV^{-2}/Nucleon)$	$< p_T >$ (GeV/c)	$-0.2 < y < 0.2$ $(pb\,GeV^{-2}/Nucleon)$	$< p_T >$ (GeV/c)	$0.2 < y < 0.7$ $(pb\,GeV^{-2}/Nucleon)$
4.25	4.35	4.30	1732.4 ± 161.7	4.30	2820.9 ± 197.4	4.30	2104.3 ± 157.2
4.35	4.45	4.40	1317.7 ± 128.8	4.40	1886.6 ± 155.5	4.40	1529.0 ± 126.8
4.45	4.60	4.52	990.4 ± 92.6	4.52	1297.0 ± 104.3	4.52	1226.8 ± 91.7
4.60	4.75	4.68	725.3 ± 69.8	4.66	875.4 ± 83.8	4.66	885.0 ± 74.4
4.75	4.90	4.82	532.5 ± 60.0	4.82	636.8 ± 68.2	4.82	463.5 ± 53.2
4.90	5.05	4.96	337.1 ± 45.6	4.98	430.0 ± 56.5	4.96	276.9 ± 42.3
5.05	5.25	5.13	213.9 ± 29.9	5.14	277.5 ± 39.0	5.14	162.7 ± 25.6
5.25	5.50	5.37	67.6 ± 14.2	5.37	155.3 ± 24.5	5.37	133.3 ± 21.3
5.50	6.00	5.71	37.7 ± 7.2	5.69	89.5 ± 13.1	5.66	34.0 ± 8.0
6.00	7.00	6.34	11.8 ± 2.9	6.28	11.9 ± 3.3	6.32	12.0 ± 2.9
7.00	8.00	–	–	7.48	2.0 ± 1.2	–	–

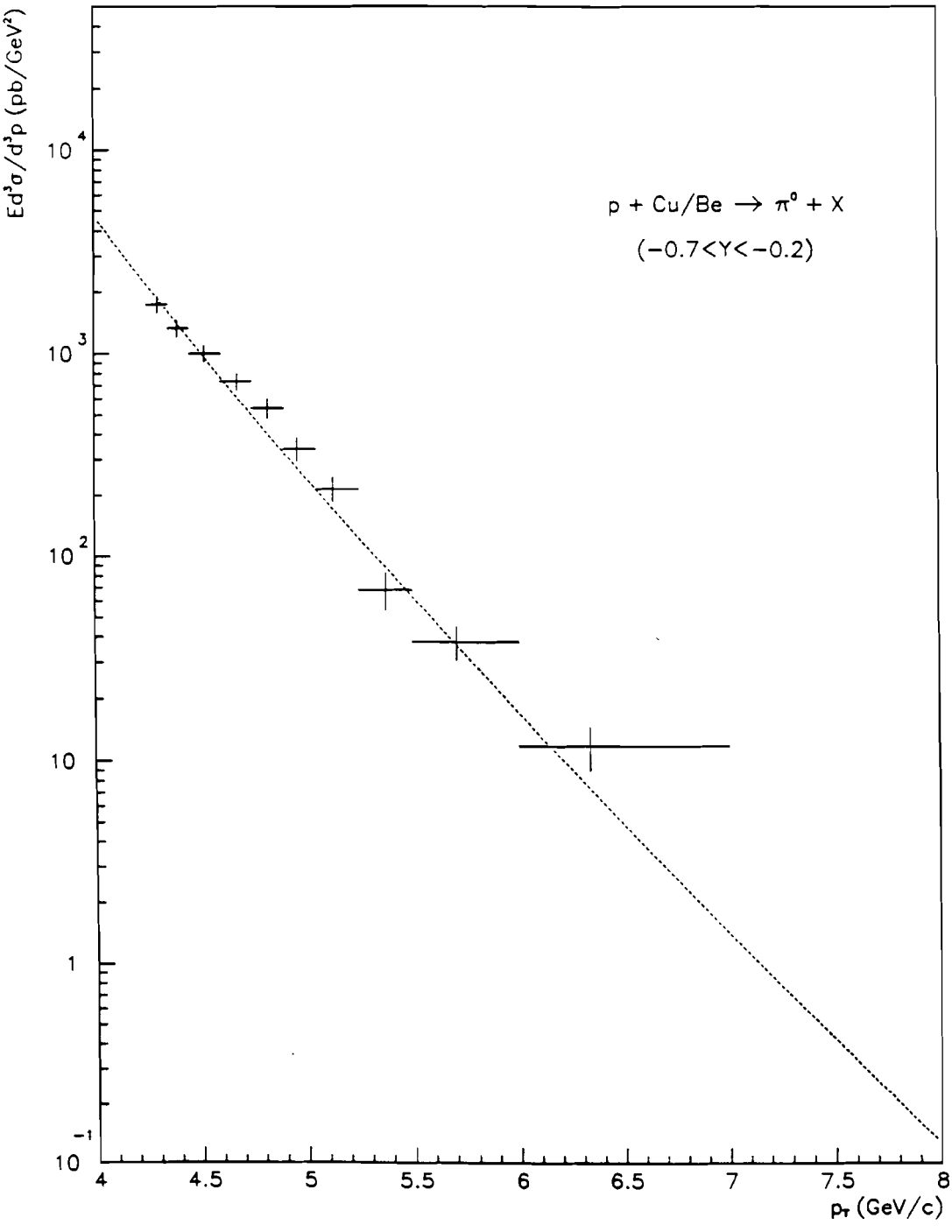

Figure 6.12: π^0 invariant cross section for 530 GeV/c incident p as a function of p_T in the rapidity range $-0.7 < y < -0.2$.

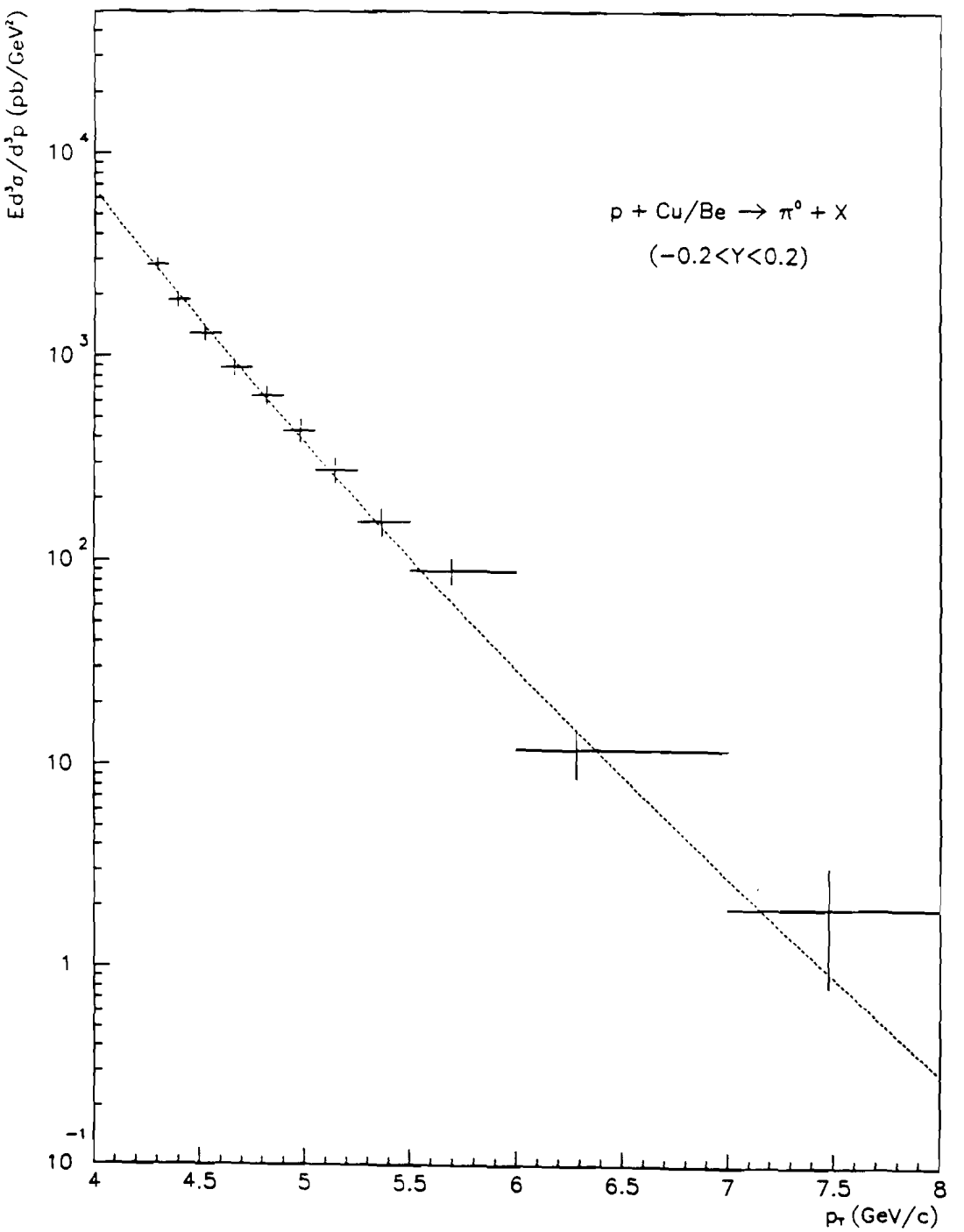

Figure 6.13: π^0 invariant cross section for 530 GeV/c incident p as a function of p_T in the rapidity range $-0.2 < y < 0.2$.

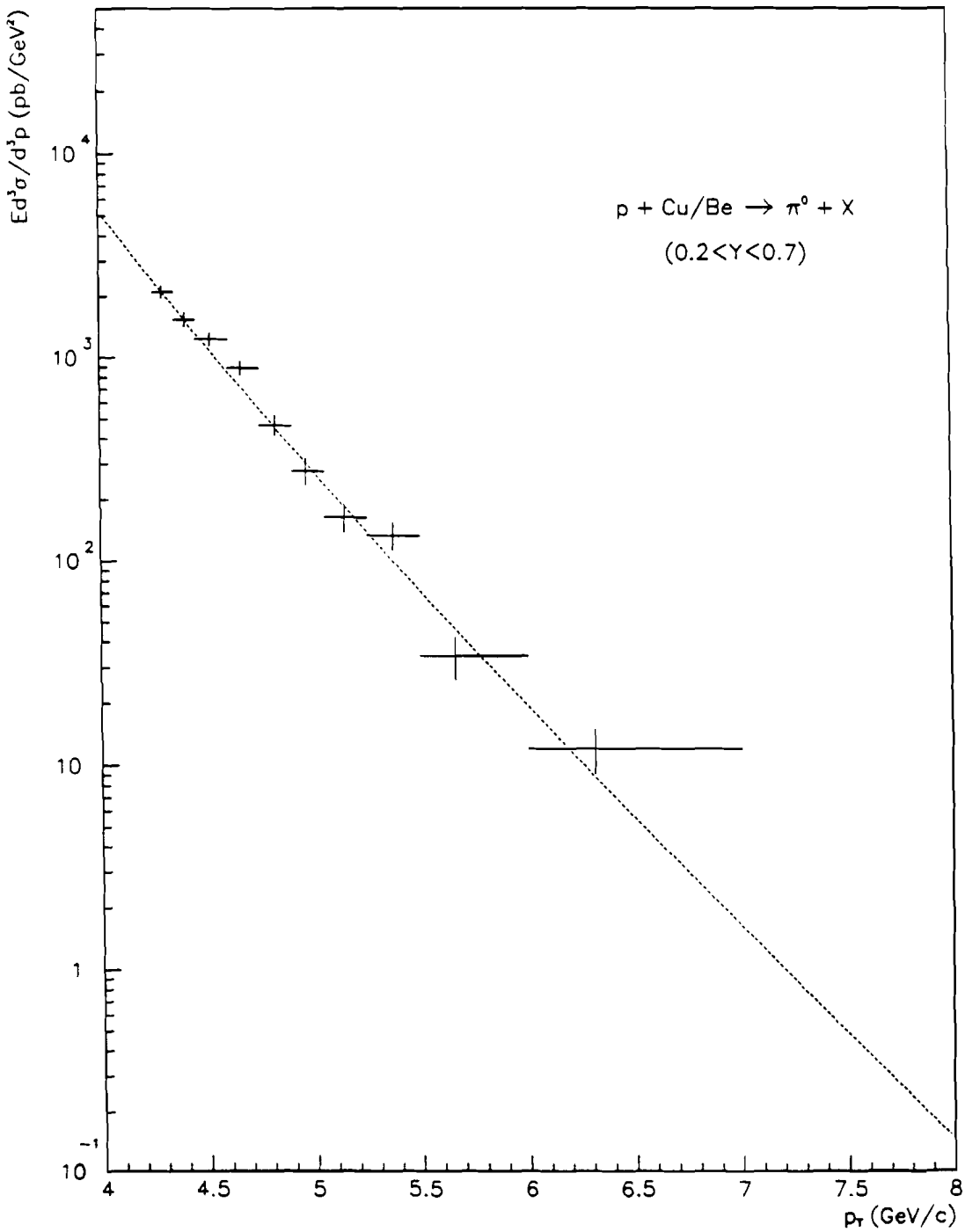

Figure 6.14: π^0 invariant cross section for 530 GeV/c incident p as a function of p_T in the rapidity range $0.2 < y < 0.7$.

Table 6.5: $\pi^+ \; Cu/Be \; \rightarrow \pi^0 X$ invariant cross section at $\sqrt{s} = 31.5\, GeV$, as a function of p_T.

p_T (GeV/c) min	max	$< p_T >$ (GeV/c)	$-0.7 < y < -0.2$ $(pb\, GeV^{-2}/Nucleon)$	$< p_T >$ (GeV/c)	$-0.2 < y < 0.2$ $(pb\, GeV^{-2}/Nucleon)$	$< p_T >$ (GeV/c)	$0.2 < y < 0.7$ $(pb\, GeV^{-2}/Nucleon)$
4.25	4.50	4.35	1448.3 ± 326.3	4.37	2935.8 ± 497.8	4.35	2469.0 ± 414.7
4.50	4.75	4.62	706.0 ± 198.7	4.62	1281.2 ± 296.4	4.60	1183.0 ± 275.4
4.75	5.00	4.88	509.7 ± 165.2	4.83	951.4 ± 240.6	4.84	427.6 ± 173.8
5.00	5.50	5.16	219.3 ± 70.3	5.24	194.3 ± 83.9	5.28	362.2 ± 94.4
5.50	6.00	–	–	5.70	111.1 ± 55.6	5.75	66.5 ± 38.8
6.00	7.00	–	–	6.34	33.9 ± 19.7	–	–
7.00	8.00	–	–	–	–	7.48	7.3 ± 7.3

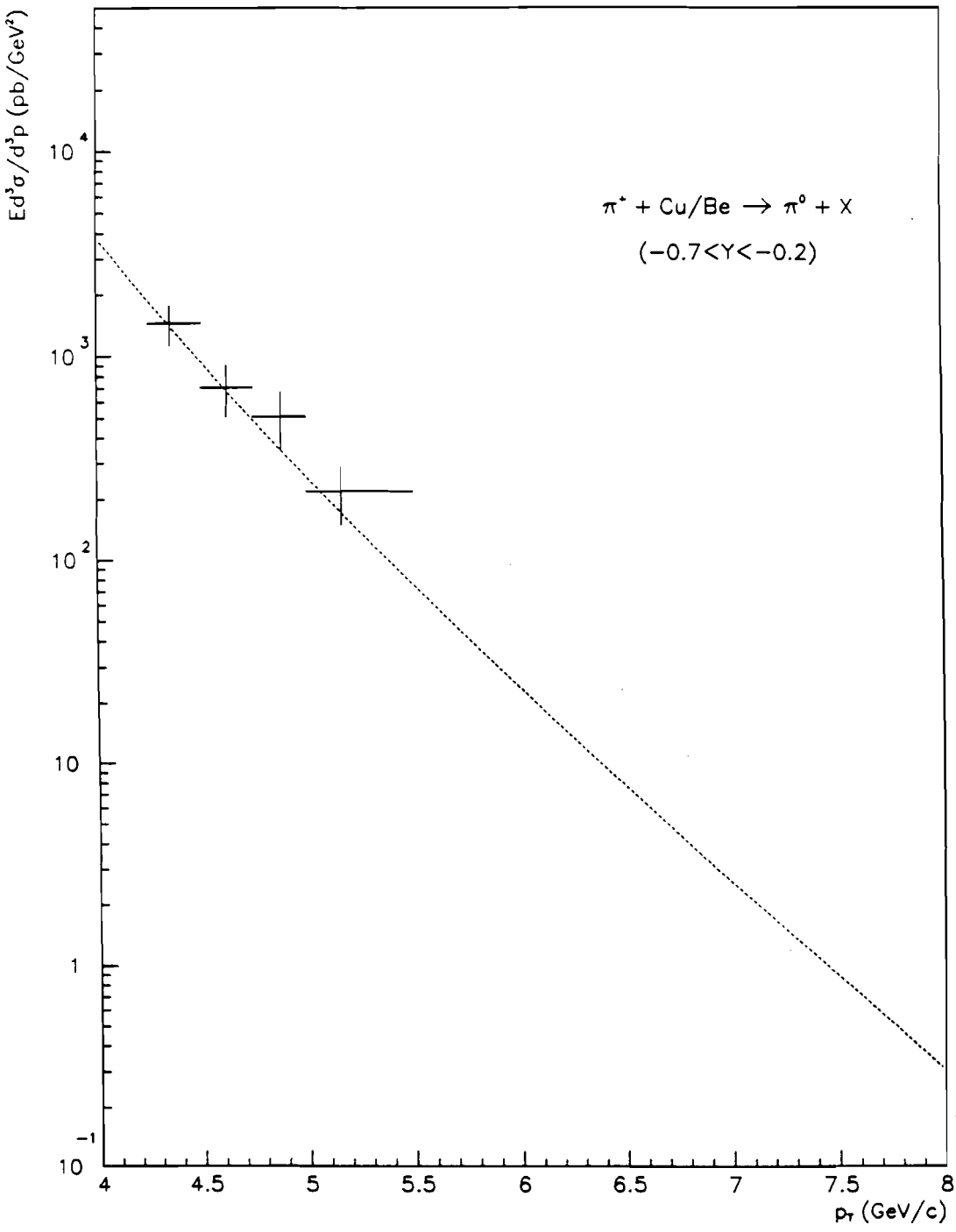

Figure 6.15: π^0 invariant cross section for $530\,GeV/c$ incident π^+ as a function of p_T in the rapidity range $-0.7 < y < -0.2$.

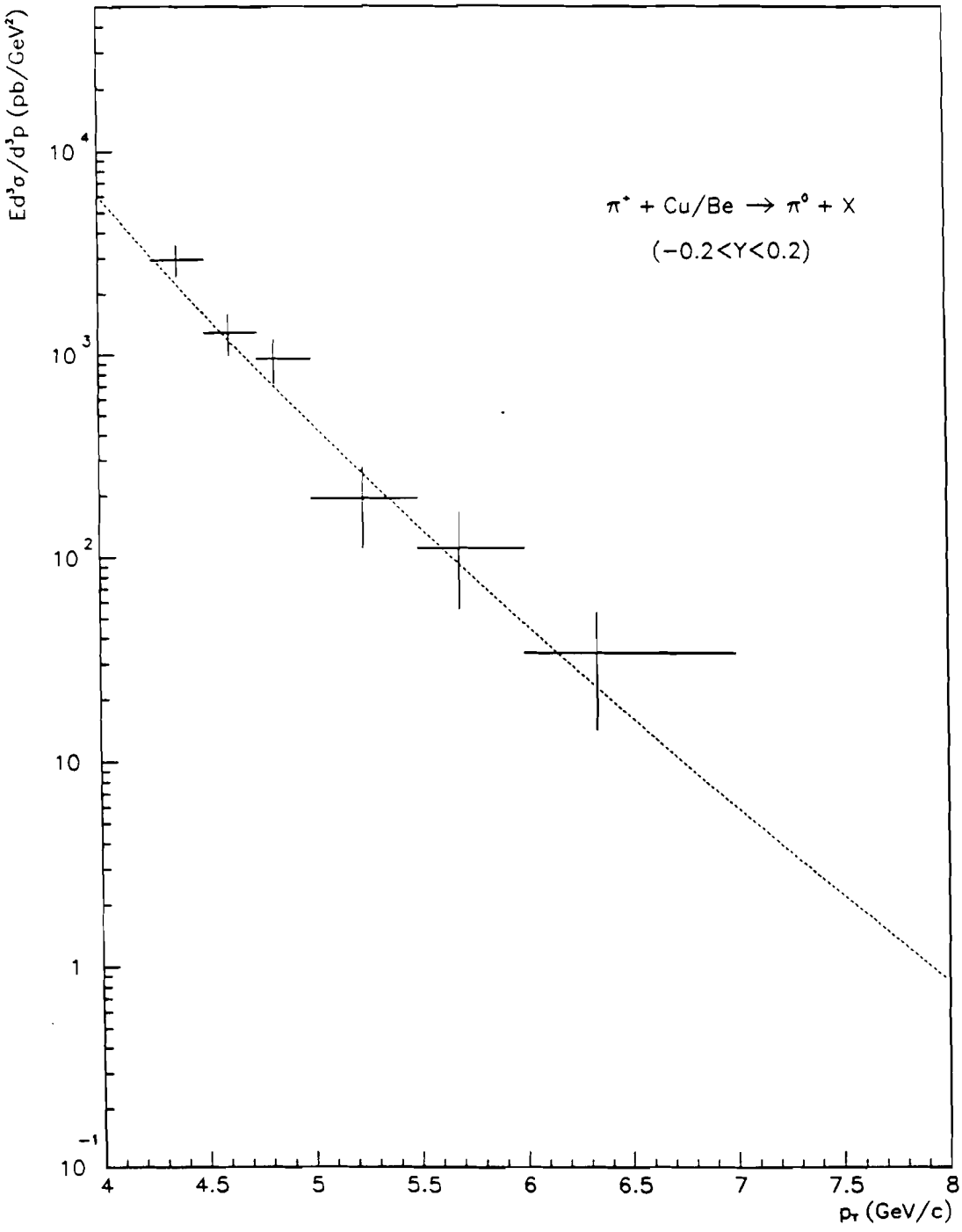

Figure 6.16: π^0 invariant cross section for 530 GeV/c incident π^+ as a function of p_T in the rapidity range $-0.2 < y < 0.2$.

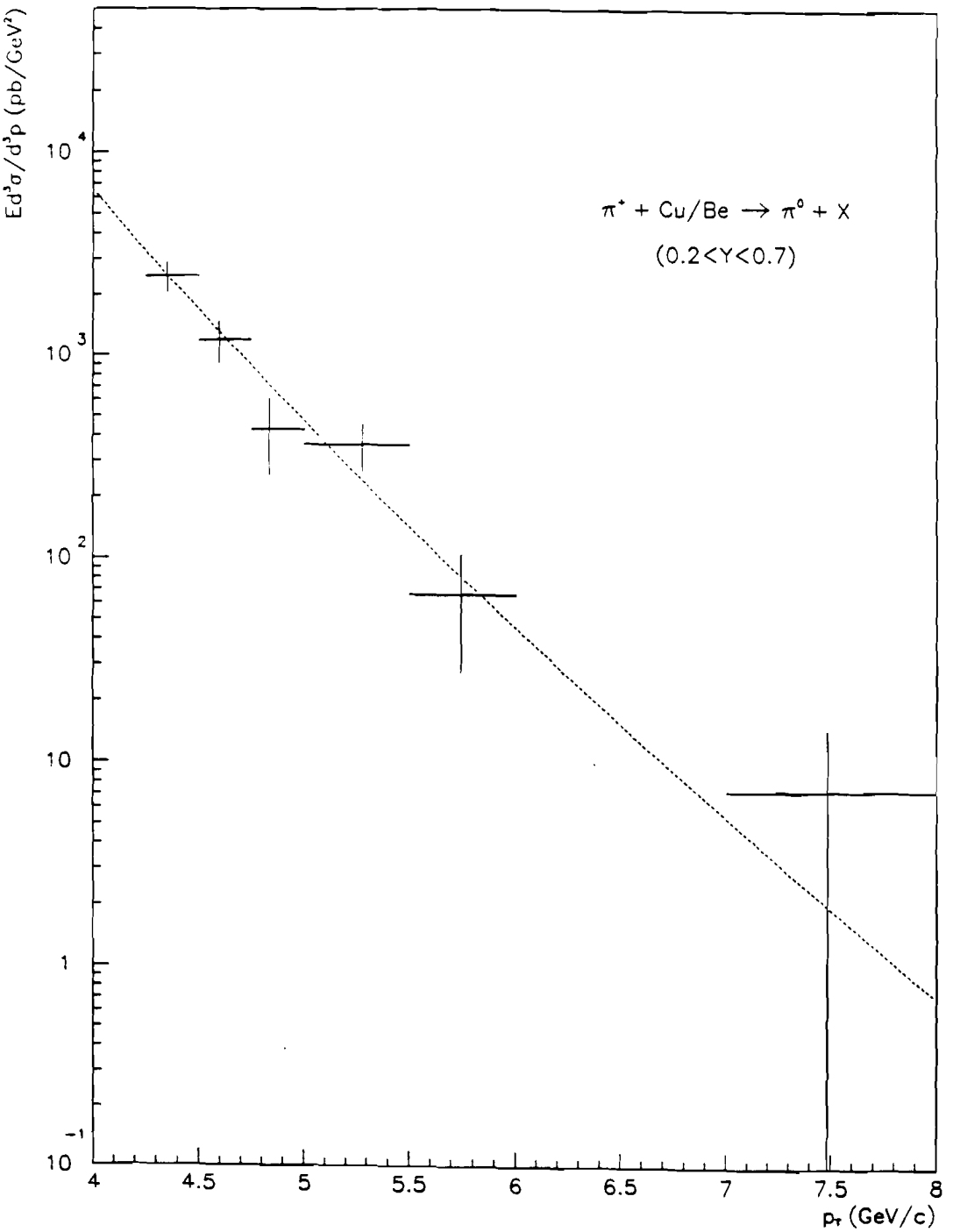

Figure 6.17: π^0 invariant cross section for 530 GeV/c incident π^+ as a function of p_T in the rapidity range $0.2 < y < 0.7$.

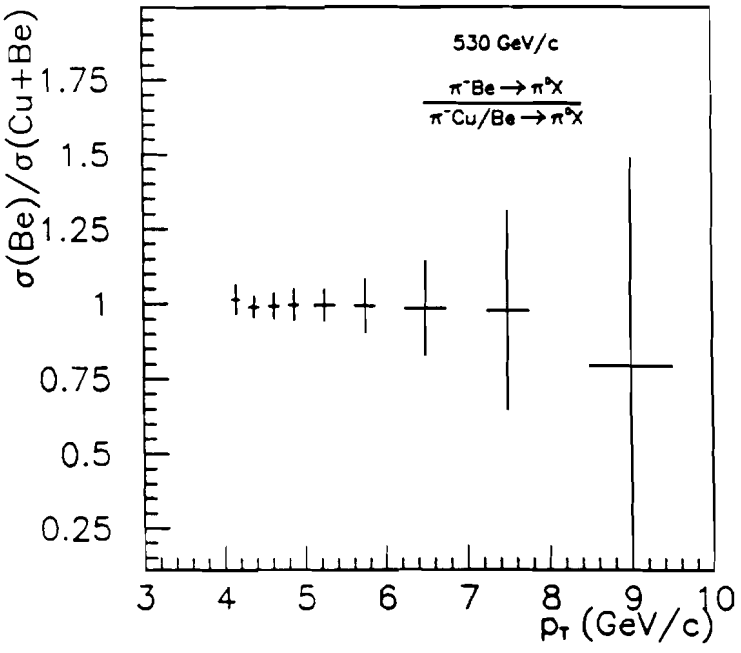

Figure 6.18: Ratio of π^0 invariant cross sections for $530\,GeV/c$ π^- incident on Be and $Cu + Be$ as a function of p_T.

anticipated above.

Experimental data for both beam types, for $p_T > 4.0\,GeV/c$ and $y > -0.7$, have been fitted using a parametrization of the form:

$$E\,\frac{d^3\sigma}{d^3p} = A\,\frac{(1 - x_D)^m}{p_T^n} \tag{6.10}$$

where x_D, already introduced in Chapter 1, is defined by:

$$x_D = \sqrt{x_T^2 + (x_F - x_0)^2}$$

We minimized a χ^2 distribution using data samples in a two-dimensional grid of 0.01 and $0.25\,GeV/c$ bin widths, for y and p_T respectively. The normalization factor A, and m, n, x_0 were free parameters. The resulting parameters of the fit are given in Table 6.6 for both negative and positive incident beams, and the fits

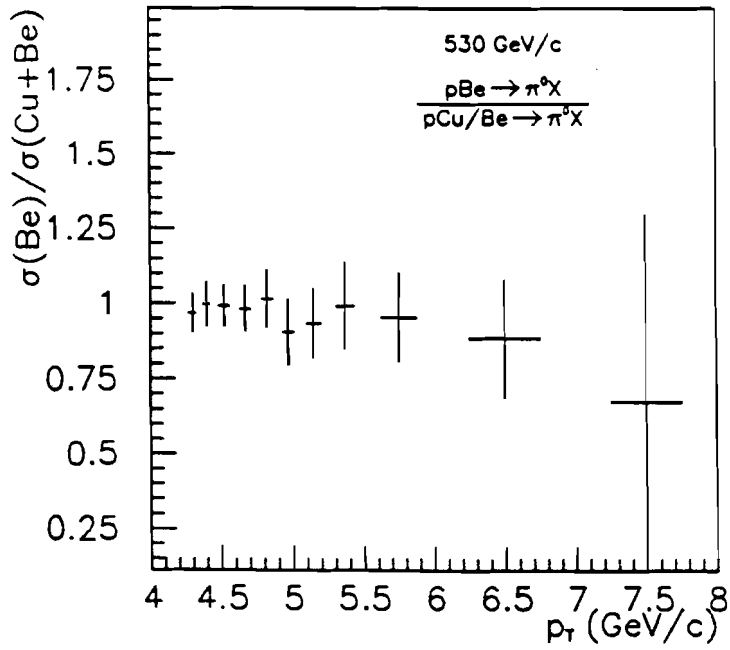

Figure 6.19: Ratio of π^0 invariant cross sections for 530 GeV/c p incident on Be and $Cu + Be$ as a function of p_T.

are superimposed on the data in Figs 6.9 through 6.17. All the parameters are strongly correlated. The fit takes into account only statistical errors.

The form of the parametrization function (6.10) characterizes the hard-scattering process both in terms of collisions among partons as well as of production of a final high-p_T hadron. The function $(1 - x_D)^m$ reflects the momentum distribution of partons inside the incident hadron (structure function). Large values of the power m suggest presence of soft-parton momentum contributions, and viceversa for small values of m. The variable x_D reflects the original x of the parton (see Chapter 1). The parameter x_0 characterizes the motion of the hadron-hadron center-of-mass system (symmetric for pN collisions, boosted forward for $\pi^{\pm}N$ collisions). Finally, the power function of p_T measures the hardness of the collision

Table 6.6: Parameters of the phenomenological fit to the π^0 cross sections.

Incident Particle	$A\ (mb/GeV^2)$	m	n	x_0	$\chi^2/d.o.f.$
π^-	17.22 ± 1.14	6.93 ± 0.18	9.07 ± 0.22	$(5.18 \pm 0.46) \times 10^{-2}$	197/136
π^+	16.04 ± 1.18	5.77 ± 0.22	9.36 ± 0.17	$(8.62 \pm 1.72) \times 10^{-2}$	40/65
p	46.90 ± 0.96	7.84 ± 0.56	9.71 ± 0.14	$(1.26 \pm 0.54) \times 10^{-2}$	122/81

and the presence of scaling violations.

The results of the fit show that:

1. The p_T dependence is somewhat steeper for protons ($n = 9.7$) than it is for pions ($n = 9.1$ for π^- and $n = 9.4$ for π^+). We therefore expect the π^0 cross section to increase at large p_T for pion relative to proton beams (see Section 6.4).

2. As can be seen from Table 6.6, the power of the momentum distribution of the quarks inside the proton is also larger for protons ($m = 7.8$) than it is for pions ($m = 6.9$ and $m = 5.8$, for π^- and π^+, respectively). This can be interpreted to mean that structure functions for pions are less peaked at small x than for protons (quarks in the pion carry larger momenta).

3. The displacement x_0 from $x_F = 0$, is virtually zero for proton data, whereas it is finite for both π^- and π^+ data.

To check the last point, we calculated the π^0 invariant cross section as a function of the variable $x_F = (2\,p_z/\sqrt{s})$, averaged over p_T intervals. Here p_z is the longitudinal component of the π^0 momentum calculated in the center-of-mass system, and s is the square of the center-of-mass energy[3].

[3]To derive the expression of the invariant differential cross section in x_F and p_T one has to multiply Expression (6.1) by the kinematic factor corresponding to the Jacobian of the phase space transformation from (y, p_T) to (x_F, p_T), namely:

$$dx_F\,dp_T = \frac{2\,E}{\sqrt{s}}\,dp_T\,dy \qquad (6.11)$$

Table 6.7: $\pi^- Cu/Be \rightarrow \pi^0 X$ invariant cross section at $\sqrt{s} = 31.5\,GeV$, as a function of x_F.

x_F min	x_F max	$< x_F >$	$4.00 < p_T < 4.25\,(GeV/c)$ $(pb\,GeV^{-2}/Nucleon)$	$4.25 < p_T < 4.50\,(GeV/c)$ $(pb\,GeV^{-2}/Nucleon)$	$4.50 < p_T < 5.50\,(GeV/c)$ $(pb\,GeV^{-2}/Nucleon)$
-0.175	-0.140	-0.1575	3786.2 ± 483.5	1155.1 ± 142.0	458.6 ± 43.7
-0.140	-0.105	-0.1225	3614.4 ± 458.6	1406.6 ± 173.0	593.3 ± 46.7
-0.105	-0.070	-0.0875	4298.8 ± 476.8	1870.5 ± 179.6	675.3 ± 51.1
-0.070	-0.035	-0.0525	5661.2 ± 518.3	2317.1 ± 206.3	629.0 ± 47.4
-0.035	0.000	-0.0175	5266.6 ± 501.0	2522.1 ± 209.4	722.6 ± 48.1
0.000	0.035	0.0175	5176.5 ± 493.7	2883.1 ± 214.0	821.2 ± 50.2
0.035	0.070	0.0525	6187.2 ± 545.0	2627.3 ± 200.7	755.5 ± 47.2
0.070	0.105	0.0875	5735.6 ± 560.8	2664.5 ± 222.5	902.0 ± 56.3
0.105	0.140	0.1225	5846.4 ± 578.6	2532.1 ± 210.6	853.9 ± 54.7
0.140	0.175	0.1575	5157.7 ± 573.0	2196.2 ± 215.3	725.0 ± 53.3

In Table 6.7 we report the values of the π^0 invariant cross sections for π^- incident on $Cu + Be$, as a function of x_F, averaged over the p_T ranges $4.0 < p_T < 4.25$, $4.25 < p_T < 4.5$, $4.5 < p_T < 5.5\,GeV/c$. Similarly, Tables 6.8 and 6.9 summarize the proton and π^+ data, averaged over the p_T ranges $4.25 < p_T < 4.5$, $4.5 < p_T < 5.0$ (protons), $4.25 < p_T < 4.5$ (π^+) GeV/c. Figures 6.20, 6.21 and 6.22 show the experimental x_F distributions and superimposed the results of the phenomenological fit (6.10). The magnitude of the cross section for π^- and p beams in the same p_T interval ($4.25 < p_T < 4.5\,GeV/c$) is nearly the same at $x_F = 0$, where the π^0 cross section with proton beam reaches a maximum, as

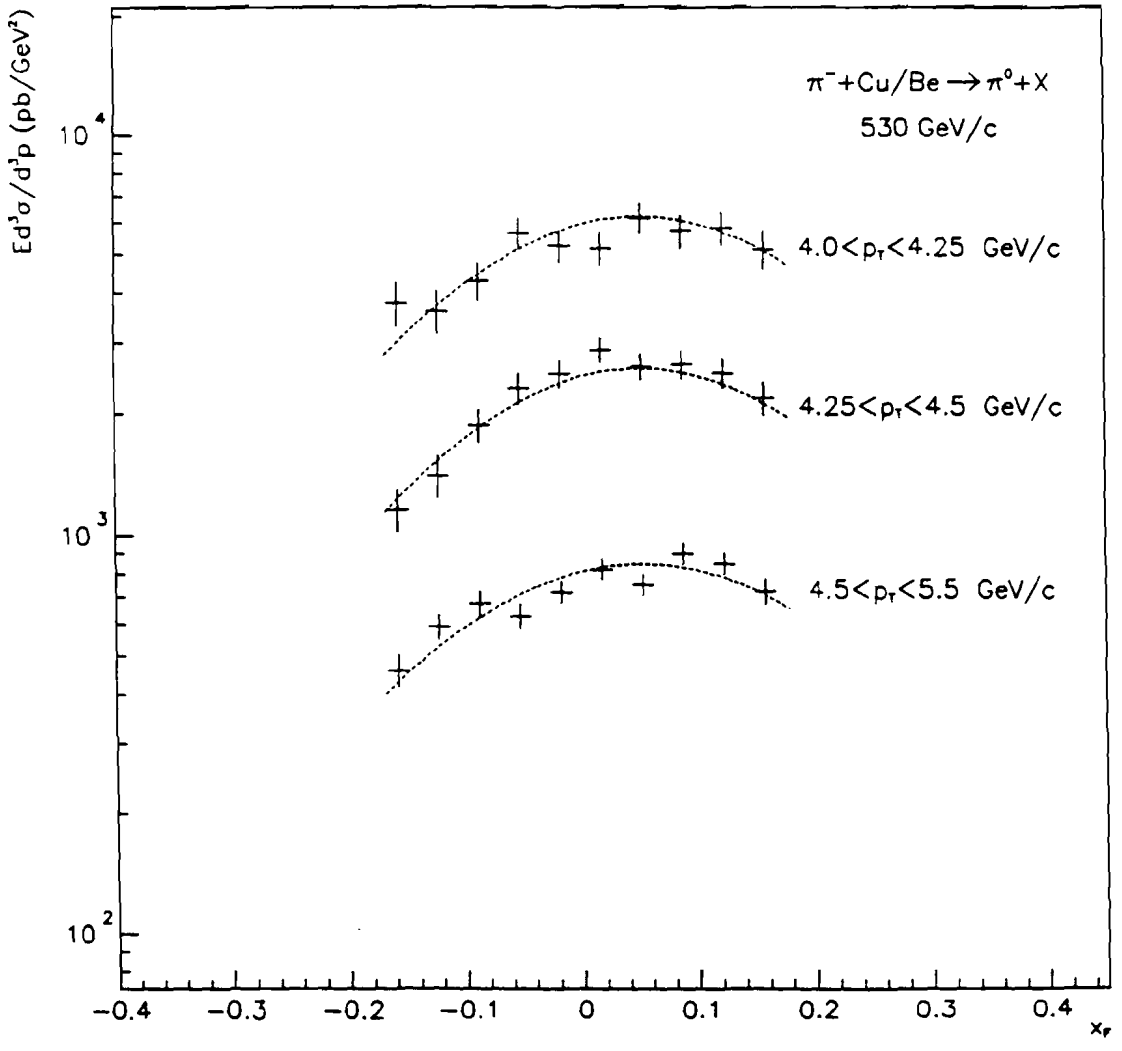

Figure 6.20: π^0 invariant cross section for 530 Gev/c π^- incident on $Cu + Be$, as a function of x_F, averaged over the indicated p_T ranges.

Table 6.8: $p\ Cu/Be \rightarrow \pi^0 X$ invariant cross section at $\sqrt{s} = 31.5\,GeV$, as a function of x_F.

x_F min	x_F max	$< x_F >$	$4.25 < p_T < 4.50\,(GeV/c)$ $(pb\,GeV^{-2}/Nucleon)$	$4.50 < p_T < 5.50\,(GeV/c)$ $(pb\,GeV^{-2}/Nucleon)$
-0.175	-0.140	-0.1575	1391.6 ± 205.4	627.1 ± 85.8
-0.140	-0.105	-0.1225	1884.6 ± 235.8	734.5 ± 87.6
-0.105	-0.070	-0.0875	1538.9 ± 184.2	796.0 ± 87.7
-0.070	-0.035	-0.0525	2373.3 ± 224.3	788.9 ± 87.0
-0.035	0.000	-0.0175	2181.0 ± 205.5	900.0 ± 89.6
0.000	0.035	0.0175	2546.3 ± 206.3	810.8 ± 82.6
0.035	0.070	0.0525	2340.4 ± 202.7	910.9 ± 90.7
0.070	0.105	0.0875	2325.1 ± 214.7	971.3 ± 92.2
0.105	0.140	0.1225	1982.1 ± 200.0	740.7 ± 83.7
0.140	0.175	0.1575	1549.6 ± 187.3	760.0 ± 88.0

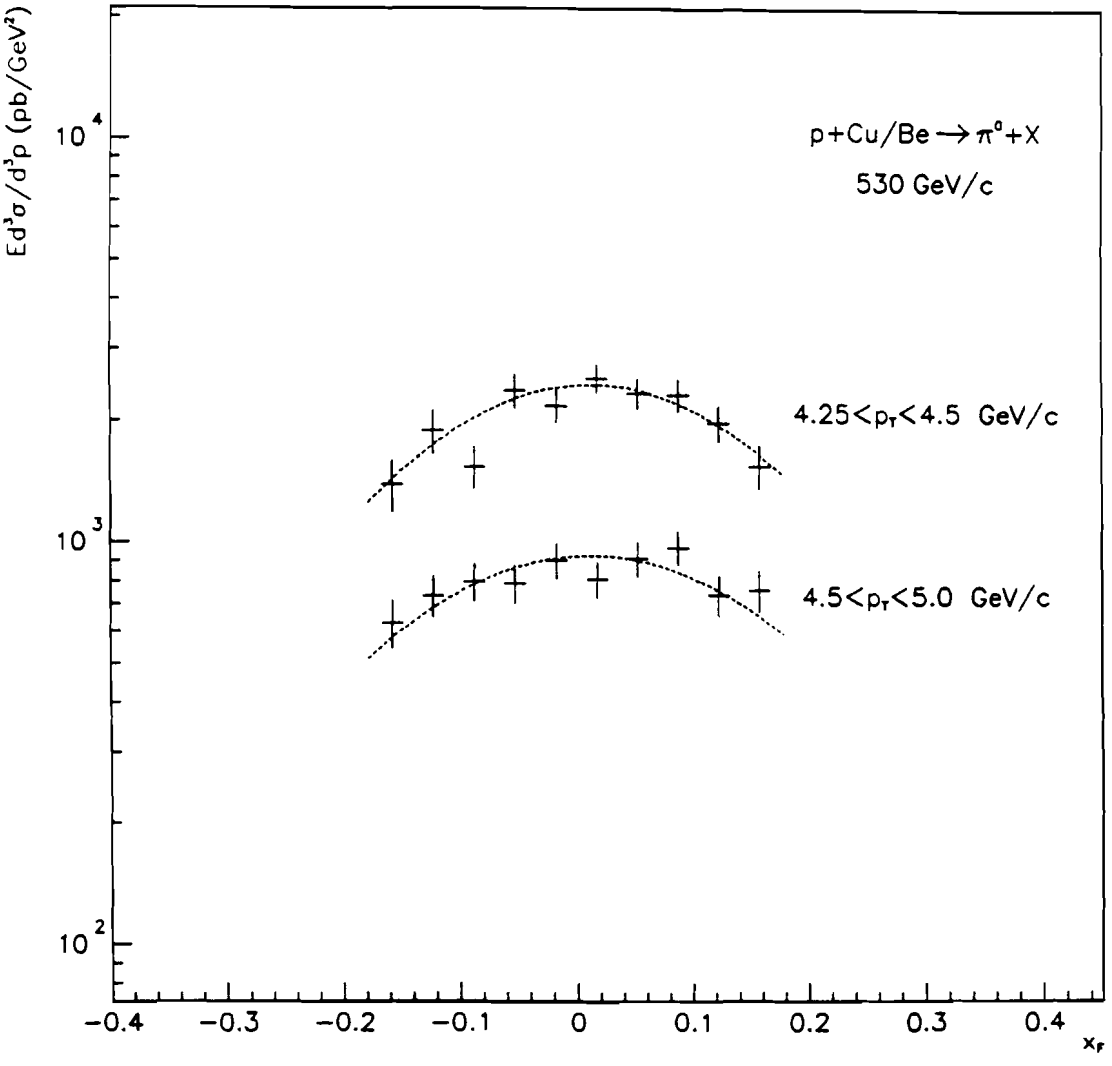

Figure 6.21: π^0 invariant cross section for 530 Gev/c p incident on $Cu + Be$, as a function of x_F, averaged over the indicated p_T ranges.

Table 6.9: $\pi^+ \; Cu/Be \; \rightarrow \pi^0 X$ invariant cross section at $\sqrt{s} = 31.5\,GeV$, as a function of x_F.

x_F min	x_F max	$< x_F >$	$4.25 < p_T < 4.50\,(GeV/c)$ $(pb\,GeV^{-2}/Nucleon)$
-0.175	-0.140	-0.1575	1472.8 ± 894.7
-0.140	-0.105	-0.1225	2085.6 ± 751.9
-0.105	-0.070	-0.0875	2213.1 ± 741.5
-0.070	-0.035	-0.0525	2460.7 ± 835.5
-0.035	0.000	-0.0175	2758.0 ± 999.9
0.000	0.035	0.0175	3791.7 ± 999.9
0.035	0.070	0.0525	3140.4 ± 879.6
0.070	0.105	0.0875	2434.3 ± 977.0
0.105	0.140	0.1225	2314.3 ± 903.3
0.140	0.175	0.1575	2522.5 ± 848.5

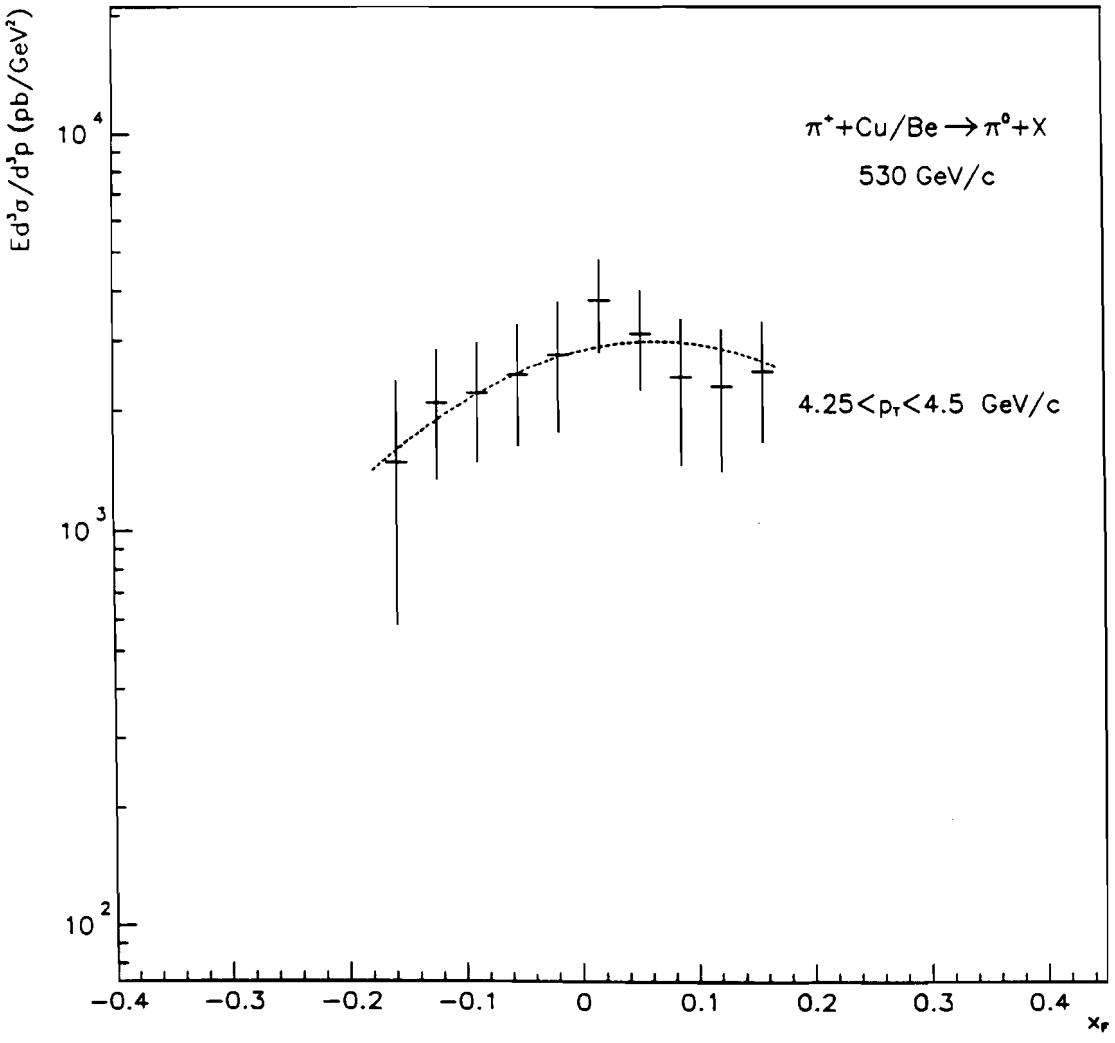

Figure 6.22: π^0 invariant cross section for 530 Gev/c π^+ incident on $Cu + Be$, as a function of x_F, averaged over the indicated p_T range.

would be required by the symmetry of constituent structures in the beam and target particles. With incident π^-s, the π^0 cross section tends to peak forward ($x_F \simeq 0.05$). The fact that the maximum of the π^0 cross section with π^- occurs for $x_F > 0$ can be understood in terms of quark-counting arguments. In fact, a valence quark in the pion carries, on average, a higher momentum than a valence quark in the nucleon, therefore the quark-quark system tends to move forward in the hadron-hadron center-of-mass system, whereas, for incident protons, it is at rest.

Our π^0 results using negative-beam data are consistent with previously measured cross sections in comparable kinematic regions of y and x_T [13,24,28,29], but at lower energies (and lower p_T). In Fig. 6.23 some of the available data on proton and nuclear targets are plotted as a function of p_T. The kinematic ranges of each experiment are also shown.

π^0 data with proton beam are compared in Fig. 6.24 to results from other experiments, [12,14,24,28,31] both for fixed-target and ISR Collider measurements, covering a wide range of energies. All results display a very strong s-dependence of the π^0 cross section at large p_T. In particular, the steepness of the p_T spectrum decreases as the energy increases. Most of the data are consistent with p_T dependences of the Form (6.10), although the power of p_T varies from 5 [14] to 10 (this experiment) to accommodate the different sets of data. The ISR data suggest a weaker dependence on p_T.

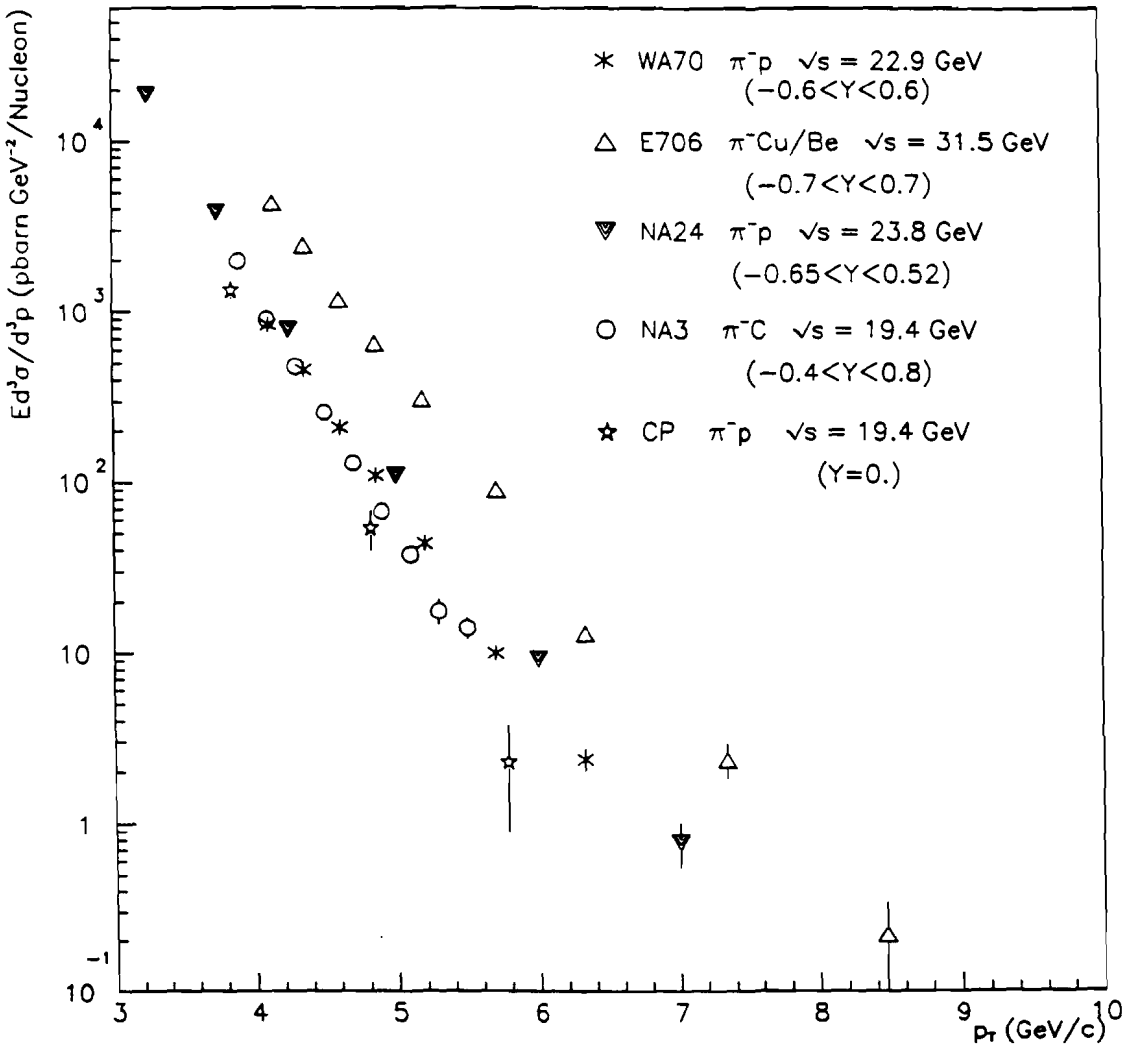

Figure 6.23: Compilation of π^0 yields for π^- interactions.

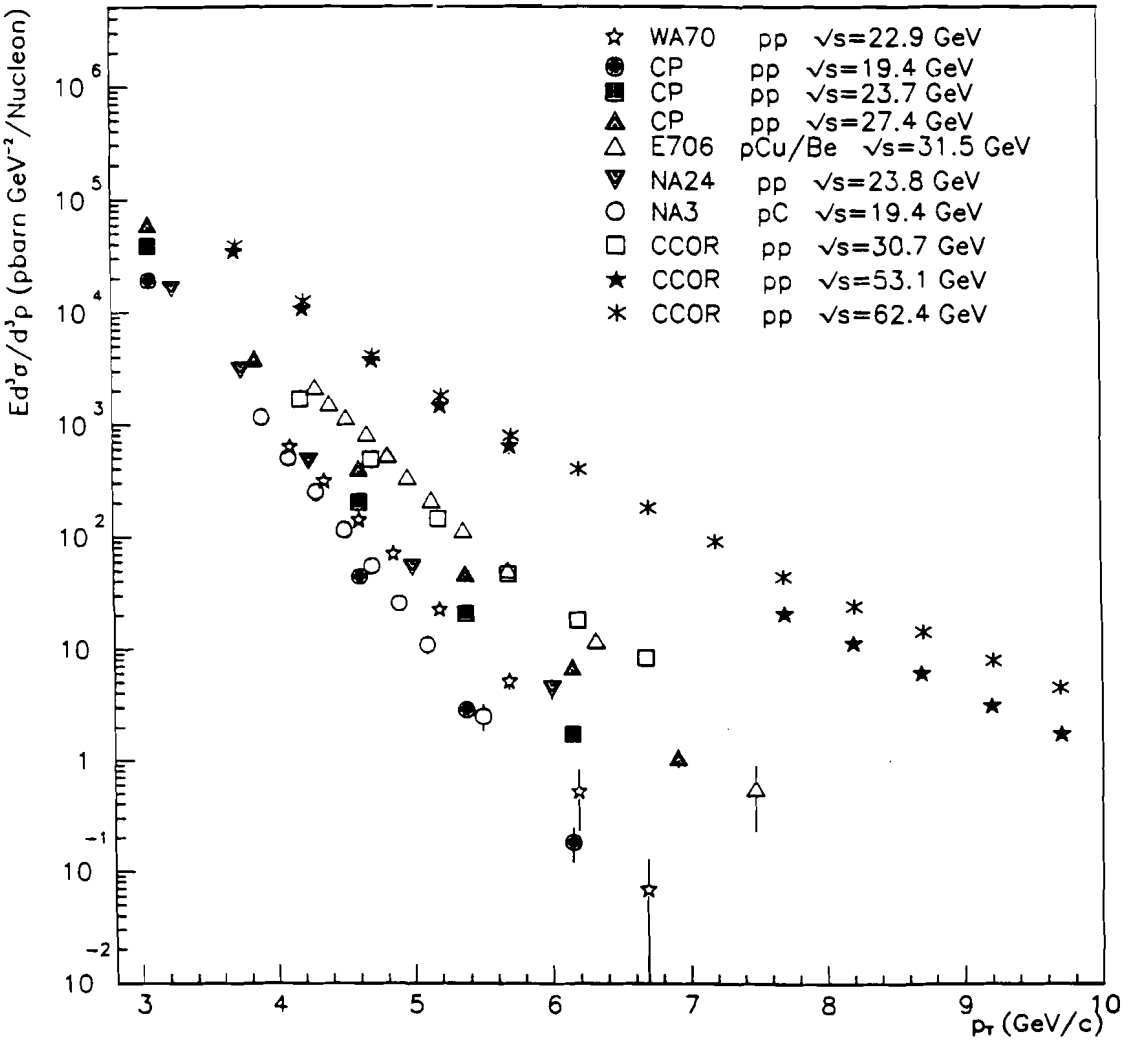

Figure 6.24: Compilation of π^0 yields for p interactions.

To check the absolute normalization of our cross sections with those of previous experiments, we show in Figs. 6.25 and 6.26 a compilation of results on π^0 production with π^- and proton beams at a specific kinematic point ($y = 0$, $p_T = 4.86\,GeV/c$ for incident π^- and $p_T = 4.61\,GeV/c$ for incident protons). The figures display the values of the π^0 invariant cross section per nucleon as a function of the center-of-mass energy ($\sqrt{s}$). At this specific kinematic point our cross section is consistent with the energy trend of previous experiments at both lower and higher values of $\sqrt{s}$. (When the value of any cross section was not available at the specific kinematic (p_T, y) point, an extrapolation was performed using our phenomenological fit.)

The displayed data do not prove that, in fact, the π^0 cross section at different energies scales in proportion to $\sqrt{s}$. At the end of Chapter 1, we mentioned that if the scaling law described by Expression (6.10) is valid, by rewriting the same expression in the form

$$E\,\frac{d^3\sigma}{d^3p} = \frac{1}{(\sqrt{s})^n}\,G(x_T) \tag{6.12}$$

then, at any value of x_T, the ratio of invariant cross section at two different energies $(\sqrt{s_1}, \sqrt{s_2})$ is equal to:

$$\frac{E\,\frac{d^3\sigma}{d^3p}(\sqrt{s_1}, x_T)}{E\,\frac{d^3\sigma}{d^3p}(\sqrt{s_2}, x_T)} = (\frac{\sqrt{s_2}}{\sqrt{s_1}})^n \tag{6.13}$$

If scaling works, then n is unique, and if it breaks down, then n must be a function of $\sqrt{s}$ or x_T. One way of addressing this issue is showed in Figs. 6.27 and 6.28. Here we plot compilations of π^0 invariant cross section multiplied by p_T^n as a

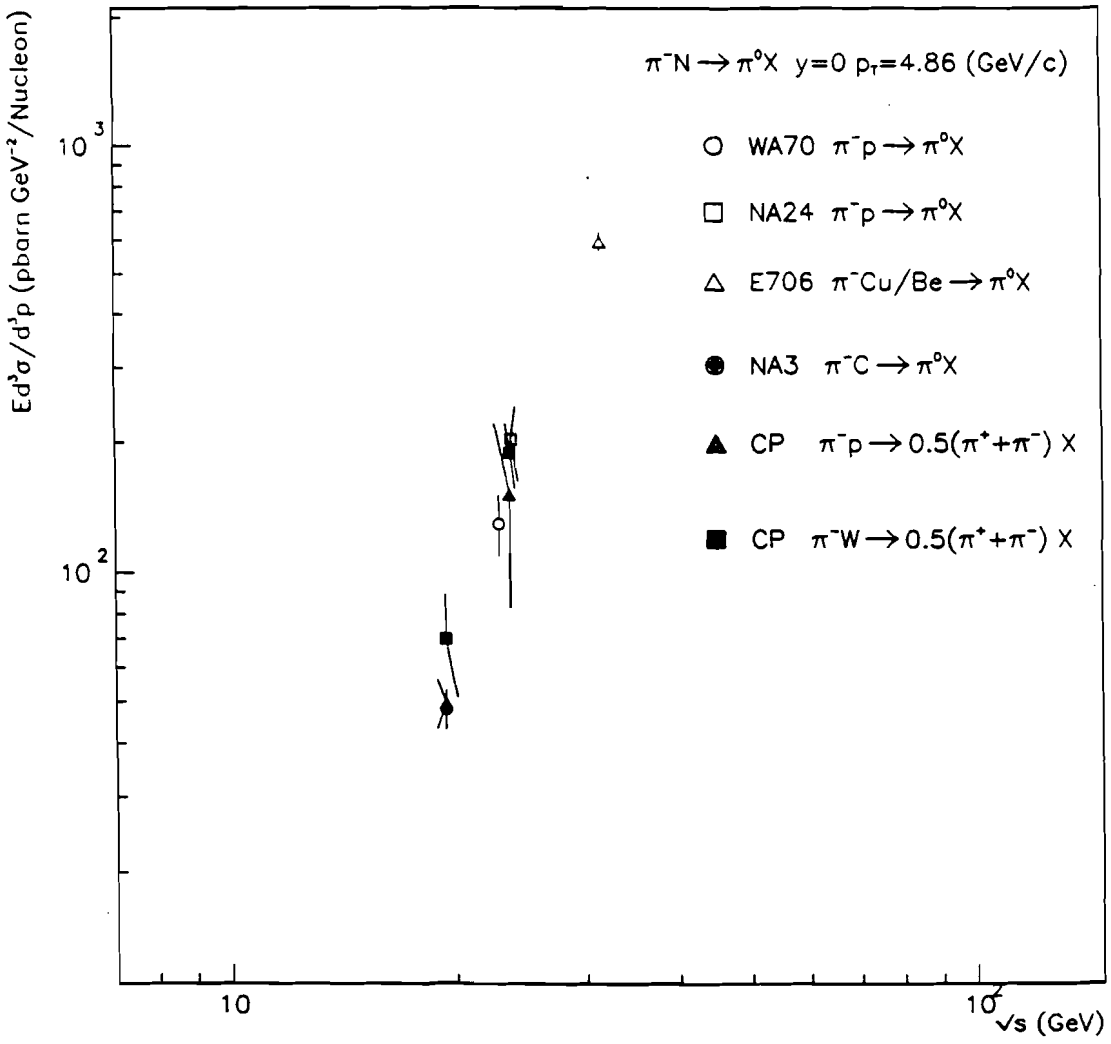

Figure 6.25: Compilation of π^0 yields for π^- interactions. Experimental data correspond to the kinematic point: $y = 0$, $p_T = 4.86\,GeV/c$.

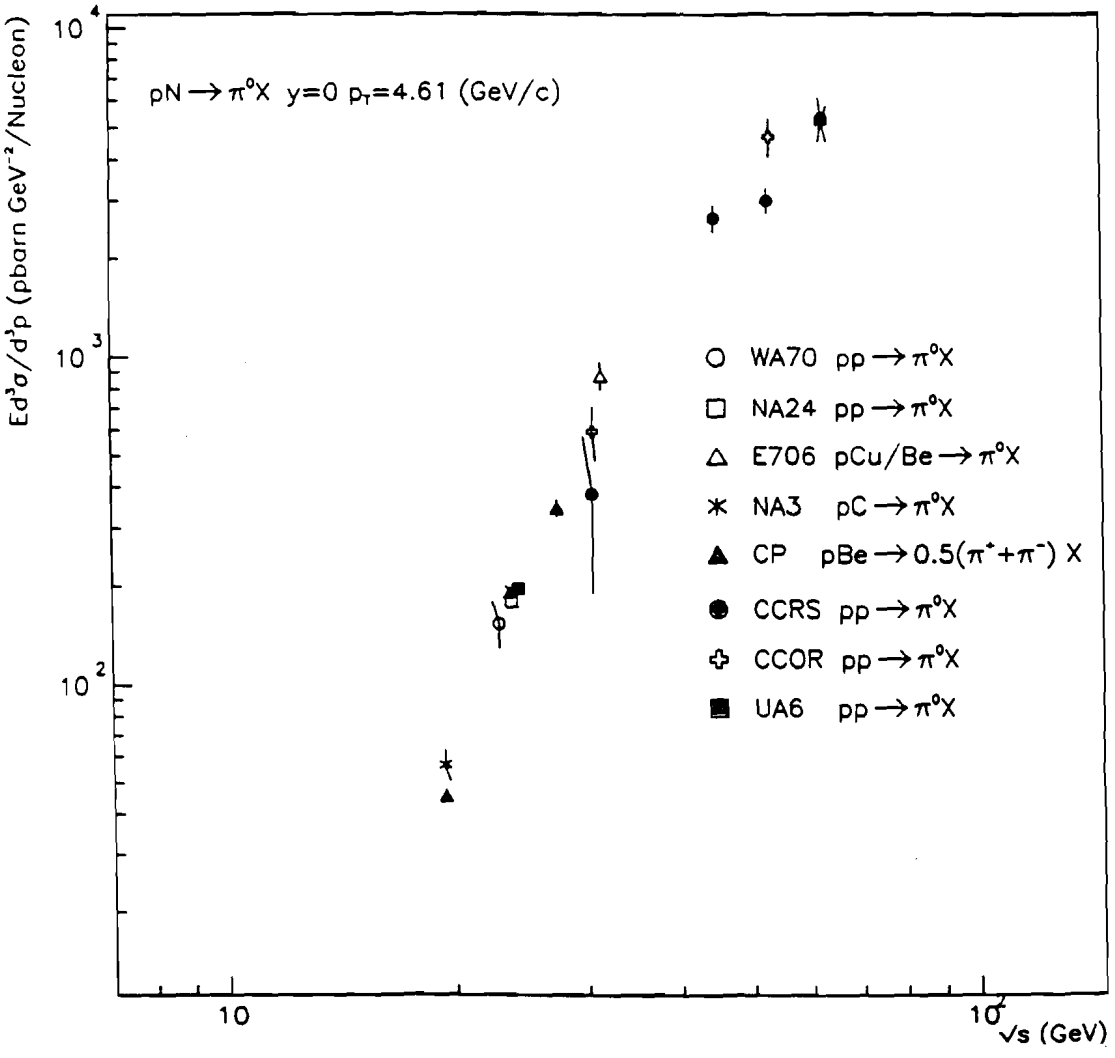

Figure 6.26: Compilation of π^0 yields for p interactions. Experimental data correspond to the kinematic point: $y = 0$, $p_T = 4.61\,GeV/c$.

function of the variable x_T $(2p_T/\sqrt{s})$. In terms of the scaling law (6.10) this choice removes the strong dependence of the cross section on p_T and, most of all, provides a way for establishing whether scaling is valid or not. In Figs. 6.27, 6.28 we set the exponent n to be equal to the value obtained from fitting our cross section with π^- and proton beams, namely $n = 9.07$ and $n = 9.71$, respectively. If indeed there is scaling, then all data points measured at different values of $\sqrt{s}$ should overlap and evolve according to a unique function of x_T. This is clearly not the case, as shown in both Fig. 6.27 and 6.28[4]. We therefore conclude that we have scale breaking, and that the functional form (6.10) is not adequate to describe all available data on π^0 production at large p_T. There is a residual dependence on energy which has to be extracted from fitting simultaneously all available data. If the normalization parameter A is itself a function of the energy then Expression (6.10) can be written as

$$E\,\frac{d^3\sigma}{d^3p} = A'\,(x_T^2+\delta^2)^{k/2}\,\frac{(1-x_D)^l}{p_T^j} \tag{6.14}$$

with A', l, j, k and δ being new parameters. The value of the parameter j can be obtained as usual from the p_T spectrum in some rapidity range; the value of l can be obtained from the shape of the rapidity distribution in some p_T range; the value of the new parameters k and δ can be obtained either from fitting all available data, or else from adjusting the power of p_T to force all the data points to overlap in the plots of Figs. 6.27 and 6.28. In fact, assuming that $l \simeq m$ (Exp. (6.10)), it follows that $j - k = n$.

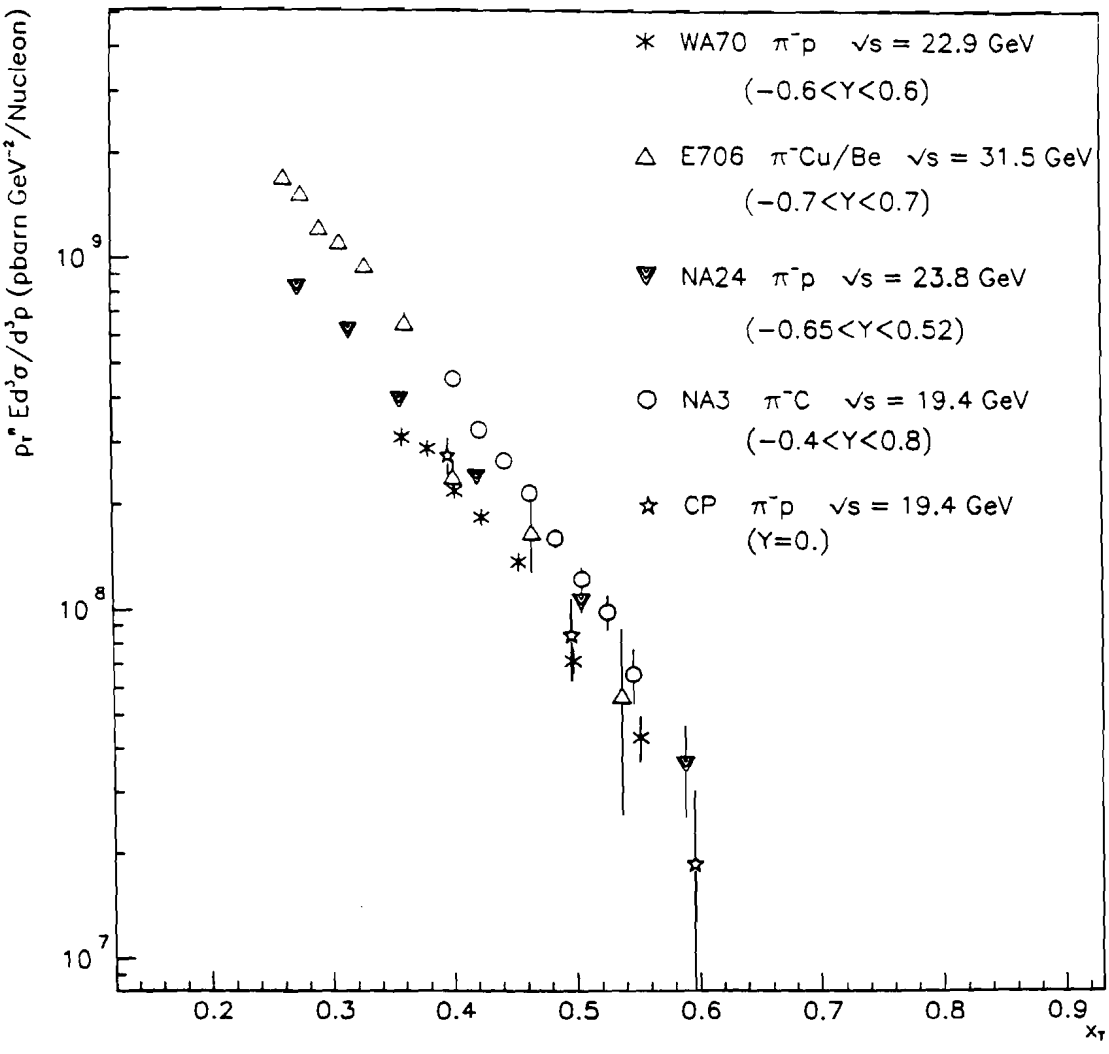

Figure 6.27: Compilation of π^0 invariant cross sections times p_T^n for π^- interactions, as a function of x_T.

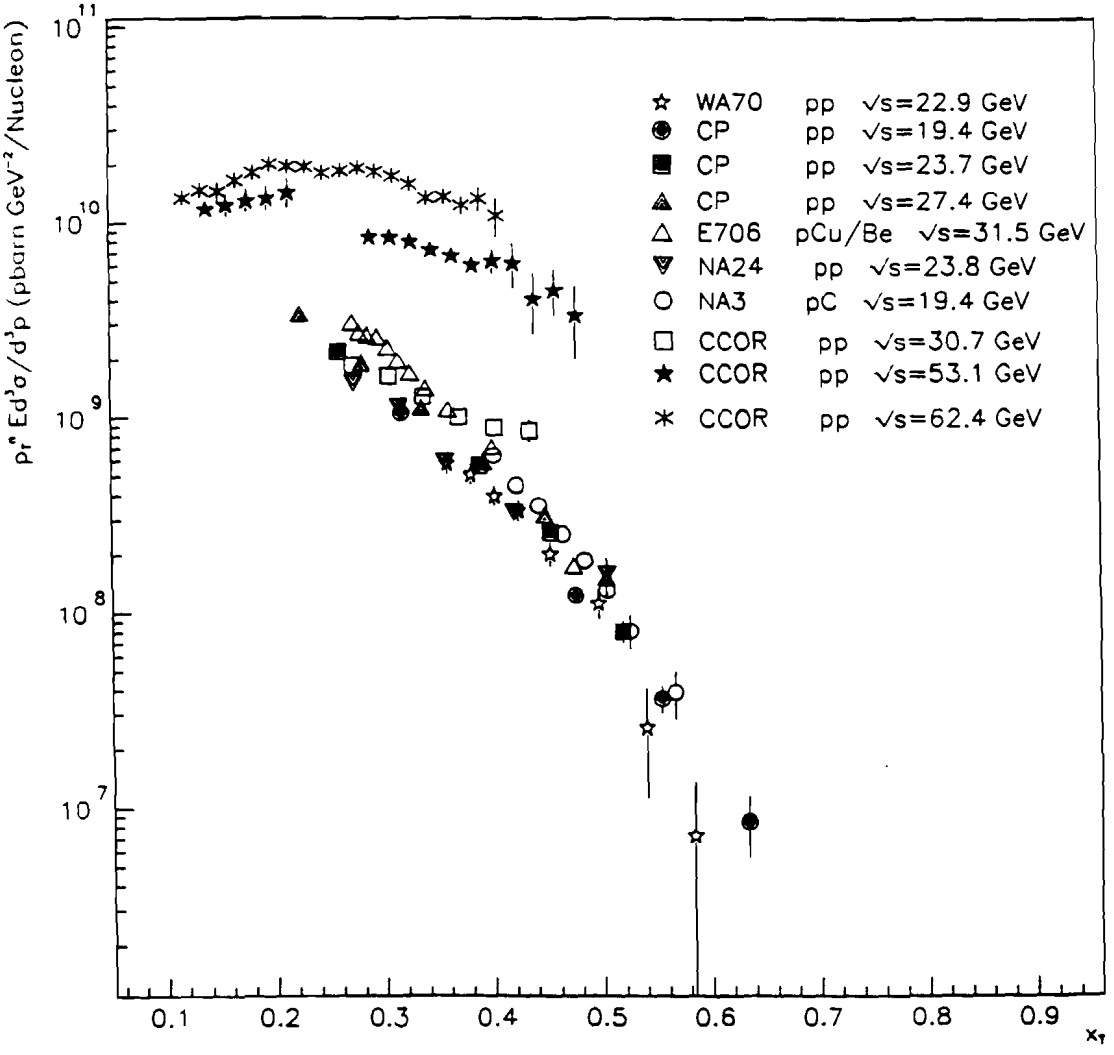

Figure 6.28: Compilation of π^0 invariant cross sections times p_T^n for p interactions, as a function of x_T.

Figures 6.29 and 6.30 are compilations of the same data displayed in Figs. 6.27 and 6.28. The only difference is the power of p_T which multiplies the cross section. In Fig. 6.29 the exponent j is equal to 7.5, and therefore $k = j - n = -1.6$. In Fig. 6.30, the exponent j is equal to 6.5, and $k = j - n = -3.0$. The solid lines superimposed on the data in both figures represent the function $A'(1-x_D)^l(x_T^2 + \delta^2)^{k/2}$ ($A' = 0.24\,mb/GeV^2$, $l = 6.9$, $\delta = 0.37$ for π^- data; $A' = 2.5\,\mu b/GeV^2$, $l = 5.5$, $\delta = 0.37$ for proton data). The residual spread of the experimental points (in particular NA3 data seem to lie systematically above the other data) could be caused by effects previously described. Nevertheless, the trend of the data in both figures confirms that a functional form of the type (6.14) is suitable to describe most of the available data.

6.5 π^0 Yields with Different Beam Particles

In this section we study the beam dependence of π^0 production. In particular, we present results on production ratios between K^- and π^-, as well as between π^+ and p beam-particles, both as a function of p_T and x_F of the produced π^0s.

In order to calculate ratios of π^0 spectra, events in the p_T and x_F distributions for all types of incident beam-particles were required to have a reconstructed vertex in the Cu or Be target segments. Furthermore, individual distributions were corrected for beam-particle absorption in the target and in the material upstream

[4]The different sets of data displayed in the figures were not scaled to the same rapidity range (for example a small interval around $y = 0$). Also, data on nuclear targets were normalized to obtain π^0 cross section on proton assuming A^α nuclear dependence with $\alpha = 1$. For these reasons, we feel that the following analysis should be considered more qualitative than quantitative.

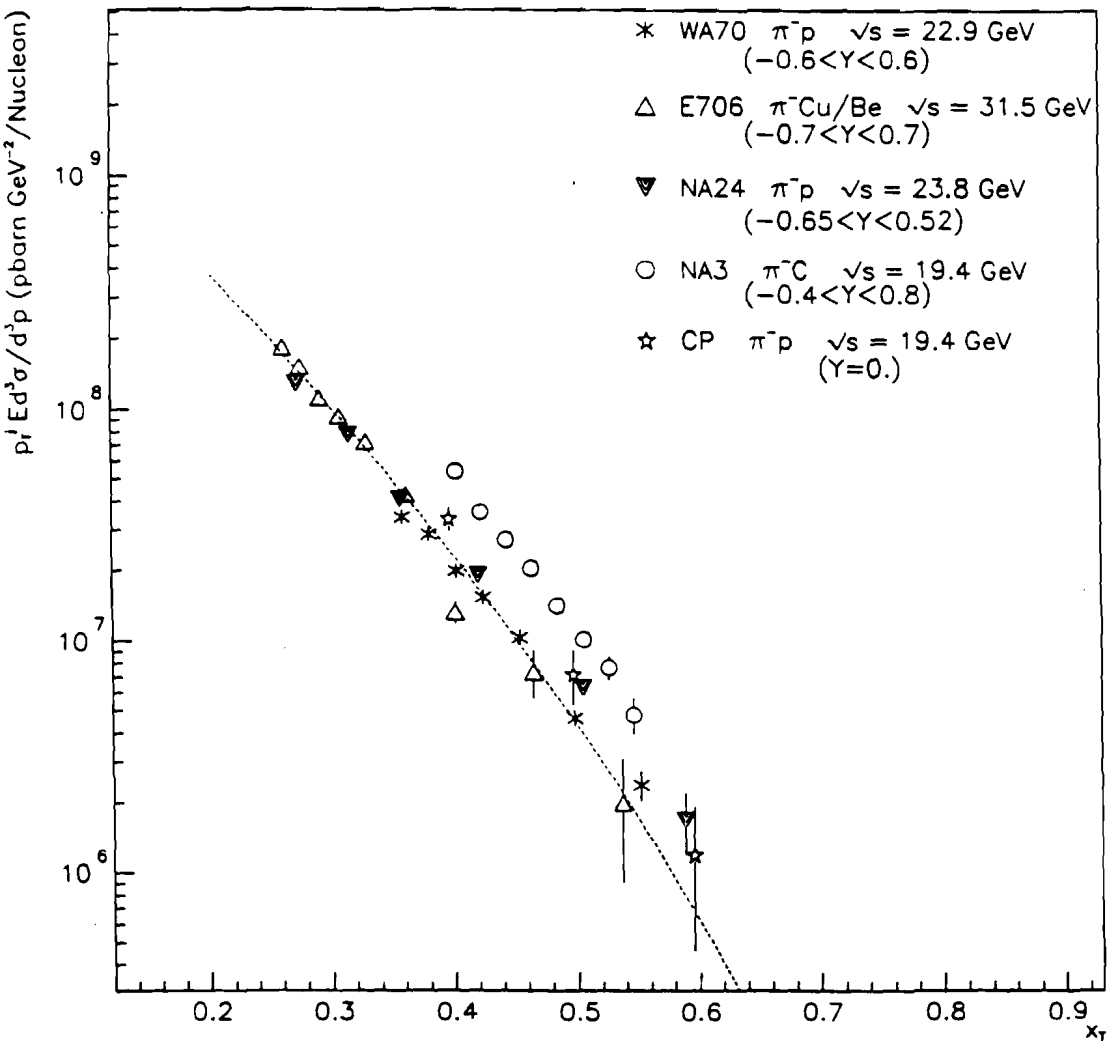

Figure 6.29: Compilation of π^0 invariant cross sections times p_T^j (j is the parameter of the new experimental fit) for π^- interactions, as a function of x_T. Superimposed is the new phenomenological fit (6.13)(see text for details).

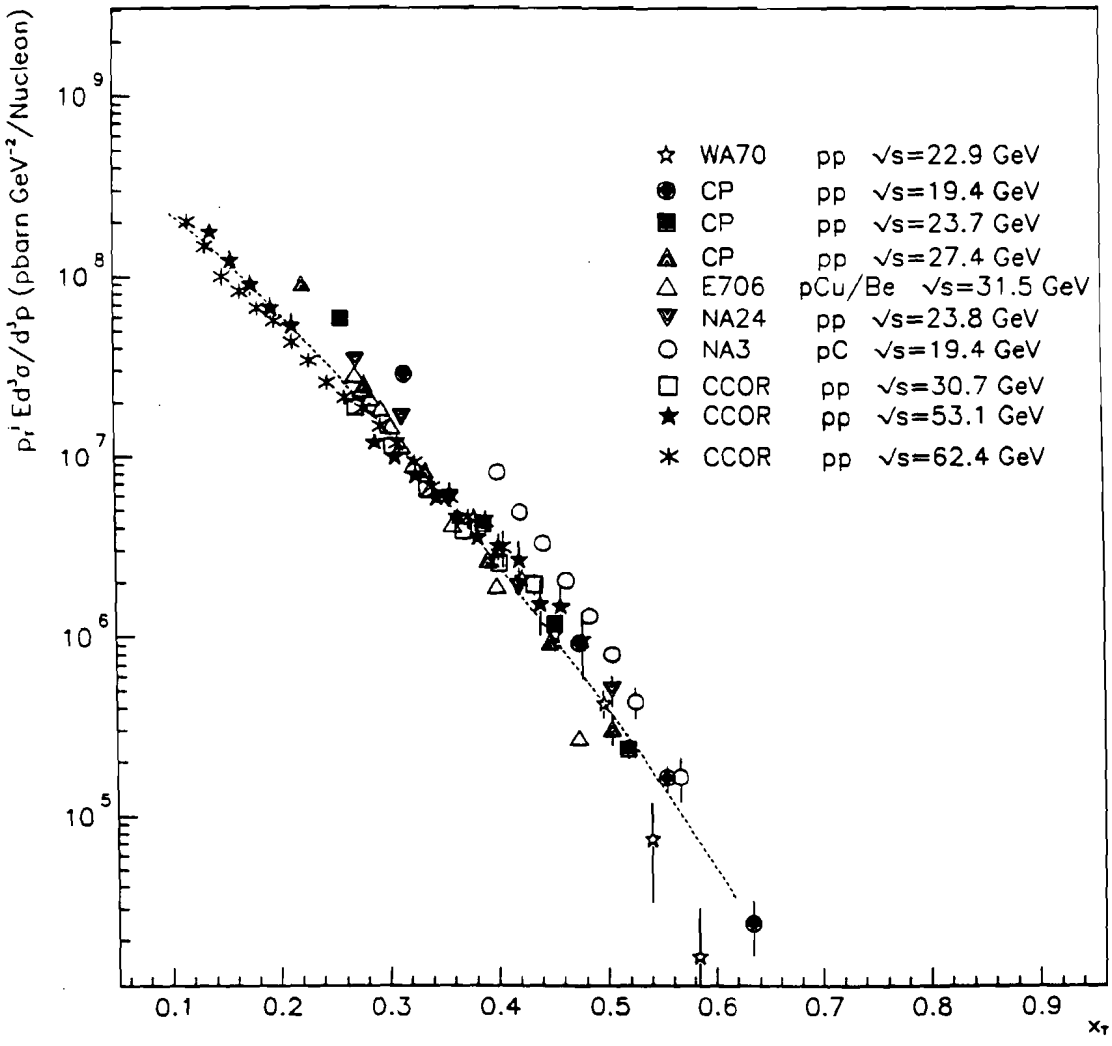

Figure 6.30: Compilation of π^0 invariant cross sections times p_T^j (j is the parameter of the new experimental fit) for p interactions, as a function of x_T. Superimposed is the new phenomenological fit (6.13) (see text for details).

of the target, and for background from other particles in the beam (corrections factors are listed in Table 6.1). No other cuts or corrections such as those described in Section 6.2, and listed in Table 6.1, were applied to the π^0 distributions. This was done so as to not further reduce statistics, and with the natural expectation that any systematic uncertainties would cancel in the calculation of ratios of distributions for incident particles in the same beam. We checked the effects of applying the extra analysis cuts on distributions for different tagged particles in the negative and positive beams, and concluded that any consequent biases would be negligible. By using ratios of such uncorrected distributions we were able to extend our kinematic regime both in rapidity and p_T outside the ranges selected for the calculation of the invariant cross sections.

We will now discuss the dependence of π^0 production on the nature of particle-type in the negative beam. Pion and kaons have similar internal structure in terms of the number of valence-quark constituents ($q\bar{q}$); both particles have the same valence antiquark ($\bar{u}$), but the valence quark in the K^- (s) is different from the valence quark in the π^- (d). π^0s have no strange valence quarks, instead they consist of an equal combination of $u\bar{u}$ and $d\bar{d}$ quark-antiquark. Figures 6.31, 6.32, 6.33 and 6.34 display the ratio of p_T distributions for $(K^- \rightarrow \pi^0)/(\pi^- \rightarrow \pi^0)$ as a function of the π^0 transverse momentum, for the center-of-mass rapidity intervals: $-1.0 < y < -0.2$, $-0.2 < y < 0.2$, $0.2 < y < 1.0$ and $-1.0 < y < 0.2$. (In the following we will simply refer to these ratios as K^-/π^-.) The K^-/π^-

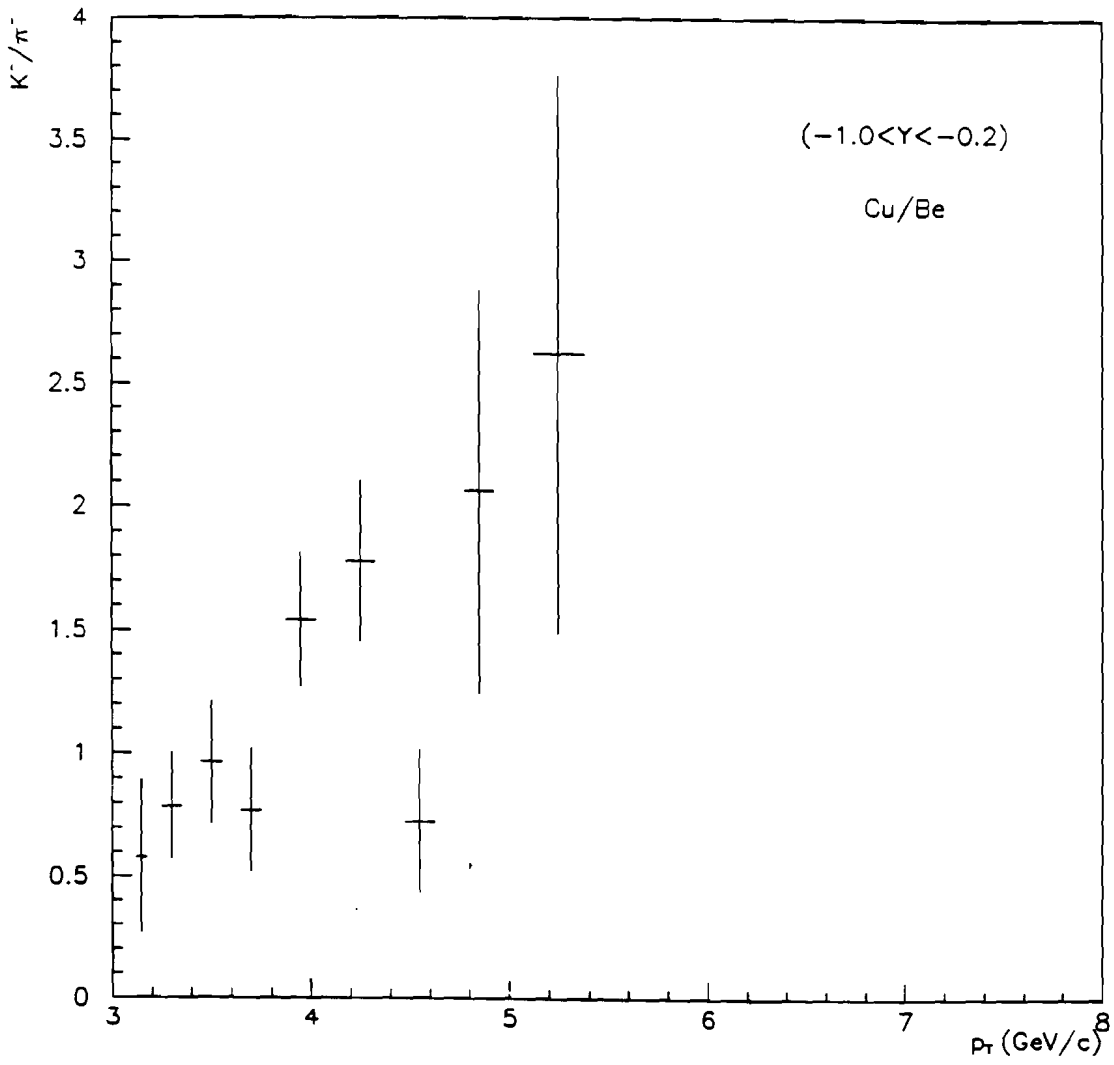

Figure 6.31: Ratio $(K^- \rightarrow \pi^0)/(\pi^- \rightarrow \pi^0)$ for $Cu+Be$ target as a function of the π^0 transverse momentum, in the center-of-mass rapidity interval $-1.0 < y < -0.2$.

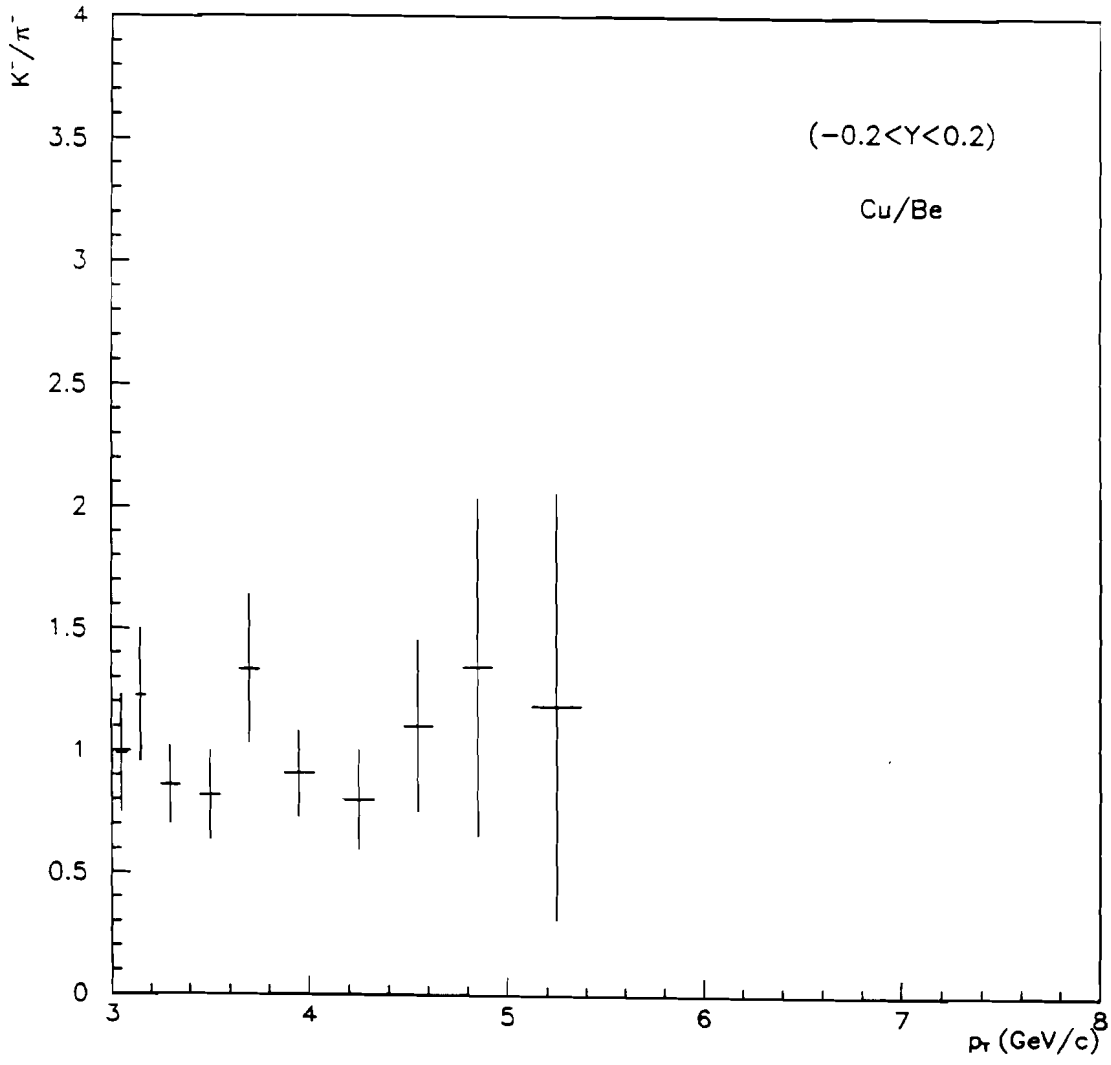

Figure 6.32: Same as Fig. 6.31, in the rapidity range $-0.2 < y < 0.2$.

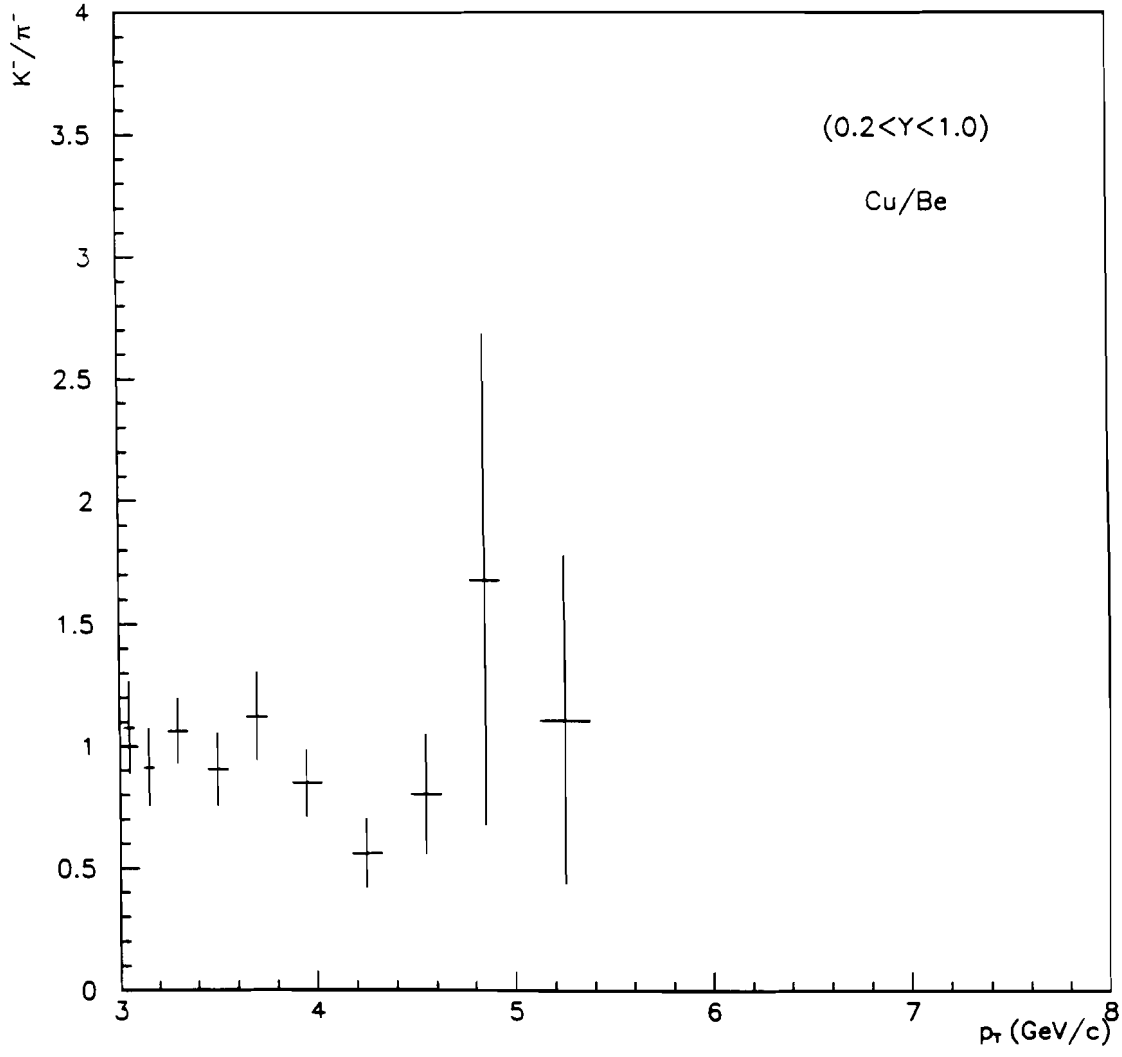

Figure 6.33: Same as Fig. 6.31, in the rapidity range $0.2 < y < 1.0$.

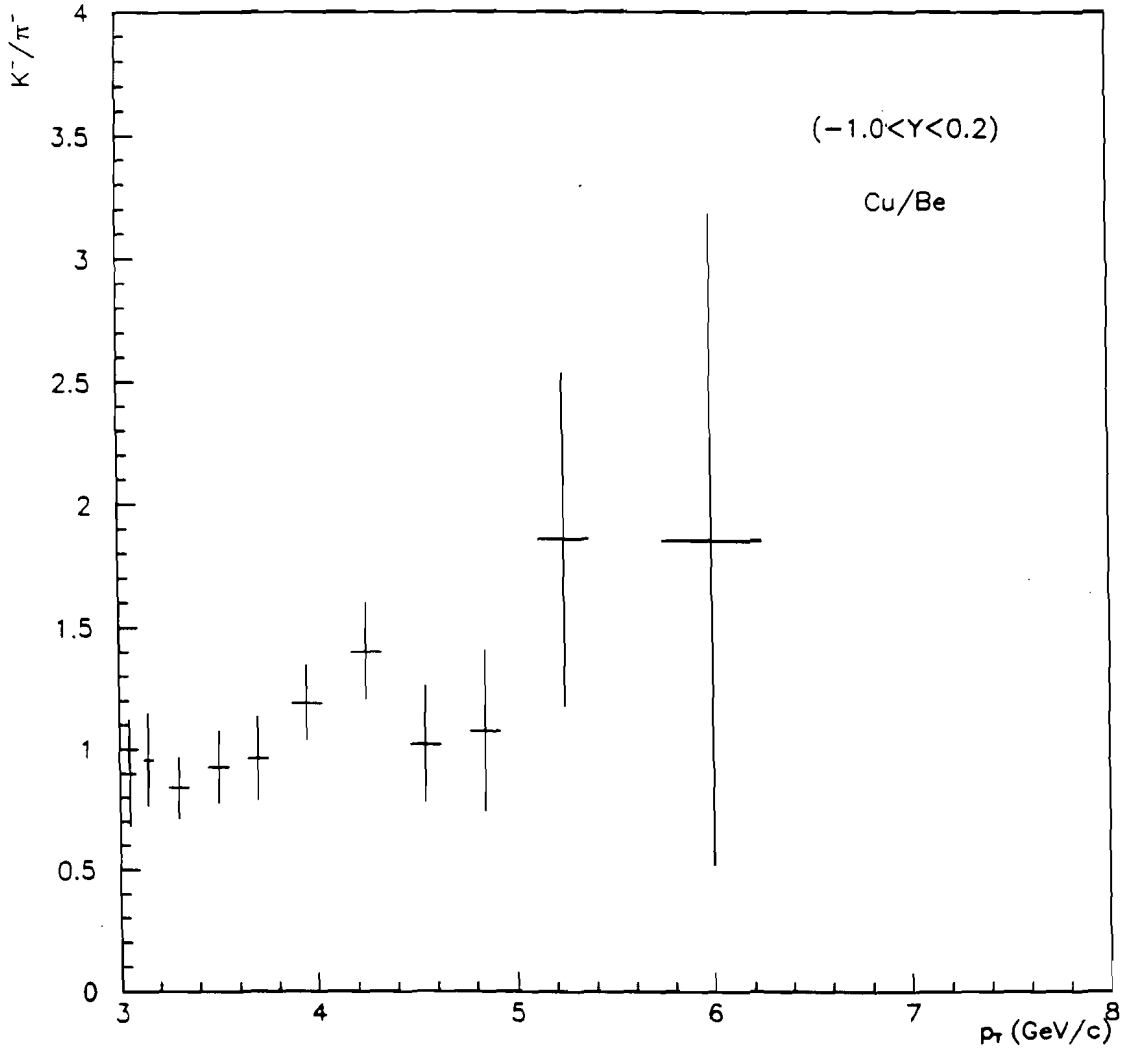

Figure 6.34: Same as Fig. 6.31, in the rapidity range $-1.0 < y < 0.2$.

ratio versus p_T appears to be constant and consistent with unity in the central and forward rapidity regions.

For backward rapidities, the K^-/π^- ratio is below unity at low p_T ($p_T < 4.0\,GeV/c$), and increases above one for larger values of p_T. Although this is an interesting effect, the K^- beam statistics are poor, and the increase of the ratio with increasing p_T has only marginal significance. The effect persists when events in coincidence with a signal from the veto wall are rejected (Fig. 6.35). This shows that the excess of π^0s at large p_T in K^- interactions, if true, is not caused by background events due to beam-halo muons. We also investigated whether any possible nuclear effects could be responsible for such an enhancement by calculating the K^-/π^- ratio in the backward rapidity region but only for data on Be. Again, in this case we reproduced the previous result. Consequently, if the effect is not a statistical fluctuation, then it cannot be attributed to an unusual A dependence.

Using the ratios of π^0 yields, and the measured invariant π^0 cross section in π^- interactions, we calculated the π^0 invariant cross section as a function of p_T for $530\,GeV/c$ K^- on the $Cu + Be$ target. This was done for the two rapidity ranges $-0.7 < y < 0.2$ and $0.2 < y < 0.7$, and the results are shown in Figs. 6.36 and 6.37. The values of the π^0 invariant cross section are also reported in Table 6.10. Previous measurements of this kind [21,58], were performed in a different kinematic regime ($x_F > 0.4$ and $p_T < 0.8\,GeV/c$), and at lower energies

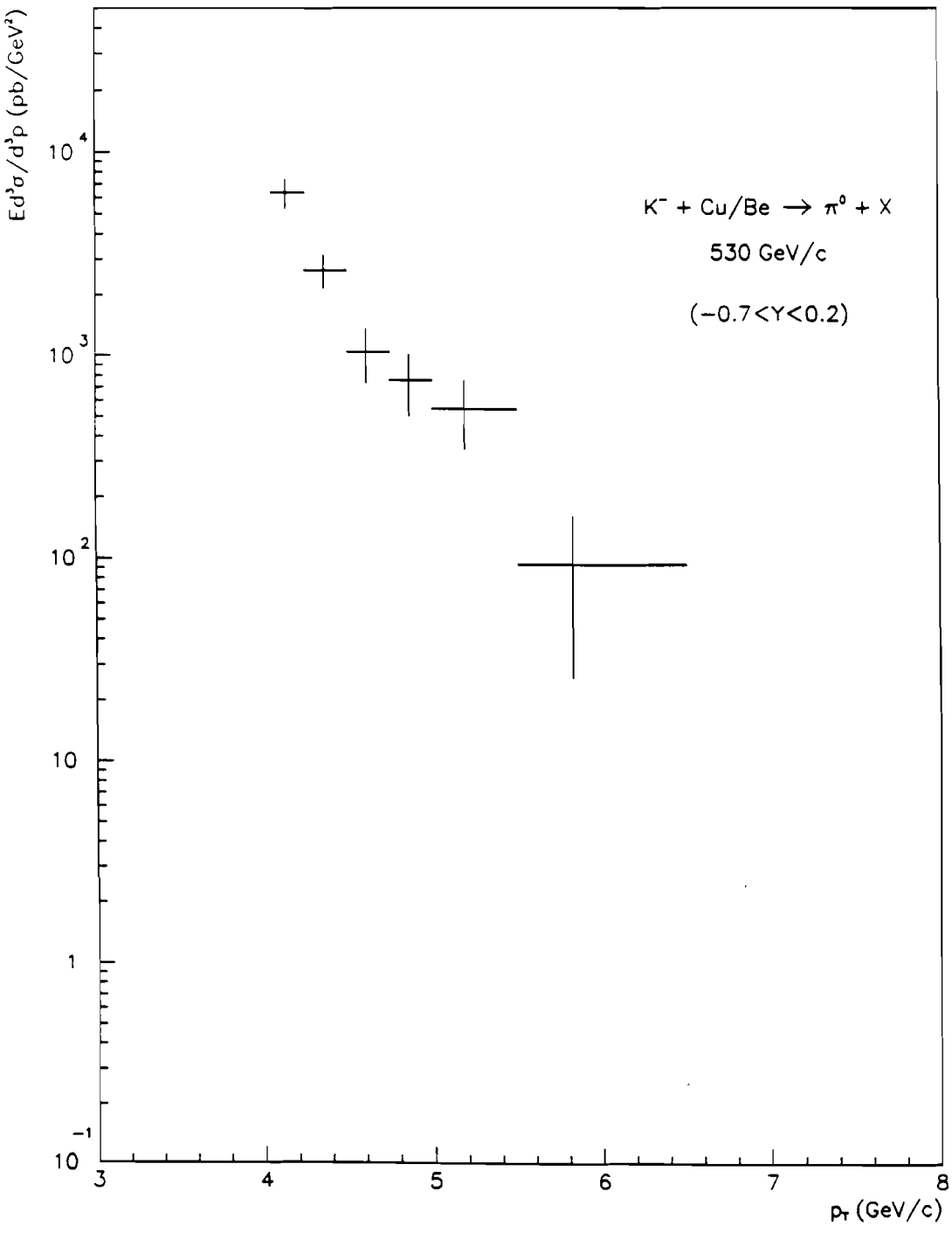

Figure 6.36: π^0 invariant cross section for 530 GeV/c K^- incident on $Cu+Be$, as a function of p_T, averaged over the center-of-mass rapidity interval $-0.7 < y < 0.2$.

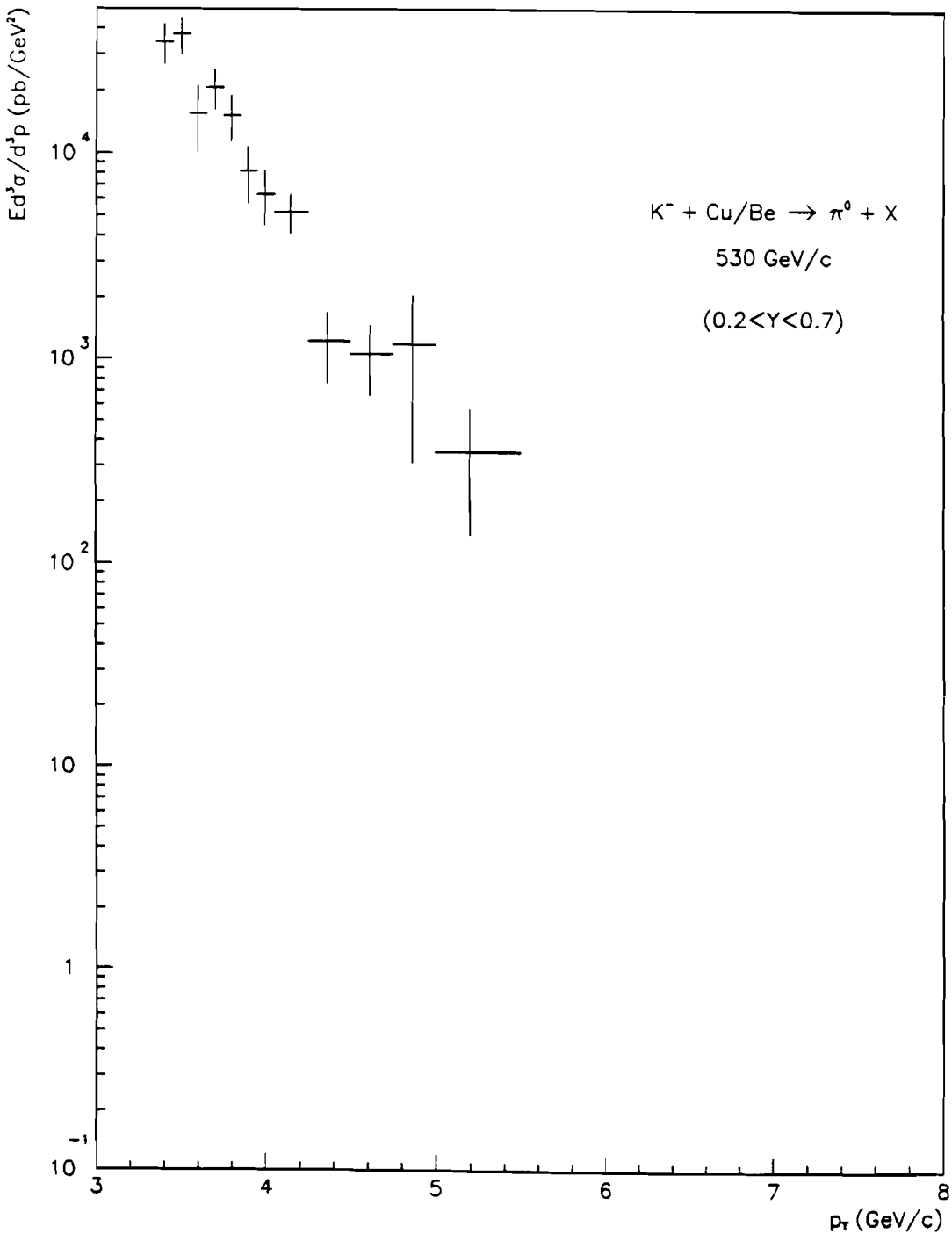

Figure 6.37: Same as Fig. 6.36, in the rapidity range $0.2 < y < 0.7$.

($58\,GeV/c$ for [21], and $100\,GeV/c$ for [58]).

Figures 6.38 and 6.39 show the K^-/π^- ratio for x_F distributions in the two p_T ranges $3.0 < p_T < 4.0$ and $4.0 < p_T < 8.0\,GeV/c$. Small but not significant deviations of the ratio from unity can be observed for $x_F \leq -0.1$ in both p_T ranges. The trend of the ratio with p_T for negative x_F is consistent with our previous observations (Figs. 6.31, 6.36). Table 6.11 summarizes the results displayed above for the ratio K^-/π^-. The Table gives the mean ratios $(K^- \rightarrow \pi^0)\,/\,(\pi^- \rightarrow \pi^0)$ integrated over the p_T range from 3.0 to $8.0\,GeV/c$, in the indicated rapidity ranges (upper row); and integrated over the x_F range from -0.2 to 0.2, in the indicated p_T ranges (bottom row). The errors quoted are statistical only.

Concerning the analysis of the positive-beam data, we present in Figs. 6.40, 6.41 and 6.42 the ratios of *uncorrected* (in the sense described above) p_T distributions for π^0s from incident π^+ and protons (labeled as π^+/p), for three center-of-mass rapidity intervals. Unlike the ratios for K^-/π^- distributions, here π^0 production reflects the greater difference between the internal structure of the incoming π^+s and protons, both in terms of the variety of valence constituents participating in the hard scattering, and the internal momenta of these constituents. The distributions of the π^+/p ratios in the central rapidity region (Fig. 6.41) shows a weak increase of the yield of π^0s with increasing p_T, starting from a value slightly above unity. In the forward rapidity region (Fig. 6.42) a similar trend with p_T is visible, but in this case the displacement of the experimental points from unity is far more

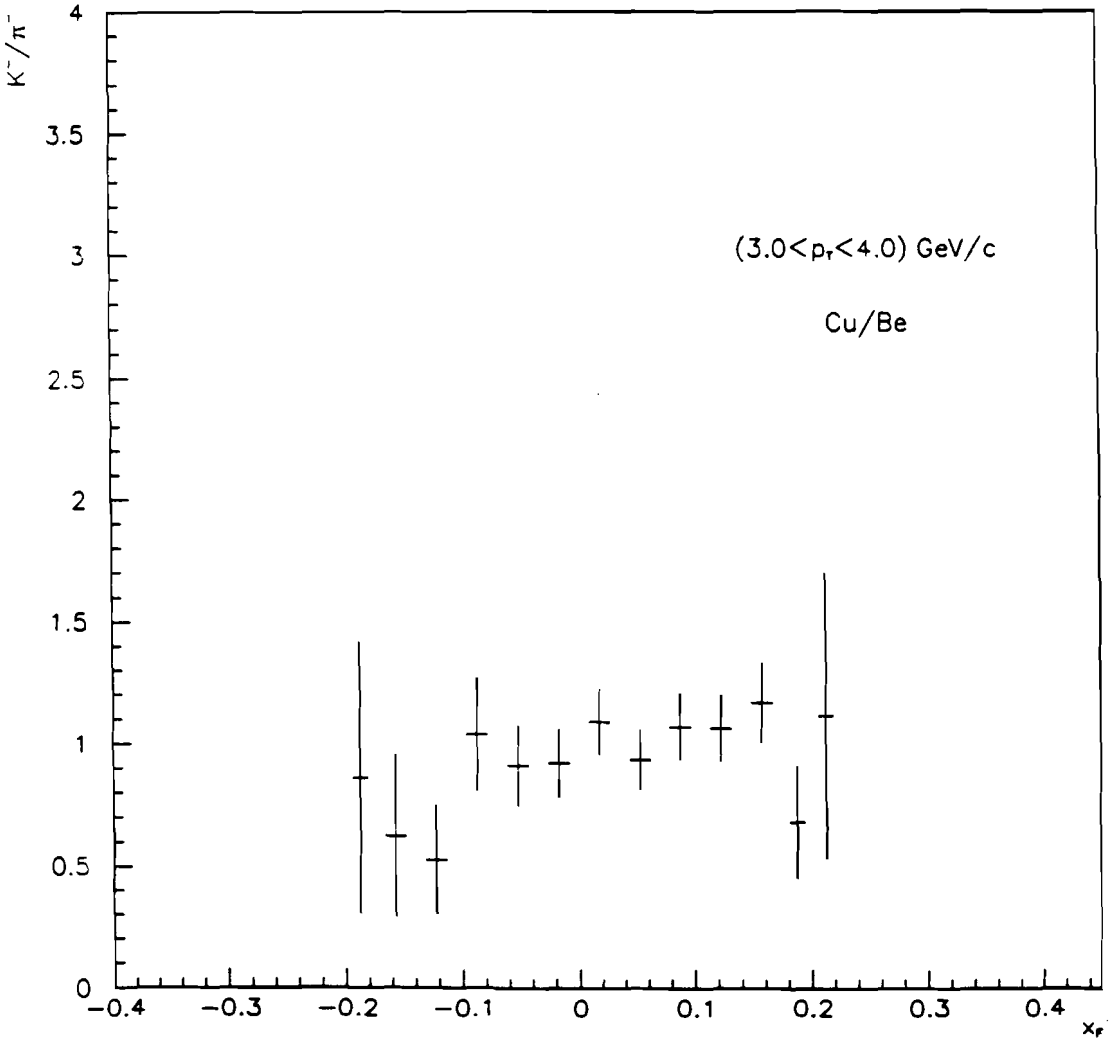

Figure 6.38: Ratio $(K^- \to \pi^0)\,/\,(\pi^- \to \pi^0)$ for $Cu + Be$ target as a function of the π^0 x_F, in the p_T range $3.0 < p_T < 4.0\,GeV/c$.

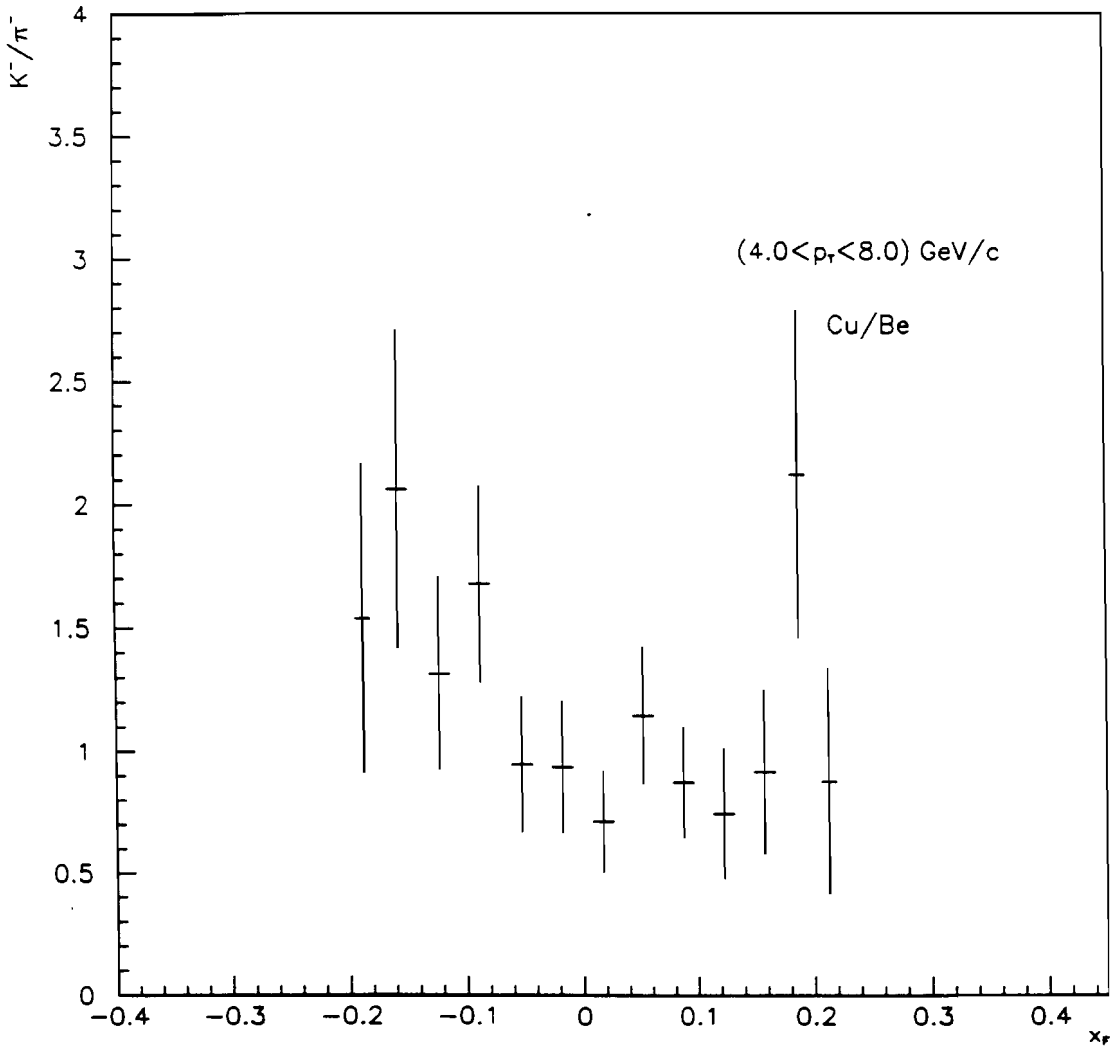

Figure 6.39: Same as Fig. 6.38, in the p_T range $4.0 < p_T < 8.0\,GeV/c$.

Table 6.11: Ratios of π^0 yields for K^- and π^- incident beam-particles.

Uncorrected	$\frac{K^- \to \pi^0}{\pi^- \to \pi^0}$ $(p_T > 3.0\,GeV/c)$	1.01 ± 0.10 $(-1.0 < y < -0.2)$	0.94 ± 0.08 $(-0.2 < y < 0.2)$	0.86 ± 0.07 $(0.2 < y < 1.0)$
Uncorrected	$\frac{K^- \to \pi^0}{\pi^- \to \pi^0}$ $(-0.2 < x_F < 0.2)$	0.99 ± 0.05 $(3.0 < p_T < 4.0\,GeV/c)$	0.99 ± 0.09 $(4.0 < p_T < 8.0\,GeV/c)$	

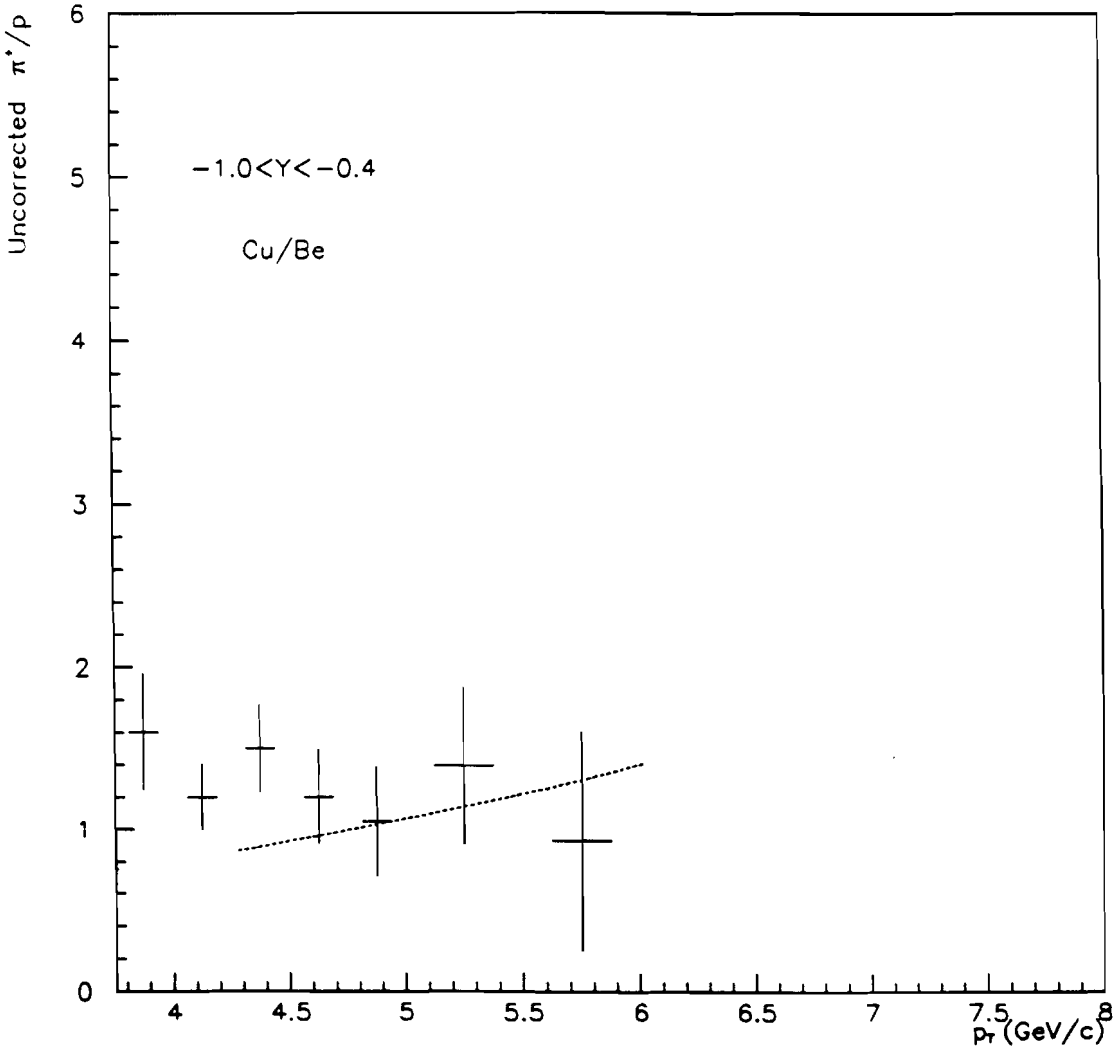

Figure 6.40: Ratio $(\pi^+ \to \pi^0) / (p \to \pi^0)$ for $Cu + Be$ target as a function of the π^0 transverse momentum, in the center-of-mass rapidity interval $-1.0 < y < -0.4$. Superimposed is the ratio of the phenomenological fits to the π^0 invariant cross sections.

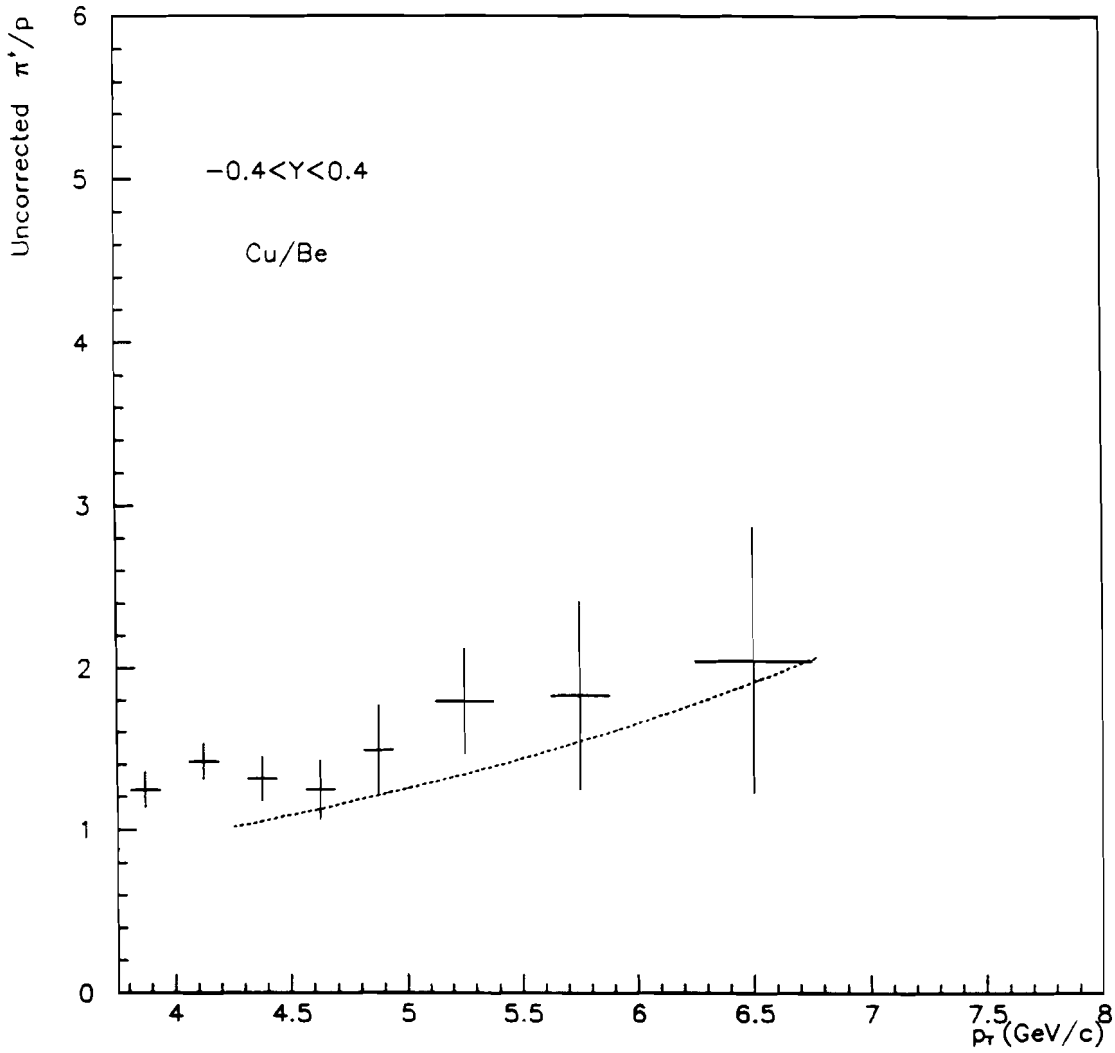

Figure 6.41: Same as Fig. 6.40, in the rapidity range $-0.4 < y < 0.4$.

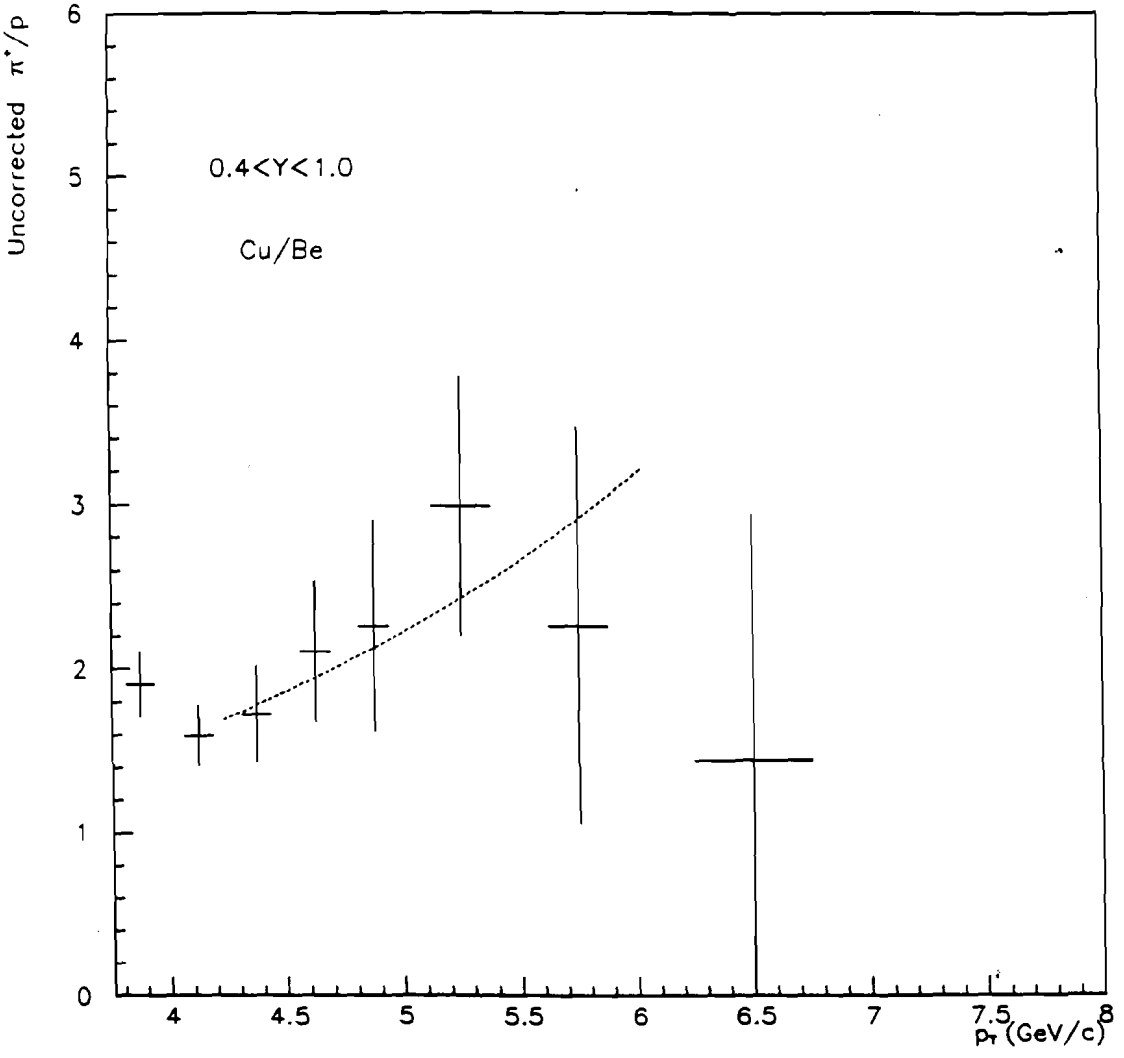

Figure 6.42: Same as Fig. 6.40, in the rapidity range $0.4 < y < 1.0$

significant. Finally, for the distribution of the ratio for the backward rapidities (Fig. 6.40), the experimental points are close to unity over the entire p_T range.

The ratios of the phenomenological fits to the fully corrected π^0 invariant cross sections for incident π^+ and p (see Section 6.3) are also shown in Figs. 6.40, 6.41 and 6.42 (dotted lines). Considering that the ratios from the statistically-poorer fitted data have typical errors of $\sim 20\%$, the agreement between the *uncorrected* and corrected yields can be regarded as quite acceptable.

π^+/p ratios as a function of x_F were also evaluated for the p_T ranges $3.25 < p_T < 4.25$, $4.25 < p_T < 5.0$, and $5.0 < p_T < 8.0\,GeV/c$, and the results are shown in Figs. 6.43, 6.44 and 6.45. Results from the phenomenological fits to the corrected π^0 invariant cross sections for $p_T > 4.25\,GeV/c$, are superimposed on the uncorrected distributions (dotted lines), and are consistent with these. The π^+/p ratios appear to be close to unity (~ 1.5), and increase somewhat with x_F.

Table 6.12 summarizes the above results. The first row gives the mean ratios $(\pi^+ \rightarrow \pi^0)\,/\,(p \rightarrow \pi^0)$, calculated by using *uncorrected* π^0 distributions, integrated over the p_T range from 3.5 to $8.0\,GeV/c$, in the indicated rapidity intervals. Similarly, the second row in the Table gives the mean ratios, this time calculated directly from the experimental cross sections, integrated over the p_T range from 4.25 to $8.0\,GeV/c$, in the indicated rapidity ranges. Although the two sets of results for the mean ratios are not directly comparable because they are calculated in different rapidity intervals, nevertheless corrected and uncorrected mean ratios

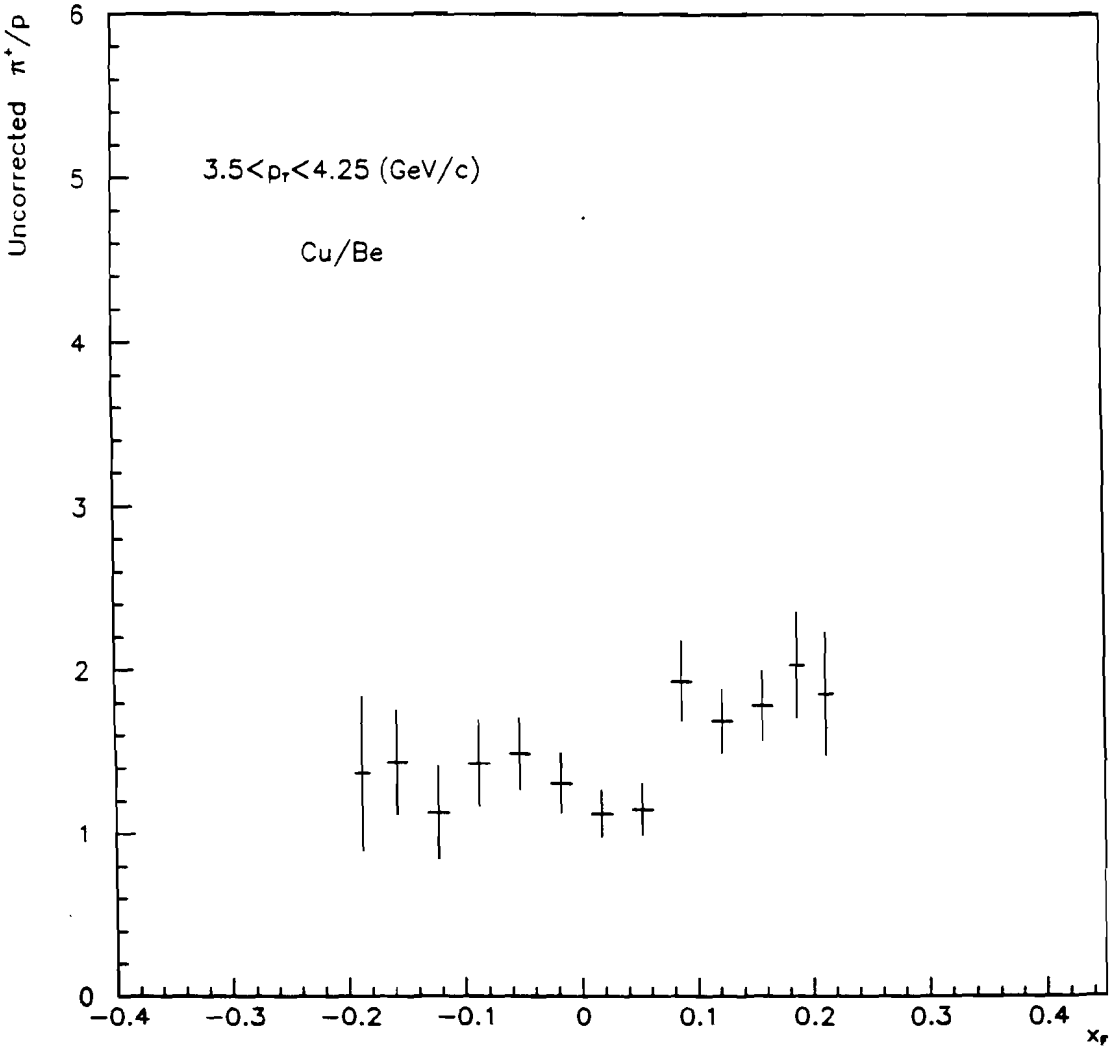

Figure 6.43: Ratio $(\pi^+ \to \pi^0)\,/\,(p \to \pi^0)$ for $Cu + Be$ target as a function of the π^0 x_F, in the p_T range $3.50 < p_T < 4.25\,GeV/c$.

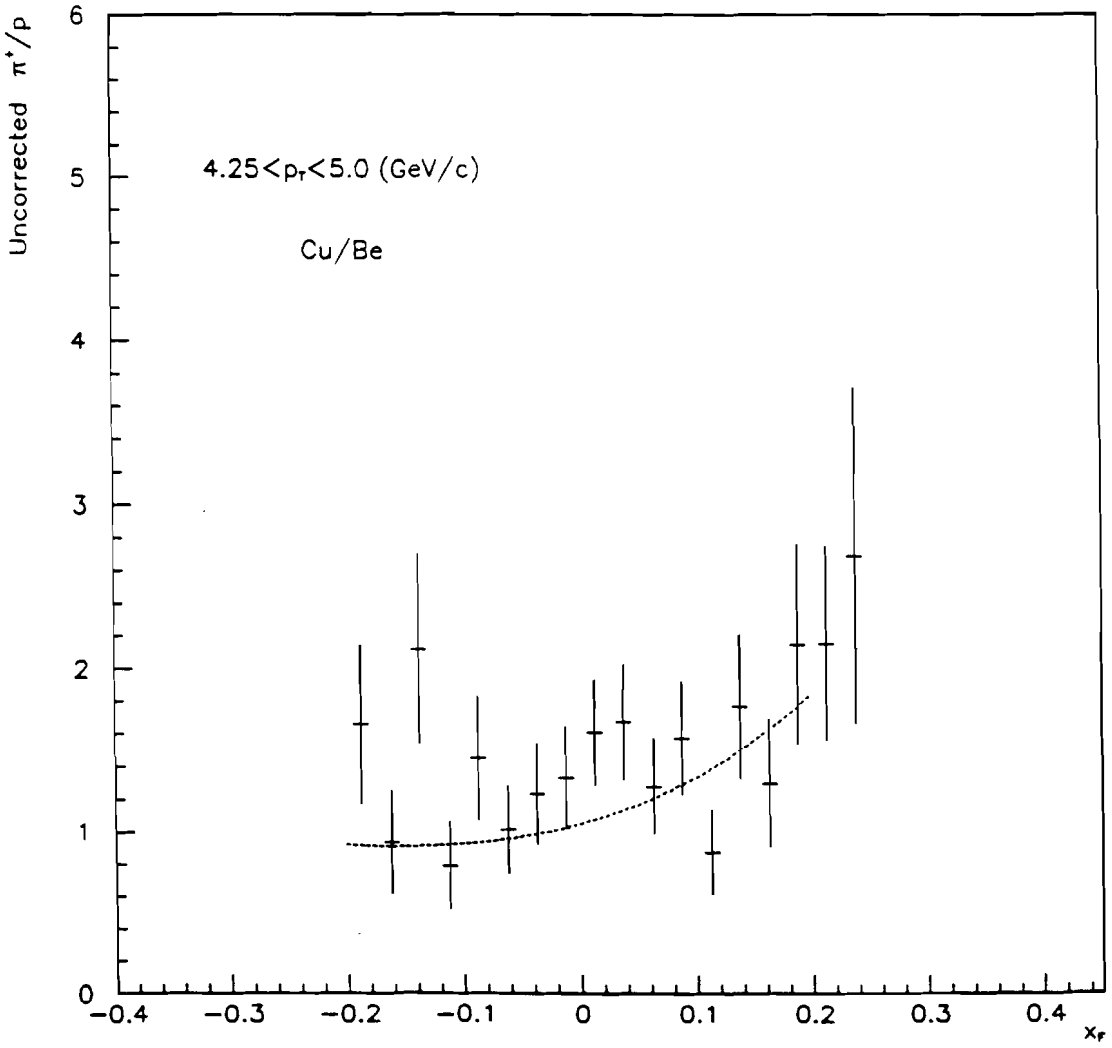

Figure 6.44: Same as Fig. 6.43, in the p_T range $4.25 < p_T < 5.0\,GeV/c$. Superimposed is the ratio of the phenomenological fits to the π^0 invariant cross sections.

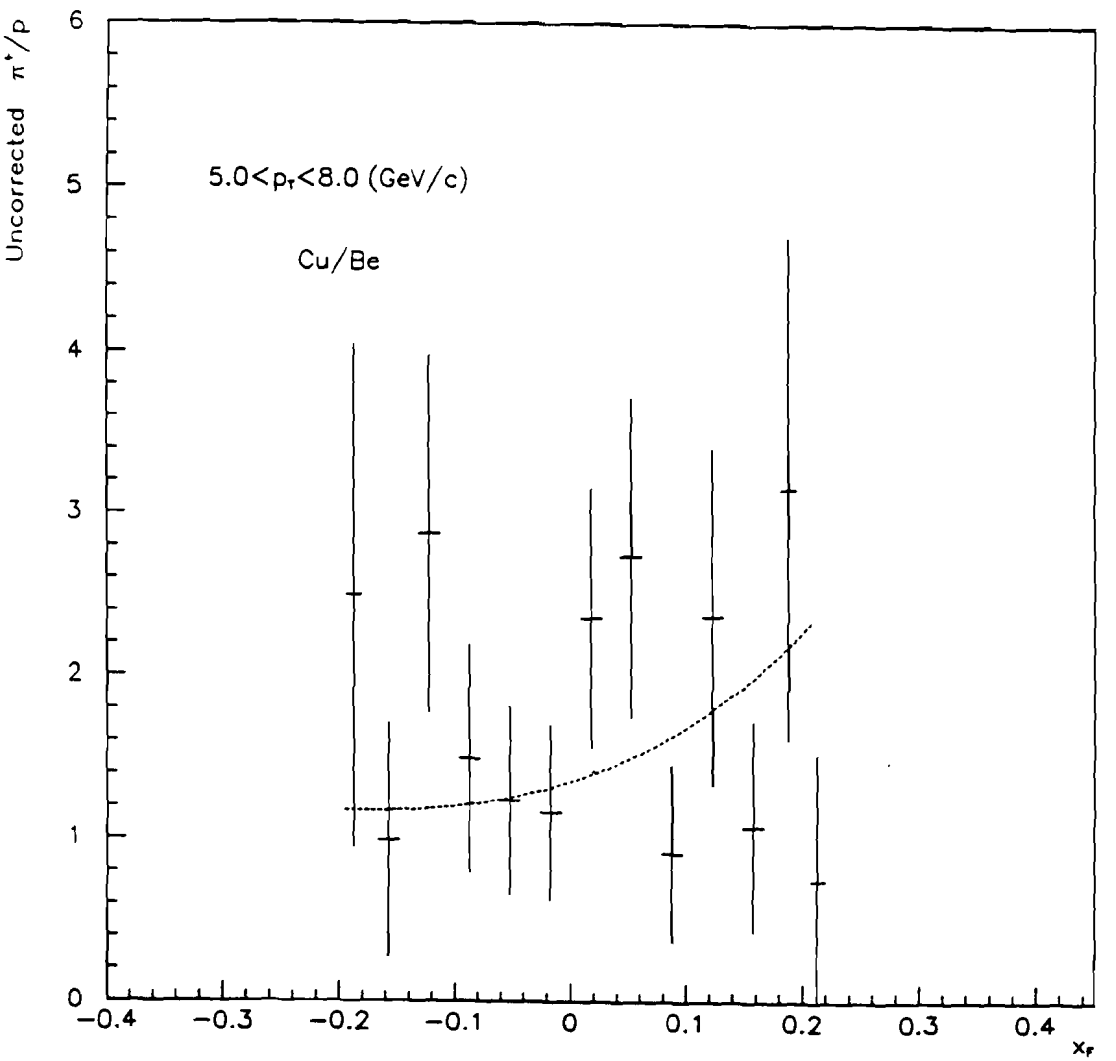

Figure 6.45: Same as Fig. 6.44, in the p_T range $5.0 < p_T < 8.0\,GeV/c$.

Table 6.12: Ratios of π^0 yields for π^+ and p incident beam-particles.

Uncorrected	$\frac{\pi^+ \to \pi^0}{p \to \pi^0}$	$(p_T > 3.5\,GeV/c)$	1.28 ± 0.12 $(-1.0 < y < -0.4)$	1.35 ± 0.06 $(-0.4 < y < 0.4)$	1.81 ± 0.12 $(0.4 < y < 1.0)$
Corrected	$\frac{\pi^+ \to \pi^0}{p \to \pi^0}$	$(p_T > 4.25\,GeV/c)$	0.99 ± 0.15 $(-0.7 < y < -0.2)$	1.21 ± 0.15 $(-0.2 < y < 0.2)$	1.42 ± 0.17 $(0.2 < y < 0.7)$
Uncorrected	$\frac{\pi^+ \to \pi^0}{p \to \pi^0}$	$(-0.2 < x_F < 0.2)$	1.43 ± 0.06 $(3.5 < p_T < 4.25\,GeV/c)$	1.34 ± 0.09 $(4.25 < p_T < 5.0\,GeV/c)$	1.43 ± 0.21 $(5.0 < p_T < 8.0\,GeV/c)$

suggest similar conclusions. Finally, the bottom row of Table 6.12 gives the mean ratios $(\pi^+ \rightarrow \pi^0) / (p \rightarrow \pi^0)$, using uncorrected π^0 spectra, integrated over the x_F range from -0.2 to 0.2, in the indicated p_T ranges. The errors quoted are statistical only.

6.6 Conclusions

The results presented in this thesis are summarized in the following.

We have measured inclusive cross sections for π^0 production at $530\,GeV/c$ using hadron beams. In the x_T range covered by the data, π^0 invariant cross sections behave as p_T^{-n} with $n > 9$, for both negative and positive beams, in agreement with results of previous experiments in similar kinematic regimes, but in contrast with the naive parton model expectation of $n = 4$. As discussed in Chapter 1, the naive parton model prediction is based on the assumption that the only non-scaling quantity in Expression (1.1), for the invariant cross section for production of hadrons at large transverse momenta, is the hard-scattering cross section for the elementary subprocess $(d\hat{\sigma}/d\hat{t})$. Scale violations in the structure and fragmentation functions, and running of the coupling constant α_s (see Chapter 1), can increase the naive expectation for the value of n from 4 to about 6, the exact amount depending on the kinematic region considered. The inclusion of the intrinsic parton momentum k_T (see Chapter 1), can further increase n from 6 to about 8, although the effect is limited to regions of moderate p_T ($< 3\,GeV/c$). Inclusion of additional production mechanisms (meson-quark scattering [59]) could

account for the residual discrepancy between theoretical predictions and experimental distributions.

From the experimental results presented in this chapter and from the considerations outlined in Chapter 1, it appears that theoretical predictions formulated in the framework of perturbative QCD do not provide a consistent description of the processes responsible for the production of large-p_T hadrons, at least in the kinematic regime explored by our data. The perturbative approach seems to provide a more appropriate description of the phenomena at larger energies (see, for example, the ISR data), where QCD with asymptotic freedom (see Chapter 1) has been applied with greater success.

The compilations of π^0 invariant cross sections presented in Figs. 6.27 and 6.28 confirm the existence of scale breaking at fixed x_T, and different center-of-mass energies. As a consequence, the parametrization function (1.4) or (6.10), which factorizes the explicit p_T dependence of the cross section from the dimensionless function $F(x_D)$, does not provide an adequate description of data at different energies ($\sqrt{s}$) and fixed x_T if a constant power (n) of p_T is selected. As an alternative, we propose the functional form (6.14) to describe most of the available data on π^0 production at large p_T.

Concerning the dependence of π^0 production on the nature of particle-type, our results suggest that for negative beam, π^- and K^- particles appear to have equal yields of π^0s at large p_T ($p_T > 3.0\,GeV/c$) for central and forward rapid-

ity regions. For backward rapidities a small enhancement of the π^0 yield for K^- relative to π^- is observed at large p_T ($p_T > 4.0\,GeV/c$). This result is, however, of statistically marginal significance. No direct comparison of the K^- data with previous results published by [21] and [22] can be made since those experiments explore substantially different kinematic regimes. Theoretically, only phenomenological models are available for describing differences of π^0 yields with K^- and π^-. From comparison to one of such models, the results in our kinematic regime do not indicate any suppression of the yield of π^0s for K^- interactions relative to π^-; at large x_F a suppression of 50% is predicted by statistical quark models [23] (see Chapter 1), and this is excluded by our data.

For positive beam, p and π^+ particles contribute differently to the yield of large-p_T π^0s. This is due primarily to differences in the number of elementary constituents in the two beam-particle types, and the internal momenta of these constituents. Our results for the ratios of π^0 spectra confirm similar observations obtained in previous experiments (see Chapter 1), and are consistent with theoretical predictions from QCD and phenomenological models describing production of hadrons at large p_T. For example, according to the Constituent Interchange Model (*CIM*) [59] meson beams are predicted to be more effective in producing particles at large x_T because of the fewer number of beam constituent spectators. We indeed observe an overall larger yield of large-p_T π^0s in the π^+/p ratio, which increases with p_T, in central and forward rapidity regions, consistent with the

above interpretation. At fixed p_T, the yield of π^0s increases for forward rapidities. This increase can be understood in terms of simple quark dynamics, where on average valence quarks in the meson carry $\sim 3/2$ larger momentum fractions than the quarks in the proton. Thus the increase of the π^0 yield with increasing rapidity for π^+ relative to proton can be related to the motion of the parton-parton center-of-mass system which is different for π^+ and proton collisions with nucleons (see Chapter 1).

Finally, using the ratios of π^0 yields for negative beam, and the measured π^0 invariant cross section in π^- interactions, we calculated the π^0 invariant cross section as a function of p_T, for $p_T > 3.5\,GeV/c$, for $530\,GeV/c$ K^- on the $Cu + Be$ target. This is the first measurement of this kind in this kinematic regime. Previous measurements using K^- beams correspond to center-of-mass energies 5 to 10 times lower than the present data.

In conclusion, we have measured π^0 production at large p_T, for different incident particles (π^+, π^-, K^- and p), from a partial data sample of events recorded during the 1987-1988 Fermilab fixed-target run of the E706 spectrometer. Our data have been used to study broad issues of scaling and will be of value in future investigations of constituent fragmentation and general tests of QCD.

We should not let ourselves be burnt for our opinions: we are not that sure of them. But perhaps for this: that we may have and change our opinions.

Friedrich Nietzsche

Bibliography

[1] D.J. Gross and F. Wilczek, Phys. Rev. Lett. 30, 1343 (1973).

[2] D.J. Gross and F. Wilczek, Phys. Rev. D8, 3633 (1973).

[3] H.D. Politzer, Phys. Rev. Lett. 30, 1346 (1973).

[4] G. Altarelli and G. Parisi, Nucl. Phys. B126, 298 (1977).

[5] R. Cutler and D.Silver, Phys. Rev. D16, 679 (1977); Phys. Rev. D17, 196 (1978).

[6] B.L. Combridge et al., Phys. Lett. 234 (1977).

[7] S.D. Ellis et al., Rev. Mod. Phys. 49, 753 (1977).

[8] J.F. Owens, "Large-Momentum-Transfer Production of Direct Photons, Jets and Particles", Rev. of Modern Physics, V 50, 2, 465 (1987).

[9] R.K. Ellis "Large Transverse Momentum and Higher Twist Phenomena", Fermilab-Conf-88/162-T, Nov 1988.

[10] P. Aurenche et al., Nucl. Phys. B286, 509 (1987).

[11] P. Aurenche et al., Nucl. Phys. B297, 661 (1988).

[12] D. Antreasyan et al., Phys. Rev. D19, 764 (1979).

[13] H. Frisch et al., Phys. Rev. D27, 1001 (1983).

[14] A.L.S. Angelis et al., Phys. Lett. 79B 505 (1978).

[15] F.W. Busser et al., Nucl. Phys. B106 1 (1976).

[16] A.G. Clark et al., Phys. Lett. 74B 267 (1978).

[17] G. Donaldson et al., Phys. Lett. 73B 375 (1978).

[18] G. Donaldson et al., Phys. Rev. Lett. V36 19 1110 (1976).

[19] J. Povlis et al., Phys. Rev. Lett. V51 11 967 (1983).

[20] J. Antille et al., Phys. Lett. B 194 4 568 (1987).

[21] F. Paub et al., Z. Phys. C Particles and Fields 27 211 (1985).

[22] J. Badier et al., Phys. Lett. 93B 354 45 (1980).

[23] V.V. Anisovich, V.M. Shekhter, Nucl. Phys. B55 455 (1973).

[24] J. Badier et al., Z. Phys. C Particles and Fields 30 7 (1986).

[25] V. Ajinenko et al., Z. Phys. C Particles and Fields 35 7 (1987).

[26] M. Aguilar-Benitez et al., Z. Phys. C Particles and Fields 34 419 (1987).

[27] H.J. Frisch et al., Phys. Rev. D19, 764 (1979).

[28] C. De Marzo et al., Physical Review D36 1 16 (1987).

[29] M. Bonesini et al., Z. Phys. C Particles and Fields 37 39 (1987).

[30] H.U. Bengtsson et al., Comp. Phys. Comm. 34 251, (1985) and Comp. Phys. Comm. 27 243 (1982).

[31] M. Bonesini et al., Z. Phys. C Particles and Fields 38 371 (1988).

[32] A.S. Carroll et al., Phys. Lett. 80B 3 319 (1979).

[33] Multi Wire Proportional Chamber Readout System, MPWC-1, Nanometric Systems, Inc., 451 S. Boulevard Oak Park, Il. 60302.

[34] E. Engels et al., Nucl. Instr. and Meth. A253, 523 (1987).

[35] C.A. Nelson Jr et al., Nucl. Instr. and Meth. 216, 381 (1983).

[36] W.E. DeSoi, Ph.D. Thesis, U. of Rochester, (1990), unpublished.

[37] U. Amaldi, Physica Scripta, V23, 409-424 (1981).

[38] C. Lirakis, Ph.D. Thesis, Northeastern University (1989).

[39] C.W. Fabjan CERN-EP/85-54 (1985).

[40] T.D. Droedge, K.J. Turner and T.K. Ohska, Fermilab note PIN 52H/CDF-119 (1982), unpublished.

[41] T.F. Droedge, F. Lobkowicz and F. Fukushima, IEEE Trans. Nucl. Sci. NS-25 (1978).

[42] K.J. Turner et al., Fermilab note PIN 77A (1983), unpublished.

[43] P.R. Evans, "Ionization Chambers" London, Richelieu 404 (1974).

[44] R. Wigmans, Nucl. Instr. and Meth. A259 389, (1987).

[45] C. Yosef, Ph.D. Thesis Northeastern University (1990), unpublished.

[46] K.W. Hartman, Ph.D. Thesis Pennsylvania State U. (1990), unpublished.

[47] A. Sinanidis, Ph.D. Thesis Northeastern U. (1989), unpublished.

[48] R. Ford and W.R. Nelson, SLAC pub 210 (1978).

[49] D. Skow, private communication.

[50] R. Brun, GEANT3, CERN DD/EE/84-1.

[51] G. Alverson, E706 Internal Note 139 (1985).

[52] J. Kleinard, J. Zoll, PATCHY REFERENCE MANUAL, CERN PROGRAM LIBRARY, CERN, (1983), unpublished.

[53] R. Brun, M. Goosens, J. Zoll ZEBRA, CERN PROGRAM LIBRARY Q100, DD/EE/85-6, CERN (1985), unpublished.

[54] DI3000 User's Guide, Precision Visuals, Inc. Boulder, Colorado (1984)

[55] J.P. Mansour, Ph.D. Thesis University of Rochester (1990), unpublished.

[56] S. Easo, Ph.D. Thesis Pennstate Univeristy (1989), unpublished.

[57] I. Kourbanis, Ph.D. Thesis Northeastern University (1989).

[58] R.G. Kennet et al., Nucl. Phys. B177, 1 (1981).

[59] R. Blankenbecler et al., Phys. Rev. D, 12 11, 3469 (1975).